Electron crystallography of nanoparticles

Erica Cordero Oyonarte

Normandie Université

UNIVERSITÉ CAEN NORMANDIE

THÈSE

Pour obtenir le diplôme de doctorat

Spécialité **CHIMIE**

Préparée au sein de l'**Université de Caen Normandie**

Electron crystallography of nanoparticles

Présentée et soutenue par

ERICA CORDERO OYONARTE

Thèse soutenue le 07/11/2024

devant le jury composé de :

M. PHILIPPE BOULLAY	Directeur de recherche au CNRS - ENSICAEN	Directeur de thèse
MME VALERIE PRALONG	Directeur de recherche au CNRS - Université de Caen Normandie (UCN)	Président du jury
M. DAVID GONZALEZ CALATAYUD	Maître de conférences - Universidad Autonoma de MADRID	Membre du jury
MME MARIA TERESA CALDÈS	Chargé de recherche HDR - Institut des matériaux Jean Rouxel	Rapporteur du jury
M. PASCAL ROUSSEL	Directeur de recherche au CNRS - ECOLE NATIONALE SUPERIEURE de CHIMIE	Rapporteur du jury

Thèse dirigée par **PHILIPPE BOULLAY** (Laboratoire de cristallographie et sciences des materiaux (Caen))

ED 591 PSIME

RISMA

ACKNOWLEDGEMENT

First of all, I would like to express my deepest gratitude to my thesis supervisor, Philippe Boullay, for his endless patience and for sharing with me both his technical knowledge of TEM and his crystallographic expertise, which have enabled me to carry out this project.

I am also grateful to the NanED project for giving me the opportunity to experience enriching moments that have helped me grow as a researcher. In particular, I would like to thank Mauro Gemmi and Joke Hedermann for welcoming me into their research groups and sharing their knowledge on the use of different microscopes and disciplines, as well as showing me new ways of organization and teamwork. My gratitude also goes to all the PhD students in NanED, who, despite the distance between countries, have been a fundamental support, both in theoretical matters and on a personal level. A special thanks to Sara Passuti, my office mate and friend, for her unconditional support throughout these years.

I would also like to extend my thanks to all my collaborators, whose roles have been essential to this project. Luca Rebecchi, Ilka Kriegel, Ana Castellanos-Aliaga, and David Portehault for providing me with the key samples for my research. Lukas Palatinus for sharing his deep knowledge of dynamical refinement. Valerie Pralong and Armance Sagot for teaching me the basics of synthesis and electrochemical measurements. A very special thank you to David González Calatayud for his tireless efforts to find interesting samples for my project, his concern for my future, and his valuable advice on my professional development.

I would also like to thank the administrative staff of the CRISMAT laboratory, and researchers such as Olivier Pérez and Carmelo Prestipino, who helped me with X-ray diffraction techniques, both in the experimental part and in data analysis.

A very special acknowledgment to my family, whose emotional support has been invaluable. Being abroad and away from home hasn’t been easy, but their closeness and constant encouragement have been crucial in getting through this stage.

Lastly, thank you to the members of the jury for agreeing to be part of this process and for evaluating this thesis.

TABLE OF CONTENTS

INTRODUCTION

Electron diffraction for structural crystallography has grown considerably after the development of dedicated protocols for data acquisition and analysis, to the point where it was listed in Science magazine as one of the major scientific breakthroughs of the year 2018[1]. The so-called "3D" electron diffraction[2] (3D ED) is a novel method for atomic structure determination of inorganic, organic and macromolecular compounds when their crystal size falls in the scale of few tens of nanometer or even below. In many cases, compounds of high commercial value or with medical applications, are in fact available only as nanocrystals or show phase/polymorphic transitions during crystal growth. 3D ED is an extraordinary new tool to disclose the nature of all these nanocrystalline materials, shedding new light and bringing new knowledge into different scientific fields, from materials science to physics of diffraction, from instrument engineering to chemical production and pharmacology.

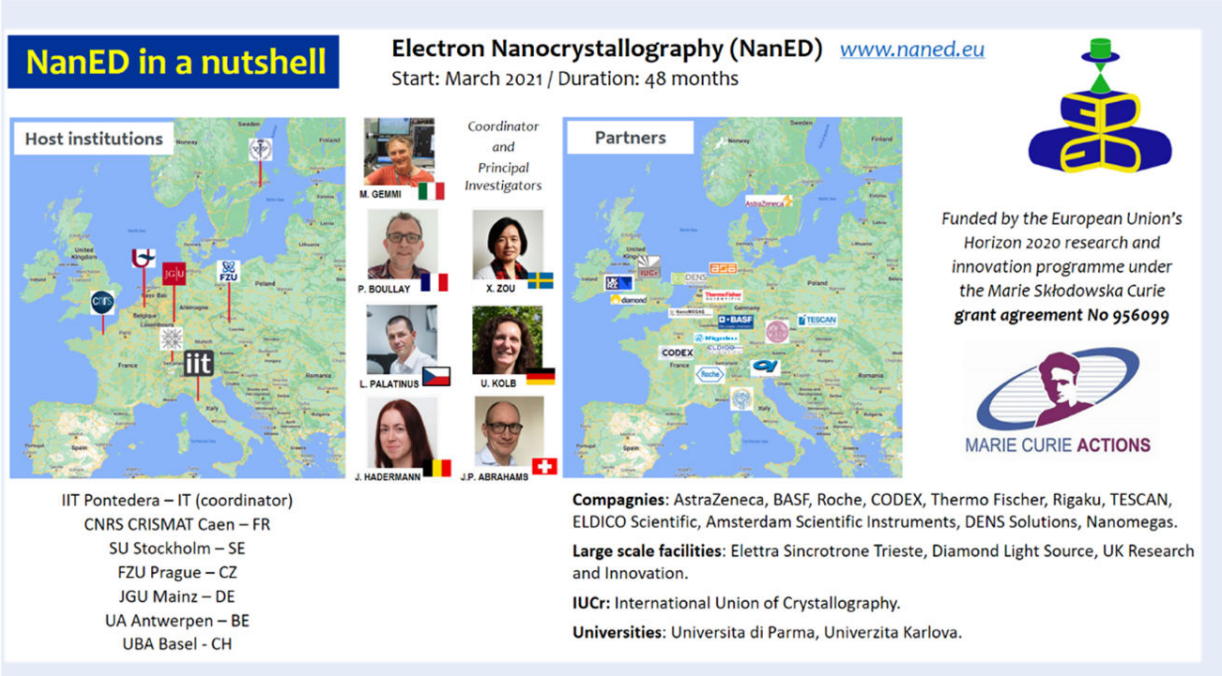

***Figure 1**. 3D Electron Diffraction framework: Host institutions, supervisors and partners involved.*

Up to now, the development of 3D ED has remained limited to a few laboratories and has been slowed by the lack of young researchers trained in this field at PhD level. To address this issue, several European scientists active in the field and a group of small and large companies have decided to join forces (**Figure 1**). This took shape within the framework of the Marie Skłodowska-Curie European Innovative Training Networks (ITN), where the Electron Nanocrystallography (NanED) project has been selected under the grant agreement N°956099. As a training program, NanED aims to train a new generation of electron crystallographers, able to master and develop 3D ED techniques in an interdisciplinary and interconnected network. An intensive program was planned, with participation in several schools and periods of secondment to academic and industrial partners (see list in Appendix 1). These activities lasted around 6 months in total.

As a research program, NanED aims to boost the dissemination of 3D ED in academic and industrial laboratories with two main objectives:

1- Develop 3D ED to make it more efficient and accessible by establishing optimized and portable strategies for sample preparation, data collection and analysis.
2- Apply 3D ED to different types of compounds and materials, from cement to macromolecules.

These objectives are reflected in 4 scientific work packages and involve 14 PhD students in 7 academic centers. Each PhD student is assigned an "early-stage research" (ESR) project. The work presented in this manuscript is part of the work package 4 (WP4) entitled *crystallography beyond nanocrystals* and concerns the ESR 13 *Electron Crystallography of Nanoparticles* (**Figure 2**). WP4 aims to expand the applicability of 3D ED to complex nanomaterials and define a “Road Map to Nano”. Nowadays, nanoparticles and nanostructured materials are produced by large-scale industry and infiltrate our daily lives due to their wide range of uses as a functional material: high mechanical quality materials, absorbents, smart glasses, battery electrodes, cosmetics, food additives or health care. Most of the nanoparticles on the market possess a simple and known crystal structure (silica, silver, titanium dioxide, zinc oxide, …). Nonetheless studies involving nanoparticles tend to develop towards more complex systems

potentially leading to more complex crystal structures, raising the question of how far 3D ED can help us understand their fine structure.

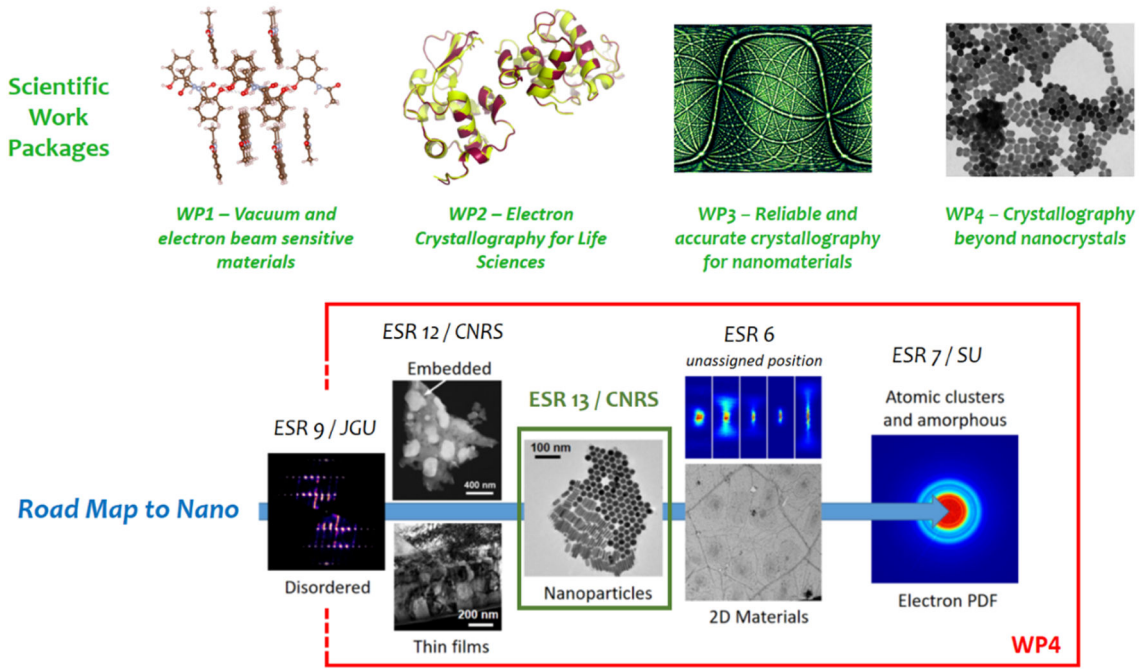

***Figure 2**. The scientific part of NanED project is divided into 4 work packages. The work carried out as part of my thesis falls withing work package number 4.*

This thesis is structured into five chapters. The first two chapters provide an overview of how nanoparticles (NPs) have driven advancements in different scientific fields and examine the structural characterization techniques commonly employed. Given that this research primarily focuses on exploring the crystal structure of individual NPs using 3D ED (a method that offers distinct advantages over other techniques for studying nanomaterials) a comprehensive review of the theoretical concepts essential for understanding this work is also included.

The following chapters will focus on the results of the different cases studied. In the first experiment 'Round Robin experiment', all 14 PhD students involved in this project participated. For this experiment, two inorganic compounds were provided, which initially had unknown structure to us but were already known in the literature. Datasets were collected using different microscopes and setups to obtain a comprehensive overview of how accurate the 3D ED technique can be. The subsequent experiments will focus on the main goal of this thesis, which was establishing protocols for acquiring high-

quality data from NPs with crystal sizes below 100 nm and to proceed with their structural analysis. For this purpose, the work was divided into two categories: large NPs (with lateral dimensions between 70 and 30 nm) and small NPs (ranging from 20 to 10 nm in diameter). For the large NPs, the synthesized and studied compound was TiO_2 brookite. A detailed study was performed using different microscopes and data acquisition protocols, and the final structure obtained was compared with a reference structure from literature to demonstrate the reliability of the results. However, when attempting to apply these protocols to the small NPs, where the studied compounds were TiO_2 anatase and ITO, different challenges arose. Consequently, Chapter 4 will discuss the challenges, solutions, and limitations associated with small NPs analysis by 3D ED.

Finally, once the protocols for data acquisition on NPs of different sizes are established, we will apply them to "real" cases and see how 3D ED can provide information to help chemists and material scientists in their research. The first case will involve detecting light atoms, in particular Lithium (Li), in the previously mentioned TiO_2 brookite NPs. The second case will focus on determining the ratio of Mg and Li atoms that occupy the same atomic position in the $MgTi_2O_5$ compound. Both cases have potential future applications in battery technology. The final case will focus on catalytic applications, where the goal was to check whether there is any ordering between Cu and Si in the $CuSi_2P_3$ compound.

CHAPTER 1

NANOPARTICLES

NPs are generally described as nano-sized crystals with at least one dimension (length, width, or height) within the nanometer scale. In this thesis, we are going to consider the biggest limit at 100nm. In 1959, the American physicist Richard Feynman first introduced the term nanotechnology [3], and since then, this field continues to be in development. Throughout this thesis, NPs will be the material of interest, and different characterization techniques will be addressed. NPs hold substantial attention across diverse fields due to their unique attributes and the potential advantages they present. One of the primary factors driving interest in these materials is their size dependent behavior, a characteristic not observed in bulk materials [4]. Therefore, throughout this Chapter 1, we will present different cases where NPs have significantly enhanced properties across different scientific fields (see **Figure 3**).

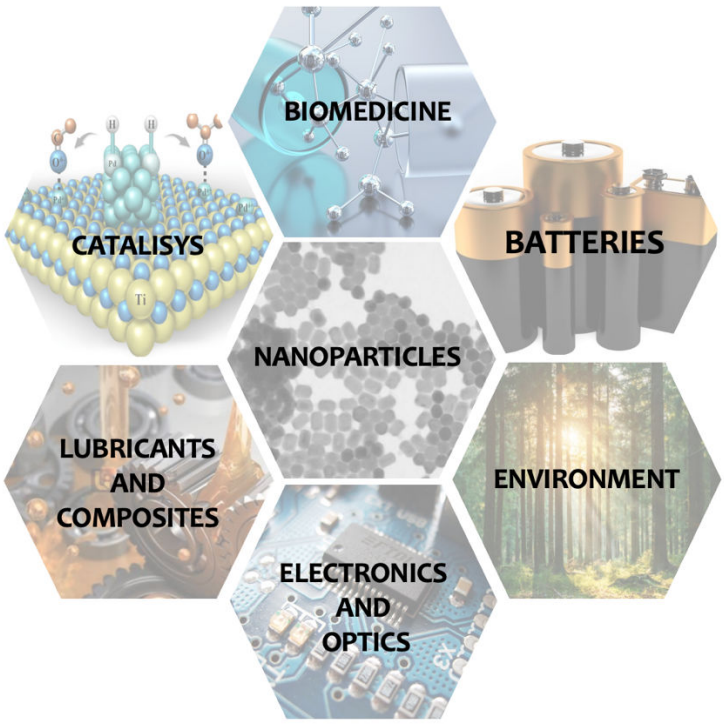

Figure 3. *Nanoparticles and its applications in different scientific fields.*

1.1. The importance of NPs in different scientific fields

1.1.1. Electronics and optics

NPs have revolutionized the field of electronics and optics, providing significant advancements. These miniaturized materials, including noble metals, semiconductors, oxides, and alloys, have been integrated into electronics devices, leading to products with prospects for improvement in the coming decades. In particular, emphasis has been placed on developing flexible, foldable, and stretchable electronic devices, as well as devices for applications in electrophotonics [5].

A more detailed understanding of the critical electronic properties at the nanoscale has allowed greater control over the interaction between materials and processes, promoting a new era of more precise and higher-performing electronic devices. Moreover, this success has also brought great interest and investment to the sector, reflected in the exponential growth of companies and private capital invested in nanotechnology. Nearly 900 companies were involved in the development of nano-engineered materials and devices in 2015, with private investment reaching a global value of 1 trillion dollars, thus highlighting the economic and technological impact in this area, which will continue to be omnipresent, especially in the electronic industry, offering some new-generation products with increasingly greater structural and dynamic complexity.

For instance, among areas where these advances have had a significant impact are displays or devices that can stretch without losing their properties. The nanofabrication employed to manufacture superconductors based on quantum wires are a key asset for 21st century nanotechnology. The improvement and competition of conventional transistors with the arrival of MOSFETs[6] (metal oxide semiconductor-field- effect transistors). The use of silver NPs inks in circuit boards, CMOS [7] (complementary metal-oxide semiconductors) have helped to improve flexibility properties.

Therefore, nanoparticles play a critical role in advancing electronics and optics, serving as the cornerstone for the next generation of high-performance electronic devices and optical systems. These technological advancements stand as a clear demonstration of the transformative power of nanoscale technologies.

1.1.2. Catalysis

NPs, especially supported metal nanoparticles (M-NPs), have been a crucial component in catalyzing chemical reactions, mainly in oxidations and hydrogenations. These nanoparticles typically include metals such as Copper (Cu), Gold (Au), Platinum (Pt), Palladium (Pd), Ruthenium (Ru), Silver (Ag), Cobalt (Co), and Nickel (Ni), all valued for their distinctive catalytic properties[8].

M-NPs are noted for offering a high surface-to-volume ratio and high zeta potentials, which prevent the aggregation of nanoclusters and allow for improved catalytic activity per unit area. These properties are critical because as the particle size decreases, the percentage of atoms on the surface significantly increases, enhancing catalytic efficacy[9]. Moreover, the ability to recycle and reuse these catalysts without cross-contamination with the final product offers considerable economic and environmental advantages.

Specifically, copper nanoparticles (Cu-NPs)[10] are used in organic reactions such as Suzuki and Heck reactions, where these copper-based catalysts have demonstrated high activity and selectivity, as was the case in the oxidation of methylene blue using Cu-NPs, achieving 99% activity. Gold nanoparticles (Au-NPs)[11] have transformed the perception of catalysis due to their efficiency in low-temperature reactions, such as CO oxidation and selective hydrogenation of nitro compounds. Gold shows high selective toward desired products in various reactions. Platinum nanoparticles (Pt-NPs)[12] have been extensively used in reducing emissions in automobiles and in energy production in fuel cells, effective in the oxidation of organic compounds and in the reforming of ethanol to produce hydrogen. Ruthenium nanoparticles (Ru-NPs)[13] have been essential in the hydrogenation of biomass-derived compounds, transforming them into high-value liquid fuel components. Silver nanoparticles (Ag-NPs)[14] are well-known for their use in the oxidation of alcohols and in the reduction of nitro aromatic compounds to amines. Lastly, cobalt (Co-NPs) and nickel nanoparticles (Ni-NPs) [8,15] have been recognized as effective in Fischer-Tropsch processes to produce liquid fuels from synthesis gas and in the methanation of CO_2 respectively.

1.1.3. Lubricants and composites

Investigating how two surfaces interact when they come into contact, resulting in friction and wear phenomena, is very important in the field of lubricants to improve their

properties[16]. This is crucial for optimizing energy efficiency and reducing wear on machinery. Lubricants, derived from mineral oils or synthetic blends, require additives to meet the specifications set by the original equipment manufacturers, offering significant improvements such as antioxidation, tribological characteristics, and thermal properties.

In the energy sector, studies have determined that up to the one-third of fuel energy can be lost due to friction in vehicle components such as engines and brakes. The emergence of advanced friction reduction technologies could significantly decrease these losses in the coming years, thus representing a considerable economic saving on a global scale[17].

Lubricants consist of a base oil and additives that enhance specific properties. These base oils can be mineral, synthetic, or biological, chosen according to the application´s requirements. Mineral oils are the most common and are derived from petroleum, while synthetic oils offer superior performance in extreme conditions, and biological oils are preferred in both the food and pharmaceutical industries due to their low risk of contamination.

Among the additives, nano-additives[18] emerge as a very powerful solution due to their ability to act at the microscopic level, offering thermal stability and appropriate surface reactivity. The nano-additives used can be of various types such as metals, metal oxides, carbon materials, and boron-based nanoparticles, each with specific properties and applications that help to reduce friction and wear. In particular, the use of nanoparticles like TiO_2, ZnO[19], and more complex compounds such as Al_2O_3/TiO_2[20] nanocomposite, have been shown to significantly improve wear resistance and reduce friction among various lubricant systems. Moreover, these additives are effective not only in mineral and synthetic oils but also in chemically modified biological bases such as epoxidized vegetable oils.

The tribological properties [20] of nano-carbons such as fullerenes, nanotubes, and graphene are notable for their potential to favorably modify friction and wear characteristics due to their unique structure and ability to form protective films between contact surfaces.

In summary, the incorporation of nanoparticles into lubricants represents a promising advancement for lubrication technology, with the potential to improve energy efficiency, extend the lifespan of machinery, and reduce environmental impact through more effective and ecologically rational formulations.

1.1.4. Batteries

The implementation of nanotechnology and the application of advanced methods have overcome many of the limitations that traditional batteries faced[21]. One of the areas that has been most explored is Li rechargeable batteries[22], which currently dominate this field. The ability to control shape and size at the nanometric level has been crucial. These nanostructures enable shorter diffusion times, high stability during charge/discharge, and for enlarged surface more efficient electrochemical reaction something that was not possible at the bulk.

These nanostructured materials have improved the capacity, stability, and efficiency of batteries as they offer optimized channels for ion and electron transport, and also act as catalysts or traps for active intermediaries. Below are some examples where these materials have been relevant.

In the case of cathodes, silicon and titanium have shown a considerable increase in specific capacity due to their ability to form alloy compounds with Li. Specifically, for silicon, its performance has improved almost 9 times compared to traditional graphite. Additionally, in the case of Li iron phosphate ($LiFePO_4$)[23], regarding the reduction of their particle size to the nanoscale significantly enhance their performance, allowing for a faster and more efficient charge/discharge process, often demanded in high power applications. In the case of anode materials, the development of solid electrolytes has led to improvements in safety issues associates with liquid electrolytes. In the case of 3D electrodes, they have allowed an increase in volumetric capacity and safety, promoting higher energy densities and longer lifecycles compared to thin-film technology. Lastly, although these materials are based on carbon, presenting challenges in terms of capacity and cycle stability, these nano-scale modifications (carbon nanostructures) have enabled significant improvements, achieving reversible capacities over 1000 mAh/g.

In summary, the use of nanotechnology in batteries is not only a promising advance to improve energy density and charging efficiency, but it is also crucial for integrating renewable energy sources such as wind, water, and solar into the electrical network. This is due to the ability of improved batteries to handle high charges and discharges without significant degradation, which is essential for efficiently storing energy when these sources are not available. Therefore, control over the morphology of these nanomaterials is a critical factor to highlight that allows the exploration of unique physical and chemical

properties, thereby preparing the way for a next generation of batteries with better performance and greater safety.

1.1.5. Environment

Currently, there are many causes for which the environment can be damage or deteriorated. Below, some examples will be shown where advances in nanotechnology have helped to create more environmentally friendly applications.

In the case of contaminant detection, some these nanomaterials have the capability to identify toxins and chemicals at extremely low levels, facilitating more efficient early interventions[24]. Decontaminating soils and groundwater is another task for nanomaterials, capable of absorbing and decomposing pollutants more efficiently than conventional technologies. For this, certain metals such as iron or zinc are used to effectively treat contaminated waters. There are also NPs that can be injected directly into the contaminated site and are capable of neutralizing or decomposing the present contaminants, such as heavy metals or volatile organic compounds. Titanium dioxide nanoparticles (TiO_2) are essential in water purification, showing better results in the removal of contaminants and pathogens.

Automobiles generate around 18% of CO_2 emissions, the main gas responsible for the greenhouse effect. The development of nanocatalysts has been able to reduce emissions of these harmful gases, ensuring they meet environmental standards without compromising their performance. These catalysts can not only be applied in the automobile field, but it is also possible to use them in industrial plants minimizing the formation of pollutants from their origin, thus reducing their subsequent treatment and release of ultrafine particles and other contaminants.

In agricultural productivity[25], nanofertilizers and nanoherbicides significantly improve the health of plants and increase their productivity, ensuring a more efficient use of resources such as water and nutrients, which is key to facing demographic growth and climate change. These activities are also aimed at reducing the amount of chemicals released into the environment to minimize pest resistance and contamination. Nanotechnological biosensors also allow for rapid and precise detection of pathogens and the assessment of plant health, favoring more informed and timely agricultural

interventions. Finally, there are also nanoparticles that allow for controlled release of fertilizers reducing the environmental impact due to less nutrient leaching.

In conclusion, these nanotechnological advances offer multiple benefits for the protection and improvement of the environment, enhancing efficiency in the various sectors mentioned above, and allowing for more suitable management of natural resources.

1.1.6. Drug delivery and health care

Nanoparticles are nanomaterials that can have different shapes, surface areas, reactivity, higher efficiency, and lower toxicity[26]. Thanks to all these properties, they have become an important icon in the world of healthcare. Their use in improving the delivery and efficacy of medications allows for targeted and controlled administration of drugs to specific tissues with minimal side effects, thereby enhancing the bioavailability and stability of the medications. By encapsulating the drugs within nanoparticles, the active ingredients are protected from the external environment, resulting in better stability and absorption in the body. These nanoparticles also have the capability to target specific tissues or cells, such as tumors, improving the effectiveness of the treatment and reducing damage to healthy cells. They also allow for controlled and sustained release of medications, which is crucial for treatments requiring consistent, regulated dosing to be more effective. Some specific examples of these nanoparticles could be liposomes and micelles, which are used as vehicles to transform lipophilic and hydrophilic drugs, improving the solubility and delivery of medications. These nanoparticles are biodegradable biopolymer-based nanoparticles and allow the encapsulation of drugs within a shell that targets specific cells, releasing the medication in a controlled manner. They are becoming increasingly important in healthcare applications[27] due to properties such as biocompatibility, biodegradability, non-toxicity, and stability, as these nanomaterials are derived from natural sources such as animals, plants, algae, fungi, and bacteria.

Superparamagnetic nanoparticles[28] are commonly used in magnetic resonance imaging (MRI) to enhance the visualization of tumors and other pathologies.

Moreover, their use as a protective barrier is very effective due to their antibacterial and antifungal properties, as is the case with silver nanoparticles (AgNPs)[29], which are capable of releasing silver ions that have been proven effective against more than 650

types of bacteria, fungi, and algae. These nanoparticles have a wide use in antimicrobial textiles, such as in the manufacture of clothing, socks, and other textiles that require these antimicrobial properties to prevent odors or the transmission of infections, or even in medical equipment as coating to prevent bacterial and fungal infections in hospitals.

Their versatility and exceptional properties, position nanoparticles as a focal point of research and development in cutting-edge technology and innovative solutions. Consequently, the characterization of those materials to understand their morphology, crystalline structure, size distribution, coating, and physical properties is essential to define the nanotechnology applications of those novel materials. Such detailed understanding of nanoparticle characteristics not only aids to maximizing their potential in various fields but also plays a crucial role in the ongoing development and innovation within the nanotechnology area.

1.2. NP characterization

The study of structure properties in a material is facilitated by the interaction of matter with radiation. To analyze phenomena unfolding at the atomic scale, the wavelength of the radiation must approximate or be smaller than the interatomic distances which are of the order of 0.1 nm (1Å). Consequently, X-rays, neutrons, and electrons stand out as the predominant radiations employed for the meticulous exploration of condensed matter using diffraction techniques.

Since its beginnings in 1895, X-ray techniques have improved their performance with the development of faster detectors, much more effective processing algorithms, more powerful energy sources, and the development of direct methods to address the phase problem. Thanks to all these advancements, this technique has become one of the most used in the characterization of materials including nanomaterials. The most common method for the ab initio determination of crystal structures is single crystal X-ray diffraction (SCXRD) and, when available, structure determination based on SCXRD will be used in this thesis as “reference structure”. However, it has severe limitations when applied to nanoparticles due to the sample size. Indeed, the size of nanoparticles is often well below the typical crystal dimensions of a single crystal used in SCXRD (few μm3) even considering synchrotron radiation as a source. Nanoparticles may contain a relatively small number of unit cells, making it challenging to obtain a diffraction pattern

with sufficient intensity for analysis. Considering diffraction techniques only, one way to circumvent this is to collect X-ray diffraction data for an assembly of nanoparticles to increase the scattered signal. This is typically done in Powder X-ray diffraction (PXRD) which can provide useful information when the structure of the nanoparticles can be extrapolated from an already known "reference structure". If, due to peak broadening and overlapping, the PXRD pattern cannot be clearly identified as related to a known crystal structure, then PXRD might be of limited help. Nevertheless, this technique is still the most widely used for nanoparticle analysis, and is therefore an important point of comparison for the results we'll obtain with 3D ED. For these reasons, in what follows, I will present a few elements related to SCXRD and PXRD.

1.2.1. Powder X-rays Diffraction Technique

The technique is used on crystalline powder sample (bulk characterization technique), where it is assumed that the crystals are in different orientations and enough to get reproducible diagrams. A powder diffractometer can be presented in either Bragg-Brentano (reflection) or Debye-Scherrer (transmission) configuration (see **Figure 4**), with the latter being the configuration used in this thesis, in particular capillary geometry experiments. To perform experiments using this specific setup, a monochromatic X-ray beam of a given energy, which typically uses molybdenum (Mo) or Copper (Cu) in a conventional laboratory diffractometer, is aimed at the sample. These photons then reach the capillary that contains the sample, which is composed of numerous crystals oriented in different directions. The sample is continuously spinning throughout the experiment. Finally, a diffraction takes place and is captured by a detector, thus recording the intensity and the angle of dispersion of the X-rays.

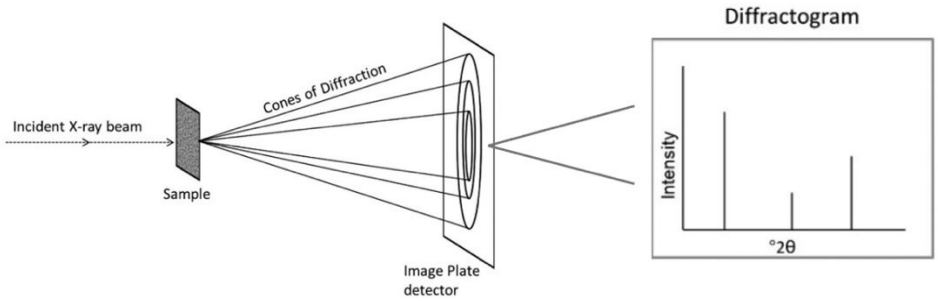

***Figure 4**. Scheme of a transmission configuration experiment with a 2D detector perpendicular to the incident beam and the resulting diffractogram[30].*

When aiming to achieve reproducible PXRD diffractograms, it is important to recognize that, while working with NPs, the diffracted peaks exhibit broadening, and the absolute intensities became lower. This broadening occurs because, in PXRD, the peaks arise from the summation of all atoms within the crystal lattice. Conversely, NPs contain significantly less atoms, which prevents the lattice summation from converging to a sharp diffraction line, instead causing the peaks to broaden. This broadening effect, increases while decreasing particle size, taking this as an advantage, it is possible to use it in the determination of particle´s sizes as will be explained in detail in section 1.2.3.

Different information can be extracted from the diffractogram as shown in **Figure 5**. The peak position and intensity are primarily related to the structural information of the sample, while the peak width and shape are relevant parameters for obtaining microstructural information.

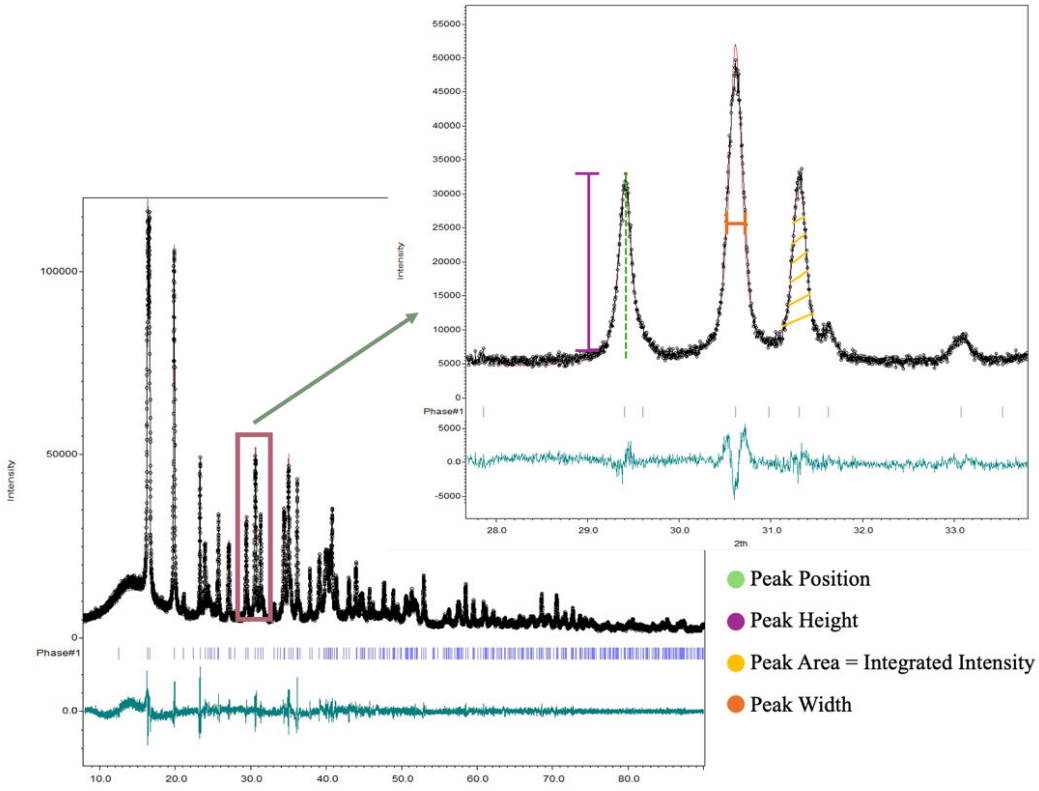

***Figure 5**. Diffractogram of an PXRD experiment.*

Using synchrotron radiation sources offers several improvements over laboratory X-ray techniques. The radiation spectrum is much broader, providing access to a wider range of wavelengths for analysis, not limited to just the Cu K_α and Mo K_α lines. This capability to select the appropriate wavelength also enables the mitigation of absorption effects and

radiation damage, which are wavelength dependent. Synchrotron radiation´s brightness is enhanced by the small cross-section of the charged particle beam and the high degree of collimation. Additionally, this type of radiation is fully linearly polarized, which allows for the emission of electron bunches at precisely defined time intervals.

In this thesis, all the synchrotron radiation experiments were performed at Elettra Synchrotron, specifically at the *MCX beamline* where one of the secondments associated with ESR13 took place.

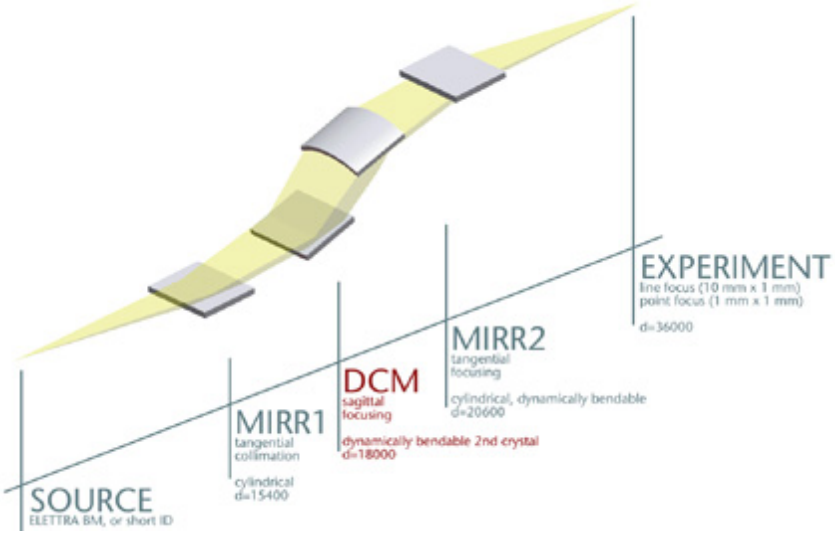

***Figure 6**. MCX beamline scheme at Elettra Synchrotron, composed primarily of two mirrors and a double-crystal monochromator.*

The light source for this synchrotron is the bending magnet radiation. This specific beamline can work in a range of energy between 6 and 20 keV. As shown in **Figure 6**, it includes two platinum-coated mirrors and a Si (111) double crystal monochromator. The first mirror collimates the beam, and the monochromator focuses it. The second flat, flexible mirror adjusts its curvature for optimal focus. The monochromator's two silicon crystals (DCM) provide an energy resolution of 0.014%, directing photons parallel to the original beam but shifted to avoid the direct beam. This setup uses adjustable crystals for precise focusing and alignment.

1.2.2. The Rietveld method

The Rietveld method is a powerful technique for structural refinement based on the analysis of the overall profile of X-ray powder diffraction diagrams. It involves

simulating a diffraction pattern from a structural model and then adjusting the model parameters to closely match the observed data.

To reconstruct the diffraction pattern, the intensity of the i-th point is calculated by summing contributions around the Bragg reflection with the continuous background as follows:

$$y_{ci} = y_{bi} + \sum_{\Phi=1}^{N} S_{\Phi} \sum_{k=1}^{k} M_{\Phi k} Lp_{\Phi k} |F_{hkl}|^2 PSF_{\Phi k} \quad (1.1)$$

Where:

- y_{bi} is the intensity of the continuous background.
- S_{Φ} is the scale factor of the phase Φ
- $M_{\Phi k}$ is the multiplicity of the k-th reflection vector of phase Φ
- $Lp_{\Phi k}$ is the Lorentz-Polarization factor.
- $|F_{hkl}|$ is the modulus of the structure factor.
- $P_{\Phi k}$ accounts for the preferred orientation effect on the k-th reflection of phase
- $PSF_{\Phi k}$ is the profile shape function of the k-th reflection of phase Φ
- If Φ = 1, it indicates a single phase, while Φ > 1 indicates multiple phases.

Profile parameters are refined simultaneously with structural parameters. To simulate the profile, a mathematical function such as Pseudo-Voigt, which is a linear combination (weighted sum) of a Gaussian and Lorentzian function, is used, taking into account possible peak asymmetry effects at low angles. A polynomial function is used to model the background noise and zero shift of the diffractogram, which is also refined. Preferred orientation effects of the crystallites and anisotropic broadening of reflections are considered during refinements.

For structural parameters, the scale factor is refined, as well as atom positions, isotropic or anisotropic atomic displacement parameters, and occupancy factors. Convergence of the refinements is monitored by the least squares method, minimizing a cost function representing the sum of squared deviation between the observed ($y_{i,obs}$) and calculated ($y_{i,cal}$):

$$S = \sum_{i=1}^{n} w_i \left[y_{i,obs} - y_{i,cal} \right] \quad (1.2)$$

Where w_i is a weighting factor, generally taken as $w_i = {}^{1}/_{\sigma_i}$ with σ_i being the standard deviation of the $y_{i,obs}$ measurement.

Structural refinements using Rietveld method are performed using software such as Jana2020[31] or Fullprof[32]. The quality of these refinements is verified using various agreement factors:

1. Bragg Factor:

$$\boldsymbol{R_{Bragg}} = \frac{\sum_k |I_{k,obs} - I_{k,cal}|}{\sum_k I_{k,obs}} \tag{1.3}$$

2. Observed structure factor:

$$\boldsymbol{R_{obs}} = \frac{\sum_k |F_{k,obs} - F_{k,cal}|}{\sum_k F_{k,obs}} \qquad \boldsymbol{wR_{obs}} = \frac{\sum_k w_k |I_{k,obs} - I_{k,cal}|}{\sum_k I_{k,obs}} \tag{1.4}$$

Profile Factors:

$$\boldsymbol{R_{exp}} = \frac{[N - P + C]^{1/2}}{\sum w_i {y_i}^2} \quad \boldsymbol{R_p} = \frac{\sum_i |y_i - y_{ic}|}{\sum_i y_i} \quad \mathbf{w}\boldsymbol{R_p} = \sqrt{\frac{\sum_i |y_i - y_{ic}|^2}{\sum_i wi {y_i}^2}} \tag{1.5}$$

For the Rietveld refinement based on powder data, if the Bragg factor is below 10%, the proposed structural model is considered plausible, provided that all interatomic distances and atomic displacement are coherent. Good agreement between observed and calculated diagrams, indicated by the factors R_p and wR_p , are also crucial indicators to consider.

1.2.3. Determining NP size by Scherrer equation

In 1918, Scherrer established the equation that relates the width of x-ray diffraction peaks to the size of crystalline particles[33], which is shown an inverse dependence as follows:

$$p = K\varepsilon = \frac{K\lambda}{\beta cos\theta} \tag{1.6}$$

Where:

- p is the 'true' crystallite size.
- ε is the apparent crystallite size.
- K is the Scherrer constant (shape factor).
- λ is the wavelength.
- β is the width of the diffraction peak (corrected for the instrumental broadening), given in radians.
- θ is the Bragg angle.

By calibrating the peak with a reference sample to obtain the instrumental contribution, it is possible to determine the width of the diffraction peak due to the sample contribution. Using this information, the Scherrer equation can be applied to estimate the nanoparticle size. Correcting the peak width for the instrumental contribution ensures that the peak broadening reflects only the properties of the material, such as crystallite size. This method allows for precise determination of nanoparticle size and shape from the diffraction pattern.

1.2.4. Single Crystal X-Ray diffraction (SCXRD)

Single crystal X-ray diffraction was used for ab-initio structure determination of isolated crystals as early as 1913 and the work by W. L. Bragg [34]. The foundational principles are analogous to those used in powder X-ray diffraction; however, the analysis is performed on a single crystal rather than a polycrystalline sample. Unlike PXRD, which produces a spectrum derived from the reciprocal space of many particles, single crystal diffraction generates a clear pattern characterized by sharp spots on a dark background. The intensities recorded while rotating the sample along different axes are proportional to the square modulus of the Fourier Transform of the electronic density. This information described by the geometry of the scattered intensities, provides details about atomic position, cell parameters and consequently, structural information about the sample.

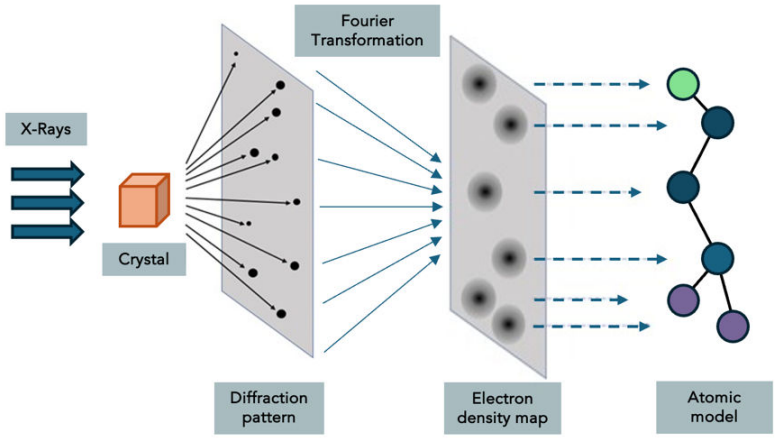

***Figure** 7. Single crystal XRD experiment representation. X-rays interact with the crystal, producing a diffraction pattern. By applying a Fourier transform to this pattern, an electron density map is generated, which is then used to determine and solve the atomic structure of the crystal.*

However, as mentioned earlier, this technique faces size limitations. Analyzing crystals smaller than 10 microns presents challenges in sample preparation, data acquisition, and therefore, in obtaining the crystal solution making this technique not suitable for NPs. 3D ED approaches (detailed in the next section) are in fact single crystal electron diffraction and, in this sense, offer similarities with SCXRD in terms of data acquisition and analysis. The advantage is that 3D ED can overcome the crystal size limitation, making it possible to analyze single nanoparticles smaller than 100 nm.

1.2.5. Transmission Electron Microscopy Techniques

With a wide range of diffraction, imaging, and spectroscopic methods available, transmission electron microscopy (TEM) is another widely used approach to nanoparticle characterization. Compared to X-rays, electrons have shorter wavelength (approximately 2pm), leading to stronger interactions with matter, and the ability to focus the electron beam to extremely fine probe sizes (down to 1nm) making this technique ideal for samples with volumes below a few μm^3. Knoll and Ruska built the first transmission electron microscope in 1931 [35], where their initial idea was to demonstrate theoretically that thin electromagnetic coils would have exactly the same effect on electrons as a thin glass lens has on light. For the light microscope, Abbe diffraction limit is based on the Rayleigh criterion, $d = \lambda / 2\sin\theta$ giving the smallest detail that can be solved in a microscope as a function of the wavelength lambda, and the numerical aperture, n sinus theta. This similar formula holds for Electron Microscopy where lambda is the

wavelength of the electrons (λ = 2.5x10^{-12} at 200kV) and theta the maximum angle at which electrons are collected ($\theta \approx$ 10-20 mrad). Placing all the numbers in the previous formula, d will be approximately between 1.5 to 3 Armstrong, that is the reason why we can reach atomic resolution.

There are different modes in which a transmission electron microscope can be operated. Those include image, spectroscopy, and diffraction mode. Next, the different uses and specifications of each of these techniques will be discussed. Additionally, within these operating modes, there are two main illumination setups in the microscope for data collection: TEM (parallel beam) and STEM (convergent beam) mode.

Transmission Electron Microscopy Image Mode

There are several ways in TEM to form images in a microscope depending on whether the direct beam (bright field) or diffracted beam (dark field) is considered. In the bright field mode, an aperture is positioned in the back focal plane of the objective lens. This setup permits only the direct electron beam pass thought. The resulting image is formed based on how the direct beam is attenuated after interacting with the sample. In the dark field, the aperture blocks the direct beam and instead allows one or more diffracted beams to pass through the objective aperture. However, interpreting these images can be challenging due to the overlap of different contrast mechanisms occurring at the same time. Dark field images are particularly informative for analyzing features such as planar defects, stacking faults, and particle sizes. Those images can show the information related to the size, structure, and nanoparticle distribution in a specimen plane[36]. The resolution of TEM is influenced by the wavelength of the electrons, as well as aberrations from the objective lenses and the microscope´s inherent electrical and mechanical instabilities. Initially, the basic operating mode of the Transmission Electron Microscope (TEM) allowed for resolutions around 3.3Å. Although this enabled capturing high-detail images, it did not provide very specific or detailed information about the crystal structure. To achieve greater detail and resolution, High Resolution Electron Microscopy (HRTEM) was developed.

High Resolution Transmission Electron Microscopy (HRTEM)

High-resolution Transmission Electron Microscopy (HRTEM) utilizes both transmitted and scattered electron beams to create phase contrast images. This technique allows for the direct imaging of atomic structures within a sample and is extensively used to analyze crystal structures, lattice defects, and various imperfections such as point defects, stacking faults, dislocations, and grain boundaries in advanced materials[37]. The design and working principles of HRTEM are similar to those of a conventional Transmission Electron Microscope, but with enhanced capabilities for detailed structural analysis at the atomic level. The literature indicates that it has been possible to obtain information about the internal structure from HRTEM images, either in the form of lattice fringes of ultra-small NPs [38] or through cross-section observation[39,40].

High Angle Annular dark-field detector

To produce a Bright-Field STEM image, the beam is scanned across the specimen using scan coils. The electron detector then captures the interplay between the electrons emitted from the specimen and the image displayed on the screen. To enhance the interpretability of images, improvements in spatial resolution and the reduction of aberrations led to the development of the Annular Dark-Field detector, which will be explained in detail below.

This technique involves the selection of either direct or scattered electron beams utilizing electrons directly rather than apertures. Consequently, detectors collect a higher number of electrons than they do when using an objective aperture. Moreover, in ADF-STEM, adjusting the contrast becomes more straightforward and can be enhanced significantly through modifications to signal preprocessing controls such as detector gain, black levels, contrast, and brightness on the computer display. This approach minimizes the aberrations common in off-axis TEM dark-field images, leading to images with less noise. Nonetheless, while TEM mode can still achieve higher resolution, the critical decision involves determining whether resolution or contrast holds more importance in the analysis, which will depend on the specimen. In ADF-STEM, the image is formed by the ADF detector, which exclusively collects low-angle elastically scattered electrons. Although this technique is sensitive to variations in atomic number, it is also affected by changes in sample thickness, images in ADF-STEM are influenced by inelastically scattered electrons, which can impact the overall image quality and contrast.

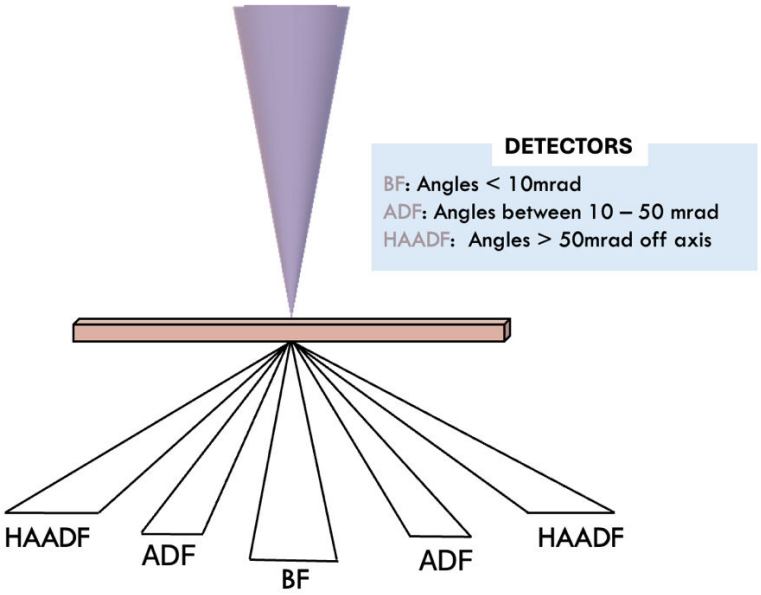

***Figure 8**. Different detectors in STEM based on the diffraction angle.*

Since the ADF detector always collects some Bragg electrons, it was necessary to develop a detector with a very large central aperture where z-contrast images could then be formed. This led to the creation of what is known today as High Angle Annular Dark-Field (HAADF) detector. Currently, HAADF is one of the most widely use imaging techniques for investigating materials at a nanoscale. This advanced detector allows for the effective discrimination of Bragg scattered electrons, enhancing imaging capabilities and providing clearer, more detailed images of crystallographic structures. HAADF-STEM tomography is able to acquire images at different tilt angles and then reconstructing the crystalline structure of nanoparticles using a range of software tools based on image processing, reconstruction algorithms, visualization technique, marching learning, and more. Although it is a more precise technique, providing a direct image interpretation of nanomaterials [41], it still needs to be combined with other techniques to solve ab-initio structures[42].

CHAPTER 2

3D ELECTRON DIFFRACTION TECHNIQUE

In the field of crystallography, the development of 3D Electron Diffraction has revolutionized the way we analyze and solve crystal structures, particularly for materials that are difficult to study using traditional X-ray diffraction techniques. As this technique will be the one investigated in this thesis, the fundamental knowledge required to understand the principles of any diffraction technique such as Bragg's law, reciprocal space, the Intensity of the Bragg's peaks, and the TEM components will be described. Additionally, the chapter will provide a detailed explanation of the specifications involved in data collection, data analysis, and refinement theory necessary to achieve a specific structural resolution using 3D ED technique.

2.1. Basics of Electron diffraction

2.1.1. Bragg´s law

When describing how electrons can interact with matter, the electron beam can be approached in two different ways: as a succession of particles and through wave theory. Consequently, it is important to draw a distinction between two phenomena that will be extensively employed throughout this thesis. Scattering, a physical process, elucidates the deviation of radiation due to interactions with matter in a particle-like manner, while diffraction will be the physical process when a wave interferes with an object yielding a pattern as a result. So, in electron diffraction, it is primarily the wave nature that is utilized to describe those interactions.

The phenomenon of diffraction was first described by William Lawrence Bragg in 1913. This pioneering scientist formulated a mathematical equation to reveal the conditions under which a crystal exhibits diffraction due to X-ray radiation. Known as Bragg's law (equation 2.1), it asserts that diffraction peaks are observed when the path difference between rays reflected by adjacent crystal planes is an integer multiple of the X-ray wavelength.

$$2d_{(\mathrm{hkl})} \cdot \sin(\theta) = \mathrm{n}\,\lambda \tag{2.1}$$

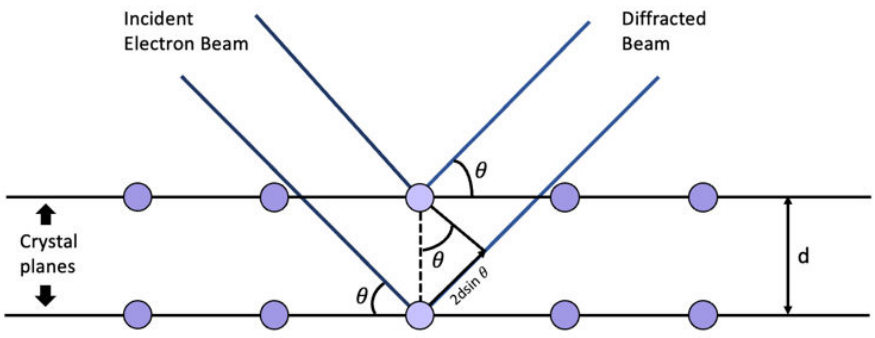

Figure 9. *Schematic representation of Bragg's diffraction phenomena.*

Where:

· d is the distance between atomic planes in the crystal (interplanar distance).

· θ is the angle of the incidence of X-rays with respect to the atomic planes.

· n is the integer that represents the order of the diffraction maximum.

· λ is the wavelength of the incident radiation.

This definition has been applied consistently since its beginning and serves to demonstrate the geometry of the diffraction phenomena when employing either X-ray, neutrons, or electron sources, with the wavelength being the only variable component.

2.1.2. Reciprocal space and Ewald Sphere

When considering the scattering phenomenon over a plane, we can define the vector **k** as the wave vector of the incident wave and **k'** as that of the diffracted wave. Therefore, **K** = **k** – **k'** represents the change in this vector due to the diffraction phenomenon. Consequently, if we are at the Bragg angle, the magnitude of the vector **K** can be rewriting as $\mathbf{K_B}$, which is proportional to the inverse distance between planes, also known as **g** (diffraction vector). Then, the Bragg diffraction of electrons occurs when **K** is equal to **g**.

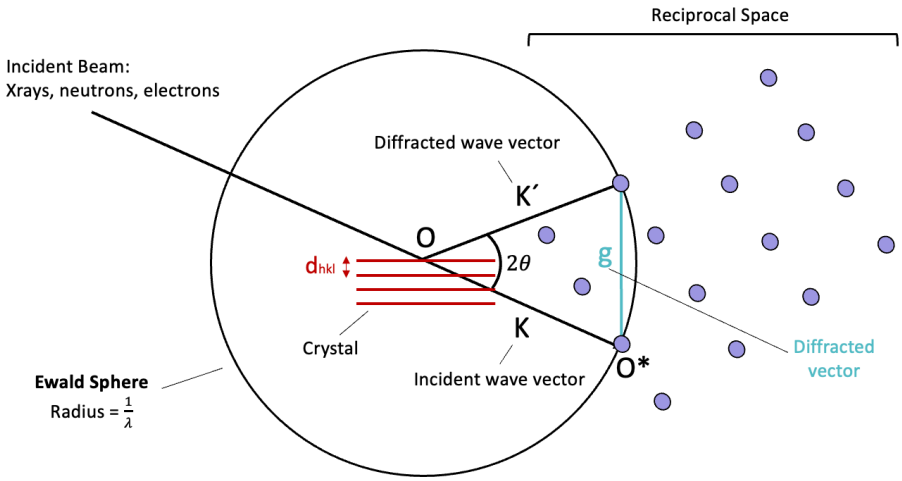

***Figure 10**. Reciprocal space representation using Ewald Sphere. **K** correspond to the incident vector, **k'** the diffracted wave vector, and **g** is the diffracted vector in reciprocal space.*

The reciprocal space is a physical representation of the diffraction geometry where each point is associated with a set of planes in the crystal (possible **g** vector). A more representative visualization of this reciprocal space will be displayed in **Figure 10** using the Ewald Sphere.

This sphere is centered at point O with a radius R equal to the reciprocal of the wavelength $\frac{1}{\lambda}$. The crystal rotation relative to the incident beam with wavelength λ implies a corresponding rotation of the reciprocal lattice about its origin, O*. Each time a node of the reciprocal lattice intersects the Ewald sphere centered on O, the crystal will give rise

to a diffraction peak in direction of **k´** so, by measuring the intensity of the scattered waves and adjusting the crystal´s orientation relative to the incident beam vector **k**, we can map out the crystal´s entire reciprocal space which provides important structural information. Through the localization of the numerous diffracted peaks, the complete geometry of the reciprocal lattice, from which the dimensions and shape of the unit cell can be derived, will provide a first information about the symmetry of the unknown structure. Here it is important to notice that the origin of the reciprocal lattice is not the center of the sphere but is at the point where the direct beam exist from the sphere. In case of a finite crystal, the diffraction condition is stringent: the diffraction vector must be a vector of the reciprocal lattice such that $\mathbf{g} = \mathbf{s}_{hkl}$.

It's important to mention that electrons have a shorter wavelength compared to X-rays. For example, in a Transmission Electron Microscope (TEM) operating at 200 kV, the wavelength of electrons is around 0.025 Å, while the wavelength typically used in XRD with CuK_α radiation is 1.5406 Å. This shorter wavelength in TEM allows for higher resolution, resulting in a much larger Ewald sphere (**Figure 11**). As a result, a greater number of diffraction peaks are produced, providing more detailed structural information.

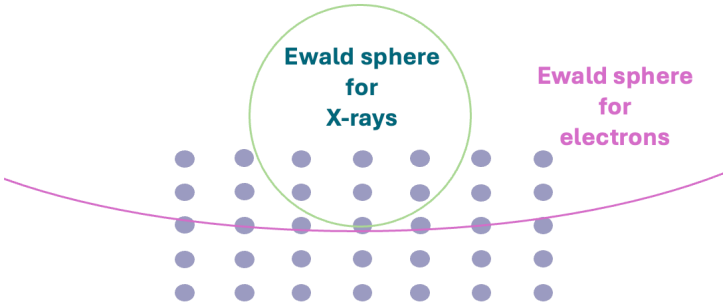

***Figure 11**. Comparison of the Ewald sphere for X-rays (green) versus electrons (pink).*

2.1.3. The Intensity

Initially, our discussion presupposed the existence of an ideal, infinite crystal. However, such a crystal does not exist. The consideration of a perfect infinite crystal results in the form factor becoming zero, except under precise diffraction conditions. In this context, it is necessary to consider the average lattice, which is influenced by the thermal vibration of atoms. This thermal vibration leads to a weakening of the Bragg peak intensity without causing their displacement or broadening. The atomic diffusion factor, denoted as $f_n(g)$,

is impacted by the attenuation term T_n = exp (-$B_n \frac{sin^2\theta}{\lambda^2}$), commonly referred to as the Deby-Weller factor. Here, the term Bn correlates with the mean square displacement U_n of atom n from its equilibrium position and is expressed by the equation $B_n = 8\pi^2 U_n$. It is important to note that thermal vibration is typically anisotropic, leading to the representation of anisotropic displacement by ellipsoids centered at average atomic positions.

However, in practice, crystals are finite in size and exhibit imperfections. These deviations from crystalline periodicity manifest as diffuse scattering in reciprocal space. The finite dimensions of the crystal necessitate the consideration of the crystal form factor. Consequently, the Fourier transform is influenced not only by the potential of the material but also by its shape, resulting in a dispersion of intensity around the nodes of the reciprocal lattice, which are no longer point-like (this elongation is inversely proportional to the specimen thickness (t)). This implies that nodes not precisely meeting Bragg conditions can still exhibit excitation. The extent of this phenomenon is contingent on the employed diffraction technique and is countered for by Lorentz factors L (θ). In electron diffraction, diffraction conditions adhere to the Bragg Law, but the nearly flat nature of the Ewald sphere in the context of reciprocal lattice (owing to the electron radiation wavelength of approximately 0.0251 Å under a 200 kV acceleration voltage) leads to more reflections at diffraction conditions.

According to the kinematic theory of diffraction and considering smaller specimens, the intensity observed in the peak of a diffraction pattern is also linked to the sample thickness and the excitation error S_h. This error signifies the deviation of a reflection from its excitation state. Mathematically, it is represented as the distance of a specific reciprocal lattice point from the Ewald sphere:

$$I_{hkl} = |F_{hkl}|^2 \frac{sin^2(\pi t S_h)}{(S_h)^2} \tag{2.2}$$

Where t denotes the sample thickness. Consequently, the intensity of a diffraction peak, as a function of S_h, follows a square sinc trend, which diverges from zero not only at a single point but also around it (see **Figure 12**). The finite size of the crystal leads to an enlargement in the diffraction spots, as previously mentioned. Thus, a diffraction peak reaches its maximum intensity when its excitation error is null. As the distance of a point from the Ewald Sphere increases, its intensity decreases, yet remains detectable within a

certain range of excitation error. This is illustrative of the excitation error problem wherein peak intensity is contingent upon whether the Ewald Sphere passes through the exact Bragg position or not.

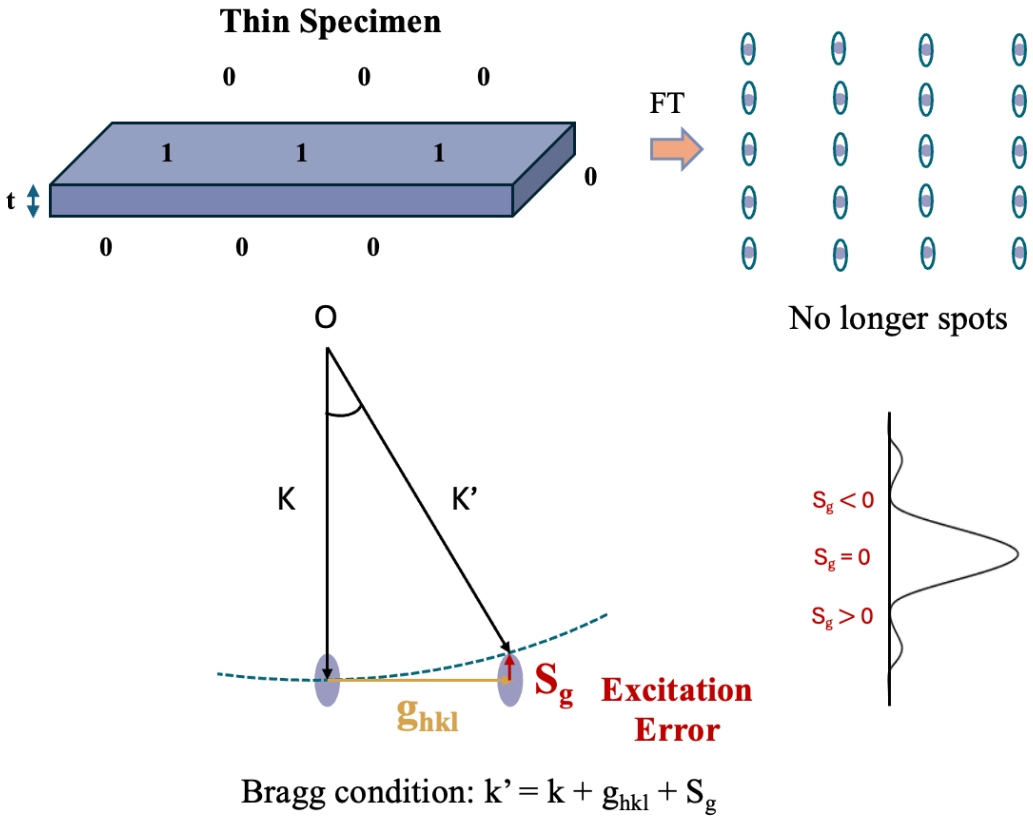

***Figure 12**.Illustration of how small samples cause broadening of diffraction spots (relrods) and the intensity profile depending on whether the Ewald Sphere passes exactly though the center of the relrod or its edges.*

2.1.4. The Transmission Electron Microscopy (TEM)

The primary instrument used for most of the experiments discussed in subsequent sections is the JEOL F200 Transmission Electron Microscope (see **Figure 13**), which will be the described in detail in this chapter. However, other microscopes with different specifications were also utilized during different secondments of the project, and their properties and specifications will be mentioned as needed.

One of the most crucial aspects of using an electron microscope is the illumination of the sample. Simplifying, electrons are emitted by a filament and accelerated by a potential difference inside the electron gun, focusing and directing the electron beam with the help

of electromagnetic lenses through the microscope column. In this context, the electron gun is the initial component of the microscope that generates and accelerates the electron beam towards the illumination system. Specifically, a Field-Emission Gun (FEG) is used. The FEG includes two anodes: the first anode creates the extraction voltage to pull electrons out of the tip, and the second anode accelerates these electrons to 200 kV.

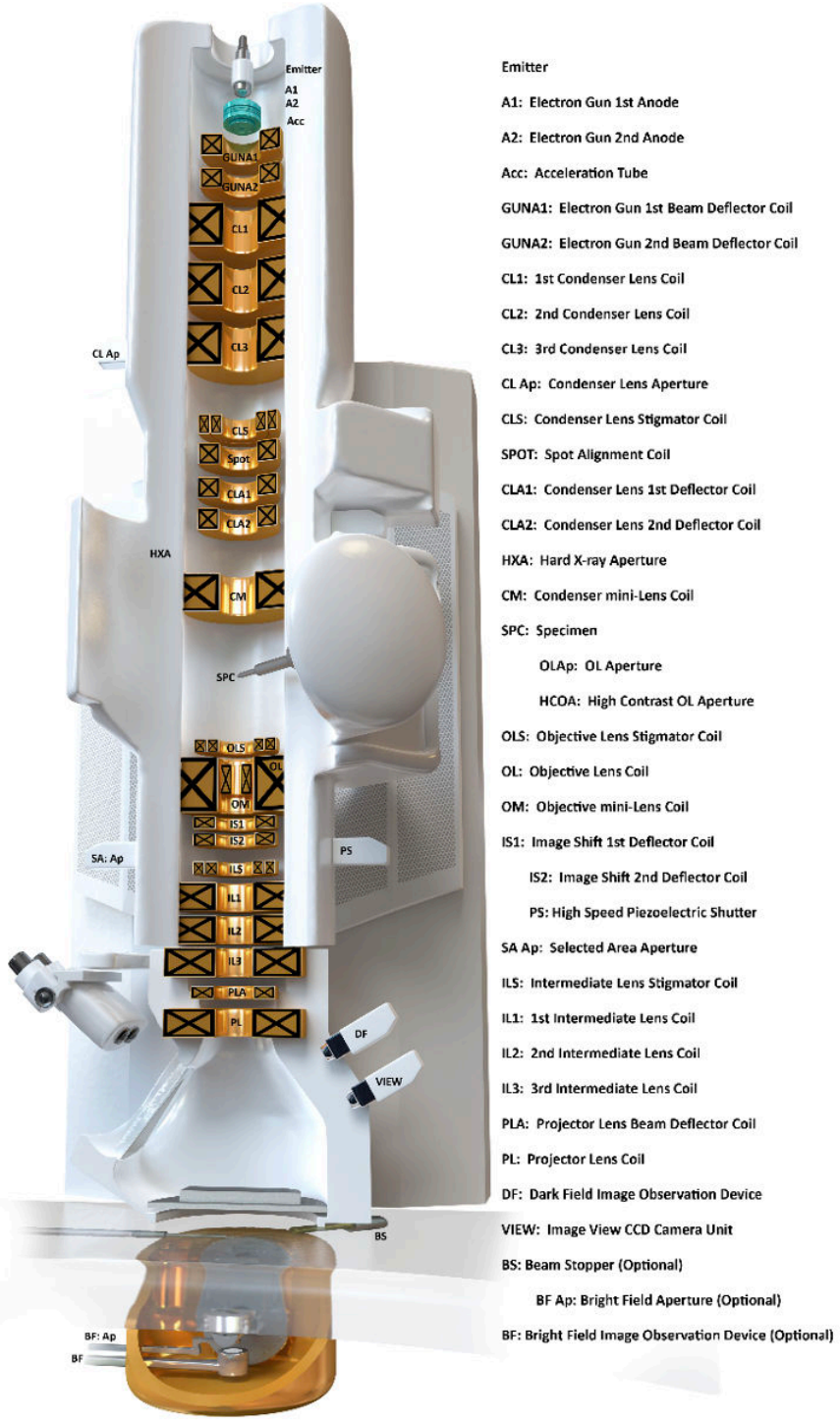

***Figure 13**. Elements present in a column of TEM JEOL F200.*

Within the microscope column, we can distinguish three main optical systems: the condenser, objective, and projection lenses. Electrons are generated in a tungsten filament (for the FEG source) and accelerated by a potential difference of 200 kV as mentioned. This electron beam reaches the condenser lens, which controls the convergence of the beam and adjust the size. Next, the condenser lens aperture is set to determine the lateral dimensions of the beam, resulting in a well-collimated and defined beam that can interact effectively with the sample. This interaction can lead to different phenomena that generate signals and gather information about the internal structure of the sample. In electron diffraction experiments, utilized for structural crystallography in this work, parallel beam conditions are used to form spots on the diffraction patterns.

To form an image, the electrons pass through the objective lens system, which is crucial as it contributes to the resolution of the image. The objective lens focuses the image by changing the focal length, as moving the lenses themselves is not possible in a TEM microscope. The first intermediate lens magnifies the initial image that is formed by the objective lens. It can be adjusted to focus on the back focal plane of the objective lens to capture the electron diffraction pattern. The electrons then pass through the projection lens system, which magnifies the image to the desired scale, enhancing magnification and contrast. Once the diffraction pattern is magnified by the projection system, it can be visualized on the viewing screen or recorded by a camera.

2.2. 3D ED techniques

In the past, 3D patterns where mostly used quantitatively to seek information about lattice parameters and symmetry elements. This was done with the acquisition of the diffraction patterns oriented in zone-axis. However, this procedure was very time consuming because not only did you have to find an isolated crystal, but you also had to orient it along a particular direction and obtain only 2D information. The acquisition of several oriented zone-axis patterns (ZAP) was necessary. These ZAP are the ones containing relevant information about symmetry elements, they were not the best for quantitative structural analysis as the dynamical effect was much greater.

However, in 2007, U. Kolb introduced the data acquisition technique known as Automated Electron Diffraction Tomography (ADT)[43,44], where the crystal was not solely randomly oriented, but in addition, a series of diffraction patterns were collected

sequentially while tilting, in a stepwise goniometer tilt (**Figure 14**). These patterns that are not intentionally oriented along a dense zone axis, have less dynamical scattering effect allowing easier data treatment and structure solution. It mirrors the approach employed in Single Crystal X-ray Diffraction but with only one rotation axis used. This methodology allowed the coverage of the maximum angular range available in microscopes (approximately 120 °). The systematic approach used to collect ED patterns also increased the data completeness compared to acquiring only for ZAP. Although the missing wedge problem remained (see below), the impact of dynamical effects was significantly reduced.

In order to achieve a more comprehensive representation of reciprocal space and address the information gaps between sequences of diffraction patterns, Mugnaioli *et al.* 2009[45] proposed combining the techniques of Precession Electron Diffraction (PED), introduced by Vincent and Midgley in 1994[46], and ADT. This integration resulted in what is known as Precession-assisted Electron Diffraction Tomography (PEDT) or precession-assisted 3D ED, following some recent naming recommendations[47] .

2.3. Protocols for data acquisition

2.3.1. Precession assisted 3D ED (a.k.a PEDT)

The principle behind PED is relatively simple. It involves using the microscope´s deflectors to tilt and rotate the electron beam around the optical axis of the microscope (SCAN) as seen in **Figure 14.**a. This motion projects a cone-shaped electron beam onto the sample, with the cone's semi-angle referred to as the precession semi-angle (ϕ), which is defined by the capabilities of the microscope. After the beam interacts with the specimen, it is then rotated in the opposite direction using deflection coils to prevent any movement of the beam on the back focal plane, ensuring a clear and reliable diffraction pattern is obtained (**Figure 14.**a).

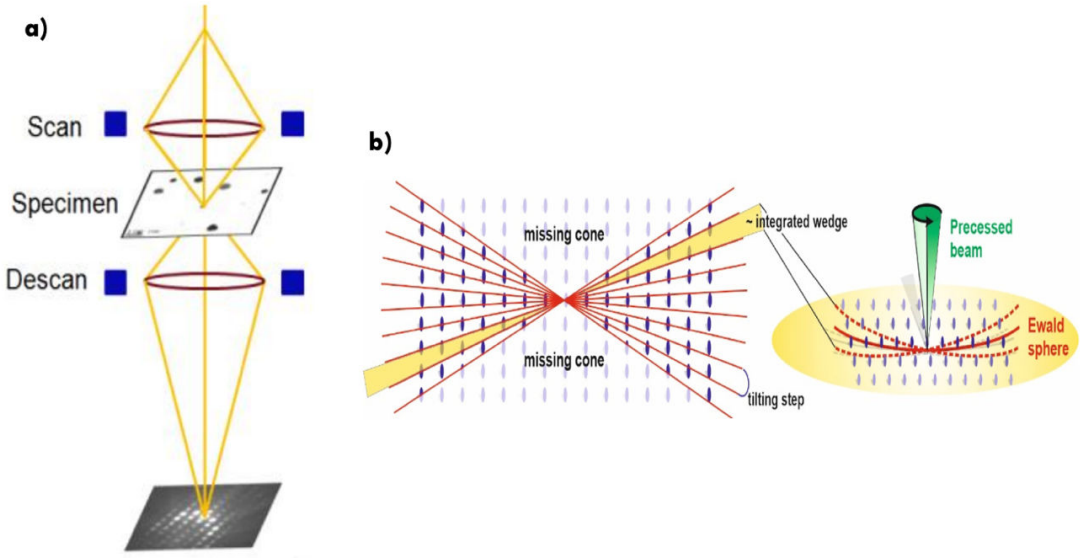

***Figure 14**. a) Representation of a cone-shape electron beam to form the Diffraction pattern[48]. b) PEDT data acquisition[49]. The precession movement of the beam allows integrated intensities.*

The precession of the beam causes the Ewald sphere to move across the reciprocal space, effectively expanding the range of reciprocal space explored with each diffraction pattern collected and allowing integrated intensities (**Figure 14**.b).

Due to the effect of multiple scattering, reflections that are not permitted by the crystal symmetry sometimes appear and are often present when precession is not applied. Implementing precession decreases the presence of these reflections, which leads to a more reliable determination of the symmetry elements. Additionally, it integrates the intensity profile of reflections over a broader area of reciprocal space, providing a more accurate representation of their real intensity. Moreover, the resolution is significantly improved, as a small precession angle can greatly increases the number of high-angle reflections. This technique also reduces the sensitivity of diffracted intensities to local thickness variations, misorientations, and the curvature of the Ewald sphere.

As previously mentioned, throughout this thesis, the primary microscope used will be a JEOL F200, and the data acquisition will be carried out using precession-assisted ED. The precession device employed is a NanoMEGAS DigiSTAR unit, with the precession semi-angle set between 1 and 1.4. This range is chosen to effectively capture high-order Laue zones (HOLZ), because if the precession angle is too large, it may cause overlap between the zero-order Laue zone (ZOLZ) and the first-order Laue zone (FOLZ), resulting in distorted intensity measurements.

2.3.2. Rotation 3D ED (a.k.a RED)

Although rotation electron diffraction was a significant advancement for obtaining integrated data more easily, it wasn´t until the emergence of fast detectors that this process could be performed continuously and automatically.

With the advent of hybrid-pixel detectors, allowing recording data at high frame rates without read-out dead time, a new approach was proposed by the group of J.P. Abrahams in 2013. In continuous Rotation Electron Diffraction (cRED)[50], the sample rotates continuously, and electron diffraction patterns are recorded on the fly. Another major difference is the duration of a data collection. In step by step, for an angular range of 90°, a "fast" acquisition will be around 10 minutes, in continuous rotation this can be less than a minute. This idea was taken up by the group of T. Gonen in 2014 under the acronym microED[51], The recommended name for this approach is continuous rotation 3D ED[47].

In fast hybrid-pixel detectors, like Cheetah M3 Medipix detector from ASI available on the F200, the read-out time is typically just a few milliseconds. This capability has enabled the continuous acquisition of diffraction patterns from a crystal. The detector can capture diffraction phenomena over a specific exposure time while the goniometer rotates continuously (as it was a film). As a result, the recorded images integrate data over the desired exposure period, making the intensity extraction from the data both easier and more accurate.

2.3.3. Precession-assisted vs continuous rotation 3D ED

Currently, the two most commonly used techniques for carrying out 3D ED experiments are precession-assisted (PEDT) and continuous rotation (cRED), which will be applied throughout this thesis. While these methods are distinguished by their data acquisition strategies (**Figure 15**), both enable the integration of intensities for subsequent dynamical refinement, leading to accurate structure solutions.

There are important differences to consider when choosing between the two protocols to achieve the best quality based on the sample´s analysis requirements. First, in terms of technical aspects, aligning the precession device is necessary and can sometime be challenging to optimize. In contrast, continuous rotation 3D ED does not require any additional alignment.

When considering the time taken to collect a single dataset, cRED is the clear winner, as it requires no interruptions while the sample rotates, and data is collected. Moreover, there are software solutions that can automate this process, completing it in less than 1 minute, which reduces potential damage to the crystal caused by the electron beam. This capability allows for the analysis and structural resolution of beam-sensitive samples (porous materials, small organic molecules or in life science). However, as we will see later, this protocol is not always feasible for data collection. In contrast, precession-assisted ED acquisition is stepwise, taking at least 10 minutes per dataset. Although more time-consuming, it can be more suitable for smaller crystals as we will see in Chapter 4.

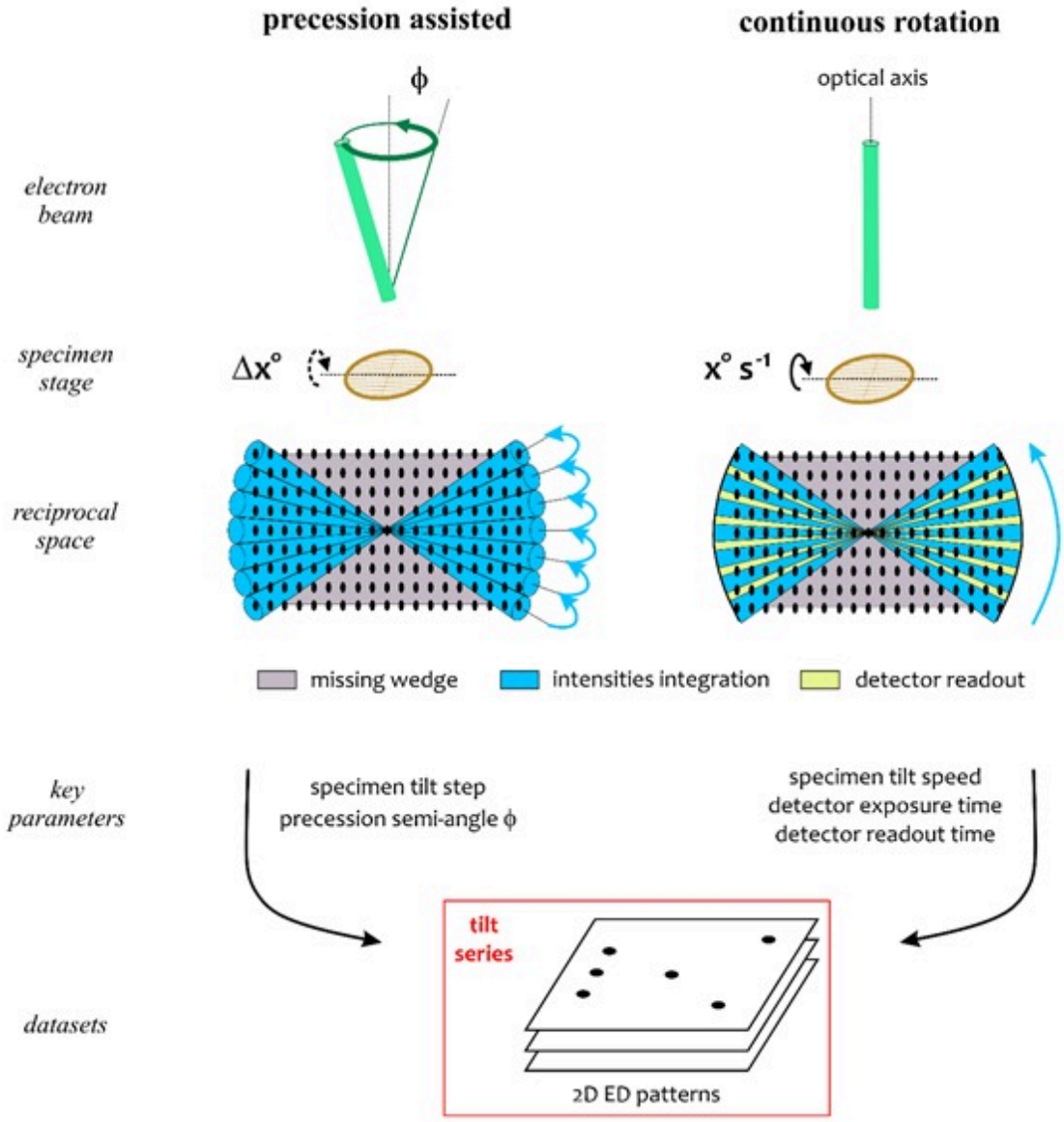

***Figure 15**. Representation of how both protocols collected the data using PEDT and cRED. At the end, a series of 2D ED patterns is obtain.*

Lastly, regarding single crystal tracking, the stepwise nature of precession-assisted ED makes it easier and more efficient to follow the crystal of interest, because it is possible to have a visual checking of the crystal every tilt step or makes use of advanced tracking routines. In cRED, as the data is acquired in a continuously way, these strategies have some limits, particularly when the crystals and the beam size are both very small. In cRED, to avoid losing the crystal while rotating the goniometer at high speed, most systems used a large beam size or selected area aperture (1μm – 700nm), which not the best option to analyze single NPs. Reducing the beam size will result in the risk to lose the crystal depending on the resolution sphere of the goniometer. In this case, smaller beam might be useable but only at the cost of an efficient tracking system.

2.3.4. Serial Electron Diffraction (SerialED)

As we have previously explained, electrons interact more strongly with the sample, which also causes more damage to the sample of interest. This means that when high energy is applied to the specimen, the bonds that form its internal structure can be destroyed more easily depending on their nature. As a result, the diffraction patterns become progressively weaker until we no longer see any diffraction peaks. This is what usually happens to beam-sensitive samples, such as macromolecules or organic materials. However, a similar phenomenon can occur with small NPs. Although they are typically inorganic and their internal structure tends to be quite stable, issues such as agglomeration or the need to obtain a sufficiently strong signal to noise ratio for refinement (which will be discussed in the following chapters) force us to focus our electron beam much more intensely on these NPs. This causes them to stop diffracting much sooner than larger-sized materials on the same compound.

Then SerialED emerged as a new data collection approach in the group of X. Zou in 2018[52] for beam sensitive materials. Again, it mirrors the field of X-rays and serial crystallography (such as SFX: Serial Femtosecond Crystallography)[53], as used in XFEL or synchrotron facilities. In these systems, crystals are exposed to X-rays for a very short duration and only one, thereby minimizing radiation damage. Additionally, this technique allows data collection at room temperature, providing more relevant information, especially for biological samples, compared to conventional X-ray crystallography.

We will illustrate this concept transposed to electron-based techniques with some recent applications in life science. This process was as follows: randomly select isolated crystals found on a TEM grid using either STEM or TEM images[54]. The program will be able to locate the selected crystals, switch to diffraction mode, and capture the diffraction pattern generated by each one independently. The main idea is to collect many diffraction pattern screenshots from different crystals, assuming that each will have a different orientation, enabling to reconstruct their 3D structure from the collected data. Although there are algorithms that automate this process, their use is very difficult for small nanoparticles, as the magnification at which they are scanned is usually high, and the program is not able to determine whether the crystal is isolated or not.

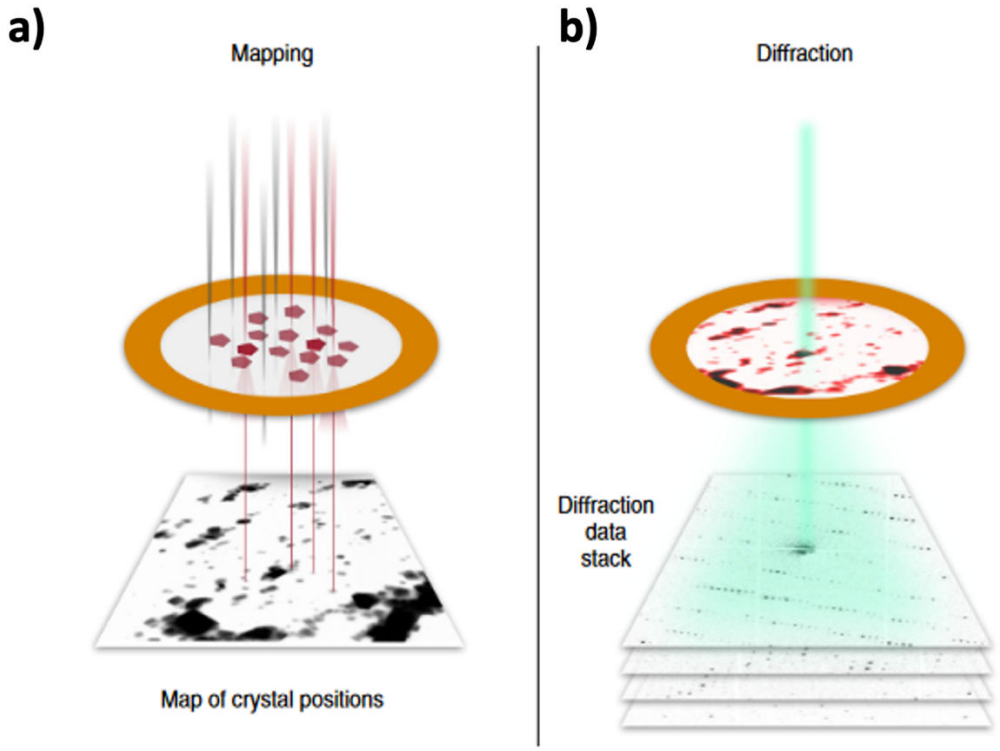

***Figure 16**. Representation of SerialED process[55]. a) The first step is mapping the grid in STEM and find the isolated crystal. b) The send step is in diffraction mode, where a diffraction pattern is acquired.*

2.4. Workflow for data analysis with PETS

PETS 2.0[56] is a computer program developed by Lukas Palatinus that allows for the Processing of Electron Diffraction tilt series collected by using different data acquisition protocols such as continuous rotation mode (cRED, MicroED), stepwise mode with

(PEDT) or without precession (ADT) and serial ED. While there are other software options available for indexing reflections to obtain unit cell parameters and extract intensities, PETS2 will be the program used for processing all datasets in this thesis. While all the procedures for handling ED data are detailed in the PETS2 manual (http://pets.fzu.cz), I feel it is relevant to provide a summary here.

Depending on the interface used for data acquisition protocols, the file with the .pts extension will either be stored and loaded directly into the program or can be created from scratch (File > new). Any modifications will be stored in the pts2 file, thereby preserving the original pts file without any changes. In the original file, there are different parameters that need to be specified for proper data processing:

There are different parameters that need to be specified for proper data processing: Lambda, which is the electron wavelength associated with the accelerating voltage of the microscope; Aperpixel, a calibration constant depending on the camera length used; ImageList / EndImageList, between which all frames (Tiff files) and their corresponding alpha tilts must be listed; Geometry, where it is important to specify the data acquisition protocol, such as static frame, precession (PEDT), or continuous rotation (cRED); NoiseParameters and SaturationLimit, which will vary depending on the detector; dstarmax and dstarmaxps, which determine the maximum diameter for data integration and peak search respectively; reflectionsize, which defines the diameter for each reflection; and i / sigma, the threshold for the intensity of reflections considered for further analysis. Once these parameters are defined, the input file is ready for processing.

2.4.1. Peak Search

To reconstruct the reciprocal space, it is important to search for the diffraction Bragg positions (.rpl file) and locate the primary beam (.cenloc file). There are three different methods to determine the position of the central beam: using the direct beam, Friedel pairs, or saved centers. In our case, the method used is Friedel pair, by identifying the reflection couples h, k, l and $\bar{h}$, $\bar{k}$, $\bar{l}$ which involves identifying pairs of reflections such as (h, k, l) and $\bar{h}$, $\bar{k}$, $\bar{l}$). The position of the central beam is then estimated as the midpoint between these paired reflections.

The threshold should be determined based on the quality of the data, having weak reflections data, this threshold has to be set lower (**Figure 17**).

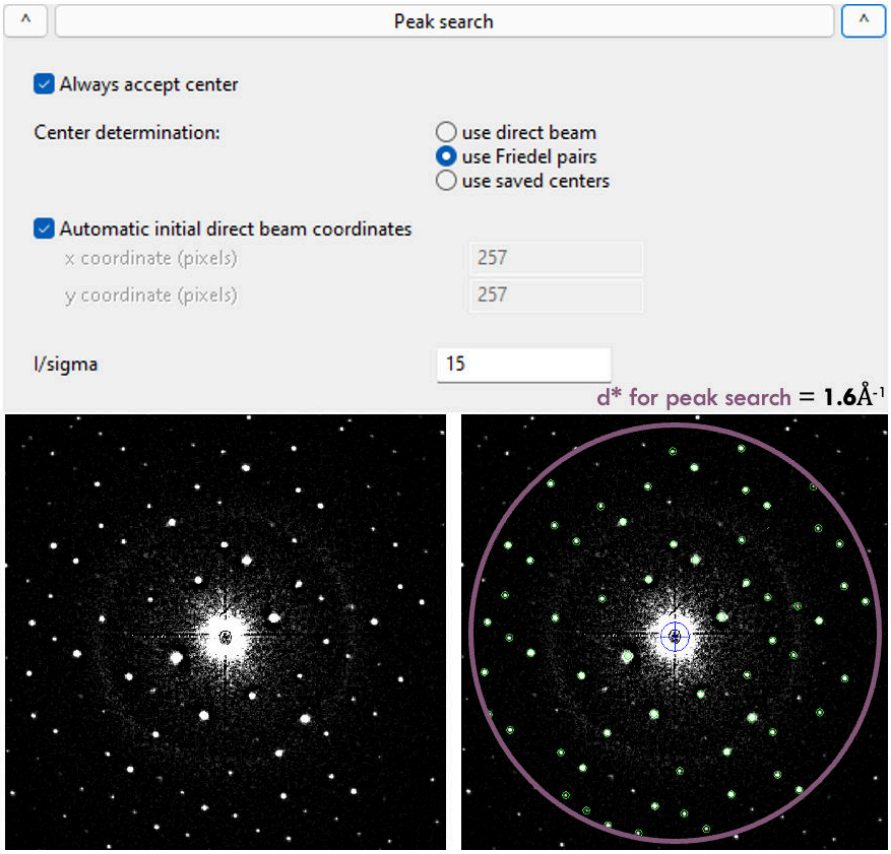

Figure 17*. Peak search window: The central beam is located using the Friedel pairs method. Additionally, a threshold of I/σ = 15 is applied to determine which reflections are considered (encircled in green) for further analysis. The purple circle determined the maximum diameter (resolution) for peak search, and it was set in the previous step by dstarmaxps parameter.*

2.4.2. Tilt Axis

This tilt axis has different orientation in the various frames collected, representing the position of the goniometer tilt axis on the images. The omega (ω) angle (see **Figure 18.**a), which is the angle between the projection of the alpha-tilt axis on the image and the horizontal axis on the frame, depends on the microscope, camera length, and focusing conditions. Therefore, it cannot be precisely calibrated and need to be optimized for each dataset, thus, this angle should be refined globally over 360 degrees. The sharper projection, the better the quality of the data (see **Figure 18**.b).

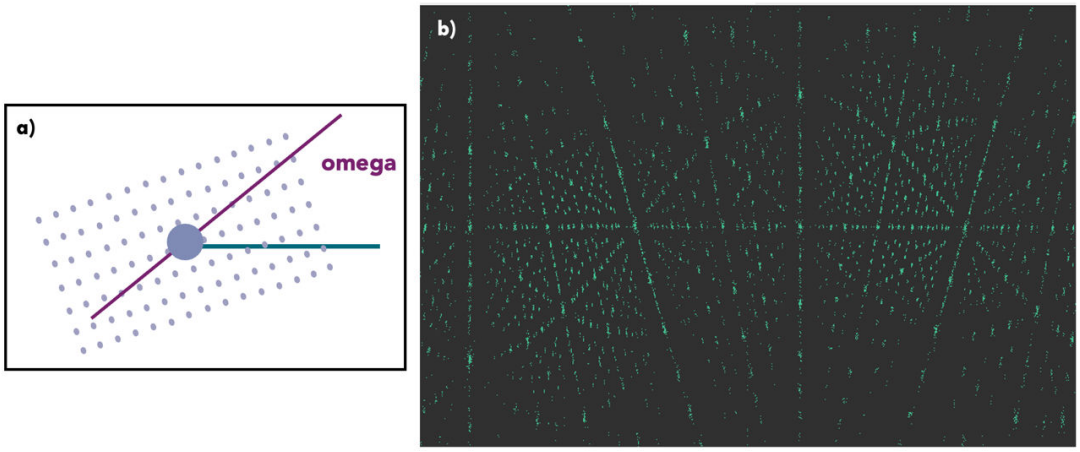

***Figure 18**. a) Omega angle representation. b) Peak positions represented in cylindrical coordinates for a refined value ω .*

2.4.3. Peak Analysis

Different space and cluster analysis will be performed here to convert the set of 2D ED pattern with an angular relationship to a 3D representation of the reciprocal space. The starting step involves analyzing the distance distribution between peaks, in the subsequent step, the diffraction pattern undergoes an auto-convolution analysis (difference space) where groups of peaks (clusters) in the auto-convolution are replaced by their cluster centers. The goal of this step is to consolidate multiple measurements of the same hkl reflection into a single peak and gather all similar peaks to avoid redundant measurements generating the necessary files for unit cell determination and indexing.

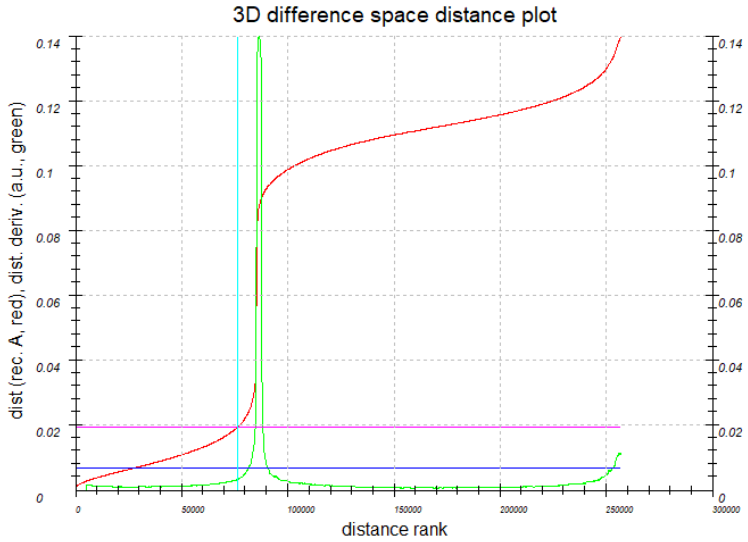

***Figure 19**. The red line represents the trend of inter-peak distances, while the green line shows its derivative. For high-quality data, the peaks should appear sharp, and the jumps between the derivatives should be clearly defined.*

2.4.4. Reciprocal Space Reconstruction

The reconstruction of the reciprocal space becomes possible once the alpha tilt of the frames, the positions of the diffraction maxima, the primary beam position in the frame, and the tilt axis orientation and the cluster analysis are determined.

***Figure 20**. 3D reconstruction of the reciprocal space where the white spots correspond to every reflection.*

2.4.5. Find Unit Cell and Orientation Matrix

This step involves determining the unit cell parameters by indexing the identified peaks and finding the orientation matrix (see **Figure 21**). To find the orientation matrix, the Cartesian coordinate system used by PETS2 must first defined: the x-axis will be parallel to the goniometer rotation axis, while the z-axis points towards the radiation source. Finally, the y-axis completes the right-handed system. The orientation matrix UB is then defined as follows:

$$\mathrm{UB} = \begin{pmatrix} a_x & b_x & c_x \\ a_y & b_y & c_y \\ a_z & b_z & c_z \end{pmatrix} \tag{2.3}$$

There are two different ways to find the orientation matrix and the cell parameters. First, it can be done automatically, where PETS2 attempts to assign unit cell parameters based on the indexing of the detected and clustered peaks. Alternatively, it can be done manually, where the user selects the parameters themselves.

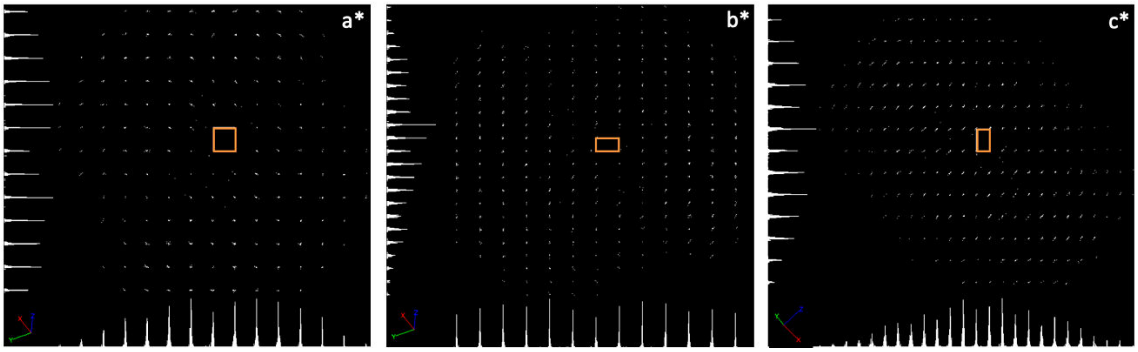

***Figure 21**. Unit cell represented in orange, based on the projected reciprocal planes (a*, b* and c*).*

2.4.6. Process Frame for Integration

In this step, the extraction of intensities from each frame is carried out using the standard peak-background method. This process involves placing a user-defined diameter (set by the reflection size parameter) at the predicted position of each reflection, assuming that it captures the entire diffracted intensity. Observed reflections are encircled in green, while unobserved ones are marked in brown (see **Figure 22**.a). The global reflection profile parameters are visualized in what is known as the Rocking curve (**Figure 22**.b), where the profile height is plotted against the excitation error. The shape of this plot varies depending on the chosen acquisition geometry and can be optimized by comparing the experimental data (blue line) with the calculated profile (red line)

In this step, the extraction of the intensities on each frame is performed using the standard peak-background method. The intensity extraction involves placing a user-defined diameter (parameter has been set by reflection size) at predicted position of a reflection, which is assumed to contain the entire diffracted intensity. In practical terms, observed reflections are marked by green circles, while unobserved reflections are shown in brown (see **Figure 22**.a). The global reflection profile parameters will be displayed in the so-called Rocking curve (**Figure 22**.b) where the profile heigh against the excitation error are computed. The shape of this plot can be varied depends on the geometry chosen and it can be optimized by comparing the blue line (experimental data) and red line (calculated profile).

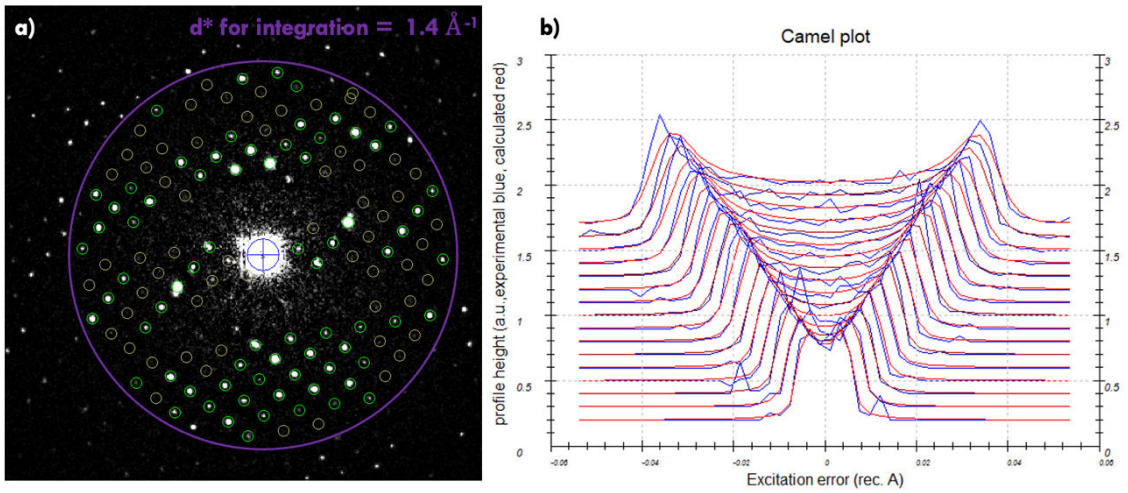

***Figure 22**. a) Experimental diffraction pattern representation where the observed reflections are shown in green while unobserved reflections are shown in brown. b) Image of a rocking curve from a PEDT experiment, with the computed data represented in red while the experimental is displayed in blue.*

2.4.7. Optimize Frame Geometry

Here, the refinement is performed on both the crystal orientation and the individual frame distortions to optimize the experimental geometry frame by frame. When tilting, if each frame (angle) has been refined, the reflections will be found precisely where they should be. However, if this step is not performed, spots in each frame may be slightly shifted, leading to a less accurate indexing procedure.

2.4.8. Finalize Integration

Upon selecting "Finalize Integration," statistics are provided, including the possible Laue class along with the relative Rint(obs) value. Based on this information, the appropriate Laue class can be identified, and the possible space group can be deduced by analyzing the systematic absences in the reciprocal space sections.

The main objective of processing crystallography diffraction data is to extract reflection intensities that can be used for detailed structural analysis. Although this extraction can be based on two different approaches (kinematical or dynamical), which will be explained in detailed in the next section.

For kinematical approach two different modes can be considered. The first one involves numerical integration of the intensity profile, which is suitable for rotation data where most reflections are fully integrated on one or two frames but not for partially measured

reflections. The second mode fits the experimental intensity profile to the normalized predicted rocking curve, with the integrated intensity equal to the scale factor of the fit. This mode is more accurate for partially measured reflections and is well-suited for PED data. In the case of dynamical approach, the intensities are not integrated across the frames. Therefore, the output file will contain a list of hkl, intensity and the standard uncertainty for each reflection on each frame. This means that one set of reflections indices may appear more than once in the list, but only once for each frame.

2.4.9. PETS2 data Processing for Serial ED

In this case, finding the orientation matrix, as explained in section 2.4.5, is not possible. Therefore, an alternative approach known as template matching must be applied. Template matching involves comparing each 2D diffraction pattern with a set of simulated diffraction patterns (templates), where each template corresponds to a known crystal orientation. However, for this method to work, at least, the unit cell parameters and Laue class of the compound must be known in advance. By matching the experimental pattern to the closest simulated template, the orientation of the crystal can be determined. Essentially, this method seeks to find the best match between the experimental data and the simulated diffraction patterns, which represent crystals in different orientations.

For the analysis in PETS2, the first step is to create an input file that specifies essential parameters such as wavelength, noise parameters, calibration constant, etc., in the same way as we did for precession-assisted ED or cRED data. Once the input has been created, the workflow is as follows.

Press peak search to obtain the center of each frame. In our case, the Friedel pair method was chosen. Once we found the center on each frame, the program should be closed, saving the project, and modifying the following keywords:

globalsearch no by the word yes and adding the step between templates, the maximal resolution of the templates and the maximal deviation from the actual frame orientation (where the value 10 is a good number to start).

referencecell and then write the cell parameters of the compound being analyzed.

Save the project and reopen PETS2. Go to ‘Finalize integration’ to set the correct, or at least expected Laue class. After these steps, the indexing can be start, where the program

will attempt to find the best template matching from the simulated patterns with respect to the experimental ones.

Finally, run 'process frames for integration,' increasing the default mosaicity value to approximately 0.25. This process will generate frame intensities and also place circles on the expected reflections. At this stage, it's important to review all the frames and remove those where a good matching was not achieved.

Once these steps are completed, you can continue working in PETS2 as previously explained, keeping in mind not to refine the tilt axis.

2.5. Structure solution

When the data processing is completed in PETS2, a file (cif_pets) is created and used as input for the structure solution. In this thesis, this process will be carried out using Jana2020. The structure solution is achieved through the Superflip [57] tool, which employs the Charge-Flipping algorithm to solve the phase problem. For the convergence of this algorithm to be possible, the input file must contain at least the lattice parameters, the expected symmetry of the structure, and the list of reflections, then the missing phase information is computed, recreating this way a complete Fourier map from which electrostatic potential density map, and hence the atomic structure according to the crystal symmetry can be extrapolated.

2.6. Dynamical scattering theory and structure refinement

In the past decade, several 3D electron diffraction (ED) data collection protocols[47] have emerged as powerful tools for crystal structure analysis, even applicable to complex cases such as incommensurate modulated structures[58,59]. By reconstructing the reciprocal space in three dimensions, these protocols enable the determination of unit cell parameters, indexing of reflections, and integration to generate a list of diffracted intensities versus hkl. With 3D ED, it has been demonstrated that the kinematical approximation is sufficient for utilizing diffracted intensities in one of the commonly used methods in X-ray crystallography to achieve the "structure solution" step. This initial structural model is then used to calculate intensities, which can be compared with experimental data, and through least-squares fitting, the model can be improved to achieve the best match

between calculated and experimental intensities. This process, commonly referred to as "structure refinement," was traditionally conducted under the assumption of the kinematical approximation, using software specifically designed for X-ray crystallography. While the kinematical approximation is suitable for X-ray diffraction in most cases, it is usually inadequate for electron diffraction, leading to high figures of merit (typically R1 or Robs about 20-30% versus 2-5% for single crystal X-ray diffraction). Consequently, it has raised legitimate concerns regarding the reliability and accuracy of the structure refinement process from 3D ED datasets.

Regardless of the 3D ED protocol employed, including those integrating diffracted intensity relrods (see PEDT and cRED previously described in section 2.3), intensities calculated using the kinematic approximation do not match with experimental observations. As complete elimination of dynamic conditions in electron diffraction is unattainable, it became crucial to address these effects by identifying the parameters that could impact diffracted intensities. Several efforts have been made to account for dynamical scattering effects in the calculation of diffracted intensities, primarily focusing on zone-axis patterns, thus utilizing a limited number of reflections[60,61,62]. In 2013, L. Palatinus et al.[63] demonstrated the feasibility of incorporating full dynamical scattering effects into the calculation of diffracted intensities using precession-assisted electron diffraction[64] on zone-axis patterns for refining structural models. Compared to previous works, this article represents a significant advancement by highlighting the substantial benefits of utilizing integrated intensities. It enables a more accurate determination of the crystal's thickness and orientation, offering a robust solution for structural refinements through the least squares method taking dynamical conditions into account. This capability to perform full dynamical refinement was further extended in 2015 to the analysis of precession-assisted ED data[65, 66] and, recently, to cRED data[67]. First implemented in the Jana2006 software, it is now accessible in Jana2020[31].

The use of dynamical theory in refinement involves several steps. The first step involves 3D ED data integration and the selection of observed intensities, which will be considered for the structure refinement. The second step involves calculating the theoretical diffracted intensities that will be compared with observed intensities. To do this several key parameters will be taken into account. In particular, the crystal thickness and the orientation of patterns, which directly influence intensities, need to be optimized and refined.

2.6.1. Specificities of intensities integration for dynamical refinement

The integration process for intensities differs depending on whether the objective is to solve a structure and refine it using the kinematic approximation or to utilize dynamical scattering theory for refinement. With the selection of a lattice and the orientation matrix, the PETS 2.0 program[56] can identify, index, and integrate the reflections present in each frame of the dataset. In the standard integration mode, the resulting file provides a list associating each reflection of indices hkl with its intensity I and its standard error σ(I). Each reflection appears only once in this file, with the diffracted intensity resulting from the complete integration of that reflection across all images where it is present.

However, the integration mode for dynamical refinement operates differently as multiple scattering events are highly sensitive to the crystal's orientation. To properly account for these effects during the dynamical refinement of PEDT datasets, a list of reflections (hkl, I, σ(I)) is created for each PED patterns present in the tilt series. For cRED datasets, the tilt series is first reduced by combining several experimental frames in order to generate what are referred to as virtual frames[67]. In both cases, the resulting output file consists of n lists of reflections corresponding to the n experimental frames, for precession-assisted ED, or n virtual frames, for cRED. The same reflection hkl can therefore be listed multiple times if it appears on multiple diagrams. Hence, for the same 3D ED dataset, the number of reflections utilized in dynamical refinement is significantly higher compared to the kinematic case. This will also have an impact on the indicators used to assess the accuracy of structure refinement in that, for example, the reliability factor on observed intensities will not be calculated on the basis of intensities averaged over equivalent reflections. The refinement procedure will thus be done frame by frame with a scale factor and agreement factors associated to each frame. A global set of reliability factors will then be derived from the refinement.

At this stage, a first selection of the reflection is performed by defining which reflections are integrated with the parameter $\mathbf{g_{max}(data)}$**.** It defines the maximum resolution limit defined by the length of the diffraction vector (in $Å^{-1}$). There is no strict default value but in most of the results shown in this thesis, g_{max} will be set to 1.4 $Å^{-1}$. For a TEM operating at 200 kV, this value corresponds to sin(theta)/lambda= 0.7 and a resolution of d_{min}=0.714 Å.

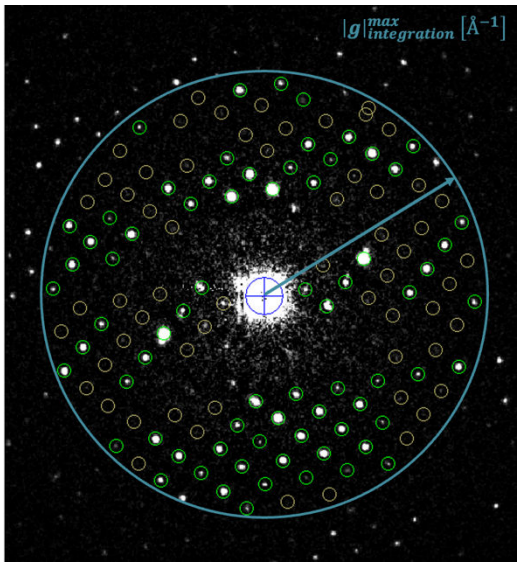

***Figure 23**. Diffraction pattern of a PEDT dataset showing the integration step with the maximum resolution limit represented by the blue circle. The green circles correspond to integration box of observed reflections, while the brown circles are the integration box where reflections based on the theoretical calculations should be.*

2.6.2. Method for calculating the diffracted intensities.

There are two methods for calculating electron diffracted intensities while considering multiple scattering: the so-called multi-slice method[68,69] and the Bloch wave formalism[70,71].

With the multi-slice method, the crystal is divided into thin slices perpendicular to the direction of the incident electron beam. For each slice, the electrostatic potential of the crystal is projected onto a plane. Electrons propagate through vacuum between the slices and are diffracted as it passes through each slice, taking into account interactions with the electrostatic potential. The effect of the crystal on the incident electron wavefunction is weak and mainly represented by a phase term introduced by each slice as well as by the effects of Fresnel diffraction. This method is suitable when applied to oriented zone-axis diffraction patterns and for simulating high-resolution transmission electron microscopy (HRTEM) images[72].

The second method is the Bloch wave formalism, which involves solving the time-independent Schrödinger equation. The wavefunction is expanded on the basis of Bloch waves describing the propagation states of electrons in a periodic crystal. This formalism is used to calculate intensities of 3D ED patterns as it offers more flexibility than the

multi-slice approach, particularly for intensity calculations on non-oriented zones axis patterns. The process for calculating intensities can be divided into several steps:

The first step is to define all reflections contributing to diffraction, i.e., those close enough to the Ewald sphere (with an excitation error S_g less than a threshold value to be defined) and involved in the refinement. To do this, a structure matrix named A needs to be constructed, which is independent of the crystal's orientation. This matrix A is a square matrix with the number of columns equal to the number of beams considered in the calculation.

For example, for three beams, the matrix A can be written as follows:

$$\mathrm{A} = \begin{pmatrix} 2K & U_{-g} & U_{-h} \\ U_g & 2KS_g & U_{g-h} \\ U_h & U_{h-g} & 2KS_h \end{pmatrix} \tag{2.4}$$

The diagonal elements of the matrix are given by a_{ii}, and the off-diagonal elements are denoted by a_{ij}:

$$a_{ii} = \frac{|K|^2 - |K + g_i|^2}{\left(1 + g_{n,i} / K_n\right)^{1/2}} \tag{2.5}$$

$$a_{ij} = \frac{U_{gi-gj}}{\left(1 + g_{n,i} / K_n\right)^{1/2}\left(1 + g_{n,j} / K_n\right)^{1/2}} \tag{2.6}$$

With $i = 1 \ldots, N_{beams}$,

$i, j = 1 \ldots, N_{beams}$; $i \neq j$,

n is the normal to the surface of incidence of the incident beam,

$g_{n,i}$ is the projection of the vector g_i onto n. g_i being a set of diffraction vectors of the beams considered in the calculation,

$K_{n,i}$ is the projection onto n of the wave vectors of the indecent beams,

$U_{g,i}$ are the calculated structure factors.

If electron backscattering is neglected, the diffracted waves for a thickness *t* can be represented by the elements of the first column of the scattering matrix denoted as *S*,

where t is the crystal thickness, A is the structure matrix, and K_n is the projection of the incident beam onto the crystal's entry surface.

$$\mathrm{S} = \exp\left(\frac{2_{\pi i t} A}{2K_n}\right) \tag{2.7}$$

$$I_{hi} = |S_{i1}|^2 \tag{2.8}$$

Intensities are obtained as the square amplitudes of these elements, and each intensity depends on the thickness, crystal orientation, structure factors, and considered beams. Once the intensity model is calculated, the rest of the procedure will be the same as for structure refinements in the kinematical approximation involving the least squares method.

2.6.3. Parameters for Reflection Selection

The selection of reflections that are involved in the refinement is a crucial step to ensure the success of the dynamical refinement. The choice is made based on parameters characterizing these reflections. The more important parameters are described below and schematized in Figure 24. Most are specific to electron diffraction dynamical refinement and are not found in the case of kinematical refinement from X-ray diffraction data. Generally, they can be classified into two categories:

Parameters related to observed intensities Iobs

S_g^{max}(data): S_g the excitation error of a reflection is independent of the integration method. The limit applied to all reflections will be denoted S_g^{max}(data). It defines a constant thickness band around the Ewald sphere (see **Figure 24**), and only reflections with S_g^0 close enough to the allowed limit are considered. By increasing the value of this parameter, more reflections are included, but they are also further away from the Ewald sphere and therefore generally have lower intensities.

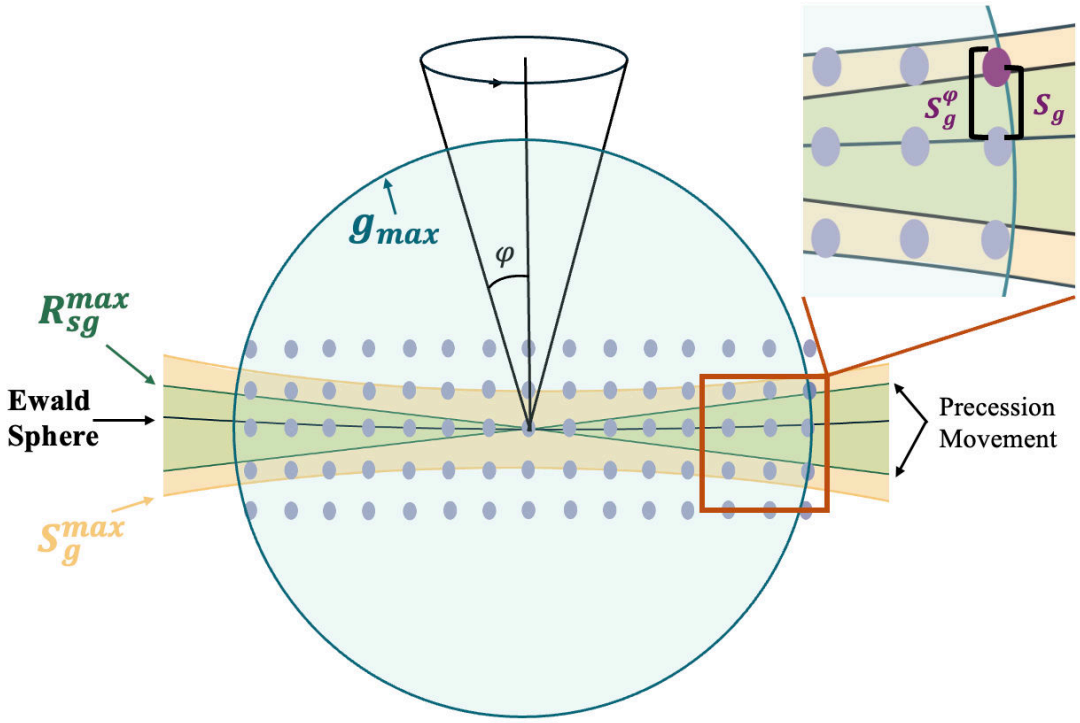

***Figure 24**. Ewald Sphere representation where the different parameters for reflection selection during integration and dynamical refinement are indicated. gmax: maximal resolution of experimental data [Å^{-1}], S_g^{max}:maximal excitation error of experimental data, $R_{S_g^{max}}$:ratio between Sg and the precession movement amplitude at the point g.*

R_{Sg}: this is the most important selection parameter. It is specific to the integration method. As an illustration for precession-assisted 3D ED, this parameter not only imposes a distance limit by selecting a reduced portion of the Ewald sphere, but this distance is also compared to the precession movement amplitude. This amplitude denoted S_g^{ϕ} (**Figure 24**), can be described as a maximum and minimum excitation error reached by the precession movement around a reflection. It is deduced from the precession geometry and is defined by equation 2.9 for a reflection g and a precession semi-angle φ.

$$\left|S_g^{\phi}\right| \simeq S_g^{\phi} \pm |g|\emptyset \qquad (2.9)$$

This way, only reflections close enough to the Ewald sphere with a certain ratio of the precession movement amplitude are considered in the refinement. This ratio R_{Sg} can be expressed as the ratio between the maximum excitation S_g^0 for a given reflection g and the amplitude S_g^{ϕ} (equation 2.10) and green zone in **Figure 24**. Concretely, this ratio describes how a reflection is covered by the precession movement. In **Figure 24**,

reflections located in the green zone are those for which the ratio between the maximum excitation error and the amplitude allowed by the precession movement is less than the selected value of R_{Sg}^{max} (see below). If R_{sg} of a reflection is less than 1, the Bragg condition is met during the precession movement. The reflection will pass into exact diffraction condition twice during the precession circuit. With R_{Sg}^{max}=1, a reflection will pass into Bragg condition at a single point, and if R_{Sg} is greater than 1, the reflection will not reach the Bragg condition during the precession circuit. This reflection is not necessarily absent or weak on the image. Indeed, a reflection can give a significant signal relatively far from the Bragg condition under certain conditions, especially for very thin samples. Finally, a reflection in exact Bragg position (located on the Ewald sphere) will have R_{Sg}= 0.

$$R_{Sg} = \frac{S_g}{S_g^{\phi}} \tag{2.10}$$

$\boldsymbol{R_{Sg}^{max}}$ ratio depends on the integration method (precession movement or continuous rotation). By setting the parameter R_{Sg} to a value less than 1, the selected reflections will be less influenced by crystal imperfections. This is because the first effect of these imperfections in reciprocal space can be described as the convolution of a perfect diffraction pattern and an attenuation function. Considering almost the entirety of the reflection intensity (i.e., with R_{Sg} less than 1) makes them less sensitive to this disturbance. By integrating only part of the reflection, the influence of this disturbance is greater. In the electron diffraction parameters panel in Jana 2020 (**Figure 25**), by increasing the parameter R_{Sg}^{max} more reflection will be considered in the calculation. By default, in Jana2020, R_{Sg} is set at a value of 0.66.

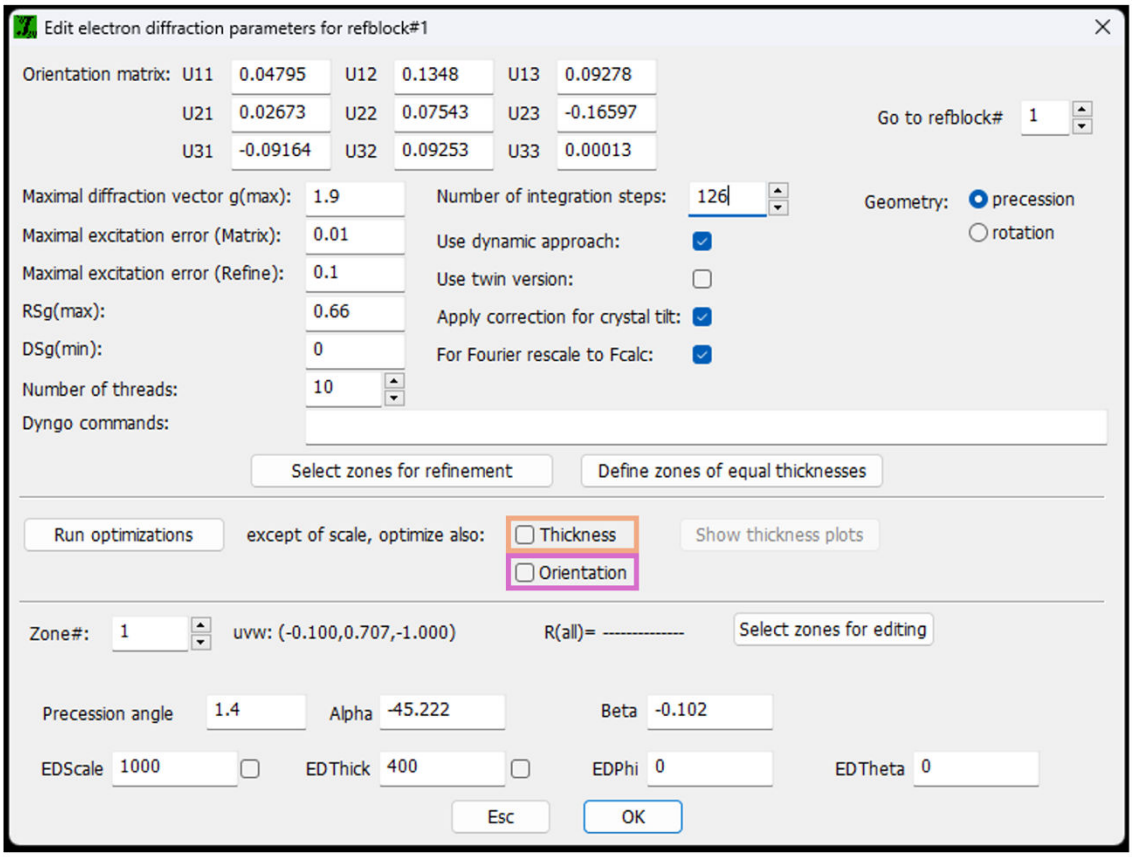

***Figure 25**. Jana Panel correspond to 'Edit electron diffraction parameters' window. Here it is possible to set the parameters for the refinement. Thickness (orange box) and orientation (pink box) can be refined.*

Parameters related to the calculated intensities Icalc

The parameters S_g^{max}(matrix) and g^{max}(matrix) determine the number of beams entering the structure matrix, which will then be used in the calculation of intensities. They are the counterparts of S_g^{max}(data) and g^{max}(data) but related to calculated and not observed intensities. S_g^{max}(matrix) is determined from vectorial equation 2.11:

$$S_g = \frac{|K|^2 - |K+g|^2}{2|K|} \qquad (2.11)$$

In the electron diffraction parameters panel in Jana 2020 (**Figure 25**), default values are applied for these two parameters and are generally not modified. g^{max}(matrix) is set with respect to the value g^{max}(data) used during the integration. By default, in Jana2020, g^{max} (matrix) is set at the value of g^{max}(data) + 0.2. S_g^{max}(matrix) is set to 0.01.

The parameter denoted $\mathbf{N_{step}}$ is related to the integration method (precession movement or continuous rotation). It is a calculation parameter that indicates the number of

evaluations of diffracted intensities along the integration circuit (a circle for precession or a line for continuous rotation). The higher the value is the more accurate is the evaluation, but this will significantly increase the calculation time.

2.6.4. Determination of the Average Crystal Thickness

During a 3D ED acquisition, the thickness of the crystal traversed by the electron beam will vary with the inclination angle of the sample holder. Moreover, the chosen crystal may not necessarily have a uniform thickness over the entire selected area. Describing diffracted intensities from an irregularly shaped crystal is challenging. Studies by L. Palatinus et al.[9] demonstrate that in most electron diffraction experiments, the crystal can be approximated as a collection of small sections parallel to each other with constant widths and variable thicknesses (**Figure 26**). Diffracted intensities can be calculated as an incoherent sum of all diffraction patterns emerging from each of these small sections. Therefore, the relative positions of the sections are not important, and knowledge of the exact shape of the crystal is not required. The crystal shape can be simplified by approximating it with a few simple geometric shapes such as a cylinder, wedges, or lenses. In the case of electron precession data, intensities are much less sensitive to variations in crystal thickness, and therefore, approximating the crystal shape as a simple geometric shape is sufficient to describe thickness variations.

The crystal thickness must be refined for each diffraction frame in a precession-assisted ED dataset (or each virtual frame in cRED). This procedure is included in the Dyngo program associated with Jana2020 (**Figure 25**). It involves calculating the weighted factor on the amplitudes wR1(all) as a function of thickness and allows obtaining the type of curve presented in **Figure 26**. This calculation can be performed considering the structural model obtained directly at the structure solution step or after a structure refinement assuming kinematical approximation. It provides an initial estimation of the quality of both the dataset and the structural model. When the thickness optimization works well, the wR1(all) curve as a function of thickness exhibits a single minimum for the considered diffraction pattern. Notice that optimization curves of a dataset acquired without precession do not exhibit a clear minimum and are usually not suitable for this optimization step. Also, the observed wR1(all) values are much higher than those obtained from data collected with precession. Once the thickness optimization is performed for all patterns, an average thickness for the crystal is determined during an

initial calculation cycle. Since all patterns come from the same crystal, it is assumed to have a constant thickness, and a correction will then be applied to account for thickness variations due to the crystal shape and its inclination during data acquisition. This is an option activated by default in the electron diffraction parameters panel in Jana 2020 (Figure 25). The thickness model can be also changed by passing the command to Dyngo.

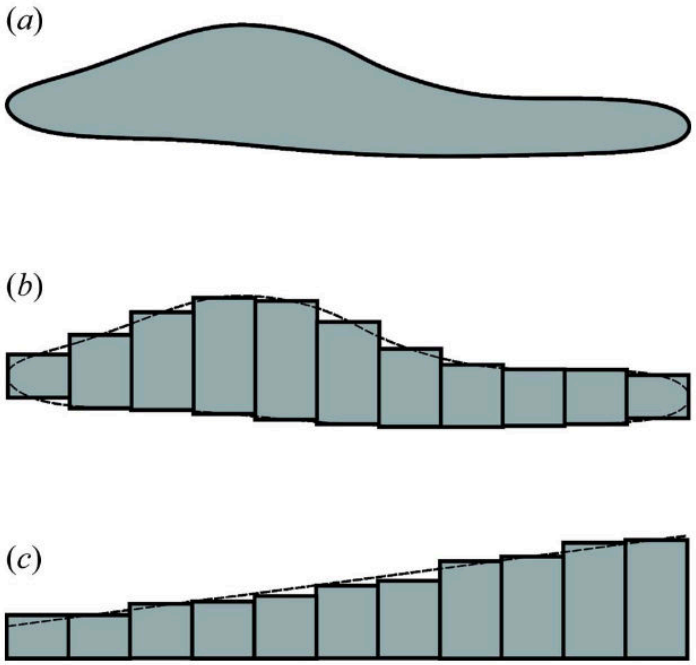

***Figure 26**. a) Schematic representation of an irregular crystal shaped crystal. b) Approximation of the crystal by sections of constant width. c)Approximation of the crystal shape after rearrangement of the sections giving the same diffraction pattern[73].*

2.6.5. Optimization of Image Orientations

The orientation of a 3D ED patterns is initially determined by the chosen lattice and the crystal orientation matrix during the integration step. However, many effects can cause a difference between the calculated orientation and the actual orientation. These effects include the lack of precision in the orientation matrix due in part to the lack of precision in the exact position of the goniometer or to the small movements of the crystal during acquisition. It is thus necessary to adjust the orientation for each pattern in the dataset. Unlike the average thickness, which is a parameter included in the least squares refinement, orientation is optimized separately. Indeed, a change in orientation induces a change in the excitation error Sg. Since this parameter is a reflection selection parameter, the number of reflections considered in the refinement (in matrix A) can be modified.

Consequently, intensities are not monotonic functions of orientation parameters, and the least squares refinement, which is based on the assumption of a continuous gradient, could be destabilized. Importantly, it was shown that without an integration method (PEDT or cRED), the ED intensities are heavily influenced (wR1(all) factor) by a slight misorientation. The use of an integration method helps to reduce the influence of misorientations on the intensities and thus on the wR1(all) factor. This is a major requirement for successful dynamical refinements.

During the refinement in Jana2020, an orientation optimization can be performed based on the structural model where the orientation deviation is described by two Euler angles:

> ***EDPhi***: rotation around the z-axis during data acquisition. This is the axis pointing from the sample to the electron beam and defines the direction of the inclination angle.
>
> ***EDTheta***: deviation of the sample inclination angle during 3D ED data.

Initially, and before any optimization procedure, the crystal orientation is defined by the orientation matrix. This condition corresponds to EDPhi and EDTheta = 0. To optimize the orientation, the program starts by searching for a minimum of the wR1(all) factor around the initial orientation The procedure used by the Dyngo software is based on the "downhill simplex method"[74]. It is a heuristic optimization algorithm adapted to minimize continuous functions in N-dimensional spaces. The quality of the optimization depends on the precision of the orientation matrix, but this can be limited by the goniometer of the microscope, the uncertainty of the orientation matrix itself, or small movements of the crystal during acquisition due to electron beam irradiation. For users of the program PETS2.0, an option is available to perform a first orientation optimization based on geometry during the 3D ED data integration.

Various tests have shown that the orientation optimization benefits the refinement by providing structures closer to the references and better merit factors. The deviation EDTheta from the initial rotation angle is expected to be about a few tenths of a degree. This is generally the case, but it can happen that the orientation parameters diverge towards higher values exceeding 1 degree. This is particularly the case for structures with small lattice parameters since there are, on average, fewer reflections per frame and therefore less information or sensitivity in certain directions. Moreover, the optimization process may fail when frames are dominated by a few very strong reflections. To avoid

aberrant results, frames for which the calculated deviation EDTheta are too large shall be excluded from the structure refinement.

2.7. Refinement considerations in Jana2020

It is important to understand what we mean by refinement, what is based on, and which parameters are important to consider for the results to be reliable.

In the previous section, we discussed the two different refinements applied for electron diffraction data, using namely the kinematical or the dynamical approach.

Before exploring into details, we will define the most important parameters considered in both refinements:

1. Number of total reflections: All the reflections that appear in the recorded frame.
2. Number of observed reflections: The reflections that count for the refinement and need to have an I/σ ratio equal or greater than 3.
3. Number of refined parameters: The value of these parameters will vary depending on whether we are performing kinematical or dynamical refinement.

Lastly, it is generally admitted that if the number of observed reflections is equal to or greater than 10 times the number of refined parameters, the results shall be statistically reliable.

Regarding the differences in refinement, kinematical refinement is based on the kinematical approximation, where the average of symmetry-equivalent reflections is used. Here we assume that symmetry-equivalent reflections have identical intensities regardless of where they were collected during the 3D electron diffraction (ED) data acquisition.

In contrast, dynamical refinement[67] is based on dynamical scattering theory, which describes how simultaneously excited beams interfere as they propagate through the crystal, resulting in intensities that deviate from those expected by kinematical approach. These deviations depend on the crystal's thickness, orientation, and the structure factors of all interfering beams. Therefore, in dynamical refinement equivalent reflections cannot be averaged because, due to multiple scattering events, there is no reason for these reflections to be identical.

A better illustration of dynamical refinement can be seen in the following figure:

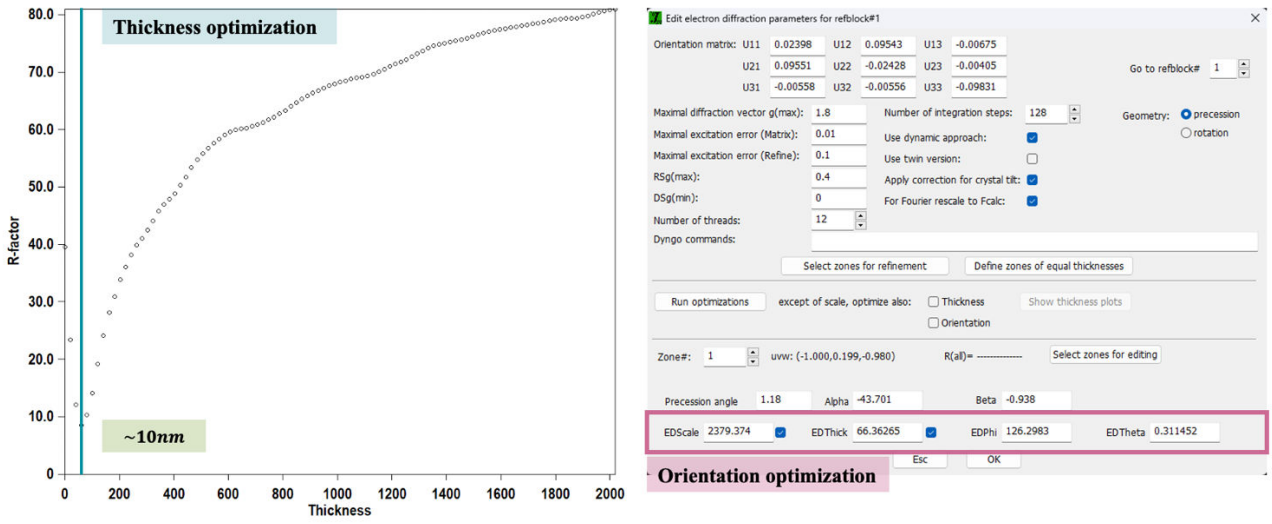

Figure 27*. (left) thickness optimization graph where the Rvalues are computed for different thickness. The minimum in the graph correspond with the estimated thickness. (left) 'Edit electron parameters' window, where the pink box correspond to the refined parameters involved.*

2.7.1. Refined Parameters

The number of parameters to refine depends on various factors. First, there is the scale factor (Figure 28 (orange box)), which is used to adjust the calculated intensities of diffraction sports to match the observed intensities. For kinematical refinement, this scale factor is refined only once for the entire dataset. In contrast, for dynamical refinement, the scale factor is refined for each frame.

Second, the specific atomic positions (**Figure 28** (pink box)), or the x, y, z coordinates of each atom, need to be refined, except for those atoms located in special positions within the sample.

The third parameter is de UISO value or thermal factor (Figure 28 (blue box)), which describes how atoms in a crystal displace from their average positions due to thermal energy.

Lastly, if it relevant to the sample, another parameter to refine is occupancy (**Figure 28** (green box)). If the material has two atoms sharing the same atomic position, it is possible to determine the ration of both elements at that specific position.

All these possibilities can be displayed in the M40 file from Jana (**Figure 28**).

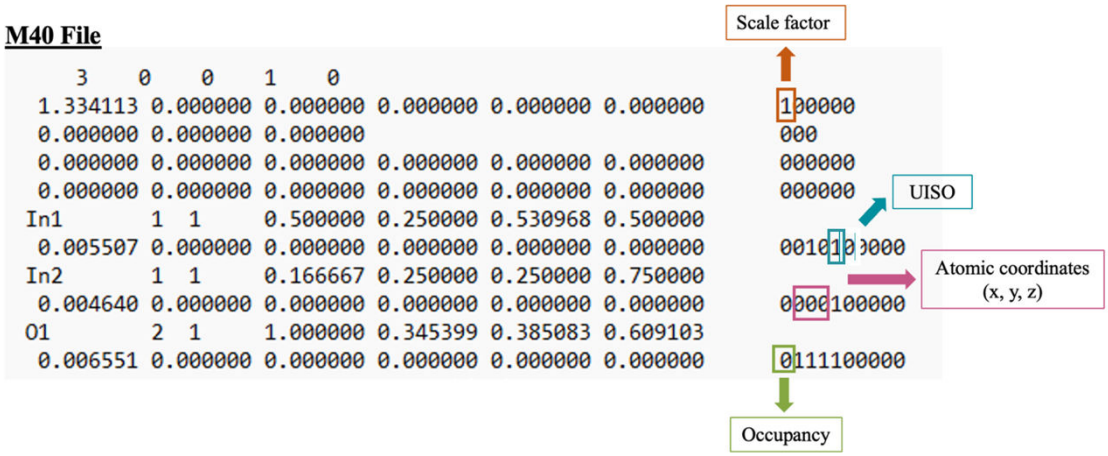

Figure 28. *M40 Jana file (the example is taking from ITO compound). In this file is possible to find information about the species of the compound, and refined parameters (Those where a number 1 appear): Scale factor, UISO value, Atomic coordinates, and Occupancy.*

CHAPTER 3

TESTING 3D ED TECHNIQUE

Much of the literature that appears when characterizing nanoparticles using 3D ED specifies that structural resolution of nano-sized crystals is possible. However, many of these source's lack of information related to the size of the materials actually investigated using 3D ED. Some informal reports such as A. Stewart at ELDICO webinare[75] , indicated that it should be possible to analyze the structure of 10 nm NPs by 3D ED, but there is no evidence that this analysis can be performed experimentally. That's the main aim of this thesis: to provide an answer to this question and, above all, to find out how to go about it and discuss the results. But before that, it would be interesting to get an idea of what can be achieved with 3D ED for larger crystals, in terms of the quality and precision of structural refinements.

In this chapter, the main results of the *NanED Round Robin*[76] will be given in order to gain a comprehensive understanding of the capabilities and information that this technique can provide whatever the equipment, technique or person involved. Following this preliminary assessment, the focus will shift to the analysis of "large" NPs, aiming to develop standard protocols for the acquisition of high-quality data and the subsequent structural solution.

3.1. Study of large crystals – NanED Round Robin

The NanED project proposed a *Round Robin* experiment in which relatively large crystals (1 μm to 500 nm) were analyzed to understand the fundamental information that this technique can offer together with its limitations. For each of the 14 PhD students (ESRs) participating in the NanED project was given two "unknown" inorganic compounds (plus one organic not discussed here). Although we had no prior knowledge of their crystal structure because it could bias the experiment, these structures were well-known and documented in the literature and databases.

3.1.1. Epidote $Ca_2Al_2(Fe,Al)(SiO_4)(Si_2O_7)O(OH)$

The first case was a macro crystal of a mineral silicate. The sample is a natural epidote from Val d'Ossola Italy (see **Figure 29**). The structural details are shown in **Table 1**, presenting a monoclinic symmetry with 19 atoms in the unit cell.

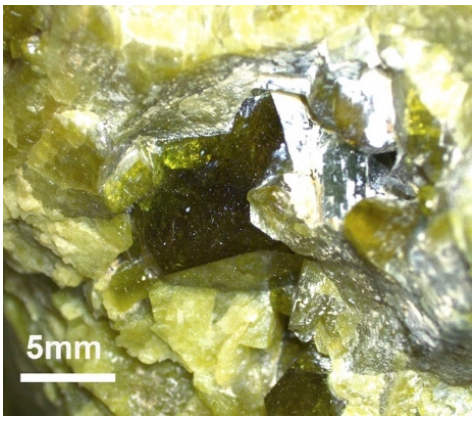

Figure 29. *Epidote crystal image from Val d'Ossola (Italy)*

Crystal system	Monoclinic
Space group	$P2_1/m$
Unit cell	a=8.89470(10) Å, b=5.61480(10) Å, c=10.1562(2) Å, b=115.4010(11)°
Atoms in the asymmetric unit	**19**: 3 Si; 2Al; 2Ca; 1Al/Fe; 10 O; 1H

Table 1. *The structure specifications for Epidote mineral. These parameters were obtained by SCXRD at CRISMAT laboratory.*

The challenges for 3D ED analyzing this sample were its moderate beam sensitivity, the presence of a site with mixed occupancy between Aluminum (Al) and Iron (Fe) and the direct detection and refinement of the H atom present in the structure.

3.1.2. Natrolite $Na_2Al_2Si_3O_{10} \cdot 2(H_2O)$

The second case involves a mineral from the zeolite family called Natrolite shown in **Figure 30**. This mineral was provided by the research group from Mariánská Skála in Ústí nad Labem, Czechia. The mineral present an orthorhombic symmetry, with 12 atoms in the asymmetric unit cell (see **Table 2**). The results were obtained at CRISMAT laboratory, by SCXRD analysis.

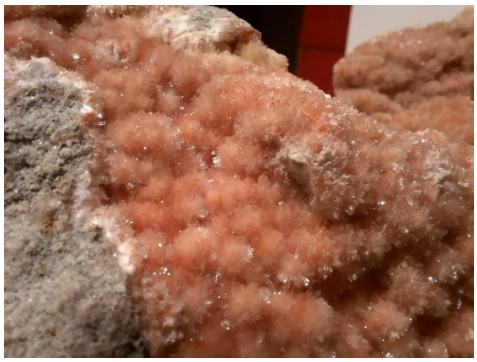

***Figure 30**. Natrolite crystals image from Mariánská Skála, Czechia.*

Crystal system	Orthorhombic
Space group	Fdd2
Unit cell	a=18.6323(3) Å, b=18.2877(2) Å, c=6.58310(10) Å
Atoms in the asymmetric unit	**12**: 2 Si; 1Al; 1Na; 6 O; 2H

***Table 2**. The structure specifications for Natrolite mineral. Those parameters were obtained by SCXRD at CRISMAT laboratory.*

The challenges for 3D ED analyzing this sample were distinguishing the Al tetrahedra from the Si tetrahedra by comparing the cation-oxygen distances, determining the hydrogen positions of the water molecules, and providing evidence of the possibility of establishing the absolute structure since Natrolite is not centrosymmetric.

3.1.3. Round Robin Experiment Design

For both Epidote and Natrolite, the sample preparation was not complicated. A small amount of powder from each sample was placed in a small mortar, dissolved with a bit of ethanol, and then ground to achieve crystals small enough to be analyzed by 3D ED. A drop of this mixture was placed on the grid and dried with an infrared lamp.

In order to test the influence of different parameters, several experiments were designed using different microscopes, illumination systems, detectors, and data acquisition protocols as shown in **Table 3** where the yellow background is the individual experiment explained in detail.

Lab	TEM	HT kV	Technique	Detectors	Illumination
1	Zeiss Libra 120	120	PEDT/CRED	Timepix	ND
2	Fei Tecnai G2	200	CRED	Timepix	ND
3	Fei Tecnai G2 20	200	PEDT/CRED	Medipix3	ND
4	Fei Tecnai F30 STWIN	300	PEDT	Ultrascan4000	ND
5	Jeol 2100	200	CRED	Timepix	SAED
6	**Jeol F200**	**200**	**PEDT**	**Medipix3/Rio16**	**ND**
7	Jeol F200	200	CRED	Medipix3	SAED

***Table 3**. Experimental setups of the different laboratories involved in the round Robin. In yellow is the setup corresponding to the one used at CRISMAT.*

The experiments have already been designed, but it is important to highlight some key points from **Table 3**. Considering data collection, three different protocols have been selected:

1. Precession-assisted 3DED (PEDT): In this method, data acquisition is performed stepwise with selected cone semi-apertures ranging from 1° to 1.4°.
2. Continuous rotation 3DED (cRED): Here, diffraction patterns are collected continuously while the crystal rotates. The rotation speed depends on the exposure time.

3. Step-wise 3D ED (EDT): This method also involves stepwise data collection. However, unlike PEDT, precession is not applied in this protocol.

For the illumination system, there were just two options: the first one is Selected Area Electron Diffraction (SAED), where the area where diffraction is to be performed is selected using an aperture located below the sample holder, in the image plane. The second one is Nano-beam Diffraction (ND) mode, where the sample is illuminated using a beam whose dimensions is controlled by the condenser lens aperture.

The last important thing will be to distinguish between the detectors. There are two main classifications: direct hybrid-pixel detectors (such as Timepix) and indirect detectors (such as Rio 16). The primary difference is that direct detectors capture electrons directly and convert them into a number of counts / hits, offering higher sensitivity and resolution. In contrast, indirect detectors use a scintillator to convert electron into light, which is then converted into counts by the camera, often resulting in lower sensitivity and resolution.

3.1.4. NanED Round Robin results (CRISMAT)

Firstly, I will present the results obtained at CRISMAT, noting that a JEOL F200 microscope was used operating at 200kV in probe mode, with a spot size of 5 and a condenser lens aperture of 10 μm. The data acquisition protocol was precession-assisted ED with a precession angle of 1.2, a tilt step of approximately 1°, a camera length of 300 nm and an exposition time of 0.2 s. GATAN Rio16 and ASI Cheetah M3 detectors were used. The experiments for both compounds were conducted at room temperature (293K) using a JEOL tomographic holder.

Epidote

Without prior knowledge of the sample being analyzed, the first step was to conduct a chemical analysis using EDX analysis to identify the chemical species presents in the sample, which tested positive for Calcium (Ca), Silicon (Si), Aluminum (Al), Iron (Fe) and Oxygen (O).

The data collection was performed without any issues; a beam size smaller than the crystal was used, and by employing the precession-assisted ED protocol, we were able to consistently visualize and ensure that the same region of the crystal was being analyzed throughout the experiment. Although the material exhibited moderate sensitivity to the

electron beam, we successfully collected a sufficient number of frames for the 3D reconstruction of the reciprocal space. The data acquisition time was typically about 20 to 25 minutes.

The data processing involved PETS2 and Jana2020 for structure solution and refinements [73]. The structure solution proceeds smoothly, and all atomic positions were found except for H. An uncertainty was present about the exact location of Fe, Si and Al. The way to distinguish between them, at this preliminary stage, is by examining their bonding with other atoms. Si atoms typically form tetrahedral structures, whereas Al atoms generally form octahedral structures. Therefore, once the atomic positions of both Ca and O were established, the Si and Al atoms were added based on their coordination geometry.

From the initial model, kinematical refinement could be performed, and Bond Valence Sum (BVS) calculations were used to properly assign the atomic species on their position. Combining this method with charge balance, the results suggested that 1 H atom shall be present and attached to position O_7. However, no evidence of H atoms in the Fourier difference maps was present whatever the dataset and the detector. At this stage, the Robs value is in the range 25-30% (see **Table 4**, pink background), which is high even for 3D ED standards. Also, notice that for the data collected with the RIO detector, some ADPs were found to be non-positively defined.

Going to dynamical refinement (see **Table 4**, blue background), this later problem disappeared and, whatever the detector, all ADPs were positively defined. The Robs values were divided by a factor of two and, when performing a Fourier difference map, the H atom expected close to O_7 can be found based on the existence of residual density and, even, refined (see **Figure 31.**a). In the structure, the Fe atomic site is actually a mix Fe/Al site with an occupancy of about 65-70% Fe and 30-35% Al from the literature. While the ADPs value (Uiso~0.01Å^2) for this Fe site was a bit higher than the ones obtained for Al or Si atomic sites (Uiso~0.002Å^2), it was not clear whether the site of the Fe atom is characterized by full occupancy, mixed occupancy with Al or by an amount of vacancies since the R values don't show much difference (few tenth of percent). We finally decided to retain the solution were Fe1 site possess a mixed Fe/Al occupancy. If we try to refine the occupancy on this site, we obtain a ratio Fe/Al: 70/30 and 80/20, respectively for the RIO16 and Cheetah M3 results. We are here close to the limit of what

3D ED can reach and mix occupancy sites represent some significant challenge for 3D ED.

	RIO16	Cheetah M3
Electron wavelength λ (Å)	0.0251	
Number of frames	116	95
Tilt range (°)	115	110
Precession angle (°)	1.18	1.25
Resolution $\sin(\theta_{max})/\lambda$ (Å^{-1})	0.9	0.9
Measured, observed[$I>3\sigma(I)$] reflections	2877, 2124	2697, 2647
No. of refined parameters, restraints	54, 0	54, 0
***R*(obs), *R*(all), *wR*(all), GoF(all)**	0.274, 0.311, 0.624, 11.57	0.272, 0.274, 0.537, 16.63
Measured, observed[$I>3\sigma(I)$] reflections	10071, 9473	9287, 7586
No. of refined parameters, restraints	167, 0	153, 0
g_{max} (Å^{-1}), $S_{g,max}$ (Å^{-1}), R_{Sg}, steps	2, 0.01, 0.4, 126	2, 0.01, 0.4, 126
***R*(obs), *R*(all), *wR*(all), GoF(all)**	0.143, 0.149, 0.324, 9.72	0.134, 0.146, 0.279, 5.09

Table 4. *Refinement results for Epidote crystal obtained at CRISMAT. Pink and blue background correspond to kinematical and dynamical refinement respectively.*

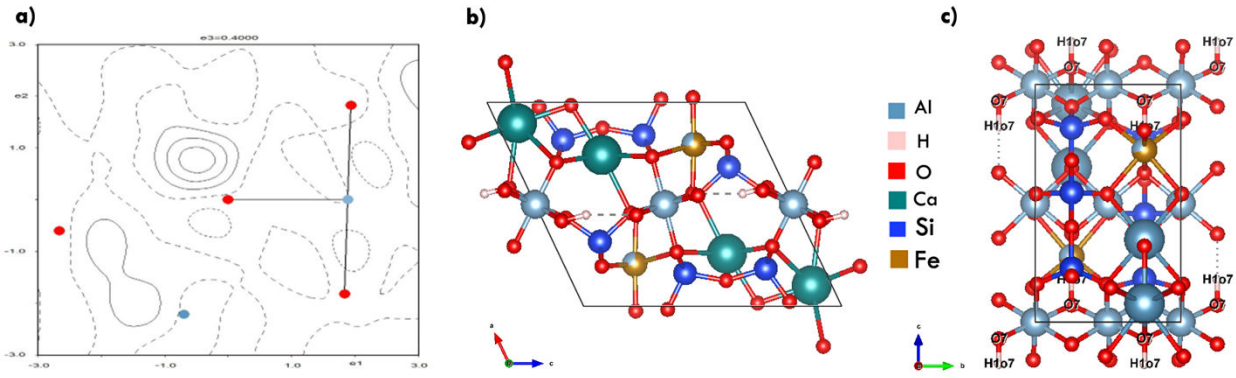

Figure 31. *Final structure for Epidote after dynamical refinement obtained with a RIO16 detector. a) Fourier difference map calculated on an Epidote data set refined dynamically before the H detection. The positive peak corresponding to the hydroxyl group is clearly visible. b) Epidote crystal structure view along a axis. c) Epidote crystal structure view along b axis.*

The final structure model can be seen in **Figure 31.**a and c and the details containing the atomic positions, ADP values y occupancy are shown in **Table 5**.

Space Group $P2_1/m$ (11), a =8.846(3) Å, b =5.612(3) Å *c* = 10.125(5) Å					
R(obs)=14.27, R(all)=14.92 , wR(all)=32.41, GoF(obs)=9.72					
measured / observed [I>3σ(I)] reflections= 10017 / 9473, 167 refined parameters					
g_{max} (Å^{-1})=2.0, Sg_{max} (Å^{-1})=0.01, RSg_{max}=0.4, steps=126					
Atom	**x**	**y**	**z**	***U* (Å^2)**	**Occ.**
Ca_1	0.8970(2)	0.75	0.0079(2)	1.0	0.013(3)
Ca_2	0.7421(2)	0.75	0.3484(2)	1.0	0.007(3)
Al_1	0.5	0	0	1.0	0.004(3)
Al_2	0.5	0	0.5	1.0	0.004(3)
Al/Fe	1.2069(2)	1.25	0.2755(2)	0.301/0.698	0.008(4)
Si_1	0.1616(3)	0.75	0.4540(2)	1.0	0.003(3)
Si_2	0.3166(2)	-0.25	0.1815(2)	1.0	0.003(3)
Si_3	0.8158(3)	1.25	0.2254(2)	1.0	0.004(3)
O_1	0.7060(3)	1.0128(5)	0.1595(2)	1.0	0.008(4)
O_2	0.9847(4)	0.75	0.3200(3)	1.0	0.008(5)
O_3	0.4327(4)	-0.25	0.0932(3)	1.0	0.005(5)
O_4	0.8737(5)	1.25	0.4007(4)	1.0	0.011(6)
O_5	0.4568(4)	-0.25	0.3538(3)	1.0	0.004(4)
O_6	0.2665(3)	0.9943(5)	0.4601(2)	1.0	0.007(4)
O_7	0.5817(4)	-0.25	-0.0714(3)	1.0	0.006(5)
O_8	0.1961(3)	-0.4817(5)	0.1443(2)	1.0	0.007(3)
O_9	0.9766(5)	1.25	0.1931(4)	1.0	0.010(6)
O_{10}	0.4474(4)	0.25	0.3712(3)	1.0	0.004(4)
H	0.5520(26)	-0.25	-0.1770(20)	1.0	0.007

***Table 5**. Epidote structural parameters obtained from single crystal 3D ED data with a RIO16 detector. The occupancy for Al/Fe in the same atomic position was refined and the values obtained for the ratio were (0.301/0.698)*

Natrolite

Following the steps performed for Epidote, a chemical analysis was performed, where the presence of Sodium (Na), Silicon (Si), Aluminum (Al) and Oxygen (O) was defined.

From data analysis and structure solution, a false solution can be found with SG I-42d and cell parameters a ~ 13.15Å and c ~ 6.6Å. The structure is similar to the correct one but with a mixed Si/Al tetrahedral site. Accuracy on cell parameters is important here to select the orthorhombic cell instead of the quadratic one. Finally, to obtain the correct model, the reflections were indexed using an orthorhombic symmetry with a = 18.62(5) Å, b = 18.32(5) Å and c = 6.59(2) Å, and F-centering lattice.

From kinematical refinement, the charge balance and BVS calculations tell us that H atoms shall be present and attached to position O6 but no evidence of H atoms in Fourier difference maps. From dynamical refinement, 2 H atoms appear on Fourier difference maps and were added to the refinement with soft distance constraints (see **Figure 32**.a).

The results for both kinematical and dynamical refinements are shown in **Table 6**, where we can see that Robs for dynamical refinement shows lower values than for the kinematical ones. Nonetheless, for the RIO16 results, the reduction is quite small i.e. from 21.6% to 17.0% only. This later value is high for dynamical refinements and point towards some “unresolved problems” presumably due to a moderate quality of the dataset. The situation observed for the Cheetah M3 results is more in tune with what we could expect i.e. a reduction of about half the Robs value going from kinematical to dynamical refinements. Taking the inverted structure and performing dynamical structure refinements, a clear distinction between the enantiomorphs can still be obtained in both RIO16 and Cheetah M3 cases. The Natrolite final model details obtained for Cheetah M3 detector are shown in table **Table 7**, and a representation of the crystal model is shown in **Figure 32**.b.

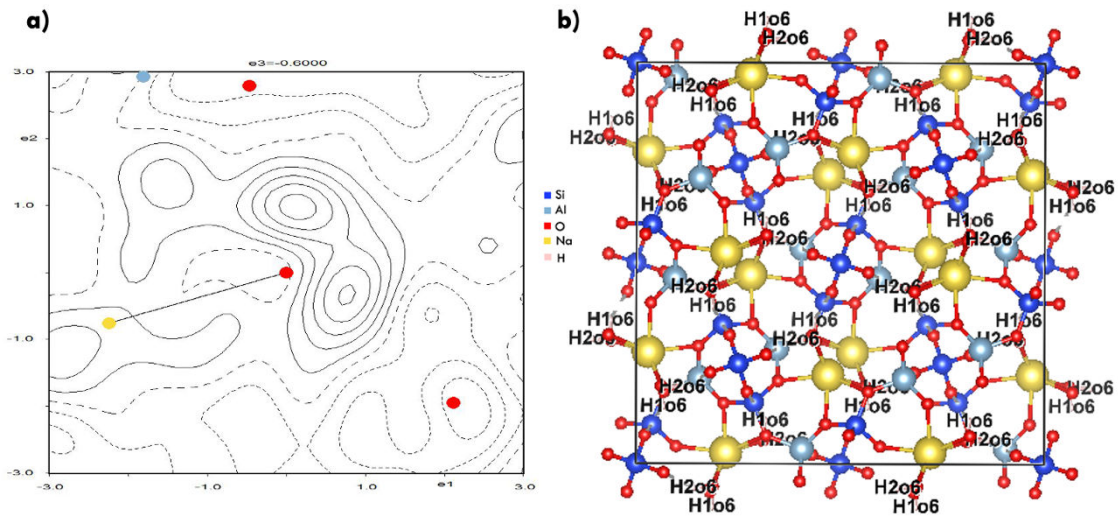

Figure 32. *Structure model for Natrolite after dynamical refinement. a) Fourier difference map calculated on a Natrolite data set dynamically the H detection. Two positive peaks corresponding to the H of water molecule are clearly visible. b) Natrolite crystal structure view along c.*

	RIO16	**Cheetah M3**
Electron wavelength λ (Å)	0.0251	
Number of frames	105	109
Tilt range (°)	104	107.5
Precession angle (°)	1.4	1.35
Resolution $\sin(\theta_{max})/\lambda$ (Å^{-1})	0.75	0.8
Measured, observed[$I>3\sigma(I)$] reflections	2423, 2048	1995, 1742
No. of refined parameters, restraints	38, 0	38, 0
***R*(obs), *R*(all), *wR*(all), GoF(all)**	0.216, 0.246, 0.433, 11.4	0.184, 0.205, 0.337, 7.68
Measured, observed[$I>3\sigma(I)$] reflections	9072, 5650	8760, 5107
No. of refined parameters, restraints	143, 0	153, 0
g_{max} (Å^{-1}), $S_{g,max}$ (Å^{-1}), R_{Sg}, steps	1.8, 0.01, 0.4, 126	1.8, 0.01, 0.4, 128
***R*(obs), *R*(all), *wR*(all), GoF(all)**	0.170, 0.256, 0.332, 5.48	0.107, 0.153, 0.209, 3.12

Table 6. *Refinement results for Natrolite crystal obtained at CRISMAT. Pink and blue background correspond to kinematical and dynamical refinement respectively.*

Space Group Fdd2(43), a =18.6079(17) Å, b =18.2645(17) Å *c* = 6.5900(68) Å					
R(obs)=10.7, R(all)=15.3 , wR(all)=0.209, GoF(obs)=3.12					
measured / observed [I>3σ(I)] reflections= 8760 / 5107, 153 refined parameters					
g_{max} (Å^{-1})=1.8, Sg_{max} (Å^{-1})=0.01, RSg_{max}=0.66, steps=126					
Atom	**x**	**y**	**z**	**Occ**	**U (Å^2)**
Si_1	0.5	0.5	0.16315(29)	1.0	0.0039(6)
Si_2	0.7883(1)	0.1534(1)	0.04135(29)	1.0	0.0039(4)
Al	0.9064(1)	0.0370(1)	0.0480(29)	1.0	0.0035(5)
O_1	0.0987(2)	0.0432(2)	0.1909(29)	1.0	0.0109(8)
O_2	0.4319(2)	0.0225(1)	0.2981(29)	1.0	0.0125(7)
O_3	0.7136(2)	0.1514(2)	-0.0865(30)	1.0	0.0099(7)
O_4	0.7714(2)	0.1790(2)	0.27310(30)	1.0	0.0148(8)
O_5	0.8178(2)	0.0703(2)	0.05570(30)	1.0	0.0080(6)
O_6	1.0611(3)	0.1932(3)	-0.19622(30)	1.0	0.0224(9)
Na	0.97003(2)	0.22141(2)	0.04834(30)	1.0	0.0160(7)
H_1	1.06099(21)	0.15029(20)	-0.29439(49)	1.0	0.0486(80)
H_2	1.10652(18)	0.19134(16)	-0.13592(42)	1.0	0.0265(66)

***Table** 7. Natrolite structural parameters obtained from single crystal 3D ED data*

3.1.5. Structure comparison

To check the accuracy of the 3D ED structure determination, single crystals from the same batches of samples were measured with single crystal x-ray diffraction. The instruments used were a Rigaku XtaLAB Synergy (CRISMAT), equipped with a Mo source. We used the X-ray refined structures as reference for a comparison with the 3D ED results.

The comparison was carried out using the COMPSTRU utility of the Bilbao Crystallographic Server[77], which delivers the shift of each atomic position of the two compared structures. In COMPSTRU, "the difference between the two models is quantified by evaluation of the global distortion decomposed into a spontaneous strain (lattice deformation) and atomic displacement field representing the distances between the paired atoms of the two structures." Therefore, before comparing the atomic positions of the checked structure with the reference one, the software deforms its unit cell to make it most similar to the reference, and then it evaluates the atomic shifts. So, if the atomic coordinates are very similar, but the unit cell is significantly different due to calibration

and experimental deformation errors, the two structures will be similar anyway. In the case of ED data this is crucial since the accuracy in the unit cell parameters is much worse than X-ray data due to unavoidable calibration errors. All the data of the *Round Robin* have been collected in microscopes which are not dedicated to 3D ED only, so every time an experiment is carried out the instrument should be realigned with unavoidable calibration errors which are further worsen by intrinsic astigmatism of the lens system. Globally, the *NanED Round Robin* results show that the errors can reach 1-2% in the unit cell parameter lengths and 0.5° in the angles. This is actually a critical point, where the accuracy remains poor with respect to X-ray. In this prospective, dedicated instruments like the recent electron diffractometers (Eldico ED-1 and Rigaku Synergy-ED), could improve the figures. Having machines where ED experiments are the only performed experiments and whose camera length is fine calibrated and kept fixed, we think it can bring the cell accuracy beyond 1% in length and 0.1° in the angles. Another option is to have some internal reference collected at the same conditions, if possible, at the same time, in order to calibrate accurately the *Aperpixel* value and the distortions induced by the TEM lenses. This was recently illustrated in case of scanning precession-assisted electron diffraction tomography experiments realized on thin films[78] in the framework of the NanED project and the PhD of Sara Passuti[79].

Lab	**Kinematical**		**Dynamical**			
	max.dist (Å)	av. dist (Å)	max.dist (Å)	av. dist (Å)	Fe occupancy	H detection
1	0.119	0.066	0.060	0.024	.66(4)	Yes
2	0.074	0.031	0.019	0.007	.57(3)	Yes
3	0.044	0.023	0.014	0.005	.811(16)	Yes
3	0.052	0.023	0.016	0.006	.6795(9)	Yes
4	0.134	0.045	0.050	0.019	-	No
5	0.032	0.015			-	Yes
6 (M3)	0.042	0.019	0.032	0.015	0.805(17)	Yes
6 (RIO)	0.078	0.035	0.028	0.012	0.699(17)	Yes
7	0.056	0.022			-	No
Aver	**0.070**	**0.031**	**0.031**	**0.013**		

***Table 8**. Comparison results for the epidote structure. In yellow are the results from CRISMAT.*

Lab	Kinematical		Dynamical		
	max.dist (Å)	av. dist (Å)	max.dist (Å)	av. dist (Å)	H detection
1	0.128	0.060	0.063	0.032	Yes
1	0.037	0.021			No
3	0.022	0.015	0.023	0.013	Yes
3	0.037	0.021	0.020	0.010	Yes
5	0.031	0.015			Yes
6 (M3)	0.035	0.025	0.035	0.014	Yes
6 (RIO)	0.062	0.033	0.038	0.018	Yes
7	0.100	0.050			No
Aver	**0.057**	**0.030**	**0.036**	**0.017**	

***Table 9**. Comparison results for the natrolite structure. In yellow are the results from CRISMAT.*

As key parameters for the structure comparison, we considered here the maximum (max. dist in Å) and the average shift (av. dist. in Å) given by COMPSTRU. The comparison results are reported in **Table 8** and **Table 9** for epidote and natrolite, respectively. Note that the hydrogen atoms were not considered in the comparison since it is known that the maximum of the electrostatic potential and of the electron density, the quantities responsible for electrons and x-ray scattering, respectively, are significantly shifted in the case of H[80].

Globally, for both epidote and natrolite, we observe a good accuracy in the structure determination for both kinematical and dynamical refinement with a maximum error in the atomic position of 0.13 Å and an average error, on average, about 0.03Å for kinematical refinements. The dynamical refinement always improves the structure model (SCXRD reference structure refinement), bringing the average error below 0.02 Å with a remarkable success of a structure having an average error of 0.005 Å. Refinements obtained at CRISMAT are in the average compared to the whole set of results. This means that for dynamical structure refinements performed on large crystals, we can expect an accuracy below 0.02Å and 0.04Å for the average and maximal error on atomic positions, respectively.

From these results, we can conclude that the 3D ED technique is suitable for use with large crystals, allowing for the successful structure analysis of both compounds studied. In the first case (Epidote), the positions of the Al and Si atoms were determined based on their coordination geometry. Additionally, the electrostatic potential signal from the hydrogen atoms was detected, but only after dynamical refinement, which underscores the importance of accounting for multiple scattering events when working with electron diffraction data. A similar observation was made in the second case (Natrolite), where the signal from the hydrogen atoms became visible only when examining the difference Fourier maps during dynamical refinement. Furthermore, the power of this technique is not limited to the detection of hydrogen atoms; it also enables differentiation of the absolute structure by simply evaluating and comparing the Robs values obtained through dynamical refinement.

Now that we have a better view of what results can be obtained on large crystals, we can proceed to perform experiments on NPs. The first material to be tested, with the aim of developing protocols for the acquisition of high-quality data and subsequent structural resolution, will be TiO_2 brookite, which will be referred to as 'large NPs' throughout this chapter, as they are the largest nanoparticles characterized in this thesis.

3.2. Study of large NPs

Now that we have a better view of what results can be obtained on large crystals, we can examine whether reducing the crystal size will impact the quality of the structure determination. To test this, we will begin by studying what we refer to as 'large NPs', which are those whose longest dimension is around 70 nm. For this, the chosen material was TiO_2 brookite nanorods (**Figure 33** (right)). NPs often have known, and simple structure compared to the ones used in the *Round Robin*. While simple, all the x, y, and z atomic parameters of the 3 atomic positions are refinable parameters, which provide elements to be compared with the reference structure. This reference data is from the ISCD database [Code36408] and the article published by E. P. Meagher and G.A. Lager in 1979[81] (**Figure 33** (left)). The structure analysis was done using SC-XRD and the cell parameters and atomic positions are described in **Table 10**.

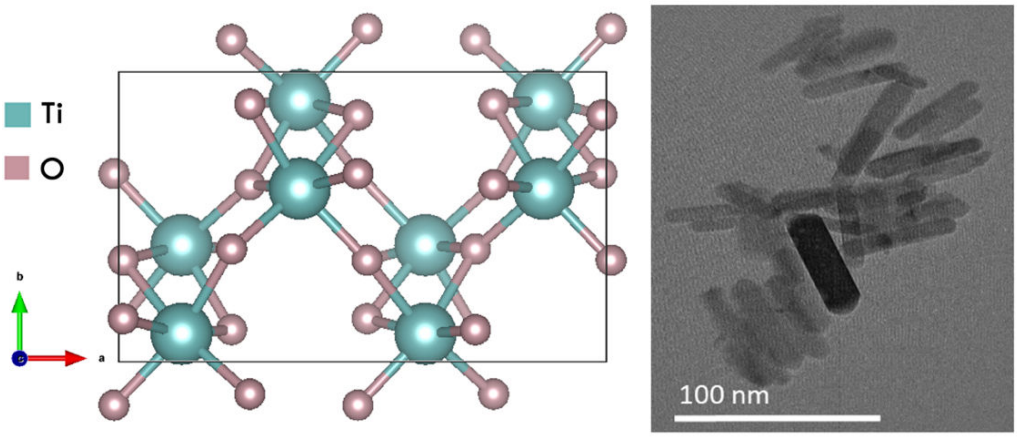

***Figure 33**. (left) Structure of TiO_2 brookite represented in a projection along the [100] direction (reference ISCD 36408). (right) TEM image where size and shape of TiO_2 brookite NPs can be estimated.*

SG: Pbca (61), a = 9.1740(2) Å, b = 5.4490(2) Å, c = 5.1380(2) Å					
Atom	**x**	**y**	**z**	**Occ**	**Biso**
Ti1	0.1289 (1)	0.0972(1)	0.8628(1)	1	0.37(3)
O1	0.0095(4)	0.1491(5)	0.1835(5)	1	0.46(6)
O2	0.2314(4)	0.1110(4)	0.5366(6)	1	0.53(7)

***Table 10**. Structural parameters of TiO_2 brookite (based on ISCD 36408). All the coordinates (in red) can be refined for this model compound.*

Titanium dioxide (TiO_2) NPs are used in a wide range of applications and exist in three main phases[82]: anatase, brookite and rutile. As a bulk material, rutile is the stable phase; whereas brookite and anatase are metastable and easy to transform to rutile when heated. The phase relationships and transition kinetics may be dramatically modified when the grain size is small enough. This is because the phase stability depends upon surface energy differences among the three phases. Anatase with the grain size below 14 nm is more stable than rutile. This explains that anatase phase is preferably synthesized at nanometer size. Anatase is also more stable than brookite for NPs with a size smaller than 11 nm which suggests that a phase transition from brookite to anatase also may take place. Given the above considerations, obtaining TiO_2 in the form of NPs combining both a controlled particle size and a single polymorph is not trivial as illustrated in **Figure 34**.

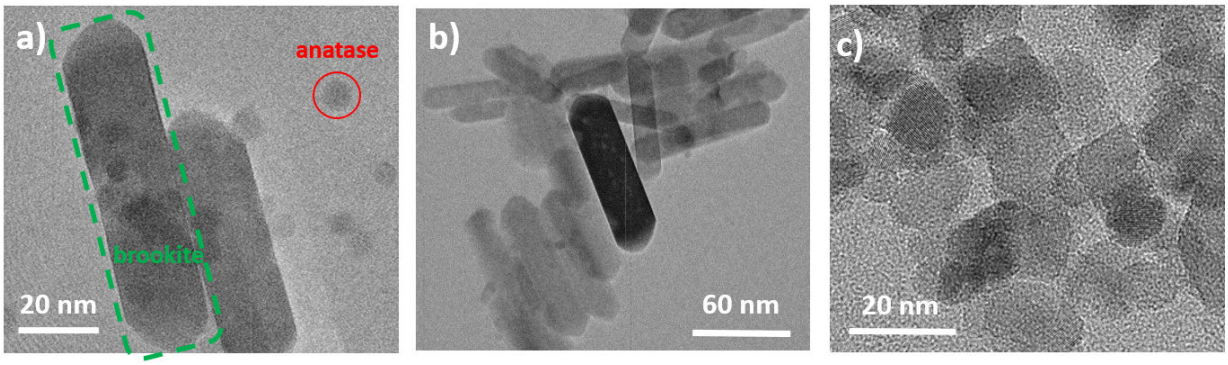

***Figure 34**. TiO_2 brookite synthesis. a) mix of TiO_2 brookite and TiO_2 anatase. b) TiO_2 brookite nanorods c) TiO_2 anatase.*

TiO_2 brookite was synthesised at CRISMAT laboratory using a hydrothermal approach[83]. In a Teflon cup, placed within a stainless-steel autoclave (Berghof, DAB-3), 0.8 mL of Titanium (IV) bis (ammonium lactato) dihydroxide (TALH, Sigma-Aldrich) was combined with 7M Urea (Sigma-Aldrich) to achieve a final volume of 8mL. The Teflon cup was sealed within the autoclave and subjected to a temperature of 200°C for 24h using an electric furnace. After the reaction, the Teflon cup was cooled at room temperature, and the resulting product was washed with ethanol and centrifuged to isolate the purified residue. This final product was subsequently dried at 60°C in an oven. Under these conditions, TiO_2 brookite NPs were obtained in the form of nanorods of approximately 70 nm in length and around 30 nm in width (**Figure 34**.b). It is important to note that, although the majority of the product obtained was TiO_2 brookite, there were still some residual anatase particles remaining, with sizes around 5 nm.

3.3. PXRD Characterization of TiO_2 brookite

For compounds that do not exhibit nanometric size, it is often possible to obtain single crystals large enough to allow for structural determination using SCXRD. However, when working with NPs, SCXRD is not possible due to size limitations, and thus PXRD becomes the primary method of analysis.

In this context, and thanks to one of the secondments I completed during my PhD at the Elettra Synchrotron, specifically on the *MCX beamline*, a XRDP experiment was performed on this compound, where the structural model was determined after Rietveld refinement. Additionally, although working with NPs typically results in decreased resolution due to peak broadening, this effect is advantageous for determining the shape

and size of these nano compounds by applying the Scherrer equation (Chapter 1, section 1.2.3).

At the *MCX beamline*, calibration measurements were performed using a silicon crystal to precisely calibrate the instrument´s wavelengths. Since the instrument operates in a particle accelerator, the selected wavelengths may not be as precising known as those from a laboratory diffractometer. The sample powder was carefully loaded into a 0.3 mm diameter capillary tube to perform measurements in transmission geometry. The entire process of a single experiment, from preparation to data acquisition, took approximately 4 hours (without counting for alignment). For this experiment, the 2θ range was set from 10° to 90°, with a step size of 0.005° and an exposure time of 1 second per step.

For brookite, an energy of 12 keV (λ=1Å) was used and the Rietveld refinement was done using FullProf software. The structural parameters obtained in the final model are presented in **Table 11**. A total of 380 reflections were observed in the diffraction pattern, and 56 parameters were refined during the analysis. The fitted powder patterns (**Figure 35**) and reliability factors for the refinement (R_{Bragg} = 3.87 and R_{wp} = 13.6) indicate a good match between the experimental data and the theoretical model.

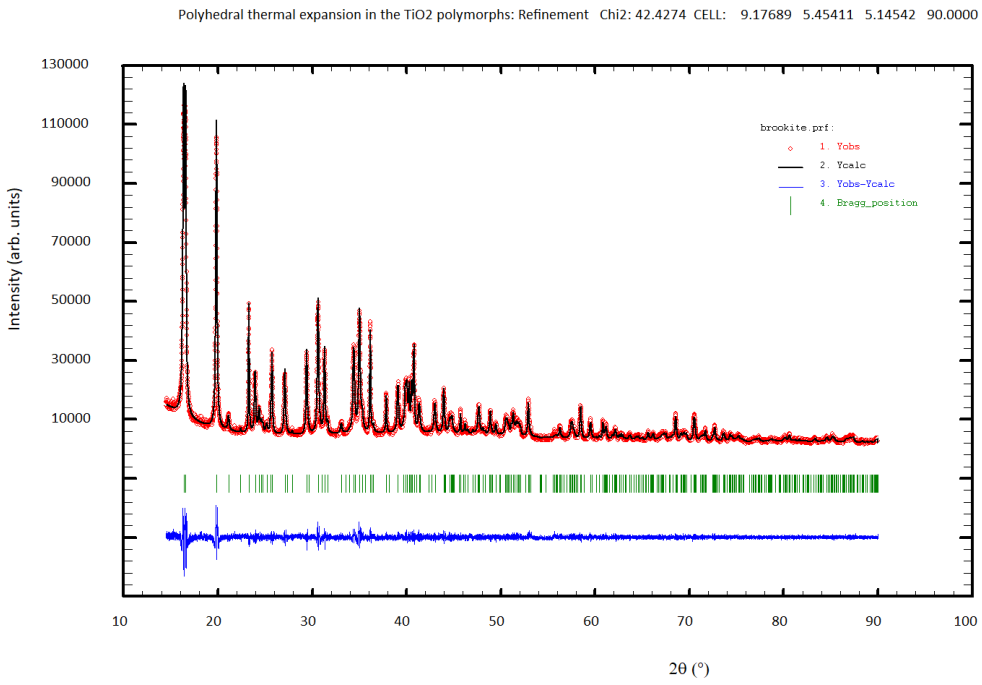

***Figure 35**. Plot of the Rietveld refinement of brookite against PXRD data. The experimental data is represented with red points, the calculated pattern with a black line and the difference plot with a blue line. The green marks correspond to peaks at the Bragg position.*

SG: Pbca (61) with a= 9.17689(8) Å, b= 5.45411(4) Å and c=5.14542(3) Å					
number of reflections=66; number of refined parameters=56; R_{Bragg}=3.87; R_{wp}=13.6					
Atom	**x**	**y**	**z**	**Occ**	***U*(Å²)**
Ti_1	0.12861(7)	0.09955(12)	0.86377(11)	1	0.009
O_1	0.01407(28)	0.14718(38)	0.18485(36)	1	0.003
O_2	0.22281(22)	0.11147(48)	0.54003(32)	1	0.008

ADP anisotropic parameters						
Atom	β_{11}	β_{22}	β_{33}	β_{12}	β_{13}	β_{23}
Ti_1	0.00304(8)	0.01179(24)	0.01139(27)	-0.00147(16)	-0.00064(16)	0.00132(28)
O_1	0.00541(35)	0.00209(83)	0.00707(103)	-0.00165(40)	-0.00002(44)	0.00113(79)
O_2	0.00116(30)	0.01213(95)	0.01381(88)	-0.00115(64)	0.00029(38)	-0.00045(95)

Table 11. *TiO_2 brookite structural parameters obtained from PXRD data.*

When working with NPs, a broadening effect on the diffraction peaks is observed. This can be used to obtain microstructural information about the sample like the size and shape of the diffracting volume. Therefore, using the Scherrer equation, the average diffracting volume was estimated, with its dimensions and shape shown in **Figure 36**. the rod-like structure, previously observed in the TEM images (**Figure 34**), can also be seen. The longer axis measures approximately 48.0 nm, while the shorter axis in one direction is around 20.1 nm, and the width along the other axis is approximately 15.6 nm.

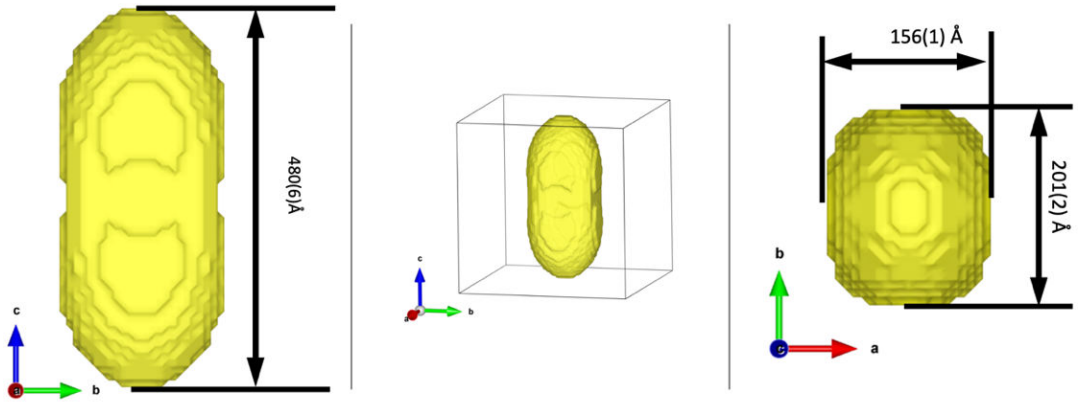

Figure 36. *TiO_2 brookite volume representation estimated by the application of Scherrer Equation.*

It is important to note that, in comparison with TEM images, which provide a direct and detailed view of individual NPs, PXRD offers an average diffracted volume that represents a statistical overview of the sample's shape. As a result, the dimensions obtained from PXRD may not exactly match those observed in TEM images.

Therefore, concluding this section, we can confirm that by performing a PXRD experiment using synchrotron radiation, where sample preparation and data collection took at least 4 hours, it was possible to achieve a reliable structural model with strong statistical support in the Rietveld Refinement, indicating a good match between the experimentally determined structure and theoretical calculations. Additionally, the shape and size of these NPs were successfully estimated using the Scherrer equation.

3.4. 3D ED data acquisition on 'large NPs': TiO_2 brookite

Typically, for larger crystals, having them closely spaced on a TEM grid does not present a significant problem because it is possible to use a smaller beam size than the crystal itself, allowing for an analysis that focuses on a specific region without interference from neighboring crystals. However, when collecting data on NPs, the beam size often exceeds the smallest dimension of the NP. This means that if we want to analyze a single isolated NP, we must ensure that there are no other particles nearby that could influence the analysis. Unfortunately, finding such dispersion is challenging because NPs have a strong tendency to agglomerate.

The primary reason for this behavior is their high surface-to-volume ratio, which leads to increased surface energy. When these particles agglomerate, they reduce their surface energy, making them more stable. This effect becomes even more pronounced as the size of the NPs decreases. Therefore, ensuring proper dispersion to collect data from a single isolated NP is the first challenge that must be addressed in the analysis.

The standard procedure for preparing a TEM grid with relatively large crystals, as compared to NPs, is as follows: A small amount of solvent is first added to the mortar, followed by the powdered sample, which is then ground. Next, only one drop of this solution is subsequently placed onto the TEM grid intended for analysis. However, due to the tendency of NPs to agglomerate, this protocol is no longer suitable, necessitating

the development of new dispersion methods. The initial approach to prevent agglomeration involved further diluting the powdered sample with a larger volume of solvent. While this provided some improvement, the NPs still remained agglomerated. The next idea was to identify a solvent that could more effectively enhance dispersion. For this purpose, different solvents were tested in the preparation of the TEM grid: ethanol, hexane, and Dimethyl Carbonate (DMC). ethanol, a polar protic solvent, has a high dipole moment due to the electronegativity difference between atoms and can form hydrogen bonds with water molecules, making it effective for dispersing polar and hydrophilic NPs. DMC, on the other hand, is a polar aprotic solvent, meaning it does not form hydrogen bonds, which can sometimes be more suitable for dispersing certain polar nanoparticles. Lastly, Hexane is a non-polar solvent that is much more effective for dispersing hydrophobic NPs.

The dispersion quality was observed under the TEM as it was not possible to identify the nanorods using an optical microscope due to their small size. The results showed that ethanol was the most effective solvent, providing the best dispersion of the NPs on the TEM grid, while hexane and DMC were less effective in achieving uniform dispersion. Consequently, ethanol was chosen as the solvent for all subsequent TEM grid preparation.

Finding the best solvent to disperse the NPs does not necessarily mean that they are sufficiently dispersed for single-crystal analysis in the TEM. Therefore, to further enhance the dispersion effect, an ultrasonic bath was used. Different durations were tested, and it was found that less than 20 minutes was not effective. Thus, the dispersion process required a minimum duration of 20 minutes in the ultrasonic bath.

Once we have the dispersion under control and the grid prepared, the next step to consider is using the ion cleaner for a short period, around 1 minute, to prevent contamination on the TEM grid caused by the degradation of the carbon film due to the electron beam.

In an initial observation of the sample under the TEM, we found that this specimen was quite stable, meaning it was suitable for data collection at room temperature. This stability was maintained for an extended period, even when we used a very small beam (around 50 nm) that concentrated more electrons on the sample. Thus, the stability of this material was a positive indicator for its selection as a test sample, as it allowed us to explore different protocols for data acquisition (such as cRED or PEDT) and to experiment with different beam sizes and exposure times.

Thanks to the secondments offered through this Marie Curie fellowship, I had the opportunity to work with different microscopes, each with unique characteristics, allowing me to test TiO_2 brookite on them. Additionally, through a collaboration with ELDICO company, we collected data using the ED-1 diffractometer. This new instrument gathers data on crystal experiments in way similar to conventional SCXRD diffractometers that we can find in a scientific laboratory. However, by using an electron source instead of X-rays, it can acquire data from much smaller crystals.

The setup varied depending on the microscope or diffractometer used. In **Table 12**, the operating voltage, protocols used for data acquisition and corresponding beam size are described for any of them.

TEM	Institution	HT (kV)	Data acquisition	Beam Size (nm)
Zeiss Libra 120	IIT (Italy)	120	cRED	600
Tecnai G2 X-TWIN F20	UA (Belgium)	200	cRED	300
JeolF200	CRISMAT (France)	200	PEDT	70
ED-1 Diffractometer	ELDICO	160	cRED	750

***Table 12**. Setup description for all the experiments carried out on TiO_2 brookite. The voltage values range from 120 to 200 kV. In most the cases, cRED was used, except for the protocol used at CRISMAT. The beam sizes varied from 700 nm to approximately 70nm.*

3.4.1. Zeiss Libra 120 @ IIT Microscope

Zeiss Libra 120, working at 120kV (LaB6 source), equipped with an ASI TimePix detector was used. Using a condenser aperture of 20 µm, it is possible to form a parallel nanobeam of approximately 600 nm in diameter and use it to perform continuous rotation 3D ED experiments with a tracking system.

The TEM grid was prepared using the method previously described method, which involved ethanol as the solvent and an ultrasonic bath for at least 20 minutes. A variation in this instance was the omission of an ion cleaner, as the cRED data acquisition mode was employed. Given the 120 kV voltage and the large beam, the sample area received a minimal dose, avoiding damage to the carbon grid. Additionally, the large beam size, which significantly exceeded the nanoparticle dimensions, resulted in a less concentrated electron beam on the crystal of interest, further minimizing radiation damage. The entire data acquisition process took approximately 2 minutes once the TEM grid was prepared

The smallest beam size suitable for data acquisition using the cRED protocol on this microscope was 600 nm (see **Figure 37**, pink circle). However, to obtain a broader view of the NP distribution, the TEM image mode was selected, which covered a larger area than the beam size (**Figure 37**). Despite this adjustment, it was not possible to find a single isolated crystal that could remain in the beam's focus without interference from other crystals due to the agglomeration of the NPs. Consequently, the only solution to maintain focus on a single nanoparticle within the 600 nm beam was to use a tracking system. This system enabled continuous tracking of the isolated NP, ensuring that no other crystals contributed to the analysis.

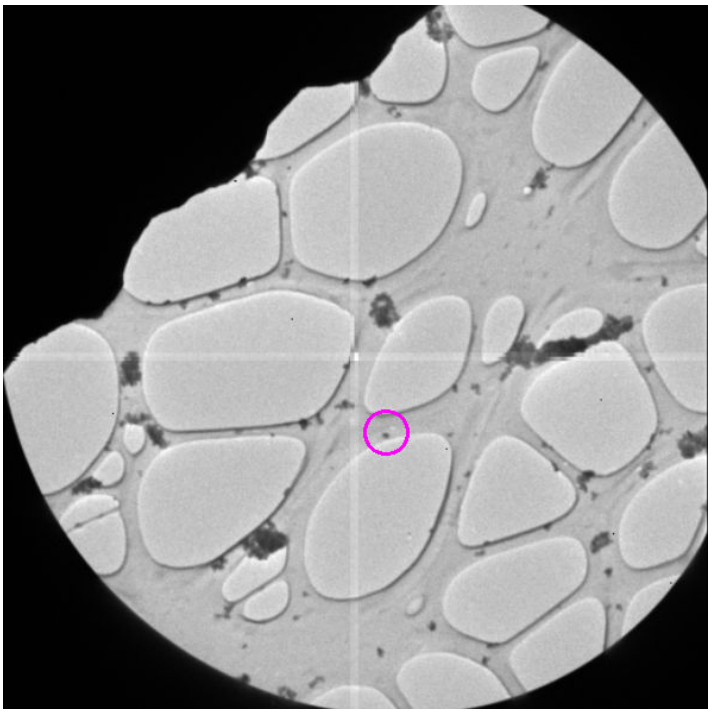

Figure 37*. TEM image obtained using a Zeiss Libra Microscope. The pink circle indicates the area covered by the electron beam, with a diameter of 600 nm.*

Zeiss Libra 120KV microscope is equipped with a crystal tracking software designed for high-precision and high-throughput 3D electron diffraction (ED) data acquisition. This algorithm operates by precisely controlling the illuminating system of the microscope to ensure accurate and consistent data collection. For that purpose, the crystal's trajectory is first recorded in low-dose mode to minimize radiation damage and preserve the crystal's integrity.

During the actual data acquisition phase, which occurs in diffraction mode, the beam is dynamically shifted to follow the pre-recorded coordinates of the crystal's trajectory. This ensures that the crystal remains consistently within the illuminated area, allowing for continuous and uninterrupted data collection throughout the entire acquisition process. This method is crucial for maintaining the accuracy and reliability of the 3D ED data.

After the data acquisition is completed, the software generates input files compatible with various data processing software. These files contain essential metadata, including information about the crystal's trajectory, beam settings, and acquisition parameters, facilitating subsequent data analysis and interpretation.

Regarding the results, at least 15 datasets were collected from different crystals in two days. After processing the data using PETS2 software, the results were evaluated. In half of the cases, the tracking system lost the crystal during the data acquisition. This issue arose not only because of the software´s limitations but also due to the mechanical stability of the goniometer. Occasionally, for reasons unrelated to the microscope, the crystal’s movement was not reproducible. We also encountered datasets where the acquisition of the data was from multiple crystals instead of a single one. Consequently, only a couple of datasets provided reliable results, offering good statistics to move on to the next step.

The workflow to follow in PETS2 software has been described in Chapter 2, section 2.4, and just the best result will be explained in detail.

After performing the peak search, the next step was to index the reflections in a given crystal system, eventually using a lattice and cell parameters. The indexing value will provide an estimate of how many reflections have been indexed relative to the total number of reflections. Therefore, the higher this value, better the experimental data will fit the selected lattice. Initially, the reflections were indexed using an orthorhombic symmetry with a = 9.1795(3) Å, b = 5.4933(1) Å and c = 5.0748(1) Å, and P-lattice (**Figure 38**), showing that 507 out of 509 reflections have been successfully indexed, resulting in an indexing rate of 99.61%, indicating a high probability of having identified the correct unit cell.

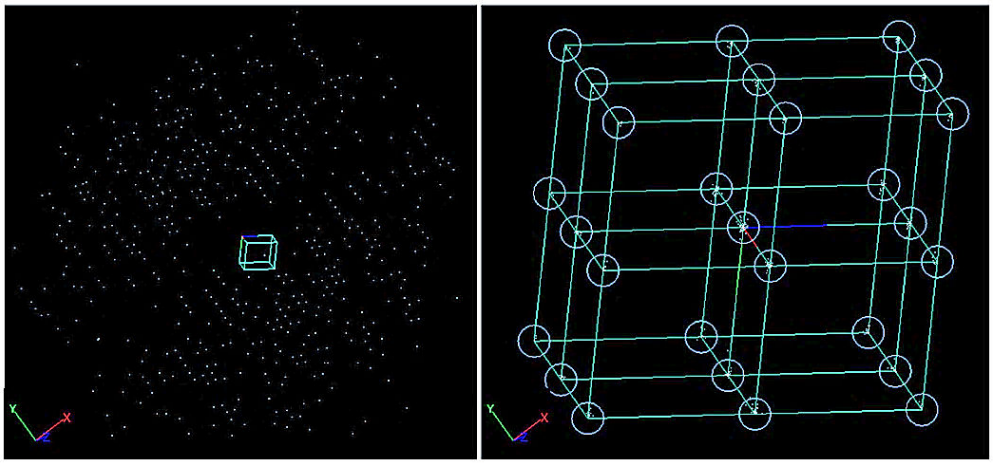

***Figure 38**. Indexation of the reflections under an orthorhombic symmetry and P-lattice. This option is available in PETS2 in 'Find Unit Cell and orientation matrix' section. (left)Representation of the reciprocal space shown the reflections in blue and the unit cell in green. (right Folding the reflections in a 2x2x2 unit cell to check for possible lattice centering. In this example, reflection clusters consistent with a P-lattice.*

The reciprocal space sections allow to visualize the 3D reciprocal space reconstruction by slicing it in different planes. This visualization gives you access to the extinctions, also known as systematic absences. These absences occur due to the symmetry of the crystal structure. By analyzing these sections, the presence of specific symmetry elements such as screw axes and glide planes can be determined. Thus, recognizing and understanding these sections, is an important step for space group determination and also can ensure that the crystallographic data is correctly interpreted, leading to more precise and reliable structural information.

From **Figure 39**. a) we can conclude that k = 2n. In particular, this absence could be indicative of the glide plane b perpendicular to a (because the symmetry is orthorhombic). From **Figure 39**. b), we can see that we have a condition on the 0kl plane, where l = 2n, meaning that we have a c glide plane perpendicular to b. From the last one (**Figure 39**. b), we can see a condition on the hk0 plane where h = 2n. Then, there is a glide plane perpendicular to c.

Considering this information, crystallography tables can be consulted to identify which space group exhibits the specified absences (k in the 0kl section, l in the k0l section, and h in the hk0 section). The only viable option that meets these criteria is Pbca, thereby confirming the P-lattice. This approach should be followed when attempting to solve ab-initio structures.

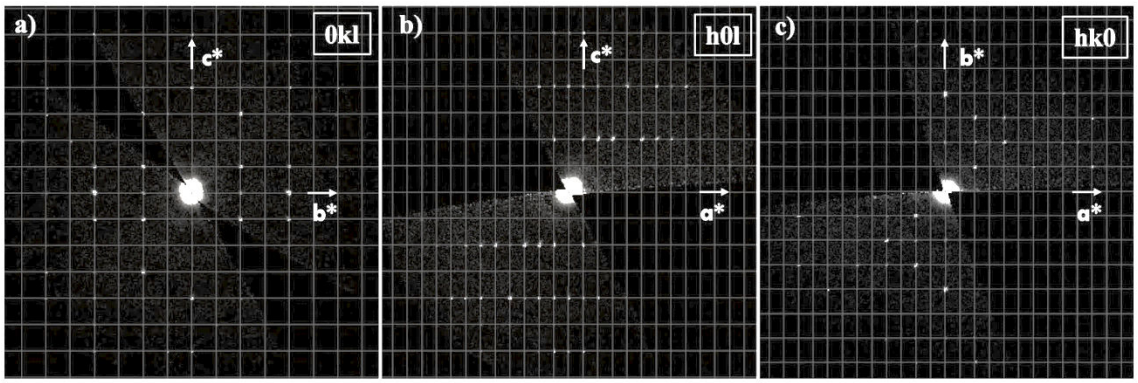

***Figure 39**. The 0kl, h0l, and hk0 sections show all reflections consistent with a P-lattice.*

It is also important to understand if the data obtained has enough quality for subsequent steps in Jana2020. Therefore, PETS2 can generate statistics that help users interpret the experimental data and optimize parameters.

On one hand, the Rint(obs) values provides information for determining the Laue class. The lower this value, the better the experimental data fits the model. Note that lower symmetry will always yield lower Rint(obs) values due to fewer symmetry operations. However, if you have already selected a symmetry, you need to remain consistent with that decision and check if it makes sense when reviewing the statistics for the Rint(obs) values. If these doesn't match, meaning having a high Rint(obs) as you can see in **Table 13** (blue box), where there is a clear jump in values, you should try to find another symmetry that fits the experimental data better.

As the selected symmetry was orthorhombic, the associated Laue class is mmm. The statistics for this are shown in **Table 13** (green box) with relatively low value.

Laue Class	-1	2/m	112/m	2/m11	**mmm**	**4/m**	4/mmm	-3	-31m	-3m1	6/m	6/mmm	m-3	m-3m
Rint(obs)	11.75	13.82	15.22	13.50	**17.00**	**49.98**	60.44	54.30	73.95	73.44	63.03	78.00	63.06	81.63

***Table 13**. Statistics from the Rint values based on the Laue Class obtained in PETS2.*

On the other hand, it is not just the Rint(obs) value that is relevant, but also the statistics related to the resolution of the experimental data. It is important to achieve the highest possible completeness, as this indicates that the data will represent the model with higher quality. Additionally, the intensity values are crucial, as they help determine where to cut off the resolution avoiding deteriorating the statistics. With I/σ lower than 3 at higher

scattering angles, the data becomes less reliable, and therefore, the resolution should be cut off at that point. Setting the resolution can also be guided in the first step by looking at the peak search. In other words, if there are no reflections beyond a certain resolution, the dstarmax is reduced. It is important to emphasize that this and all subsequent analysis will be carried out at a resolution of 1.2 $Å^{-1}$ to ensure consistency for future data comparisons.

At this point, the data should be thoroughly processed and optimized to proceed to structural resolution using the Jana2020 software. The important information we have estimated from the analysis in PETS2 includes the cell parameters, symmetry, and a suitable space group after reciprocal space section examination. This information can be inserted to help the algorithm used (charge flipping) to find the correct structure solution. Additionally, it has been demonstrated that this algorithm is capable of resolving structures with medium-quality data, which is typically uncommon when using Patterson techniques or direct methods. This capability makes it versatile tool in crystallography. When the charge flipping algorithm converges and provides a model, it is essential to closely examine the electrostatic potential density map to construct the final model accurately. This careful inspection ensures the correct identification of atomic positions before refining the model to fit the experimental data.

On the first attempt, this algorithm provides the expected solution, which is shown in **Figure 40**, then a refinement using kinematical and dynamical approaches could be done.

Regarding the refinement, it was crucial to examine the number of observed reflections to assess the quality and reliability of the results. For Robs to be considered a representative value, the number of observed reflections must be at least 10 times the number of refined parameters. In this particular example, if the number of refined parameters is 13, then the number of observed reflections must be at least 130 and since there are 256 observed reflections, the obtained Robs is considered reliable. The lower Robs value is, the better the solution found. The statistics for kinematical refinement are shown in **Table 14**, pink background.

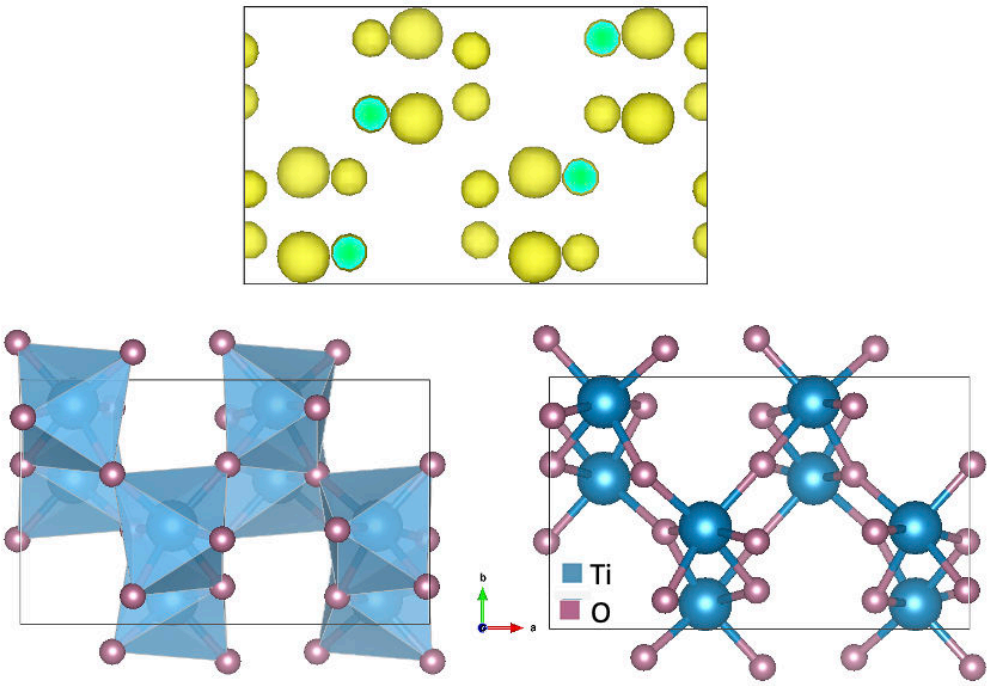

***Figure 40**. The upper image corresponds to the electrostatic potential map where the yellow isosurfaces represent the position of an atom. The model for structure solution is shown in the bottom part.*

As mentioned in previous chapters, working with electrons has a disadvantage: the multiple scattering events. Therefore, if we only analyze the data using kinematic approach, the Robs values are likely to be high which poses questions about the actual quality of the structure determination.

However, if we also consider this multiple scattering effect during the refinement, which is performed in dynamical refinement, as shown in **Table 14**, blue background, the Robs value decreases from 14.75 to 6.48. Observing such a drop in Robs values when using dynamical refinement is usually a sign that the structure has been accurately determined. Additionally, the number of observed reflections (718) is bigger than 10 times the number of observed parameters (680), confirming the reliability of the results. The details for the final model, including atomic positions (x, y, z), occupancy (occ) and Uiso (U) value are shown in **Table 15**.

	TiO_2 brookite (Zeiss Libra)
Tilt Range (°)	[-55.5, +61]
Exposure time (s)	0.5
Tilt step per frame (s)	1
Integ. Angle (°)	0.5
Cumul. Cover. *(sinθ/λ=0.8Å^{-1})*	99.6
Averaged Refl. All/Obs.	361 / 256
Rint (from PETS)	17.0
Number of refined parameters	13
Robs	14.75
Rall	17.92
Refl. All/Obs.	1425 / 718
Number of parameters	68
Robs	6.48
Rall	9.94

Table 14. *Results for TiO_2 brookite using a Zeiss Libra Microscope. Statistics for the final model after kinematical and dynamical refinement with a background in pink and blue respectively.*

Space Group Pbca (61), a =9.1795(29) Å, b =5.4933(13) Å *c* = 5.0748(10) Å					
R(obs)=6.48, R(all)=9.94 , wR(all)=13.55, GoF(obs)=6.48					
measured / observed [I>3σ(I)] reflections= 1425 / 718, 62 refined parameters					
g_{max} (Å^{-1})=1.6, Sg_{max} (Å^{-1})=0.01, RSg_{max}=0.66, steps=100					
Atom	**x**	**y**	**z**	***U* (Å^2)**	**Occ.**
Ti_1	0.37116(18)	0.4020(2)	0.8633(2)	0.0075(3)	1
O_1	0.5099(5)	0.6488(4)	0.8156(5)	0.0088(6)	1
O_2	0.2686(4)	0.3878(5)	0.5358(5)	0.0094(6)	1

Table 15. *TiO_2 brookite structural parameters obtained from single crystal 3D ED data.*

In this first example, the steps followed have been described in great detail. For subsequent analyses, the workflow was similar, with some exceptions that will be mentioned.

3.4.2. FEI-Tecnai G2 X-Twin F20 @ UA

FEI TECNAI G2 F20 X-TWIN TEM, working at 200 kV (FEG source) and equipped with an ASI Timepix hybrid-pixel detector was used in the context of the secondment at UA. Using a condenser aperture of 20 μm, it is possible to form a parallel nanobeam of approximately 250-300 nm in diameter and use it to perform continuous rotation 3D ED experiments. In this case, tracking system was not required due to the reliable stability of the goniometer.

The biggest challenge in this data acquisition mode was finding an isolated NP that would remain under the beam, which was around 275 nm in size, without other particles going into the analysis during data collection. The TEM grid preparation was done using an ultrasonic bath for 20 minutes. Additionally, centrifuge for 1 minute at 4000 rpm was used. This additional step helped to collect only the upper part and ensure that the sample was more dispersed.

The most important step was adjusting the Z-height of the microscope to ensure the sample was in the optimal focal plane with respect to the lenses while it rotated during collection of diffraction patterns. The data acquisition time was similar to that used in the previous case (IIT). Although reproducing the crystal's movement while tilting was not necessary since a tracking system was not employed, a significant portion of the time was spent locating an isolated crystal and fine-tuning the microscope's Z-height.

The first difference compared to the previous case is that the tilt range was smaller. This reduction is due to the use of cRED without a tracking system, making it more challenging to keep the NP aligned under the beam while tilting. Consequently, the tilt range become shorter. This issue would be less problematic with larger crystals, where the increased beam size provides better stability to the goniometer, allowing for a larger tilt range during data collection.

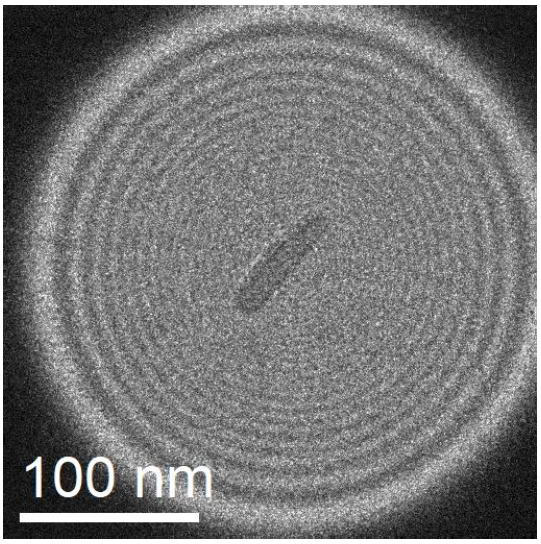

***Figure 41**. TEM image of an isolated nanoparticle (NP) captured using a Fei Tecnai G2 X-Twin Microscope. The beam size employed ranged between 250 and 300 nm, which was the smallest beam size suitable for cRED on such small crystals.*

Although the dispersion of the NPs was quite effective, only a few isolated crystals were identified. Five datasets were collected; however, in several cases, the crystal moved out of the beam's focus during data collection, or other particles interfered with the analysis. In the end, only one dataset yielded from an isolated nanorod (see **Figure 41**) reliable results for structural resolution and refinement.

Initially, the cell parameters were indexed using an orthorhombic symmetry with a = 9.1760 Å, b = 5.4926 Å and c = 5.1426 Å, and P-lattice (**Figure 42**), showing that 456 out of 457 reflections have been successfully indexed, resulting in an indexing rate of 99.78%. Examination of the reciprocal sections (**Figure 43**) confirms P lattice showing the same features as those observed in the TiO_2 brookite sample collected at IIT.

In this case, the reciprocal space sections showed the same features as those observed in the TiO_2 brookite sample collected at IIT. Therefore, for this data acquisition using cRED, the space group Pbca was also confirmed.

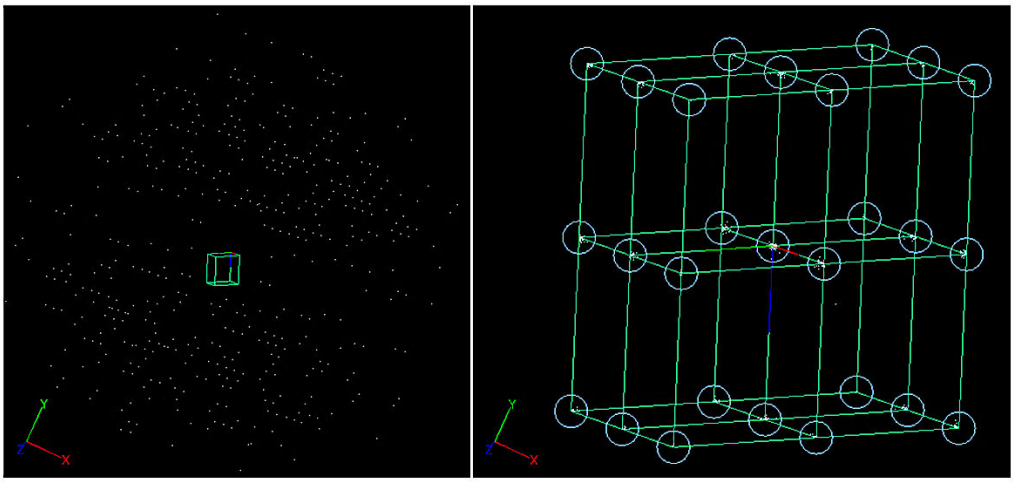

***Figure 42**. Indexation of the reflections under an orthorhombic symmetry and P-lattice. This option is available in PETS2 in 'Find Unit Cell and orientation matrix' section. (left) Representation of the reciprocal space shown the reflections in blue and the unit cell. (right) Folding the reflections in a 2x2x2 unit cell to check for possible lattice centering. In this example, reflection clusters consistent with a P-lattice.*

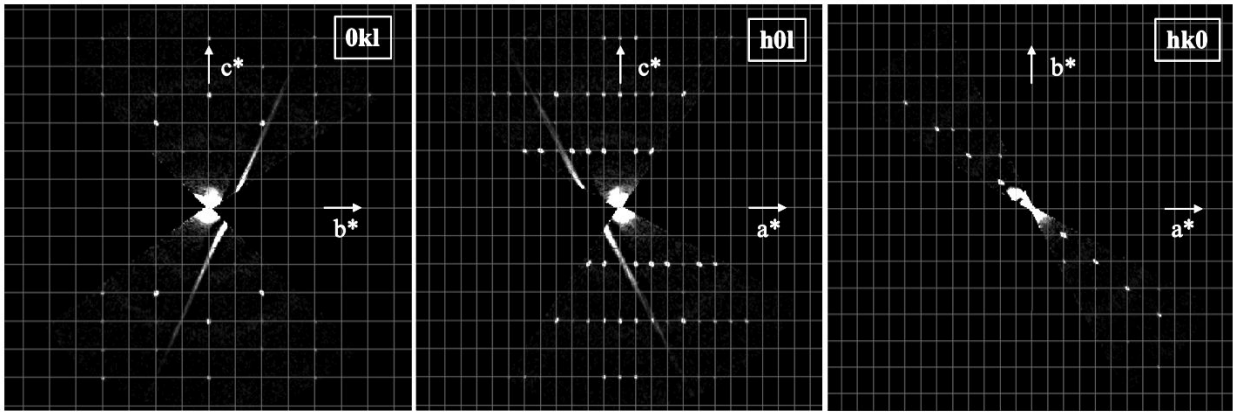

***Figure 43**. The 0kl, h0l, and hk0 sections show all reflections consistent with a P-lattice.*

The structure solution was straightforward, as in the previous case. The refinement of the structural model presented no significant challenges, and the statistical results were favorable for both refinements. Notably, there was a substantial decrease in the Robs value when accounting for the multiple scattering effect, dropping from 10.70 to 5.56, as shown in **Table 16**. The details for the final model, including atomic positions (x, y, z), occupancy (occ) and Uiso (U) value are shown in **Table 17**.

	TiO_2 brookite (UA)
Tilt Range (°)	[-45, +35]
Exposure time (s)	0.5
Tilt step per frame (s)	0.2
Integ. Angle (°)	0.1
Cumul. Cover. *(sinθ/λ=0.8Å^{-1})*	85.7
Averaged Refl. All/Obs.	307 / 180
Rint (from PETS2)	10.70
Number of refined parameters	13
Robs	14.90
Rall	20.03
Refl. All/Obs.	766 / 551
Number of parameters	54
Robs	5.56
Rall	7.43

***Table 16**. Results for TiO_2 brookite using a FEI-Tecnai G2 X-Twin F20 microscope. Statistics for kinematical and dynamical refinement with a background in pink and blue respectively.*

Space Group Pbca (61), a =9.1760 Å, b =5.4926 Å *c* = 5.1426 Å					
R(obs)=5.56, R(all)=7.43 , wR(all)=10.82, GoF(obs)=1.93					
measured / observed [I>3σ(I)] reflections= 766 / 551, 54 refined parameters					
g_{max} (Å^{-1})=1.6, Sg_{max} (Å^{-1})=0.01, RSg_{max}=0.48, steps=100					
Atom	**x**	**y**	**z**	***U* (Å^2)**	**Occ.**
Ti_1	0.62917(14)	0.4018(2)	0.13700(18)	0.0065(3)	1
O_1	0.4902(4)	0.6487(5)	0.1845(4)	0.0072(5)	1
O_2	0.7314(4)	0.3878(5)	0.4639(4)	0.0089(5)	1

***Table 17**. Structural details for the final model of TiO_2 brookite using a FEI-Tecnai G2 X-Twin F20 microscope.*

In conclusion, due to the stability of the goniometer used in this microscope, it was possible to use a smaller beam than in the case recorded by IIT, allowing for cRED to be performed on these small crystals without a tracking system. Although NP agglomeration

posed one of the greatest challenges for the analysis, it was possible to disperse the particles effectively and identify isolated NPs that remained within the beam's dimensions throughout the entire analysis. Moreover, the results obtained after dynamical refinement were highly favorable, confirming the accurate structure determination for this compound.

3.4.3. JEOL F200 @ CRISMAT-CNRS

JEOL F200 TEM, working at 200 kV (FEG source) and equipped with an ASI Cheetah Medipix3 hybrid-pixel detector was used for most of the results obtained in the present report. In this case, precession-assisted 3D ED was used. The 4-stage probe-forming optical system controls independently the intensity and the convergence angle of the electron beam. Thanks to this and using a condenser aperture of 10 µm, it is possible to form a quasi-parallel nanobeam about 10 nm or even less. Using a 600 nm beam with a tracking system proved effective for obtaining high-quality data and accurate structure solutions. Additionally, a microscope with a more stable goniometer, where the beam size was reduced to 300 nm and no tracking system was required, further confirmed the success of this approach. Applying precession-assisted ED with a smaller beam (here around 70 nm), although the acquisition time was significantly longer (more than 15 minutes per dataset) compared to cRED, offers the advantage of not losing a dataset halfway or stop the experiment because other particles interfered. With precession-assisted ED, you have the option to check at each tilt step if the crystal being analyzed remains the same, ensuring the dataset continues to originate from a single crystal. PEDT data acquisition method was also tested with different parameters such as exposure time and tilt step to see for example, if increasing the tilt step would be detrimental to the quality of the structure determination.

Here, the dispersion was not as dramatic as it was in the cRED case because using a much smaller beam size made it much easier to find an isolated crystal compared to a beam size of 300 or 600 nm. Therefore, the protocol followed for grid preparation was the same as described at the beginning of the chapter. Diluted the sample using ethanol, 20 minutes in the ultrasonic bath and 1 minute in the ion cleaner.

Various experiments were performed using this microscope, as shown in **Table 18**. Different exposures times (0.5, 1 and 1.5 seconds per frame) were tested, along with

different tilt steps per frame, choosing 1, 1.5 or 2 frames per tilt. However, both beam size and precession angle remained the same (70 nm and 1.2° respectively).

	CNRS-01	CNRS-02	CNRS-03	CNRS-04
Exposure Time (s/frame)	0.5	0.5	1.5	1
Tilt per frame	1	2	2	1.5

***Table 18**. Setup of different experiments carried out at CRISMAT Laboratory modifying the exposure time and the tilt step per frame.*

Approximately 20 datasets were collected in total for this experiment. Over 80% of the datasets were successful in providing solutions for structure determination and refinement. The remaining 20% were unsuccessful due to interference from other NPs or because, during rotation, the edge of the grid obscured the NP of interest, causing the data collection to be stopped midway through the experiment. In this section only the best datasets for every setup are represented.

The process will be the same as that used for the samples collected at both IIT and UA institutions. All datasets were initially indexed using orthorhombic symmetry, with slight variations in the cell parameters as shown in **Table 19**. It is important to note that we cannot strictly compare the results since the experiments were carried out on different crystals (synthesis batches made on different days), and although efforts were made to collect data from crystals of similar sizes, these slight variations could have impacted the data quality. Additionally, while the majority of the synthesis resulted in TiO_2 brookite, there was a small percentage of TiO_2 anatase present. If any of these smaller NPs (5 nm in size) interfered during data collection, it could have contributed to a lower indexing rate for the initial unit cell selected.

For all the different experiments, the indexing rate was consistently above 69%, and in the best case, it even exceeded 90%. These results strongly suggest that the chosen cell parameters were likely correct. However, it is important to note that achieving the highest indexing rate does not necessarily guarantee better statistical outcomes during refinement. Instead, it simply indicates a higher probability that the experimental data were accurately indexed with the correct symmetry and cell parameters. Examination of the reciprocal space sections confirms for all the cases the P lattice.

	Cell parameters (a, b, c)Å	Indexed/all	Indexed (%)
CNRS -01	9.4012(11), 5.5822(7), 5.2731(8)	1657 / 2375	69.77
CNRS-02	9.2103(21), 5.4691(11), 5.1735(9)	985 / 1091	90.28
CNRS-03	9.1949(30), 5.4719(20), 5.1207(19)	881 / 1178	74.79
CNRS-04	9.1720(20), 5.4377(14), 5.1342(12)	1184 / 1659	71.37

Table 19*. Cell parameters, number of indexed reflections for these cell parameters, and volume are shown for every experiment at CRISMAT Laboratory.*

The structure solution for all these experiments was straightforward. Furthermore, both kinematical and dynamical refinements were performed, yielding strong statistical outcomes, with low Robs values, indicating an excellent fit between the model and the experimental data (see **Table 20**).

From the data we can confirm that there is a substantial difference between kinematical and dynamical refinement methods. Specifically, dynamical refinement shows a significant reduction in Robs values by about of 10% compared to kinematical refinement.

All the different protocols tested yielded good statistical results, leading to accurate structural determination of TiO_2 brookite. However, some recommendations can be made when choosing a protocol. If the NPs are stable (meaning the beam does not cause significant damage to the crystals), a lower exposure time and smaller tilt step can be used. On the other hand, if the compound is beam-sensitive, a lower exposure time combined with a larger tilt step will be more favorable. In both cases, selecting the protocol that requires the least time for data acquisition is recommended, with the protocol having the larger tilt step being the most efficient.

The details for the final model, including atomic positions (x, y, z), occupancy (occ) and Uiso (*U*) value for CNRS-01, CNRS-02, CNRS-03 and CNRS-4 are shown in **Table 21**, **Table 22**, **Table 23**, and **Table 24** respectively.

	CNRS-01	CNRS-02	CNRS-03	CNRS-04
Tilt Range (°)	[-48, +50]	[-50, 54]	[-44, +38]	[-50, +60]
Exp. per frame (s)	0.5	0.5	1.5	1
Tilt step per frame (°)	1	2	2	1.5
Cumul. Cover. *(sinθ/λ=0.7 Å^{-1})*	87.1	97.2	71.2	95.2
Averaged Refl. all/obs.	328/312	355/259	253/235	341/ 325
Rint (from PETS2)	16.2	16.8	12.0	16.2
Number of refined parameters	13	13	13	13
Robs	17.03	18.52	17.32	19.53
Rall	17.80	22.07	18.02	19.97
Refl. all/obs.	3611/3110	1985/1891	1695/1507	2682/2184
Number of refined parameters	105	62	63	84
Robs	6.63	7.68	6.70	6.48
Rall	7.07	7.80	7.02	7.28

***Table 20**. Table showing 3D ED results obtained under different acquisition conditions for TiO_2 brookite. Pink and blue background are related to kinematical and dynamical refinements, respectively. Integration limit in PETS2 was set to 1.2 Å^{-1} in all cases.*

Space Group Pbca (61), a =9.4012(11) Å, b =5.5822(7) Å *c* = 5.2731(8) Å					
R(obs)=6.63, R(all)=7.07 , wR(all)=15.48, GoF(obs)=3.43					
measured / observed [I>3σ(I)] reflections= 3611 / 3110, 105 refined parameters					
g_{max} (Å^{-1})=1.6, Sg_{max} (Å^{-1})=0.01, RSg_{max}=0.66, steps=108					
Atom	**x**	**y**	**z**	***U*(Å^2)**	**Occ.**
Ti_1	0.62907(7)	0.59820(10)	0.36317(10)	0.00618(16)	1
O_1	0.48996(17)	0.3511(2)	0.3155(2)	0.0069(3)	1
O_2	0.36951(17)	0.3870(2)	0.5362(2)	0.0063(3)	1

***Table 21**. Structural details for the final model of CNRS-01 using a JeolF200 microscope.*

Space Group Pbca (61), a =9.2103(21) Å, b =5.4691(11) Å *c* = 5.1735(9) Å					
R(obs)=7.68, R(all)=7.80 , wR(all)=18.66, GoF(obs)=5.52					
measured / observed [I>3σ(I)] reflections= 1985 / 1891, 62 refined parameters					
g_{max} (Å^{-1})=1.6, Sg_{max} (Å^{-1})=0.01, RSg_{max}=0.66, steps=117					
Atom	**x**	**y**	**z**	***U*(Å^2)**	**Occ.**
Ti_1	0.37079(12)	0.6587(18)	0.36307(17)	0.0026(2)	1
O_1	0.5102(3)	0.6487(4)	0.3158(4)	0.0024(4)	1
O_2	0.2694(3)	0.3874(4)	0.0370(4)	0.0026(5)	1

***Table 22**. Structural details for the final model of CNRS-02 using a JeolF200 microscope.*

Space Group Pbca (61), a =9.1949(30) Å, b =5.4719(20) Å *c* = 5.1207(19) Å					
R(obs)=6.70, R(all)= 7.02, wR(all)=17.02, GoF(obs)=4.72					
measured / observed [I>3σ(I)] reflections= 1695 / 1507, 63 refined parameters					
g_{max} (Å^{-1})=1.6, Sg_{max} (Å^{-1})=0.01, RSg_{max}=0.66, steps=108					
Atom	**x**	**y**	**z**	***U* (Å^2)**	**Occ.**
Ti_1	0.3707(2)	0.59828(12)	0.13694(14)	0.0042(2)	1
O_1	0.5109(5)	0.3515(3)	0.1842(3)	0.0045(4)	1
O_2	0.2687(5)	0.6125(3)	0.4632(3)	0.0059(4)	1

***Table 23**. Structural details for the final model of CNRS-03 using a JeolF200 microscope.*

Space Group Pbca (61), a =9.1720(20) Å, b =5.4377(14) Å *c* = 5.1342(12) Å					
R(obs)=6.48, R(all)= 7.28, wR(all)=15.28, GoF(obs)=3.17					
measured / observed [I>3σ(I)] reflections= 2682 / 2184, 84 refined parameters					
g_{max} (Å^{-1})=1.6, Sg_{max} (Å^{-1})=0.01, RSg_{max}=0.66, steps=117					
Atom	**x**	**y**	**z**	***U* (Å^2)**	**Occ.**
Ti_1	0.37115(10)	0.59851(10)	0.36320(11)	0.00592(18)	1
O_1	0.5108(2)	0.3510(2)	0.3154(3)	0.0062(3)	1
O_2	0.2692(2)	0.6125(2)	0.0361(3)	0.0059(3)	1

***Table 24**. Structural details for the final model of CNRS-04 using a JeolF200 microscope*

3.4.4. ED-1 @ ELDICO Scientific AG

ELDICO ED_1 electron diffractometer (STEM mode), working at 160 kV (LaB6 source), equipped with a Dectris Quadro hybrid detector was used in collaboration with ELDICO Scientific AG company. In this case, the 3D ED data acquisitions were performed in STEM mode and using continuous rotation.

The beam size for this instrument was 750 nm due to ED-1 was designed to analyze much larger crystals (typically with lateral dimensions above 500nm) and not NPs. Thus, finding one unique brookite nanorod in the 750 nm wide electron beam was not an easy task, but it was achievable. The advantage of using this diffractometer for single crystal analysis was that the isolated nanorod remained in the beam throughout the tilt range and no tacking was necessary due to goniometer stability. TEM grid preparation was carried out in the same way as mentioned in previous case.

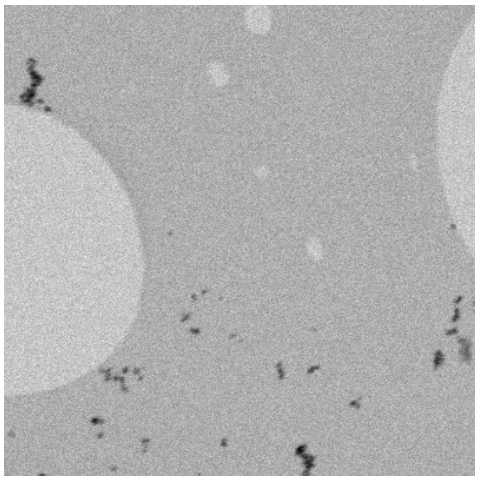

***Figure 44**. STEM image from a TEM grid region using ED1- diffractometer.*

After collecting 9 datasets, only a couple of them confirmed to be a single isolated crystal. One possible reason for this could be the use of a large set beam size, which limits the resolution in image mode to what is shown in **Figure 44**. This makes it difficult to determine whether two NPs are very close together or if they are a single particle. Additionally, other NPs could have interfered with the analysis during data collection, or the intensity of the observed reflections could be really weak.

Initially, the cell parameters were indexed using an orthorhombic symmetry with a = 9.1546(3) Å, b = 5.4354(2) Å and c = 5.1083(1) Å, and P-lattice, showing that 281 out

of 450 reflections have been successfully indexed, resulting in an indexing rate of 62.44%. Examination of the reciprocal space sections confirms a P lattice.

	TiO_2 brookite (ED-1)
Tilt Range (°)	[-60, +60]
Exposure time (s)	1
Tilt step per frame (s)	1
Integ. Angle (°)	1
Cumul. Cover. ***(sinθ/λ=0.8Å^{-1})***	95.7
Averaged Refl. All/Obs.	345 / 115
Rint (from PETS)	20.58
Number of refined parameters	13
Robs	21.4
Rall	30.84

***Table 25**. Results for TiO_2 brookite using the ED-1 Diffractometer from ELDICO company. Statistics for the final model after kinematical refinement represented with a pink background.*

The structural model was successfully obtained; however, the refinement process presented some challenges. During the kinematical refinement (**Table 25**, pink background), the statistical results were less than ideal, with the number of observed reflections smaller than 10 times the number of refined parameters. Additionally, dynamical refinement could not be achieved. This outcome can be attributed to the use of a large beam size, which increased the noise originating from the carbon film and resulted in weaker reflection intensities. Consequently, this led to a reduced number of observed reflections. It is likely that these experiments could be improved by increasing the exposure time per frame, which would enhance the intensity of the reflections and yield a greater number of observed reflections suitable for refinement.

However, a positive aspect of this approach is that, despite the challenges, it is possible to obtain a structural model from such tiny crystals using an instrument where data acquisition is completed in under 2 minutes and is fully automated. This demonstrates the potential for rapid and efficient structural determination even with small samples.

3.5. Accuracy of structure refinements

For the investigation of large NPs (TiO_2 brookite) with sizes of approximately 70 nm, different approaches for data acquisition were tested. cRED both with and without tracking system as well as precession-assisted ED were applied. These methods enabled the acquisition of high-quality data, providing detailed insights into the accurate structure allowing to access fine structural information, including isotropic atomic displacement parameters (ADPs) for these large NPs. Having access to this detailed structural information, we can now discuss how the structural final models obtained from all the different experiments carried out, differ from the bulk structure. Additionally, we will compare these findings with results from PXRD experiments performed using synchrotron radiation.

	IIT	**UA**	**CNRS01**	**CNRS02**	**CNRS03**	**CNRS04**	**ELDICO**	**Brookite PXRD**
av.dist (Å)	0.0185	0.0442	0.0108	0.0132	0.0323	0.0474	0.0304	0.0266
max.dist (Å)	0.0318	0.0917	0.162	0.0224	0.0388	0.0798	0.0495	0.0438
av.dist (Å)	0.0063	0.0064	0.0079	0.0079	0.0097	0.0097		
max.dist (Å)	0.0077	0.007	0.0127	0.0113	0.0137	0.0112		

***Table 26**. The darker pink and blue areas represent the average and maxima distance deviation of the atomic positions in comparison with reference bulk materials for both kinematical and dynamical refinement (when applied), respectively. IIT, and UA and ELDICO are results obtained from cRED data analysis. From CNRS-01 to CNRS-04 are obtained from PEDT data. Brookite PXRD is obtained from the Rietveld analysis of PXRD data.*

To assess the precision of the techniques employed and to determine any deviations in atomic positions between the reference bulk materials and those obtained through cRED, precession-assisted ED and PXRD experiments, the COMPSTRU utility of the Bilbao Crystallographic Server was used. The server provided values for the average and maximum distance deviations in atomic positions, which are presented in **Table 26** and visually represented in **Figure 45**.

A preliminary examination of **Table 26** shows that, regardless of the technique used, the maximum deviations are below 0.03 Å. This indicates that the structure of these NPs does not differ significantly from their bulk counterparts. This is not entirely surprising, as for nanoparticles of this size, the number of atoms and bonds on the surface is still relatively

minor compared to those in the core. Focusing on the 3D ED results, the maximum deviations for structures obtained using cRED are below 0.1 Å for kinematical refinements. When compared to structures obtained using PEDT, these deviations are under 0.17 Å. After performing dynamical refinement, the maximum deviation values decrease for both approaches, with cRED achieving values below 0.008 Å and PEDT showing deviations below 0.03 Å. This indicates that the accuracy of the structure determination is comparable to that obtained from larger crystals. Furthermore, while kinematical refinements yielded results similar than those from PXRD (**Figure 45**.a), the accuracy achieved through dynamical refinements surpass the one obtained by PXRD in all cases (see **Figure 45**.b). To conclude, although the ELDICO produced the least favorable results compared to the other experiments, implementing the suggested improvements for data acquisition will likely enhance the structural comparison of the model with the reference structure in the future.

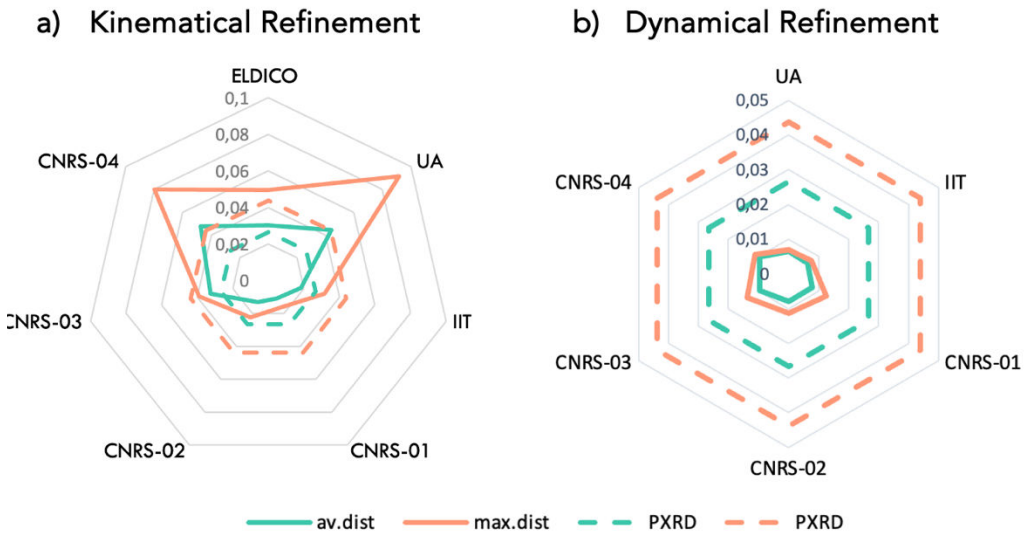

***Figure 45**. a) and b) radar plots showing the average (av. dist.) and maximal deviation (max. dist.) on atomic positions between the bulk reference and the structures obtained based on 3D ED data kinematical and dynamical refinements, respectively. In dashed lines is represented the deviations obtained for the PXRD kinematical refinement.*

3.6. Kappa refinement on TiO_2 brookite

Throughout this work, every reference to dynamical refinement has been based on the Independent Atomic Model (IAM), which simplifies the structure by assuming that all atoms are spherical and non-interacting. Although this model has demonstrated several

advantages over kinematical refinement, as explored in the previous sections, it imposes certain limitations on the accuracy of the structural representation due to its non-interacting approach. To overcome these limitations and enhance the precision of the model, the kappa refinement approach[84] was applied to the materials of interest. This application was carried out in collaboration with Ashwin Suresh, a PhD student from the nanED project, focusing on 'Charge density analysis from 3D ED data,' allowing for a more realistic description of atomic interactions.

In this new approach, only the spherical part of the multipole formalism proposed by Hansen and Coppens [85] is considered (equation 4.1, green box). The atoms are still treated as spherical; however, spherical deformations of the valence electrons are taken into account by incorporating two parameters per atom into the refinement process: P_{val} and κ. P_{val} represents the population of valence electrons transferred between the atoms allowing an estimation of the atomic charge and κ describes the contraction and expansion of the valence shell.

$$\rho_{atom}(r) = P_{core}\rho_{core}(r) + \rho_{val}K^3\rho_{val}(kr) + \sum_{l=0}^{l_{max}} k'^3 R_l(k'r) \sum_{m=-l}^{l} P_{lm}Y_{lm}(\theta,\phi) \quad (4.1)$$

TiO_2 brookite was a strong candidate for this type of refinement since the data had high completeness, and reflections were observed even at a resolution higher than 2 $Å^{-1}$. While the resolution of the different datasets collected at CRISMAT for this specific material was restricted to 1.4 $Å^{-1}$ to enable comparisons with other data acquisition protocols, reflections extended to a resolution of up to 2.2 $Å^{-1}$ leading to a completeness of 99%.

Next, the steps taken to perform this refinement will be explained in detail.

It was important to start from the best possible model using the standard dynamical refinement (IAM). For this, the dmax for integration was set to 2.2 $Å^{-1}$ and a thickness wedge model was used, selecting this geometry based on the shape of the NPs, which in this case were nanorods. Although normally the application of a thickness model with a specific geometry is not considered relevant[65], it can sometimes lead to a small decrement in the Robs value. The final model results are shown in **Table 27** where the dynamical refinement statistics, the atomic positions and the anisotropic values are represented.

Space Group Pbca (61), a =9.20054(11) Å, b =5.45713(14) Å *c* = 5.13481(12) Å					
R(obs)=5.96, R(all)= 6.90, wR(all)=7.44, GoF(obs)=3.10					
measured / observed [I>3σ(I)] reflections= 3981 / 2827, 79 refined parameters					
g_{max} (Å^{-1})=2.2, Sg_{max} (Å^{-1})=0.01, RSg_{max}=0.6, steps=140					
Atom	**x**	**y**	**z**	***U* (Å^2)**	**Occ.**
Ti_1	0.37102(10)	0.59815(7)	0.63695(7)	0.0059(2)	1
O_1	0.5109(2)	0.35156(15)	0.68435(17)	0.0060(5)	1
O_2	0.2690(2)	0.61222(15)	0.96324(17)	0.0062(5)	1

ADP anisotropic parameters (Å^2)						
Atom	*U*11	*U*22	*U*33	*U*12	*U*13	*U*23
Ti_1	0.0072(6)	0.00555(14)	0.00496(12)	0.0002(2)	0.0003(2)	-0.00001(11)
O_1	0.0061(14)	0.0061(3)	0.0058(3)	0.0038(4)	-0.0005(5)	0.0008(2)
O_2	0.0054(14)	0.0066(3)	0.0067(3)	-0.0015(5)	0.0008(5)	-0.0003(3)

***Table 27**. Best structural model from standard dynamical refinement (IAM) of TiO_2 brookite, used as the starting structure for kappa refinement.*

Once we obtained the best result using the IAM model, we proceeded to introduce the two extra parameters mentioned earlier (P_{val} and κ). To setup the kappa refinement in Jana2020 the following procedure was used. In the section 'Edit structure parameters – Edit basic parameters – Composition': Mott's formula was selected for obtaining electron atomic scattering factors from X-ray scattering factors (**Figure 46**, blue box), and Molly was used for the selection of STO wave functions (**Figure 46**, pink box). After the aforementioned selections, a new tab corresponding to Multipole parameters appears, where the core and valence electrons for each atom could be seen in **Figure 47**.

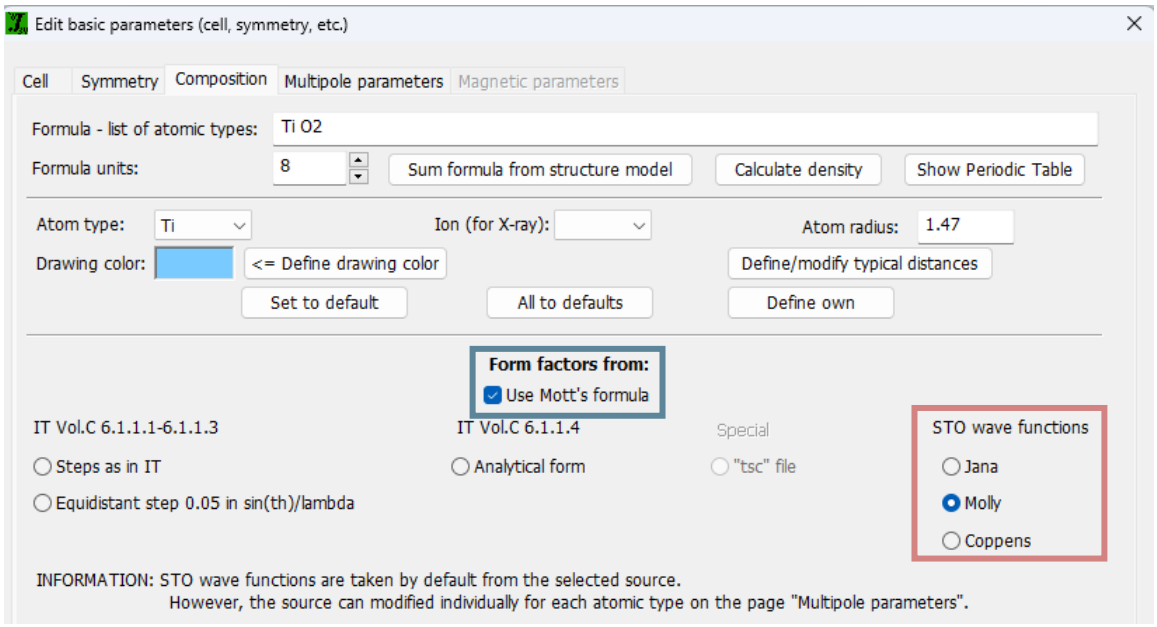

***Figure 46**. 'Edit basic parameters' section from Jana2020. In blue, Mott's formula is selected to define the Form factors. In pink, Molly option is chosen for STO wave functions.*

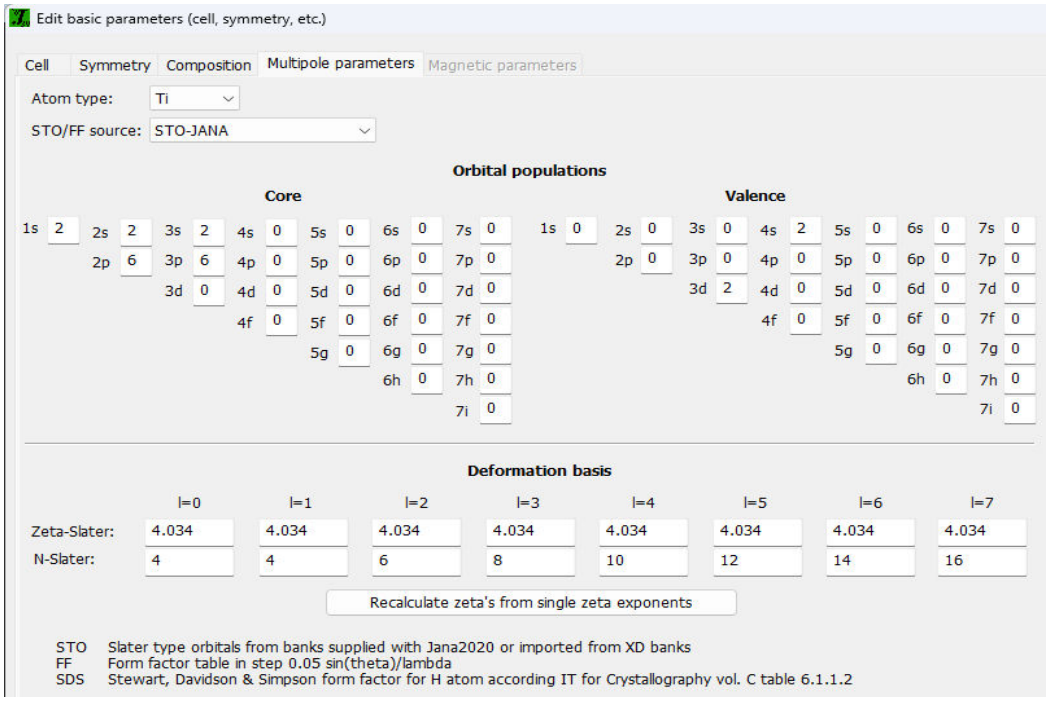

***Figure 47**. 'Edit basic parameters' section. In multipole parameters it is possible to visualize the information of both orbital populations (core and valance) of each atom in the compound.*

Correspondingly, in the 'Edit atoms' section, a new section called 'Multipole parameters' appears for each of the atoms, showing P_c (population of core electrons), P_v (population of valence electrons), and the *kappa* value (**Figure 48**).

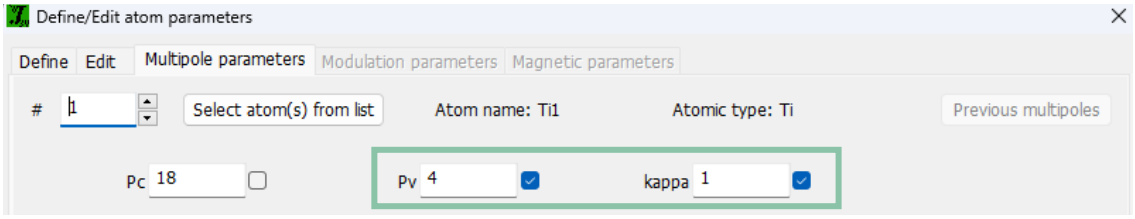

***Figure 48**. 'Define/Edit' atom parameters. In this section it is possible to select the parameters to refine for each atom.*

Only P_v and *kappa* parameters are refined (see **Figure 48** (green box)). Initially, the *kappa* parameter was set to one (for the final results, this parameter should be close to 1 and not negative otherwise the statistics for the refinement are not reliable). This process was repeated for all atoms in the compound.

Note that since O_1 and O_2 had the same chemical environment, they would have the same population of valence electrons. This could be specified in the restrictions part to help the refinement converge.

The kappa value corresponds to the expansion or contraction of the electron density. If the atom loses electrons, the electron density will expand, resulting in a kappa value slightly greater than 1 (as is the case for Ti). Conversely, if the atom gains electrons, the electron density will contract, showing a value slightly lower than 1 (as seen for O). This is coherent with the final refinement results obtained for brookite (see **Table 28**). The statistics for the final model together with atomic positions, ADP values and occupancy are shown in **Table 29**.

Ti (N_{val} = 4)			O_1, O_2* (N_{val} = 6)		
P_{val}	***Kappa***	**$q = N_{val} - P_{val}$**	**P_{val}**	***Kappa***	**$q = N_{val} - P_{val}$**
2.40(16)	1.59(12)	1.60(16)	6.80(8)	0.97(1)	-0.8(8)

**The P_{val} and k parameters of O_1 and O_2 were constrained to be equal*

***Table 28**. Kappa refinement statistics on 3D ED of TiO_2 brookite for two new parameters (P_{val}, kappa) N_{val} correspond to the number of valance electrons in the neutral state.*

Space Group Pbca (61), a =9.20054() Å, b =5.45713(14) Å *c* = 5.13481(12) Å					
R(obs)=5.46, R(all)= 6.63, wR(all)=6.72, GoF(obs)=2.79					
measured / observed [I>3σ(I)] reflections= 3981 / 2827, 83 refined parameters					
g_{max} (Å^{-1})=2.2, Sg_{max} (Å^{-1})=0.01, RSg_{max}=0.6, steps=140					
Atom	**x**	**y**	**z**	**Occ**	***U* (Å^2)**
Ti_1	0.37093(9)	0.59802(6)	0.63695(7)	1.0	0.00615(18)
O_1	0.5104(2)	0.35123(14)	0.68390(15)	1.0	0.0060(4)
O_2	0.2690(2)	0.61219(14)	0.96320(15)	1.0	0.0063(5)

ADP anisotropic parameters (Å^2)						
Atom	***U*11**	***U*22**	***U*33**	***U*12**	***U*13**	***U*23**
Ti1	0.0075(5)	0.00582(14)	0.00515(13)	0.00027(19)	0.00019(19)	0.00014(10)
O1	0.0061(13)	0.0063(3)	0.0058(3)	0.0034(4)	0.0001(4)	0.0007(2)
O2	0.0055(13)	0.0063(3)	0.0070(3)	-0.0015(4)	0.0006(4)	-0.0003(2)

***Table 29**. Final structural model after kappa refinement of TiO_2 brookite.*

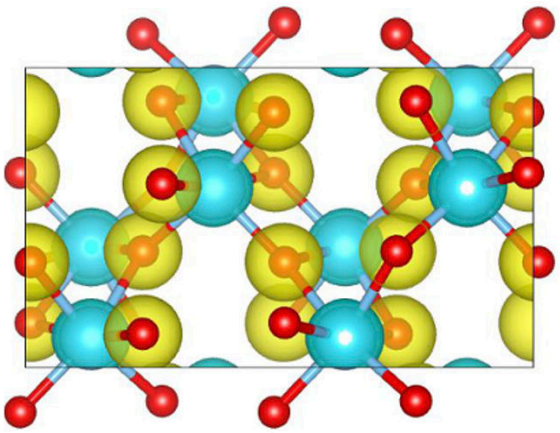

***Figure 49**. Plotted at the iso surface level of 0.1 e Å^{-3}, depicting the accumulation and depletion of charges on O atoms and from Ti atom respectively. Positive and negative isosurfaces are plotted in yellow and blue, respectively.*

The Robs value decrease from IAM refinement (5.96%) to *kappa* refinement (5.46%) indicating a better fit of the model. Additionally, the static deformation map (**Figure 49**) show the expected behavior with negative electron density around the cations and positive electron density around the anions, corresponding to the depletion and accumulation of electrons respectively.

3.7. Conclusions

This initial test on TiO_2 brookite demonstrates that ab-initio structure solution is feasible for relatively large nanoparticles (typically ranging from 50 to 100 nm). This method can be applied using a wide range of instruments, with 3D electron diffraction (ED) data collected either through precession-assisted step-by-step or continuous rotation mode and in TEM or in STEM mode. You just have to make sure that the data collected is from a single individual of good crystalline quality. If this obvious prerequisite is met, then satisfactory results can already be obtained using kinematical approximation refinements with average deviations of atomic positions with respect to references less than 0.05Å (**Table 26** and **Figure 45**.a). A certain disparity among the results are still observed with a maximal deviation up to 0.08Å. In terms of accurate structure analysis, this study shows once again that the use of full dynamical refinement brings additional benefits. Indeed, we notice a clear improvement in both reliability factors and atomic position accuracy with average and maximal deviations about 0.01Å for all datasets (**Table 26** and **Figure 45**.b). Such values are in perfect match with those obtained on larger crystals as evidenced by the *NanED Round Robin* on structure refinement quality with 3D ED. Actually, the data quality obtained by 3D ED on this example of “large NPs” are so good that kappa refinements can be performed and give plausible results.

CHAPTER 4

EXPLORING THE CRYSTAL LIMIT SIZE SUITABLE FOR 3D ED

In the previous chapter, we have discussed the case of relatively 'large' nanoparticles where both cRED and precession-assisted ED acquisition protocols could be used. For the case of TiO_2 brookite we have seen that the accuracy of the structure analysis is comparable to the one established for crystals bigger than 100 nm. However, a crucial question arises: can the same processes be effectively applied to much smaller nanoparticles with same accuracy? In this chapter, we aim to address this question by working with nanoparticles down to 10 nm in size. We will explore the major challenges encountered during data acquisition and accurate structure solution using 3D ED.

To undertake this investigation, we collaborated with two laboratories that specialize in synthesizing nanoparticles for various applications. The first collaborator was the Functional Nanosystems center of the Istituto Italiano di Tecnologia (IIT) in Genova, Italy. The second collaborator was the Institute of Ceramics and Glass, which is part of the Consejo Superior de Investigaciones Científicas (CSIC) in Madrid, Spain.

4.1. Model Compounds.

We selected two compounds that are widely used in NP form and have applications across various scientific fields and, notably, in the energy sector. Anatase TiO_2 NPs are known for their enhanced photocatalytic activity compared to the bulk form, making them particularly effective in applications such as photocatalysis for water splitting, hydrogen production or solar energy conversion[86,87]. Their nanoscale form often outperforms bulk TiO_2 in these roles due to improved light absorption and electron transport properties. Indium Tin oxide (ITO) is used as a transparent conducting oxide in various energy-related and optoelectronic applications, including solar cells, touch screens, and LED displays [88,89]. While bulk ITO has excellent electrical conductivity and optical transparency, nanoscale ITO can offer improved performance in specific applications due to better control over its optical and electrical properties[90, 91].

4.1.1. Anatase Titanium Dioxide (TiO_2 anatase)

Anatase NPs of approximately 15-20 nm (see **Figure 50**) were synthesized through a one-step semi-solvothermal route[92] using titanium (IV) tetrabutoxide ($Ti(OBut)_4$, Fluka, 98%) and tri-fluoroacetic acid (CF_3COOH, Aldrich, 70%, TFAA). In a typical procedure 5 ml of $Ti(OBut)_4$ are introduced in a 50 ml Teflon-lined stainless-steel autoclave, together with 1.9 g of TFAA. A small amount of deionized water (0.4 ml) is added to accelerate the hydrolysis reaction. The system is then heated at 200 °C for 24 h. The obtained white-brown precipitate is washed several times with water and ethanol (96%) and then dried at 105 °C. These NPs were used as a reference for the proof of concept of structure solution of "small size" nanoparticles with light chemical elements.

The structure that will be used as a reference for future structural comparisons is the one published by Horn *et al*. 1972[93] (**Table 30**) and obtained by single crystal X-ray diffraction at room temperature (ISCD code 9852). In anatase (see **Figure 50**) only 2 atomic positions (1 Ti and 1 O) are present with only one atomic coordinate to refine for the oxygen position.

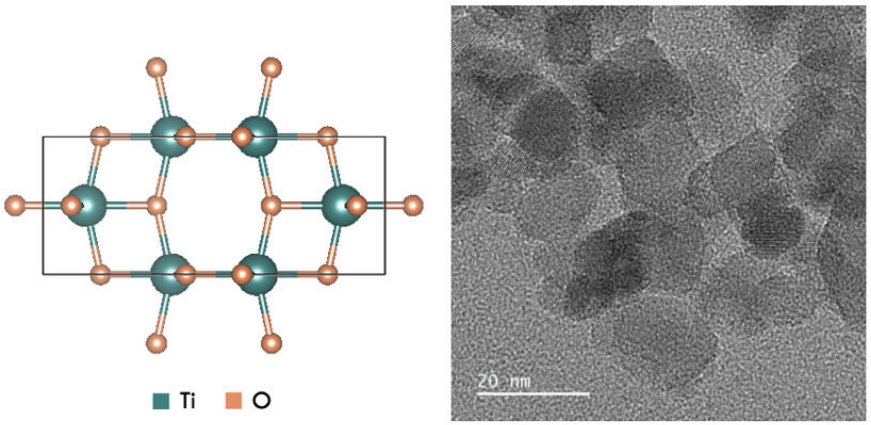

***Figure 50**. (left) structure of TiO_2 anatase represented in a projection along the [100] direction (reference ISCD 9852). (right) TEM image where size and shape of TiO_2 anatase NPs can be estimated.*

SG: $I4_1/amd$ (141) with a = 3.7842(13) Å and c = 9.5146(15) Å					
Atom	**x**	**y**	**z**	**Occ**	**Biso**
Ti1	0	0	0.5	1	0.39(6)
O1	0	0.5	0.5419(2)	1	0.61(9)

***Table 30**. Structural parameters of TiO_2 anatase (based on ISCD 9852). Only one coordinate (in red) can be refined for this model compound.*

4.1.2. Indium Tin Oxide (ITO)

ITO NPs of approximately 10nm (see **Figure 51**) were synthesized using a multi-step procedure[94]. As first step, a 500 mL three neck round flask was filled with 208 mL of oleyl alcohol (Sigma-Aldrich, 85% purity) and left at 150 °C to degas for 3 h under a flux of nitrogen. Indium (III) and tin (IV) acetate (Sigma-Aldrich) were added, along with 32 mL of oleic acid (Sigma-Aldrich, 90% purity), to a 100 mL three neck, round-bottom flask. Under stirring, the flask content was degassed for 3 h under a nitrogen flux, allowing tin and indium oleates to form. After degassing, the flask with oleyl alcohol, which will act as the reaction vessel, was kept under a flux of 0.130 L/min of nitrogen and heated to 290 °C. Indium and tin precursors were transferred in a syringe and injected in the hot oleyl alcohol using a syringe pump with an injection rate of 4.8 mL/min. NPs with an average diameter of 10 nm and a 10.8% doping level (Sn/tot) were obtained 15 min after the injection ended. The solution was then centrifuged at 5540 G for 10 min, using ethanol as antisolvent. The supernatant was discarded, the material was redispersed

in hexane, then ethanol was added, and the solution was centrifuged again using the same parameters. Finally, the NPs were stored in octane. These NPs were used as a reference for the proof of concept of structure solution of "small size" NPs with heavier chemical elements.

The structure (**Figure 51**) that will be used as a reference for structural comparison is the one published by González *et al*. 2001[95] and obtained from neutron powder diffraction (ISCD code 190347) for ITO with a Tin doping close to the one we have in our NPs. In ITO (disregarding the extra O2 position), 3 atomic positions (2 In and 1 O) are present with one atomic coordinate to refine for one indium position and the 3 atomic coordinates for the oxygen position (**Table 31**).

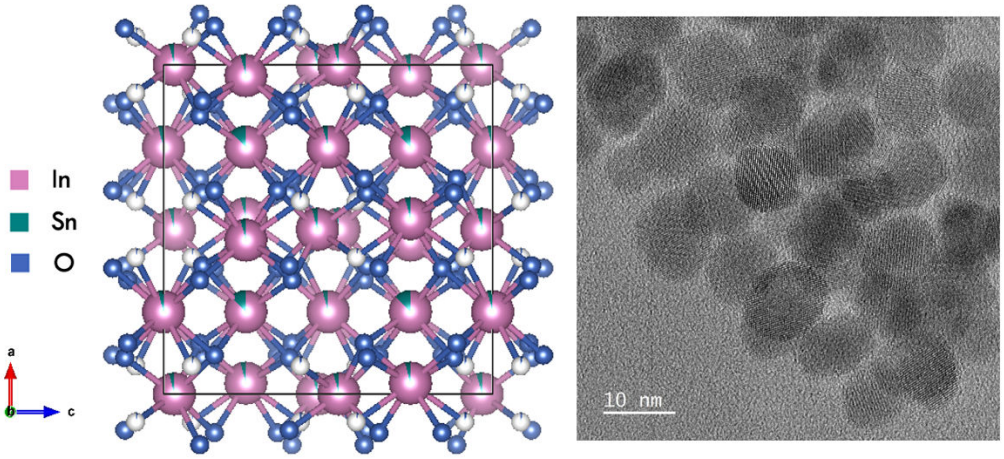

Figure 51. *(left) structure of ITO from reference ISCD 190347. The 11% Tin doping induces the presence of one low occupancy (3%) oxygen position. (right) TEM image where size and shape of ITO NPs can be estimated.*

SG: Ia$\bar{3}$ (206) with a = 10.12690(1) Å					
Atom	**x**	**y**	**z**	**Occ**	**Biso**
In_1	0.25	0.25	0.25	In/Sn: 0.89/0.11	0.443
In_2	0.4672(1)	0	0.25	In/Sn: 0.976/0.024	0.350
O_1	0.3901(1)	0.1543(1)	0.3820(1)	1	0.540
O_2	*0.085*	*0.085*	*0.085*	*0.032*	*0.544*

Table 31. *Structural parameters of ITO (11% doping) from ISCD reference 190347. The atomic coordinates that can be refined are indicated in red.*

4.2. PXRD Characterization

Thanks to the secondment at Elettra Synchrotron (*MCX beamline*), I had the opportunity to conduct experiments on the NPs used in this chapter. For both compounds a 0.3 mm capillary was filled with the powder sample, and experiments were performed using a transmission geometry. Data acquisition using the same geometry was performed on Silicon powder in order to obtain a calibration for the instrumental peak broadening. The structure parameters obtained in this section will be later compared with the reference structure and with those obtained through 3D ED.

4.2.1. Anatase

For anatase, an energy of 12 keV (λ=1Å) was used and the Rietveld refinement was done using FullProf software. The structural parameters obtained in the final model are presented in **Table 32**. A total of 66 reflections were observed in the diffraction pattern, and 13 parameters were refined during the analysis. The fitted powder patterns (**Figure 52**) and reliability factors for the refinement (R_{Bragg} = 4.34 and R_{wp} = 13.3) indicate a good match between the experimental data and the theoretical model.

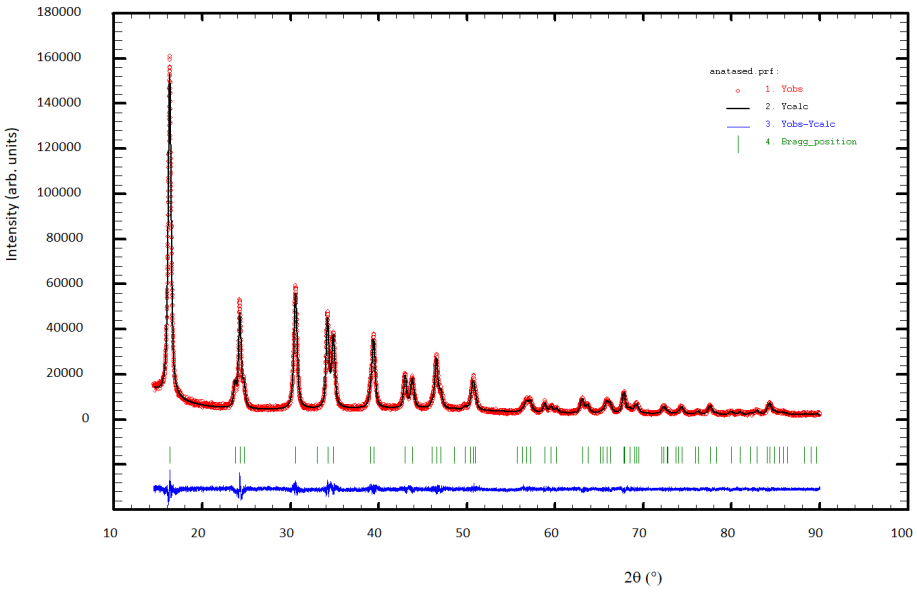

***Figure 52**. Plot of the Rietveld Refinement of TiO_2 anatase against PXRD data. The observed data (red points), calculated pattern (black line) and the difference (blue line). The green lines correspond to peaks at the Bragg position.*

SG: $I4_1/amd$ (141) with a=3.78924(4) Å and c=9.50796(11) Å					
number of reflections=66; number of refined parameters=13; R_{Bragg}=4.34; R_{wp}=13.3					
Atom	**x**	**y**	**z**	**Occ**	**U(Å²)**
Ti_1	0	0	0.5	1	0.1163(16)
O_1	0	0.5	0.20884(9)	1	0.0118(7)

ADP anisotropic parameters (Å²)						
Atom	**U_{11}**	**U_{22}**	**U_{33}**	**U_{12}**	**U_{13}**	**U_{23}**
Ti_1	0.01059(12)	0.01059(12)	0.0137(2)	0	0	0
O_1	0.0165(7)	0.0030(6)	0.0158(6)	0	0	0

Table 32. *Rietveld Refinement results of TiO_2 anatase using FullProf from PXRD experiments using synchrotron radiation.*

When working with NPs smaller than 20 nm, a broadening effect on the diffraction peaks is observed. This can be used to obtain microstructural information about the sample like the size and shape of the diffracting volume. Therefore, using the Scherrer equation, the average diffracting volume was estimated, with its dimensions and shape shown in **Figure 53**. The dimensions are approximately 9.85 nm in width and 12.6 nm in length exhibiting an oval shape.

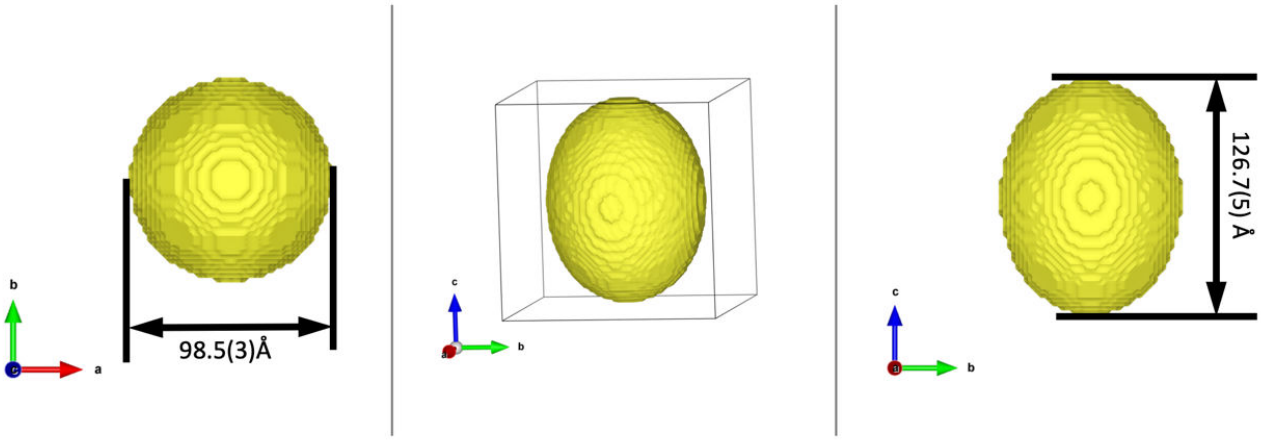

Figure 53. *Dimensions and shape estimated by the Scherrer equation for TiO_2 anatase.*

4.2.2. ITO

The same procedure was applied to ITO, with the difference in the setup being that, since tin is a heavier atom, a higher energy source was required to avoid absorption. Consequently, we operated at 17 keV (λ = 0.727Å).

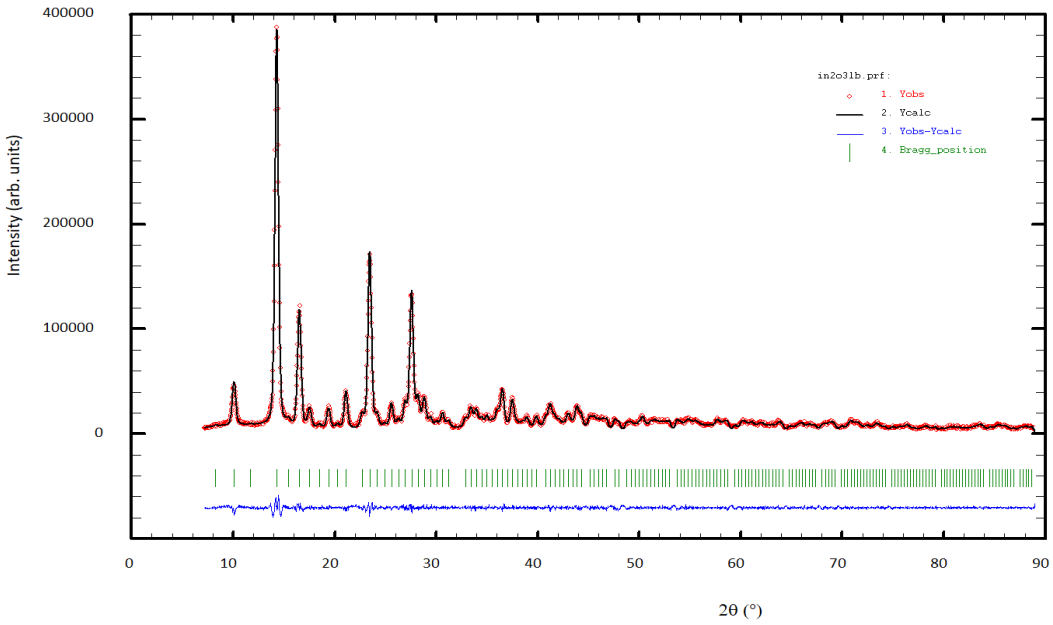

***Figure 54**. Plot of the Rietveld refinement of ITO against PXRD data. The experimental data is represented with red points, the calculated pattern with a black line and the difference plot with a blue line. The green marks correspond to peaks at the Bragg position.*

SG: Ia$\bar{3}$ (206) with a= (10.11457 Å)					
number of reflections=654; number of refined parameters=28; R_{Bragg}=3.23; R_{wp}=10.1					
Atom	**x**	**y**	**z**	**Occ**	**U Å^2)**
In_1	0.25	0.25	0.25	1	0.0104(4)
In_2	0	0.25	0.46824(8)	1	0.0095(5)
O_1	0.1106(7)	0.1540(7)	0.6132(7)	1	0.006(4)

ADP anisotropic parameters (Å^2)						
Atom	**U_{11}**	**U_{22}**	**U_{33}**	**U_{12}**	**U_{13}**	**U_{23}**
In_1	0.0104(4)	0.0104(4)	0.0104(4)	0.0017(8)	0.0017(8)	0.0017(8)
In_2	0.0104(4)	0.0080(8)	0.0100(4)	0.0001(6)	0	0
O_1	0.009(4)	0.011(4)	-0.000(3)	0.007(3)	-0.000(3)	0.002(3)

***Table 33**. Rietveld Refinement results of ITO using FullProf from PXRD experiments using synchrotron radiation.*

The structural results obtained in the final model are presented in **Table 33**. A total of 654 reflections were observed in the diffraction pattern, and 28 parameters were refined during the analysis. The reliability factors for the refinement are as follows: R_{Bragg} = 3.23 and R_{wp} = 10.1, indicating a good fit between the experimental data and the theoretical model (**Figure 54**).

As mentioned for TiO_2 anatase, the broadening on the peaks can be taken as an advantage for reaching the microstructural information. The shape and size of the ITO particles were then determined using the Scherrer equation. As shown in **Figure 55**, the NP exhibits a spherical shape with an approximate diameter of 8.31 nm.

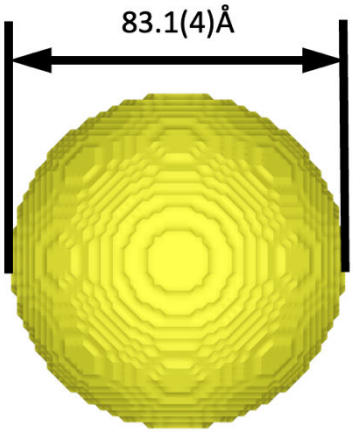

***Figure 55**. Dimensions and shape estimated by the Scherrer equation for ITO.*

4.3. 3D ED data acquisition on small NPs

In attempting to apply the protocols used for brookite to smaller NPs, namely quasi-spherical particles below 20 nm, the experimental requirements appeared much more stringent. In this section, we will present some of the challenges faced during 3D ED data collection and the solutions planned to overcome these obstacles. Let us first address the feasibility of collecting 3D ED data using cRED or precession-assisted ED on small single NP.

cRED data acquisition, when done without tracking the crystal position, relies on using a beam (or selected area) large enough to ensure that the crystal (or part of it) will stay in the beam all over the tilt range. The lower limit size of the beam (or area) is dependent on the instrument used for data acquisition. As discussed in the previous chapter,

collecting 3D ED data on small particles with a beam significantly much larger than the crystal itself may induce some difficulties:

1. Find an isolated particle that will actually stay isolated all over the tilt range.
2. The NPs being supported on a C amorphous coated grid, the signal coming from the membrane will become dominant over the signal diffracted by a single NP.
3. Most of the intensity will go to the transmitted beam contributing to an enhanced background noise at low diffraction angle.

Points 2 and 3 address a similar issue about the signal to noise ratio. To illustrate this, we can conduct an experiment to actually realize the effect of using an oversized beam (see **Figure 56**).

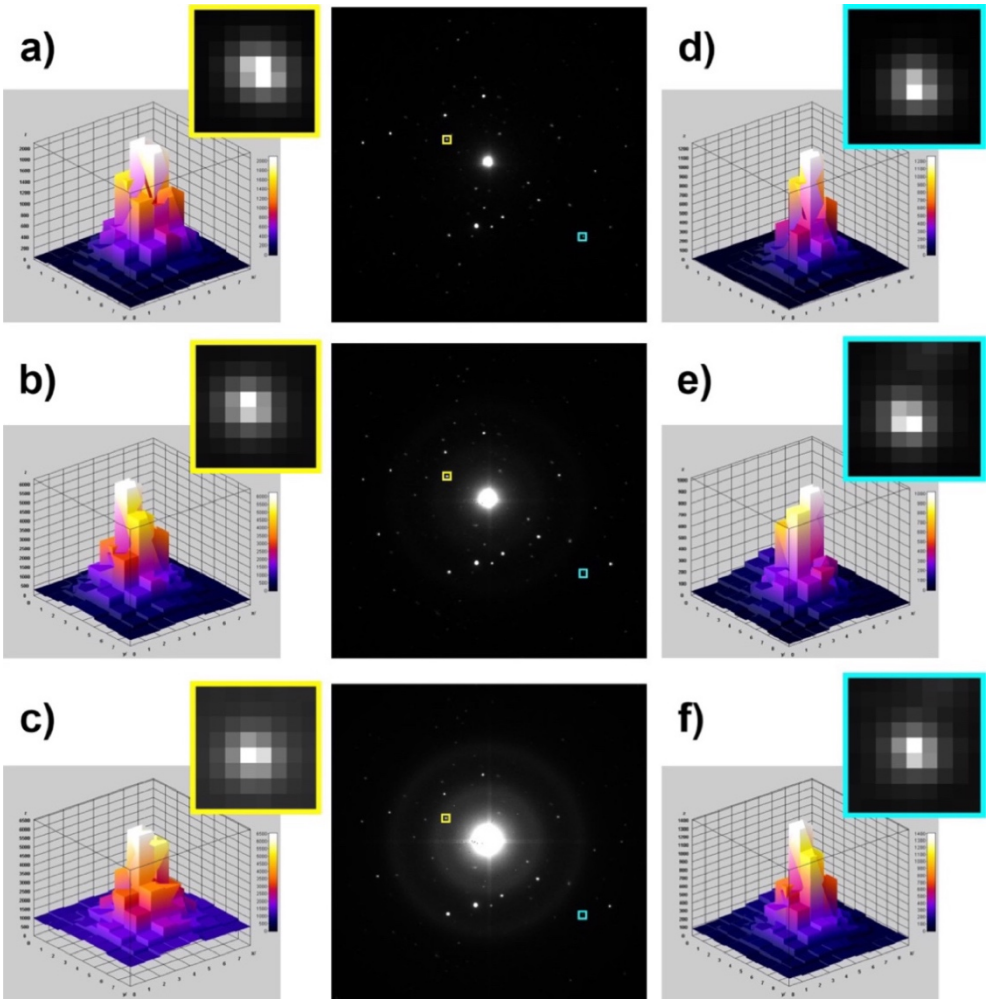

Figure 56. Effect of using different condenser lens aperture (CLA) on the background level in the diffracted signal collected by our ASI Cheetah M3 detector. *Three* CLA of 10, 40 and 100 µm *were used* corresponding to a beam size on the sample of approximately 70, 300 and 750 nm. 3D plot*s* of the intensity measured for *a* reflection diffracted at low angle are *shown in* a), b) and c) for CLA of 10, 40 and 100 µm, respectively. *Same is done for a reflection diffracted at a higher angle in d), e) and f).*

In this format we worked on nanobeam illumination changing only the condenser lens aperture (CLA) of 100 µm, 40 µm and 10 µm leading to an illuminated area of 750 nm, 300nm and 70nm, respectively. Upon initial observation, large diffuse ring patterns originating from the carbon (C) amorphous membrane are clearly visible with a 100 µm CLA, significantly reduced with a 40 µm CLA, and nearly absent when using a 10 µm CLA. This spurious signal is localized in specific areas of the detector and for the reflections in these areas (yellow boxes in **Figure 56**) a clear increase in the background noise is observed. For reflections at high diffraction angle (blue boxes in **Figure 56**), out of these areas, the signal to noise ratio is globally increased but to a lesser extent. While the characteristics of our Medipix detector allow noise free ED data collection this 'noise free' refers to electronic noise and not to noise coming from the sample environment. Using an oversized beam with such high-quality detector still allow to obtain acceptable 3D ED data but reducing the beam size to a size slightly larger than the particle size improve the signal to noise ratio providing better data. This also aligns with the general recommendations outlined in the Deliverable 3.1 of the NanED project, titled "Protocol for data collection providing optimal data quality for accurate structure refinement", available at *https://cordis.europa.eu/project/id/956099/results*. Regarding the point 1, we would not say that finding an isolated particle of 10 nm in a 750 nm beam is impossible to achieve but it will certainly require a significant amount of time. Reducing the beam size strongly enhanced the feasibility to collect 3D ED data on small isolated NPs. This is another reason why we retain this option.

For cRED, reducing the beam to less than 50 nm, for instance, will go below the confusion sphere of most, if not all instruments available at present time. This means a crystal tracking solution shall be employed. At CRISMAT, with our experimental setup, the tracking can be done by strongly defocusing the diffraction while tilting, allowing to visualize a shadow image of the crystal and correct manually the position. This option is available in Instamatic and is described in Cichocka *et al*. 2018[96]. This option is not the best as it generates a dataset where missing ED frames will be present every time a visual check is performed. A preferable option, not implemented at CRISMAT, is to record the crystal position over the tilt range and use beam deflection to follow the crystal while collecting data. This option is efficient but, to date, being mostly applied to much larger crystals and beam size with maybe the exception of the program fast-EDT[97] not available in our experimental setup. Details about crystal tracking for 3D ED can be found in the

Deliverable 1.3 of the NanED project, titled “Software able to track the crystal position during ultra-fast ED data collection and to perform wandering beam acquisition”, available at *https://cordis.europa.eu/project/id/956099/results*. Regarding cRED it appear that the necessity to use tiny electron beam is, at least for our instrumental setup, incompatible with an efficient tracking of the NPs. Therefore, the only remaining protocol that can be applied for data acquisition of these NPs is PEDT. For PEDT, the possibility to correct the crystal position while collecting 3D ED data exists by visual inspection at each tilt step. This will increase the data acquisition time but shall provide high quality data ensuring the particle is not damage.

Using the same beam size as was used for brookite, which was approximately 50-70 nm, was not an option. As previously explained, the effect of agglomeration in small NPs was much more pronounced. Therefore, the only viable solution was to reduce more the beam size. By reducing it to a size of about 20-30 nm, several advantages and disadvantages emerged. On the one hand, as just discussed, the signal to noise ratio increased, improving the quality of the data. However, due to the small size of the NPs, a longer exposure time is necessary to capture more observed reflections and to obtain statistically significant datasets. The drawback is that focusing the electron beam on a much smaller area of the sample for an extended period causes the NPs to become less stable over time, limiting the number of PED frames we can collect. This would result in incomplete datasets and limit our ability to extract pertinent information, making the results unreliable as it will be illustrated below.

The only possible solution to the issue of not having enough quality data from a single crystal was to use a tomography cryo-holder instead of the tomography holder that we typically use. This holder allows us to work under cryogenic conditions at a temperature of about -178°C, effectively ‘freezing’ the NPs and providing them with greater stability during data collection. It is important to mention that one of the drawbacks of working under these conditions is the possible formation of ice. Firstly, ice formation makes it difficult to locate the NPs of interest because the crystallized ice particles may have similar sizes and shape. Secondly, if this crystallized ice is near the NP you want to use for data acquisition, it can interfere with the analysis. In such cases, we typically keep the electron beam focused on the area with the NP of interest for a certain amount of time (usually a few tens of seconds) to remove the crystalline ice, which was much less stable than the NPs.

Small NPs generally posed a greater challenge for preparing a TEM grid suitable for 3D ED experiments. If diluted too much, there was barely any sample on the grid, whereas if too much powder was added, the NPs appeared in an agglomerated form. Therefore, preparing several grids with different dilution levels is a good option. Also, to prevent agglomeration, the ultrasonic bath time had to be extended to at least 15 minutes, compared to the time used for brookite, to promote the disaggregation of the NPs. Additionally, adding a surfactant during the synthesis process could help mitigate this undesirable effect in the final product. Overall, setting up the experiment for smaller NPs proved more challenging than for brookite. However, once the appropriate beam size and exposure time were established, along with optimal dispersion of the NPs and the use of cryo-conditions, data acquisition became possible, and the analysis could proceed as it will be demonstrated below.

4.4. 3D ED results

4.4.1. TiO_2 anatase

After several attempts to achieve the proper dispersion (which was impossible to verify through an optical microscope) and checking the entire grid at the TEM, we first tried to obtained data at room temperature. As mentioned earlier, this approach may not be the most efficient, but it is still interesting to present the results obtained under these conditions. Although it was possible to find suitable samples, only 2 or, if we were lucky, 3 datasets were collected per day of experimentation.

At first, the exposure time was set to 0.3 seconds per frame to collect the necessary frames for structural resolution and refinement at room temperature. Increasing the exposure time per frame any further caused the NPs to stop diffracting much sooner, capturing very little information from the reciprocal space, making it impossible to solve the structure. Therefore, 0.3 seconds was reasonable time to provide enough stability to the NPs to achieve a range approximately between -40 and 45 degrees, rotating the goniometer every 2 degrees, resulting in a total number of frames for analysis being around 30-35 per experiment. This setup can be considered as the first used protocol for data acquisition.

	Anatase-01	Anatase-02	Anatase-03
Tilt Range (°)	[-30, +49]	[-40, +38]	[-34, +22]
Cumul. Cover. *(sinθ/λ=0.8Å^{-1})*	88.7	93.2	98.5
Averaged Refl. All/Obs.	78/39	92/48	61/47
Rint (from PETS)	16.17	23.85	13.57
Number of refined parameters	4	4	4
Robs	31.09	13.14	15.07
Rall	35.79	19.93	15.60
Refl. All/Obs.	670/296	539/179	366/265
Number of parameters	43	36	33
Robs	6.78	6.97	6.25
Rall	12.19	18.18	8.33

***Table 34**. 3D ED results for both kinematical and dynamical refinement for some experiments carried out for anatase with PEDT datasets collected at room temperature. All the datasets where collecting using a precession angle of 1.4 Å. Kinematical and dynamical refinements are presented in the pink and blue part, respectively.*

While most experiments with datasets collected at room temperature successfully achieved structural resolution, reliability issues arose during the structure refinement process. As shown in **Table 34**, the number of observed reflections was low, generally sufficient for kinematical refinements but almost systematically inadequate for dynamical refinements, given the criterion of 10 reflections per refined parameter. As explained in Chapter 2, dynamical refinement is a frame-based approach where a scale parameter is refined for each frame, leading to a substantial increase in the total number of parameters. While we did obtain results from the room temperature analyses, these results were not as good or statistically robust as we had expected. This is why we decided to use a cryo-holder: to extend the exposure time, increase the number of observed reflections, and preserve the integrity of the particles during data collection. Consequently, in a second protocol, experiments were conducted under cryogenic conditions, the exposure time was increased to 4 seconds per frame, and the tilt step was maintained at 2 degrees per tilt.

Below, we will present the results obtained from our best dataset, which was collected at low temperature on an isolated crystal with lateral dimensions of approximately 20 nm by 15 nm (**Figure 57)**. Initially, the cell parameters were indexed using tetragonal

symmetry with a = b = 3.7931 Å and c = 9.416 Å and I-lattice centering (**Figure 58**), as attested by examination of the reciprocal space sections partly reconstructed based on the 3D ED data collected (**Figure 59**).

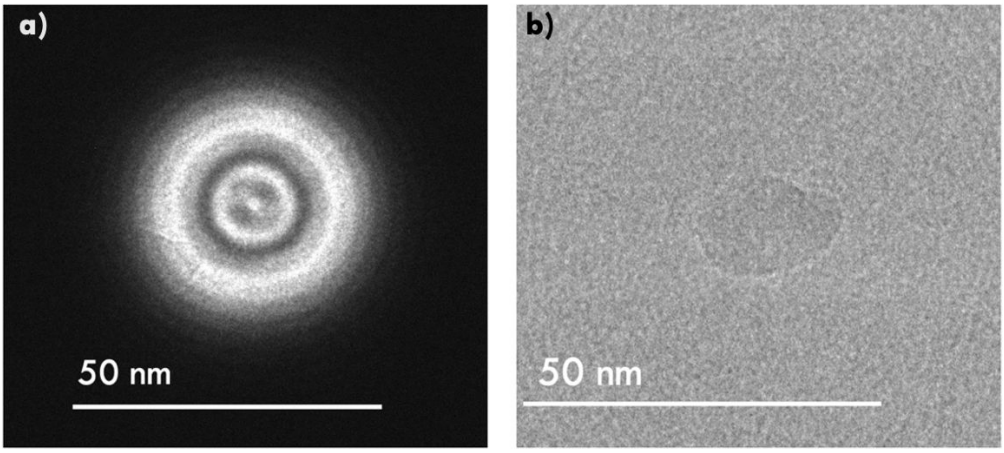

***Figure 57**. a) Visualization of the beam size used for data acquisition, approximately 30 nm in diameter. b) Image of an isolated nanoparticle (NP) identified as suitable for data acquisition and subsequent analysis, which will be used in the refinement and final.*

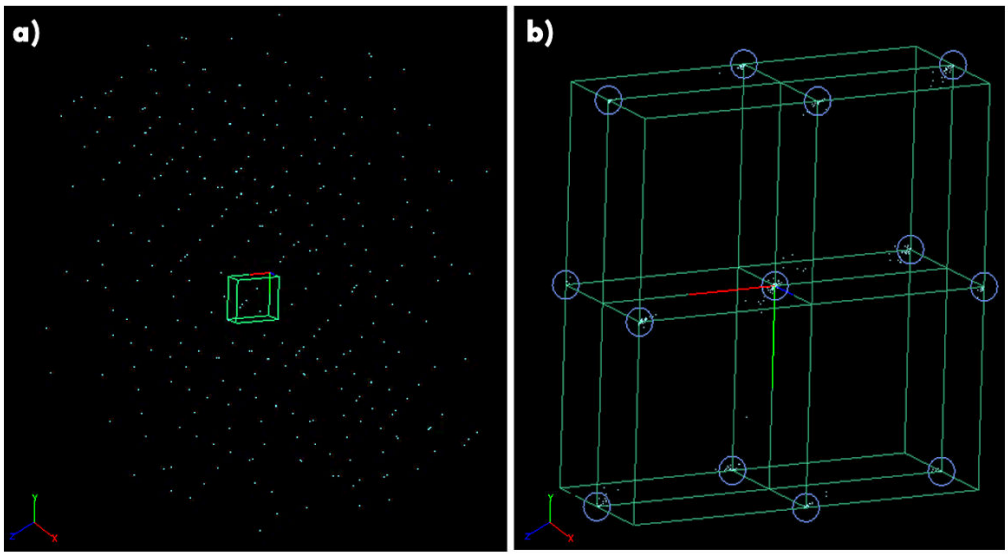

***Figure 58**. Indexation o the reflections under a tetragonal symmetry and I-centered lattice. a) Representation of the reciprocal space shown the reflections in blue and the unit cell in green. b) Folding can be applied in multiples of the unit cell (e.g., 2x2x2) to check for possible lattice centering. In this example, reflection clusters consistent with an I-lattice centering are encircled.*

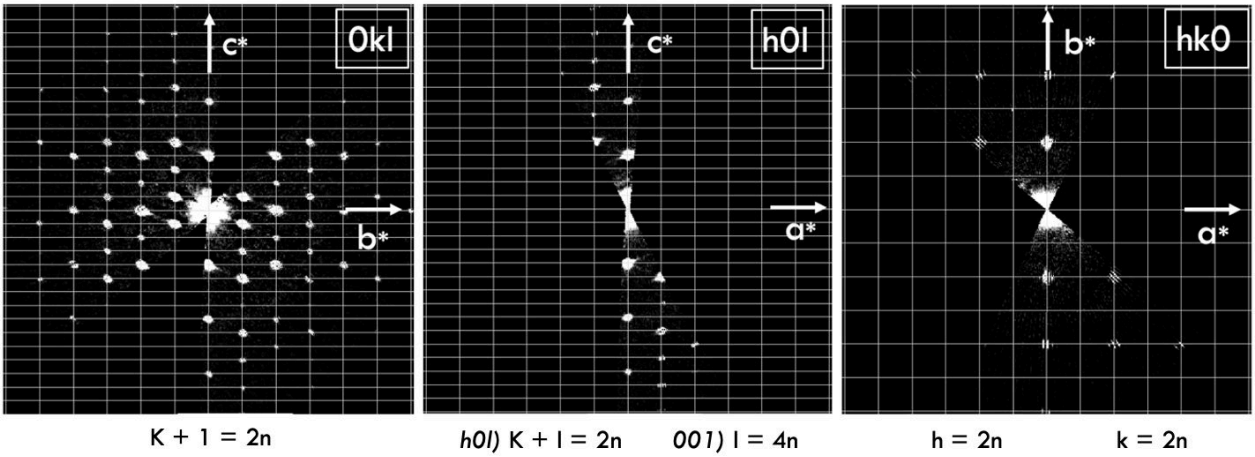

***Figure 59**. The 0kl, h0l, and hk0 sections show all reflections consistent with an I-lattice centering.*

After integrating the reflections with PETS2, the structural model was first obtained using Superflip, then kinematical and dynamical refinements were carried out in Jana2020. This result in a final solution that presented a space group $I4_1/amd$, consistent with the expected structure from the reference sample. The statistics for both refinements are shown in **Table 35**, and the atomic positions (x, y, z), occupancy (occ) and Uiso value for the final model are shown in **Table 36**.

	Anatase-04
Tilt Range (°)	[-34, +44]
Cumul. Cover. ***(sinθ/λ=0.8Å^{-1})***	100
Averaged Refl. All/Obs.	94/76
Redundancy	4.9
Rint (from PETS2)	22.7
Number of refined parameters	4
Robs	10.92
Rall	12.35
Refl. All/Obs.	591/464
Number of parameters	43
Robs	3.59
Rall	4.18

***Table 35**. The best result obtained for Anatase with PEDT data collected using a cryo-holder. Kinematical and dynamical refinements are presented in the pink and blue part respectively.*

The Robs value decreases significantly (from 10.92 to 3.59) when considering the multiple scattering effect and applying dynamical refinement. Furthermore, we can say that the refinement results are statistically founded since the number of observed reflections is equal to or greater than 10 times the number of refined parameters. Therefore, by introducing a cryo-holder for data acquisition and thereby increasing the exposure time without damaging the material, we have been able to obtain very favorable results.

Space Group $I4_1/amd$, a = 3.7918(23) Å, *c* = 9.4165(64) Å					
R(obs)=3.59, R(all)=4.18 , wR(all)=9.27, GoF(obs)=2.54					
measured / observed [I>3σ(I)] reflections=591 / 464, 43 refined parameters					
g_{max} (Å^{-1})=1.8, Sg_{max} (Å^{-1})=0.01, RSg_{max}=0.75, steps=200					
Atom	**x**	**y**	**z**	**Occ**	**Ueq (Å^2)**
Ti1	0	0	0.5	1.0	0.0061(2)
O1	0	0.5	0.54043(10)	1.0	0.0079(3)

***Table 36**. Final model for TiO_2 anatase. Atomic positions (x, y, and z), Occupancy (Occ) and Displace Atomic parameters (Ueq) value are specified.*

4.4.2. ITO

Initially, the first protocol was applied, working at room temperature with an exposure time of 0.3 seconds per frame and a tilt step of 2 degrees. In this first attempt, only two datasets were collected with a short tilt range (**Table 37**). In the case of ITO, the number of observed reflections appears satisfactory, but other issues are evident in the obtained results. For ITO-01, the Robs obtained from the dynamical refinement is much higher than that from the kinematical refinement, which is unexpected, as considering the multiple scattering effect should improve (i.e. lower) this value. This increase suggests a potential issue with the dataset, indicating that the results are unreliable. In the case of ITO-02, although the number of observed reflections is close to the limit when compared to ten times the number of refined parameters, it could be considered statistically valid. However, even though Robs decreases from the kinematical refinement to the dynamical one, if we look closely at Rall, we see a significant difference (from 11.55 to 34.55). We also observe that the number of observed reflections is very small compared to the total number of reflections (407 observed out of 2265 measured). This discrepancy may be due

to the fact that most of the measured reflections fall below the 3σ(I) threshold, likely because of their weak intensity.

	ITO-01	ITO-02
Tilt Range (°)	[-42, +14]	[-57, +6]
Cumul. Cover. ***(sin θ/λ=0.8Å^{-1})***	82.2	97.3
Averaged Refl. All/Obs.	340/273	386/193
Rint (from PETS2)	13.03	22.73
Number of refined parameters	8	8
Robs	11.56	12.02
Rall	13.78	19.74
Refl. All/Obs.	2047/1568	2265/407
Number of parameters	37	40
Robs	25.62	11.55
Rall	27.77	34.55

Table 37. *Statistics and refinement results for two different datasets collected at room temperature with small exposure time for ITO. Kinematical and dynamical refinements are presented in the pink and blue part, respectively.*

Therefore, the second protocol was applied with the goal of obtaining higher quality data and better statistics after performing the dynamical refinement. In this case, finding isolated NPs was also challenging due to ice formation, but data acquisition was more manageable since the stability of the NPs allowed for data collection over a larger tilt range and with more reflections in each collected diffraction pattern. Several datasets were collected, three of which yielded very good reliability factors and favorable statistics, as shown in **Table 38**. These results confirm that a precise structural determination was achieved. In the following, only the best result, obtained for ITO-05, will be discussed in detail.

In **Figure 60**, the beam size used and the isolated ITO-05 crystal, with a diameter of approximately 10 nm, are shown. The reflections were indexed in a cubic system with a cell parameter determined as a = 10.1390(14) Å. The I-lattice centering can be evidenced

both during the indexation with PETS2 **Figure 61** and by examination of the reciprocal space sections (**Figure 62**).

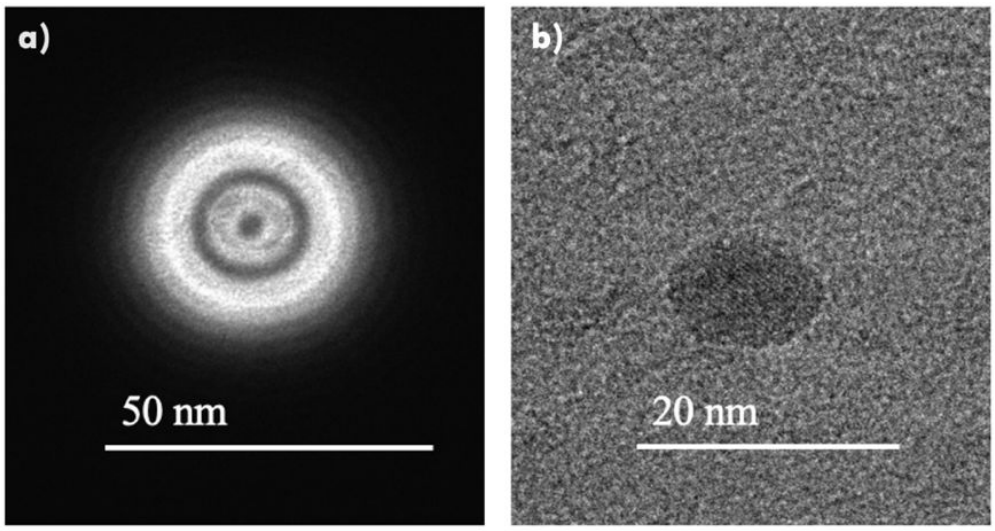

Figure 60. *a) the beam size used for data acquisition on ITO-05. b) Isolated ITO-05 NP suitable for analysis.*

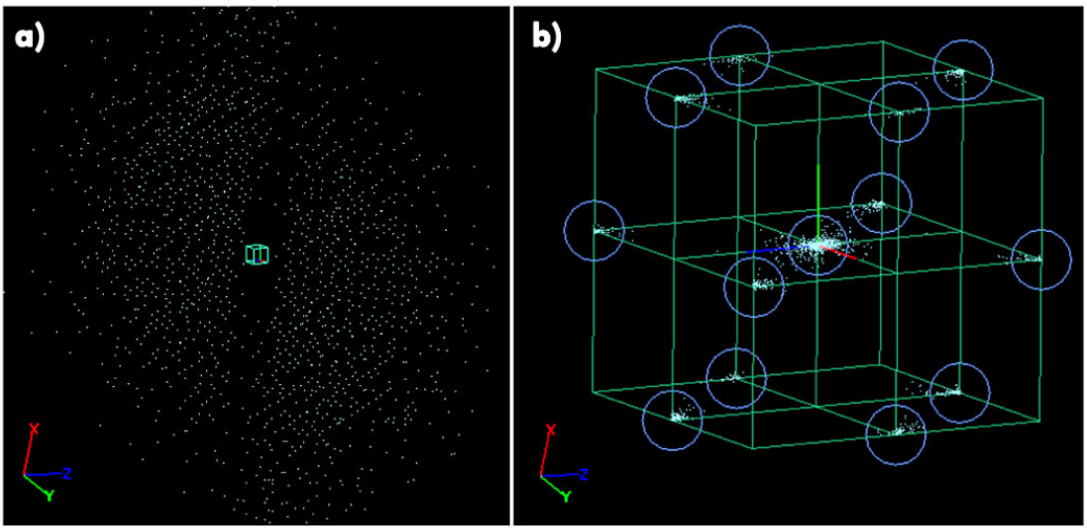

Figure 61. *Indexation of the reflections under a cubic symmetry and I-centered. This option is available in PETS2 in 'Find Unit Cell and orientation matrix' section. a) Representation of the reciprocal space shown the reflections in blue and the unit cell in green. b) Reflections folded into the unit cell multiplied by 2x2x2. This option is interesting to evidence lattice centering. Here the encircled reflection clusters are consistent with a I-lattice centering.*

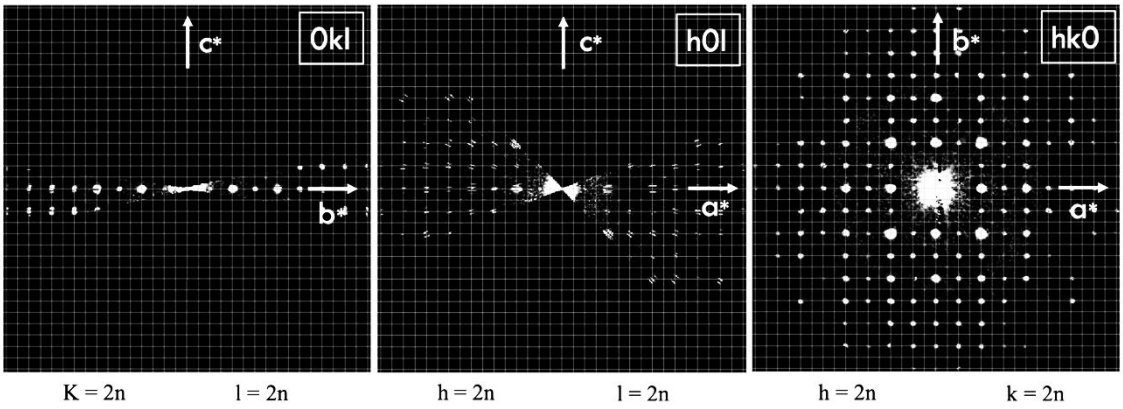

Figure 62. *The 0kl, h0l, and hk0 sections show all reflections as even consistent with F centering but also with the $Ia\bar{3}$ space group. In this case other sections would be needed or, alternatively, rely on the indexation obtained in PETS2.*

After integrating the reflections, the structural model was developed in Jana2020. Kinematical and dynamical refinements were carried out resulting in a final solution that presented a space group $Ia\bar{3}$, consistent with the expected structure from the reference sample. The statistics for both refinements are shown in **Table 38**, and the atomic positions (x, y, z) occupancy (Occ) and Uiso value for the final structure are shown in **Table 39.**

	ITO-03	**ITO-04**	**ITO-05**
Tilt Range (°)	[-42, +45]	[-42, +45]	[-44, +26]
Cumul. Cover. ***(sin θ/λ=0.8Å^{-1})***	100	99.6	100.4
Averaged Refl. All/Obs.	312/190	370/275	373/310
Rint (from PETS)	15.99	13.75	8.84
Number of refined parameters	8	8	8
Robs	11.54	7.91	6.10
Rall	13.25	10.59	7.91
Refl. All/Obs.	2434/1338	2529/1677	2386/1697
Number of refined parameters	52	51	48
Robs	7.31	6.43	4.71
Rall	11.38	8.54	6.25

Table 38*. Statistics and refinement results for three different datasets of ITO compound using the second protocol in cryogenic conditions. Kinematical and dynamical refinements are presented in the pink and blue part, respectively.*

Space Group $Ia\bar{3}$ (206), a = 10.1390 (14) Å					
R(obs)=3.59, R(all)=4.71 , wR(all)=10.59, GoF(obs)=1.42					
measured / observed [I>3σ(I)] reflections=2386 / 1697, 48 refined parameters					
g_{max} (Å^{-1}) =1.8, Sg_{max} (Å^{-1}) =0.01, RSg_{max}=0.4, steps=128					
Atom	**x**	**y**	**z**	**Occ**	**Ueq (Å^2)**
In_1	0.46784(4)	0	0.35	1.0	0.00647(10)
In_2	0.25	0.25	0.25	1.0	0.00735(8)
O_1	0.38983(15)	0.15503(15)	0.38234(15)	1.0	0.0104(3)

ADP anisotropic parameters (Å^2)						
Atom	**U_{11}**	**U_{22}**	**U_{33}**	**U_{12}**	**U_{13}**	**U_{23}**
In_1	0.00639(18)	0.00588(17)	0.00714(17)	0	0	0.00120(17)
In_2	0.0735(14)	0.00735(14)	0.00735(14)	0.00159(17)	0.00159(17)	0.00159(17)

***Table 39**. Final model for ITO-05. Atomic positions (x, y, and z), Occupancy (Occ) and Uiso value are specified.*

Although collecting 3D ED data on a 10 nm nanoparticle is not necessarily straightforward, the quality of the data and the refinements obtained for ITO were unexpectedly high, as will be discussed further below. However, determining the precise localization of Sn atoms was not possible due to the proximity of In and Sn in the periodic table and their similar electronic configurations. Although electron diffraction can probe the electrostatic potential, it faces limitations in this context. Additionally, the extra oxygen position identified through neutron powder diffraction could not be confirmed here due to its very low occupancy level (3%). Therefore, in the Tables, only In is specified, and we assume a statistical occupancy of 11% Sn at the In atomic site. In the next chapter, we will discuss how, when the difference in atomic numbers is larger, it becomes possible to refine mixed occupancy sites.

4.5. Capturing the structure of NPs in motion

Working in cryogenic conditions reduces electron beam damage to NPs and improves the quality of the 3D ED data obtained as shown in the previous section. However, something interesting appear during these experiments. The electron beam induced NPs movements due to changes in the amorphous layer that formed during the grid's cryogenization and

covered the entire grid. These movements consist of a self-rotation of the NP as soon as the beam reaches the surrounding of the particle. Electron beam energy indeed induces a local change in the amorphous layer. Bubbles front wave (see **Figure 63**) propagates and move the NPs.

This self-rotation of the NP can be exploited by collecting diffraction data while the NP is in motion. It is thus possible to collect a tilt series over a small angular range, the direction and angle of tilt being random and unknown. Nevertheless, in this way, by collecting small tilt series over many randomly oriented NPs, it should be possible to access the entire reciprocal lattice. This is close to what is done in so-called serial electron crystallography (serial ED) used for highly beam sensitive materials where one single diffraction pattern is collected per crystal[98, 55, 99].

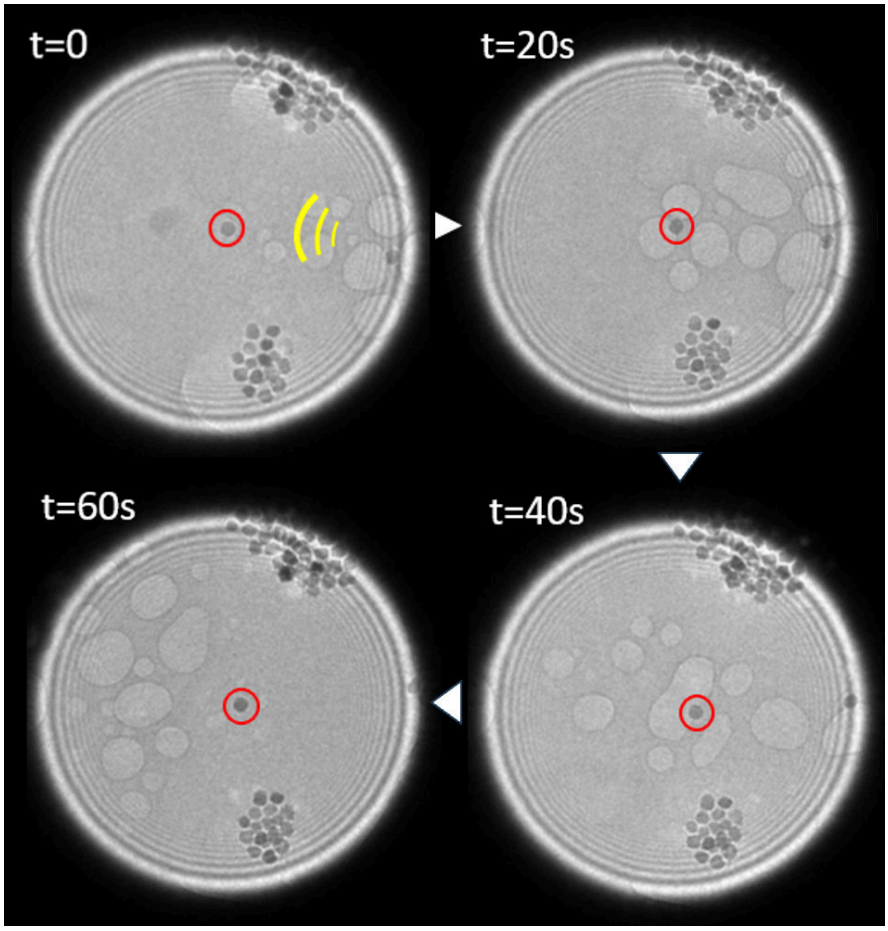

***Figure 63**. Sequential images showing the propagation of a bubble's wavefront (emphasized in yellow at t=0) from the right to the left of the images passing through an isolated NP encircled in red. Upon impact, this wavefront induces a motion of the NPs with a rotational component.*

To analyze such datasets, one must generate a large set of simulated ED patterns (templates) that we compare with the experimental patterns in order to find their orientation. To do so the cell parameters should be known. This can be obtained either by exploiting conventional 3D ED data collected over a small angular range (usually not suitable for structure solution but useable for lattice parameters determination) or by other sources such as powder X-ray diffraction. Once the experimental patterns have been indexed, the data analysis can proceed as for a conventional 3D ED dataset. This data collection strategy has been tested on ITO NP using the program PETS 2.0[56], which now supports the analysis of serial ED data (see the PETS2 manual for details). Practically more than 800 static (i.e. without precession) ED frames were recorded and used to solve the structure. Data completeness reached 100% (for $\sin\theta/\lambda$=0.8Å^{-1}) with a redundancy higher than the one usually obtained from 3D ED experiment on a single crystal. Note that although the information was truncated for structure refinement, the information limit extends beyond 2.25 Å^{-1} (see **Figure 64**), slightly better than what can be obtained from PED frames. In both cases, whether using precession for 3D ED or not for serial ED, the resolution limit of the collected datasets extends to values that are challenging to achieve with X-ray radiation. This also highlights the high crystallinity of the ITO sample.

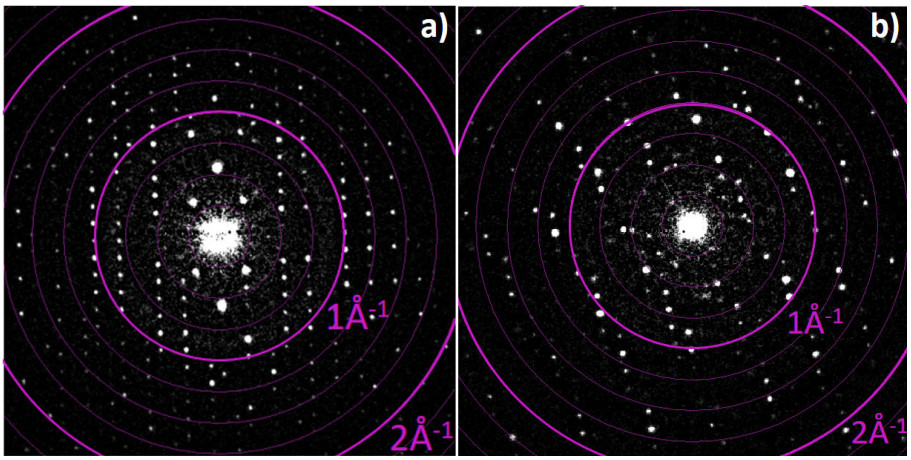

***Figure 64**. Example of diffraction patterns (background subtracted) obtained on 10 nm ITO NPs using in a) precession-assisted 3D ED and in b) static ED. In both cases, the resolution limit goes up to 2 Å^{-1} and even more for static ED (higher than 2.25 Å^{-1}).*

Based on kinematical refinements, it was possible to obtain very good R-values (see **Table 40**). In the case of 'serial ED-like' datasets, it is important to note that merging datasets from multiple single crystals can introduce artifacts such as twinning, depending on the symmetry of the compound. This was observed for ITO, which has a Laue class of m-3 and can produce diffraction patterns resembling those of Laue class m-3m when

twinned. Fortunately, such twinning can be accounted for in the refinement process using Jana2020, leading to a significant reduction in the reliability factors. However, with static ED frames, dynamical refinements are not possible, as they require optimization of both sample thickness and frame orientation. Even though the average thickness of the NPs is known and constant, optimization of frame orientation failed, preventing convergence of the refinement. Despite this, as will be discussed below, the results obtained from this serial ED data are quite good in terms of structural accuracy and could serve as a viable alternative to conventional 3D ED data acquisition. The final model information including atomic positions (x, y, z), occupancy (Occ) and atomic displacement parameters (U) are shown in **Table 41**.

	ITO-06
Tilt Range (°)	812 Static frames
Cumul. Cover. ***(sin θ/λ =0.8Å^{-1})***	100
Averaged Refl. All/Obs.	371/292
Rint (from PETS2)	9.3
Number of refined parameters	9
Robs	7.77
Rall	10.22

Table 40*. Structure refinement results obtained from 'NPs in motion' constituting of static ED frames Results obtained from 'NPs in motion' constituting of static ED frames recorded with an exposure time of 0.5s. Pink background is related to kinematical refinement.*

Space Group Ia$\bar{3}$ (206), a = 10.1043(2) Å					
R(obs)=7.77, R(all)=10.22 , wR(all)=21.98, GoF(obs)=1.71					
measured / observed [I>3σ(I)] reflections=371 / 292, 9 refined parameters					
g_{max} (Å^{-1}) =1.8, Sg_{max} (Å^{-1}) =0.01, RSg_{max}=0.66					
Atom	**x**	**y**	**z**	**Occ**	**U (Å^2)**
In_1	0.5	0.75	0.78139(19)	1.0	0.0069(5)
In_2	0.5	0.5	0.5	1.0	0.0145(9)
O_1	0.4072(8)	0.6409(8)	0.6342(8)	1.0	0.0156(17)

Table 41*. Structural parameters obtained for ITO-06 with a static frame data collection.*

4.6. Accuracy of structure refinements

For the investigation of NPs such as TiO_2 anatase and ITO with sizes ranging between 20 and 10 nm respectively, precession-assisted 3D electron diffraction (3D ED) was applied, enabling the acquisition of high-quality data, and providing detailed information about the accurate structure.

The quality of the 3D ED data allows to access fine structural information, including anisotropic atomic displacement parameters (ADPs) for crystals down to 10 nm. This is the major achievement obtained here. Having access to this detailed structural information, we can now discuss how the structure of 10 nm NPs differ from the bulk structure. Additionally, the results obtain from the PXRD experiments using synchrotron radiation and the results obtained by serial ED will be compared.

To assess the precision of the techniques employed and to determine any deviations in atomic positions between the reference bulk materials and those obtained through precession-assisted ED, serial ED, and PXRD experiments, the COMPSTRU utility of the Bilbao Crystallographic Server was utilized. The server provided values for the average and maximum distance deviations in atomic positions, which are presented in **Table 42**.

	ITO-04	**ITO-05**	**ITO-06**	**ITO-PXRD**	**Anatase-04**	**Anatase-PXRD**
max. dist. (Å)	0.0314	0.0189	0.0351	0.0483	0.0295	0.0174
max. dist. (Å)	0.0081	0.0086			0.0140	

***Table 42**. The darker pink and blue areas represent the average and maxima distance deviation of the atomic positions in comparison with reference bulk materials for both kinematical and dynamical refinement (when applied), respectively. Anatase-04, ITO-04 and ITO-05 are results obtained from PEDT data analysis. ITO-06 is obtained from the analysis of serial ED data. Anatase-PXRD and ITO-PXRD are results obtained from the Rietveld analysis of PXRD data.*

A preliminary examination of **Table 42** shows that, regardless of the technique used, the maximum deviations are below 0.05 Å. This indicates that the structure of these NPs does not differ significantly from their bulk counterparts. This is not entirely surprising, as for NPs of this size, the number of atoms and bonds on the surface is still relatively minor compared to those in the core. Focusing on the 3D ED results, the maximum deviations are approximately 0.03 Å for kinematical refinements and as low as 0.01 Å for dynamical refinements. This indicates that the accuracy of the structure determination is comparable

to that obtained from larger crystals. Furthermore, while kinematical refinements yielded results on par with or slightly better than those from PXRD, the accuracy achieved through dynamical refinements clearly surpasses that obtained by PXRD.

Regarding ITO-06 (serial ED) results, the deviations with respect to the reference bulk structure are actually lower than those obtained from PXRD data. The accuracy of atomic positions is also comparable to the results obtained from kinematical refinements of precession-assisted 3D ED data confirming that averaging a large number of static randomly oriented ED patterns can produce quality ED datasets suitable for structure analyses.

4.7. Multiple Scattering events and small Nanoparticles

As mentioned earlier, it is common to observe a significant decrease in the calculated R-values (Robs) when employing a dynamical refinement approach compared to kinematical refinement. This is what can be observed in the case of brookite (see Chapter 3), with a value of Robs typically divided by 2 or more in all cases. This serves as a tangible indicator that the analysis of 3D ED datasets using full dynamical refinement was successful, allowing for a more comprehensive consideration of dynamical effects and, ultimately, achieving increased accuracy compared to kinematical refinement. However, upon examination of **Table 38**, only a small difference is found in the R-values obtained for the two refinement methods for ITO (only 3 results are presented here, but this observation is supported by others). A hypothesis to explain these results may be that the size of the ITO NPs is reduced to such an extent that multiple scattering effects are non-existent. Therefore, could it be that with very small NPs, this effect becomes negligible, allowing us to avoid the computationally expensive dynamic treatment of data while still achieving accurate structural resolutions? In the previous section, we demonstrated that accounting for dynamical scattering effects generally leads to more accurate structure refinements. To understand why this does not correlate with a significant drop in the reliability factors and question the extent of multiple scattering events in small NPs, we must revisit the data processing methods used for kinematical and dynamical refinements (see also Chapter 2).

For kinematical refinements, the average of symmetry-equivalent reflections is used, as it is assumed that symmetry-equivalent reflections have identical intensities regardless of

where they were collected during the 3D ED data acquisition. For dynamical refinements, this is not the case, as symmetrically equivalent reflections recorded in different frames of the 3D ED data have no reason to be identical, precisely because of multiple scattering events. By working on symmetrically equivalent averaged reflections, R-values obtained by kinematical refinements are expected to be lower than for “non-averaged data”. As data processing for kinematical and dynamical refinements is different, it turns out that a direct comparison of reliability factors is not possible. In the previous chapter, dealing with larger NPs, going into such detail about the refinement was not necessary because it was evident that the effect of multiple scattering still had significant impact on the Robs values. But to answer the question posed at the beginning of this chapter, we should explore the possibilities for obtaining comparable quantities.

Kinematical refinements on “non-averaged data” can be performed in Jana2020 when importing the data from the same input file as for the traditional refinement. Doing so, we can notice a significant increase in the R-values from 7.9 to 10.1 for ITO-04 and from 6.1 to 8.3 for ITO-05, as illustrated in **Table 43**. With this we already obtain some more comparable quantities and see a significant decrease in Robs values from 10.1 to 6.4 (ITO-04) and from 8.3 to 4.7 (ITO-05). However, this is still not a fully fair comparison.

As mentioned earlier, dynamical refinements on “averaged data” can’t inherently be performed. To establish an element of comparison, it is nonetheless possible to estimate reliability factors for an "averaged data" situation based on the results obtained on “non-averaged data”. This is not a refinement result, but a post-refinement calculation that use the dynamical refinement results as an input (more details can be found in the article published by Klar *et al.* 2023[100]). Thanks to this insight, it is now possible to compare the results of the two “averaged” refinements (**Table 43**). It is then revealed a decrease of the R-values from 7.9 to 4.3 and 6.1 to 3.3, for ITO-04 and ITO-05 respectively, confirming the presence of dynamical scattering events even for such small nanoparticles.

Nonetheless, as pointed out in a recent article doubts [100] may still arise as to whether these results are a product of the distinct data processing or indeed indicative of a genuine dynamical effect. To firmly answer this question, we can perform a so-called kinematical “frame-based refinement” [100] which does not use any different input files than for a dynamical refinement. The concept of this approach is to artificially decrease the probability of interaction by modeling an electrostatic potential that is multiplied by a

very small factor (reducing the full occupancy values for all atoms up to 0.01). By reducing the atomic occupancy while keeping all other settings of the refinement identical, the effective scattering power of all atoms is reduced and thus the dynamical scattering calculated on such a modified structure is also reduced, resulting in a (almost) kinematical result with the same data and setup as the full dynamical refinement. The result (framed in green **Table 43**) indicates a reduction of the Robs values from 8.5 to 6.4 and 7.3 to 4.7, for ITO-04 and ITO-05 respectively. This confirms once again that dynamical scattering effects are present even for such small NPs and that it is important to consider the dynamical scattering effect to achieve accurate structure determination.

	averaged	**non-averaged**	**frame based non-averaged**	**"averaged"**	**frame based non-averaged**
ITO-04	**7.9**	10.1	8.5	4.3	**6.4**
ITO-05	**6.1**	8.3	7.3	3.3	**4.7**

Table 43. *Robs values obtained depending on the data processing. "Averaged" is used to indicate that an averaging over symmetry equivalent reflections is performed. "non-averaged" when no such averaging is performed. Pink and blue background are related to kinematical and dynamical refinements, respectively. Values in bold are the values usually given for kinematical and dynamical refinements. Values given in purple frames correspond to values that should be the most comparable.*

4.8. Conclusions

In this chapter, we present a ground-breaking achievement i.e. the ability to obtain accurate structure refinements using 3D ED from a single crystal down to 10 nm in size. This is probably not an absolute limit; it may be possible to collect data on even smaller particles if the experimental setup and particle stability allow.

Our primary recommendation for 3D ED data acquisition is to ensure effective dispersion of the nanoparticles on the TEM grid. Another key point is that reducing particle size necessitates increasing the exposure time during data collection to maintain a significant number of observed reflections relative to the total measured reflections. As a consequence, the time required to acquire the datasets using precession-assisted 3D ED is increased, increasing the electron dose received by the sample, which can be a problem

when the stability of the particle is not sufficient. Working in cryogenic conditions, such as cooling the sample to liquid nitrogen temperature, can be an effective option for obtaining high-quality data suitable for accurate structure determination. Although not used here, continuous rotation 3D ED could enable faster acquisition but would require better optimization of data collection and precise tracking of nanoparticle positions throughout the process. Another alternative presented here is the use of serial ED. In our case, we utilized particle motion induced by an external stimulus namely a wave of bubbles propagating through the particle. While this method may be difficult to replicate, 'true' serial ED, where a single frame is captured per crystal, could be a valuable approach for highly beam-sensitive NPs.

Interestingly, we observe the persistence of dynamical scattering effects, albeit reduced, even for a 10 nm particle. This challenges conventional wisdom and reinforces the importance of accounting for dynamic effects to achieve reliable, accurate structure refinements. When this is done, the results are excellent, regardless of the dataset, and are at least equal to or better than those obtained by X-ray powder diffraction. The use of advanced techniques like 3D ED or serial ED enables precise structural analysis, ensuring that even at the nanoscale, the crystalline structure can be accurately determined. This capability is crucial for advancing our understanding of nanomaterials and their potential applications, as will be demonstrated in the next chapter.

CHAPTER 5

CHALLENGES FROM 'REAL LAB LIFE' NPs

In the preceding chapters, detailed methodologies and protocols have been proposed and applied for the collection of data on nanoparticles of varying sizes. These protocols ensure precise and accurate structural resolution of the nanoparticles, which is important for understanding their properties and potential applications. 3D ED method has proven to be exceptionally powerful and effective in providing high resolution structural information, even for very small nanoparticles as tiny as 10 nm. The ability of this technique to solve such minute details is a testament to its precision and usefulness in the field of nanotechnology.

In this chapter, we will continue with the study of NPs, now focusing on samples that fall outside the scope of the so-called "model" samples previously used to test the capabilities of 3D ED. We will discuss the challenges faced in the structural characterization of these materials and attempt to provide responses to the questions that have arisen. Most of them are related to the functionalization of NPs, which often requires the addition of a chemical element that will alter the composition and possibly its structure. While chemists initially aim to synthesize nanoparticles with a specific crystalline structure and desired composition, precisely verifying these details can be challenging and may ultimately reveal that the actual results deviate from their original expectations. We believe that, in addition to other techniques, 3D ED can provide valuable insights. To test this, three cases are discussed here. The first two cases are related to battery materials: one involves the localization of light elements such as Li (insertion), and the other concerns determining the occupancy of an atomic site shared by two different species (mixed occupancy). The final example will illustrate the contribution of 3D ED when the presence of two chemical elements on the same atomic site leads to the discovery of an ordered structure previously unknown.

5.1. Brookite TiO_2 + Lithium

Compared to other TiO_2 polymorphs, brookite TiO_2 possesses a larger cell volume and higher density than anatase and rutile. Additionally, recent studies have shown that working with this material at the nanoscale improves its electrochemical properties due to its lower surface energy. Specifically, it shows a maximum reversible specific capacity of about 60 mA hg^{-1} after 50 cycles[101] and mitigates issues related to volume expansion during Li insertion extraction cycles[102]. In this section, we will study TiO_2 brookite after Li insertion by 3D ED to see if it is possible to locate Li in the structure. This light atom is typically quite difficult to detect by the PXRD technique and even more complicated when working with NPs.

TiO_2 brookite was synthesized in the same manner as explained in Chapter 3, Section 3.2. For Li insertion, a Swagelok cell needed to be assembled. These types of cells are widely used in battery research for testing and evaluating materials because they required only a small amount of synthesized material and are highly efficient. The Swagelok cell (see **Figure 65**) provides a tight seal and a stable environment for the electrodes and electrolyte, making it ideal for the precise and reproducible measurements.

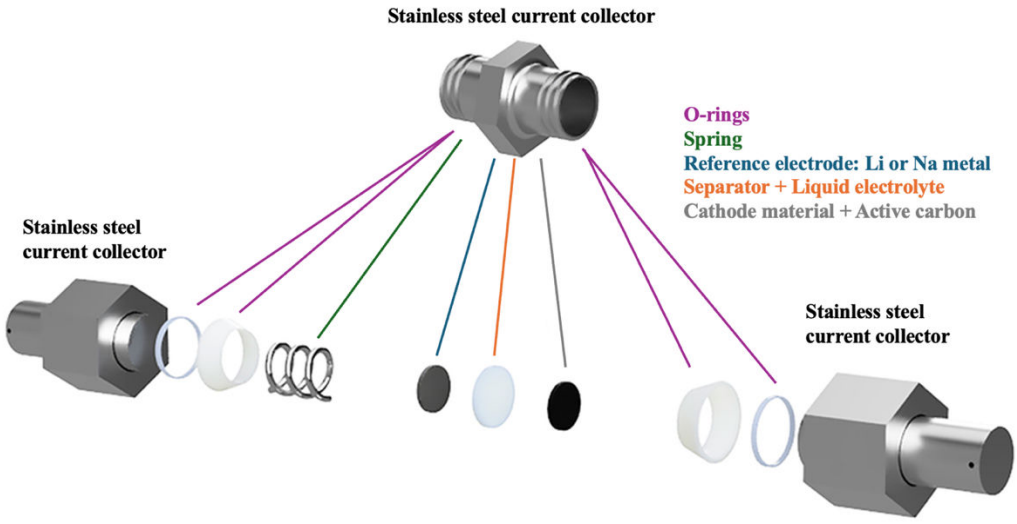

***Figure 65**. Scheme of a Swagelok Cell*

5.1.1. Building up the Swagelok Cell

The steps taken for the preparation of this specific cell are based on the following:

First, mix the material that will act as the cathode with active carbon for at least 30 minutes. Adding C enhance the electrical conductivity due to C is an excellent electrical conductor, helping to improve the electrical conductivity of the anode. This facilitates the movement of electrons through it during the battery´s charge and discharge processes.

Mixing both components for at least 30 minutes helps achieve a uniform distribution of electrical current in the cathode material, avoiding hot spots and ensuring that the material operates more efficiently and uniformly. So far, this mixing step has been done in air. However, from now on, all remaining steps must be performed in an inert argon atmosphere (glove box).

Once the well-homogenized mixture is prepared, the construction of the Swagelok cell begins. To do this, between 8 and 10 mg of this mixture should be added to the bottom, being very careful not to touch the walls to avoid the material leaking and climbing up the walls due to a capillary effect when the electrolyte is added. Next, the separator is added to ensure that the side not facing the mixture from step 2 remains uncontaminated, and approximately 10-14 drops of the appropriate electrolyte are added. Additionally, on the last disc, the desired cation is added, either Li or sodium depending on the experiment.

The final step was to seal the Swagelok cell with pressure to prevent oxygen from entering during the charging or discharging process to maintain the chemical stability of the internal components. Besides, it is important to ensure that the internal structure generated in the previous steps remains stable.

5.1.2. Electrochemical Measurements

Electrochemical measurements were carried out using EC-Lab software, which allows controlled cycling of the material of interest.

The steps taken for the preparation of this specific cell are based on the following:

Cell characteristics: In this window, the characteristics of the cell need to be specified, and information about the material used as the cathode (in this case, TiO_2 brookite) and

the intercalated ion must be added. With all this information, the theoretical capacity and the battery capacity can be calculated (**Figure 66**, pink box).

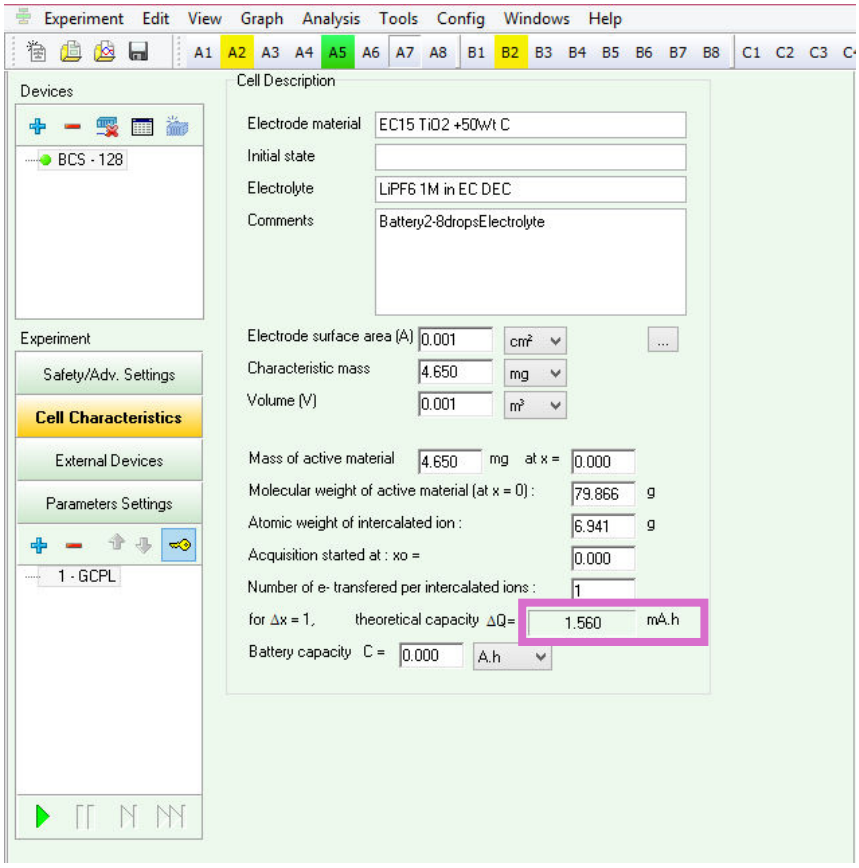

***Figure 66**. Ec-Lab software window to calculate the theoretical capacity based on the mass of TiO_2 brookite used as an anode, it´s molecular weight, and the atomic weight of the active material (Li).*

Parameters settings: This tab allows you to create the sequences of the program that will be applied. There are two sequences. The first sequence (sequence 0) is used to give the battery time to stabilize. It is possible to let it stabilize for a certain period of time by varying the t_R value, or just instruct the software to move to the next step if the potential variation with time is less than the specified value. As soon as one of the criteria is reached, the next sequence will start.

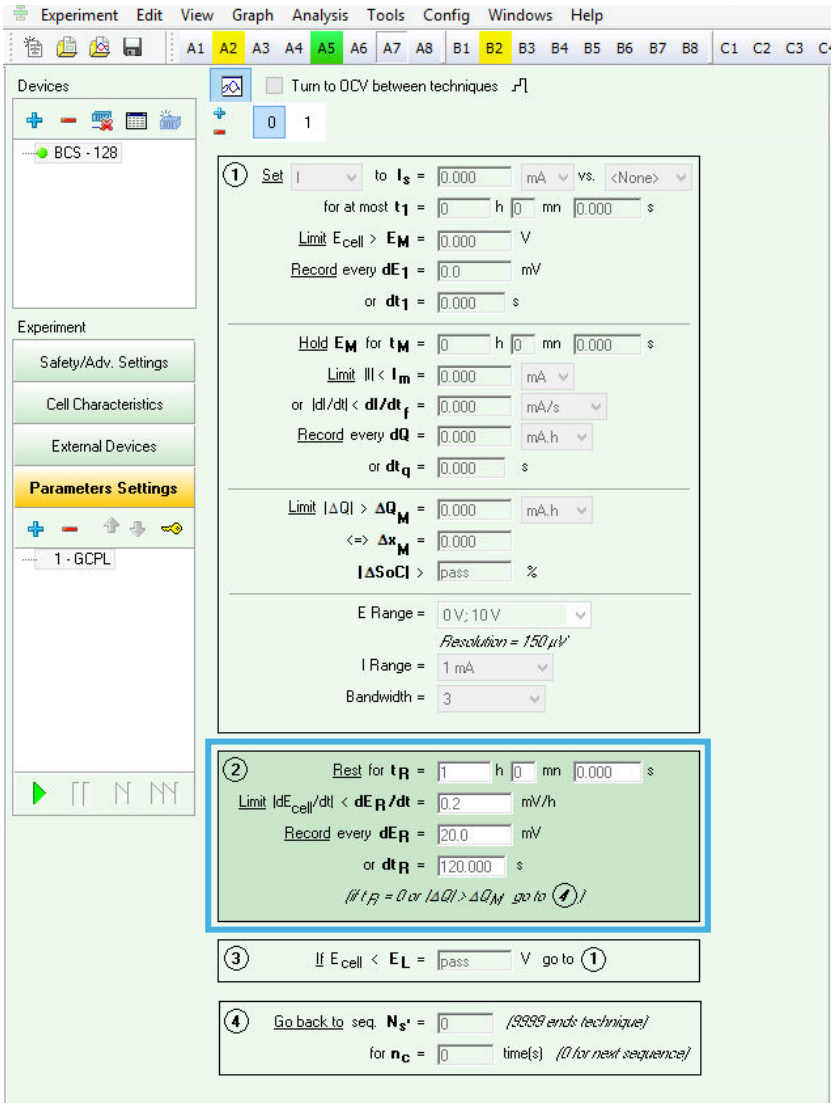

Figure 67*. Ec-Lab software window to set working conditions for sequence 1. The important parameters to set is the blue box for stabilize the cell before the cation insertion.*

For sequence 2 (see **Figure 68**, tab 1), it is necessary to specify the current you wish to impose. For example, if you want to extract a Li ion over 20 hours, corresponding to a C/20 rate, you can divide the theoretical capacity calculated in the 'Cell Characteristics' tab by 20. Additionally, you need to indicate when to stop applying the current, which can be done either by setting a specific period of time or until a certain potential is reached. If you aim to reach a certain potential, set a very long time so that this time criterion becomes negligible. Next, select the criteria for recording the data. It is possible to hold the desired potential for specific duration or until the current required to maintain if falls below the value entered. Finally, you can instruct the software to move to a specific sequence once the current one is completed and to perform multiple cycles.

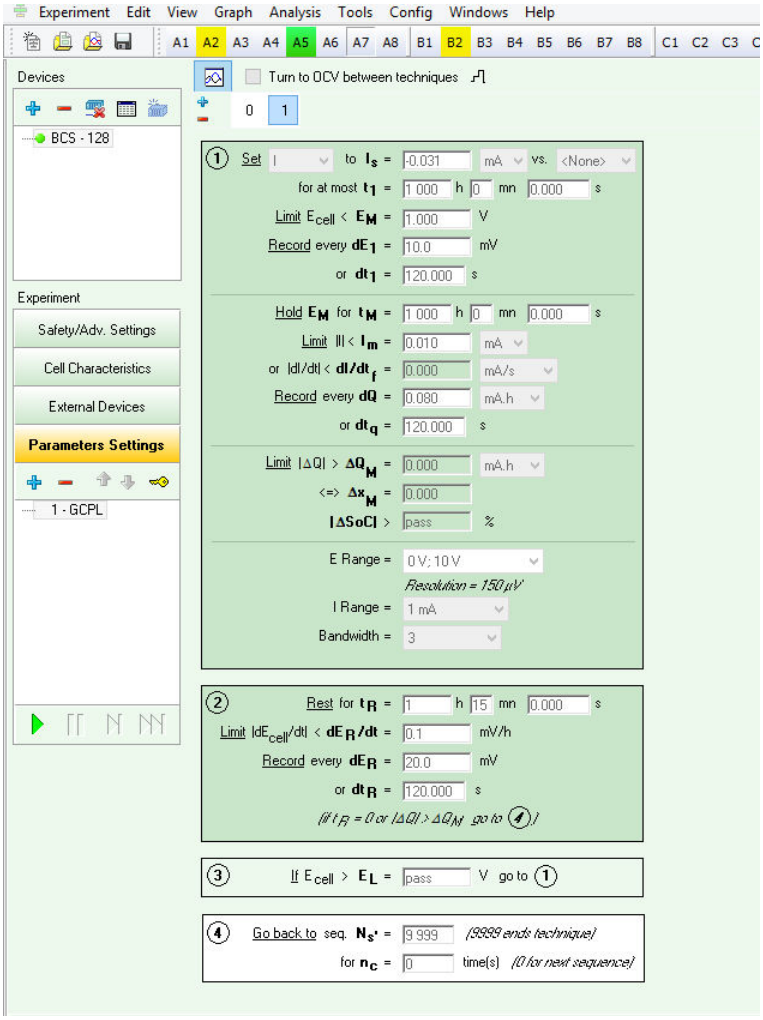

Figure 68. *Ec-Lab software window to set working conditions for sequence 2. Here all the important parameters for Li insertion should be adjust.*

First, Brookite TiO_2 was mixed with activated carbon in a 50% ratio for 30 minutes. Next, this mixture was transferred to the glove box, and the Swagelok cell assembly began. Since this cell was of small dimensions, between 8 and 10 mg of the mixture was more than sufficient for the experiment. Li was used as the intercalated ion, so the parameters to be filled were as follows:

The characteristic mass is the mass of the active material, which in this case is 4.650 mg. This value corresponds to the total amount of Brookite TiO_2 in the mixture. For instance, if the battery is filled with 9.3 mg of the mixture, and the mixture consists of 50% Brookite TiO2 and 50% activated carbon, the characteristic mass will be 4.65 mg. The molecular weight of active material (TiO_2) was 79.86 g/mol and the atomic weight of intercalated

ion (Li) was 6.941g/mol. The theoretical capacity was calculated based on all these parameters, obtaining a value of 1.856 mA/h.

Moving to the second window of the program (sequence 0), we wanted the battery to stabilize for 1 hour, so the value of t_R will be set to that time.

Finally, in the last step, it was important to adjust the current. This value was calculated as C/x, where C is the theoretical capacity (1.856 mA/h), and x is the number of hours required to insert the Li. Different speeds were tested, however the one that gave the best results was C/50.

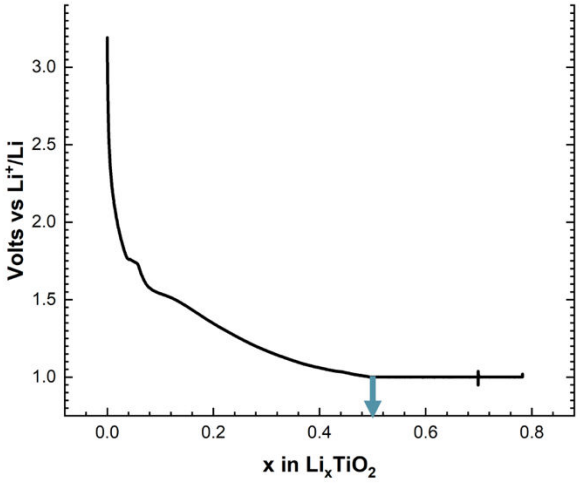

***Figure 69**. Representation of the Lithium insertion versus applied voltage. When the curve starts to be flat, no more Lithium is inserted. At this point (blue arrow) we can consider it the maximum value achieved for Lithium intercalation in the anode material (TiO_2 brookite).*

At this stage, it was crucial to insert as much Li as possible into the TiO_2 brookite structure, where the maximum amount achieved and confirmed through electrochemical measurements was around 0.5 Li per unit formula (see **Figure 69**, blue arrow). It is important to mention that there were other attempts to increase the amount of intercalated lithium by varying the preparation of the Swagelok cell, the percentage of active carbon in the mixture with TiO_2 brookite, the amount of electrolyte or even the speed for the intercalation rate. However, none of these efforts improved upon this example.

5.1.3. 3D Electron Diffraction for Li_xTiO_2

The first crucial step to consider is the preparation of the sample. It is essential that Li_xTiO_2 does not come into contact with a non-inert atmosphere, as this compound is air-sensitive. Therefore, the grid to be used in the Transmission Electron Microscope (TEM)

must be prepared in the glove box. Additionally, the use of an ultrasonic bath is not feasible, complicating the dispersion within the glove box. Furthermore, only hexane and DMF were available as solvents for preparing the grid, making it impossible to use ethanol, which had been the most effective candidate for dispersing TiO_2 brookite nanorods as discussed in Chapter 3. Nevertheless, both solvents were tested, with DMF showing the best dispersion of the NPs.

The next crucial step involved transferring this grid while maintaining an inert atmosphere from the glove box to the microscope. The only available method was to seal the grid in a vial, cover it with paraffin, and transport it to the microscope. The grid was then taken out and deposit in the holder as quick as possible. The goal was then to minimize the time taken to insert the holder and switch on the vacuum system, thereby preserving the sample´s integrity.

The set up used in these experiments is exactly the same as one used for brookite nanorods without Li insertion and PEDT was chosen as a data acquisition protocol for all the experiments in this section. Initially, we wanted to collect data at room temperature. To prevent contamination under the electron beam, the grids were prepared 2 days in advance to allow the grids to dry completely. At first, data acquisition was relatively straightforward (once agglomeration was avoided), and several datasets were collected using PEDT.

For the preliminary data analysis, PETS2 was used. The reflections were initially indexed with cell parameters similar to those used for TiO_2 brookite, showing no significant differences. Furthermore, the examination of the reciprocal space sections confirmed a P-lattice. An identical structural solution to brookite was found, and both kinematical and dynamical refinements were performed on these datasets.

Since Li is a light atom with only 2 electrons, its electrostatic potential is much lower compared to the other elements present in the structure. Therefore, a detailed examination of the difference Fourier map was necessary. This map represents the difference between the observed electrostatic potential and that predicted by the model. To identify the presence of lithium atoms, we need to look for positive density charge in the map (represented by yellow isosurfaces in the program VESTA[103]. These positive regions indicate that the observed electrostatic potential is higher than predicted, suggesting the presence of atoms or parts of atoms that are not accounted for in the current model.

To determine where Li should be placed, we referred to the structural model presented by Dambournet *et al.* 2011[104] (see **Figure 71**), which combined the Pair Distribution Function with computational methods (ICSD Code: 261746). This reference was the only one available in the ICSD database, and although the occupancy was 0.75 instead of 0.5 (as indicated by the electrochemical measurements), the model proved useful. Li exhibited octahedral coordination with O, with bond distances around 2.0 Å.

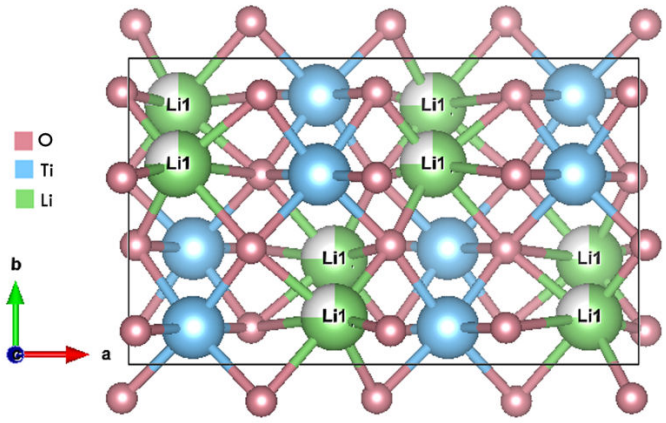

***Figure 70**. $Li_{0.75}TiO_2$ structure model.*

As shown in **Figure 71**.a, no additional density appeared on the difference Fourier map, making it impossible to identify Li using kinematical refinement. However, when examining the difference Fourier map after dynamical refinement, some positive density charges appeared. In most cases, these residual densities appeared either duplicated or disorganized (see **Figure 71**.b). In the clearest case (**Figure 71**.c), these charges were located very close to oxygen, not meeting the typical O-Li distances, hindering the identification of Li.

Since none of the analyzed datasets were favorable, a new experiment was conducted, this time under cryogenic conditions to enhance the stability of Li in the material. Working under this condition arose other disadvantages, such as ice formation. Therefore, obtaining high quality data for structural resolution becomes increasingly tedious. This is why it is important to prepare several grids before each experiment and try to find the best one before cooling down.

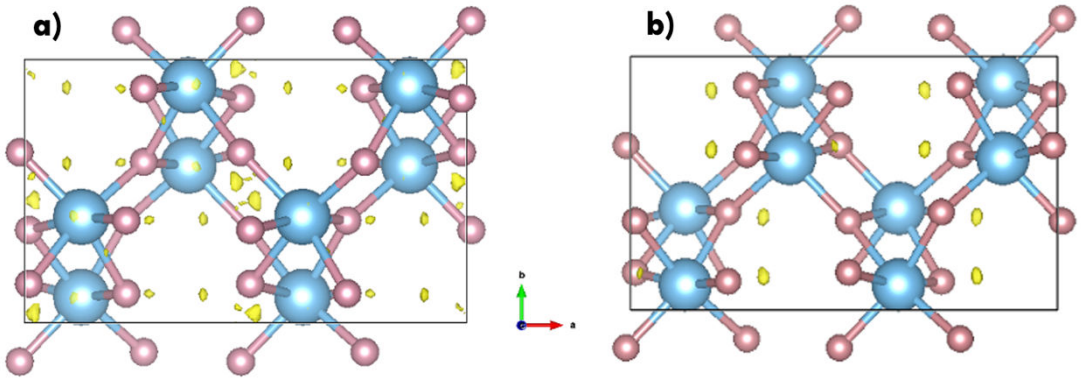

***Figure 71**. Difference Fourier map after dynamical refinement. In a) and b), the positive density charges (yellow circles) are duplicated or very close to the Oxygen atoms, not meeting O-Li distances which are usually around 2.1 Å.*

After collecting several datasets on isolated nanorods, the data were processed in the same way as in the previous experiment. Upon examining the difference Fourier map after kinematical refinement, no additional density were observed (see **Figure 72**.a). When going to dynamical refinement a significant reduction of the Robs value was obtained from 26.38% to 7.20 (see **Table 44**) and the difference Fourier map exhibits positive density charges at distances suitable for O–Li bonding (see **Figure 72**.b). As this data set appeared to be more promising, the Li position was added to the model and refined by considering an occupancy rate based on electrochemical measurements.

	TiO_2
Tilt Range (°)	[-31, + 44]
Cumul. Cover. *(sin θ/λ=0.8Å^{-1})*	71
Averaged Refl. All/Obs.	779 / 471
Rint (from PETS2)	9.05
Number of refined parameters	13
Robs	26.38
Rall	29.25
Refl. All/Obs.	2129 / 1778
Number of refined parameters	75
Robs	7.20
Rall	7.90

***Table 44**. Statistics and refinement results for TiO_2 without inserting Li in the refinement. Kinematical and dynamical refinements are presented in the pink and blue part, respectively.*

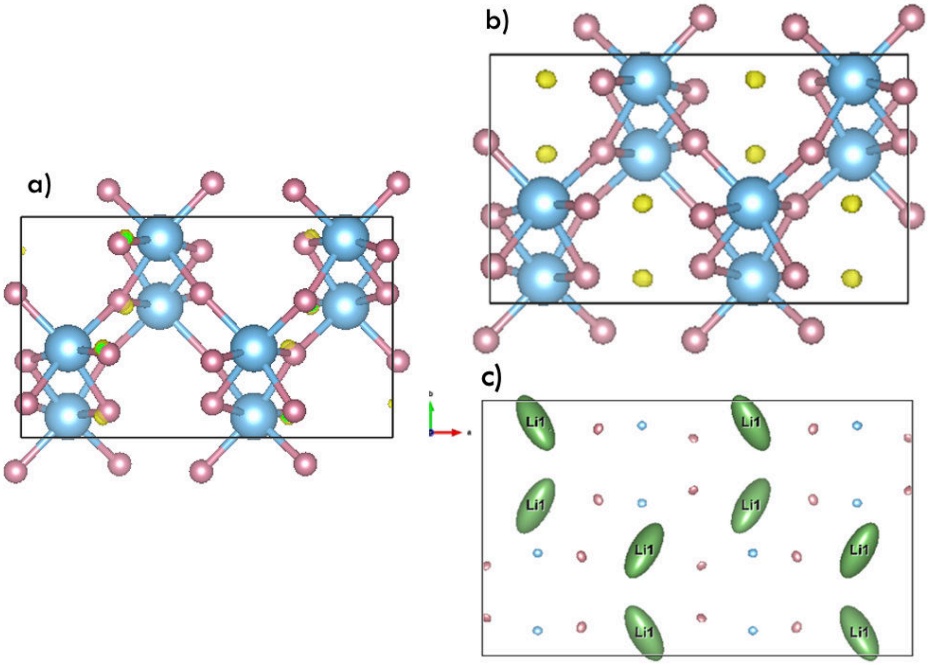

***Figure 72**. a) Difference Fourier map after kinematical refinement. The positive density charges just visible for Ti and O atoms. b) The positive density charges (yellow circles) are in a position suitable for O-Li bonding which are usually around 2.1 Å. c) The yellow circles were replaced for Li and a final structure with large ADP values was obtained.*

The $Li_{0.5}TiO_2$ structure shows a lower Robs value, thereby improving the fit of the model without Li. Combining this reduction in the Robs value with the appearance of clear positive density charges in the difference Fourier map, we can confirm the presence of Li and, therefore, its detection by 3D ED is genuine. The details for the final structural model are shown in **Table 45**. The presence of large atomic displacement parameters for the Li atom (see **Figure 72**.c) is not entirely surprising given the potential mobility of Li within the structure. Bond Valence Sum (BVS) calculations indicate a formal valence of 4.135(9), 2.49(3), 2.34(2), 1.40(8) for Ti, O_1, O_2 and Li respectively, in fairly good agreement with expected values.

In this first example we are close to the limit of what can be achieved with 3D ED and the detection of light atoms. We must therefore be very careful not to over-interpret the residuals observed on the Fourier difference maps. Ideally, several datasets should be collected with concordant results so that we can be confident of the validity of the results. In any case, the relevance of the proposed model must always be validated by chemical

considerations, such as knowledge of the distances classically obtained for the type of compound being studied, or BVS calculations.

Space Group: Bbmm(63), a = 9.1327(1) Å, b = 5.4241(16) Å, c = 5.1258(16) Å					
R(obs)=7.04, R(all)=7.75 , wR(all)=16.72, GoF(obs)=4.27					
measured / observed [I>3σ(I)] reflections=2128 / 1777, 84 refined parameters					
g_{max} (Å^{-1}) =2, Sg_{max} (Å^{-1}) =0.01, RSg_{max}=0.4 steps = 96					
Atom	**x**	**y**	**z**	**Occ**	***U* (Å^2)**
Ti_1	0.37105(8)	0.59775(15)	0.13635(11)	1.0	0.00370(17)
O_1	0.50924(19)	0.3523(4)	0.1843(3)	1.0	0.0038(4)
O_2	0.2693(2)	0.6109(4)	0.4632(3)	1.0	0.0051(4)
Li_2	0.0376(5)	0.088(19)	0.243(16)	0.5	0.15(4)

ADP anisotropic parameters (Å^2)						
Atom	U_{11}	U_{22}	U_{33}	U_{12}	U_{13}	U_{23}
Ti_1	0.0046(3)	0.0036(3)	0.00290(19)	0.0000(3)	0.0002(2)	-0.0004(2)
O_1	0.0045(7)	0.0037(8)	0.0032(4)	0.0008(6)	0.0000(4)	0.0020(5)
O_2	0.0049(7)	0.065(9)	0.0037(5)	0.0009(6)	-0.0010(5)	-0.0004(6)
Li_2	0.07(4)	0.15(11)	0.22(5)	-0.06(4)	-0.03(6)	0.08(7)

***Table 45**. Final model for $Li_{0.5}TiO_2$. Atomic positions (x, y, and z), Occupancy (Occ) and Uiso value are presented.*

5.2. Pseudo brookite $MgTi_2O_5$, mix occupancy

Continuing the research to find a material that acts as an anode for Li^+ and Na^+ intercalation, $MgTi_2O_5$ (pseudo brookite) will be presented. In its bulk form, this material was capable of intercalating 0.8 Li^+, but none of the lithium could be reversibly extracted. However, when the material was reduced to the nanoscale, it was able to intercalate 2.1 Li^+, and 1 Li^+ could be reversibly extracted as is reported by Anji Reddy *et al.* 2008 [105]. This improvement in performance enhances the material's potential as an anode for the intercalation of other cations, such as sodium, which are commonly used in the battery industry.

Understanding the detailed structure of this compound is crucial for comprehending its properties and achieving greater control when using it as an anode material. This

compound crystallizes in an orthorhombic unit cell with a pseudo brookite structure and a Bbmm space group. Its distinct characteristic is that the lattice parameters are highly sensitive to the degree of disorder [106], as the cation distribution within the structure is temperature-dependent[107]. All cations occupy two nonequivalent, highly distorted octahedral sites, M1 and M2, with M1 being larger and more distorted than M2 (see **Figure 73**). The polyhedral linkage of M1 and M2 is defined by complex edge-sharing. The larger Mg^{2+} ions tend to occupy the more distorted M1 sites, while the smaller Ti^{4+} ions generally prefer the less distorted M2 sites. One of the challenges with this sample is that the occupancy rate of these two sites can vary depending on the thermal history of the sample.

5.2.1. $MgTi_2O_5$ Model

The synthesis method for this material followed the procedure proposed by Selvamani *et al.* 2021[108], utilizing a hydrothermal process. This material was synthesized in the CRISMAT Laboratory by Edma Bigard in the form of NPs, allowing for better accommodation to stress generated by the insertion of Li^+ (or Na^+) ions, as well as a reduced diffusion path for these ions.

The first step involved preparing an aqueous urea solution by dissolving approximately 12 g of urea in 30 mL of distilled water, resulting in a solution with a concentration of around 6.66 mol L^{-1}. In this same solution, 3.84 g of magnesium nitrate (II) hexahydrate were dissolved. Simultaneously, a second solution was prepared by mixing 40 mL of ethylene glycol with 6 mL of titanium isopropoxide in a 250 mL flask. Both solutions were then combined under constant stirring at 90°C for 24 hours. The resulting product was recovered, washed with distilled water, and dried in an oven at 60°C. Finally, the product was calcined at 600°C for 2 hours, yielding $MgTi_2O_5$ NPs with heterogeneous sizes, around 30 nm.

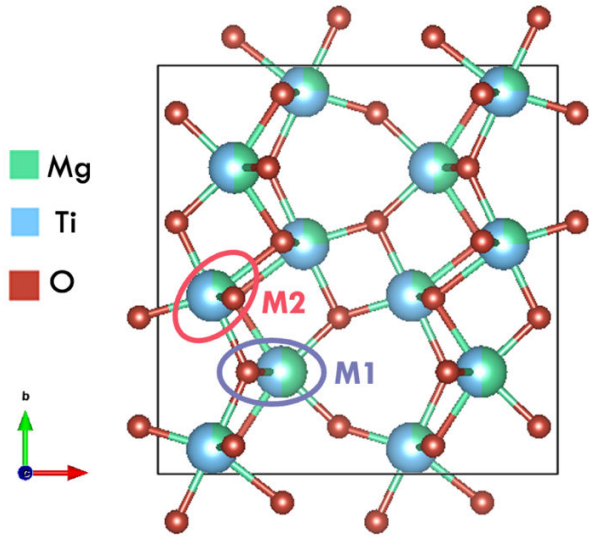

***Figure 73**. Representation of $MgTi_2O_5$ reference structure from ICSD database (Code51022). In purple, the M1 site, while in pink, the M2 site is represented.*

Space Group: Bbmm, *a = 9.7597(4)* Å, *b* = 9.9789(4) Å, *c* = 3.7478(3) Å					
Atom	**x**	**y**	**z**	**Occ**	**Biso**
Ti_1	0.80855(6)	0.25	0	0.485(5)	0.60(3)
Mg_1	0.80855(6)	0.25	0	0.515(5)	0.60(3)
Ti_2	0.13571(3)	0.43679(4)	0	0.757(5)	0.58(2)
Mg_2	0.12571(3)	0.43679(4)	0	0.243(5)	0.58(2)
O	0.22445(21)	0.25	0	1.000	0.99(4)
O	0.04705(13)	0.88376(16)	0	1.000	0.98(3)
O	0.31135(15)	0.93042(15)	0	1.000	0.86(3)

***Table 46**. Structural parameters of $MgTi_2O_5$ from ISCD reference 51022. The atomic coordinates that can be refined are indicated in red. In the blue box, the elemental ratio between Mg and Ti occupying the same atomic position.*

The structure reported by Yang *et al*. 1998 [107] (see **Figure 73**) determined using SC-XRD experiments, was taken from the ICSD database (Code 51022). The structural details shown in **Table 46**, were selected for comparison and correspond to the case where $MgTi_2O_5$ was synthesized at highest temperature ($1400°C$) [107]. However, as our synthesis conditions and the size of our crystals are very different from those used in this study, the results obtained by 3D ED on NPs may differ.

5.2.2. PXRD Characterization

PXRD data were collected using a MiniFlex 600 diffractometer equipped with a Cu X-ray tube working at 40 kV and a D-Tex Ultra detector. Rietveld refinement was carried out using Jana2020 software. Although a decent fit between the observed and theoretical model was achieved (see **Figure 74**), with Robs and Rwp values of 5.18 and 3.49, respectively, the refinement results were somewhat limited in accuracy for fine structural details, particularly in determining the Mg/Ti ratio at both the M1 and M2 atomic sites.

In the model used for the Rietveld analysis, the occupancy rates of the M1 and M2 sites were fixed based on the ICSD 51022 reference and were not refined. Under these conditions, it is possible to refine the atomic positions, but the atomic displacement parameters (ADPs) cannot be reliably obtained, requiring them to be constrained to a value of zero to prevent them from becoming negative. Since there is a strong dependence between ADPs and atomic site occupancy, the absence of positively defined ADPs (see **Table 47**) is a strong indication that this PXRD data are not of sufficient quality to allow an estimation the Mg/Ti ratio. Similarly, the atomic positions show some deviation from the initial model, resulting in an even more distorted environment for the M1 and M2 sites.

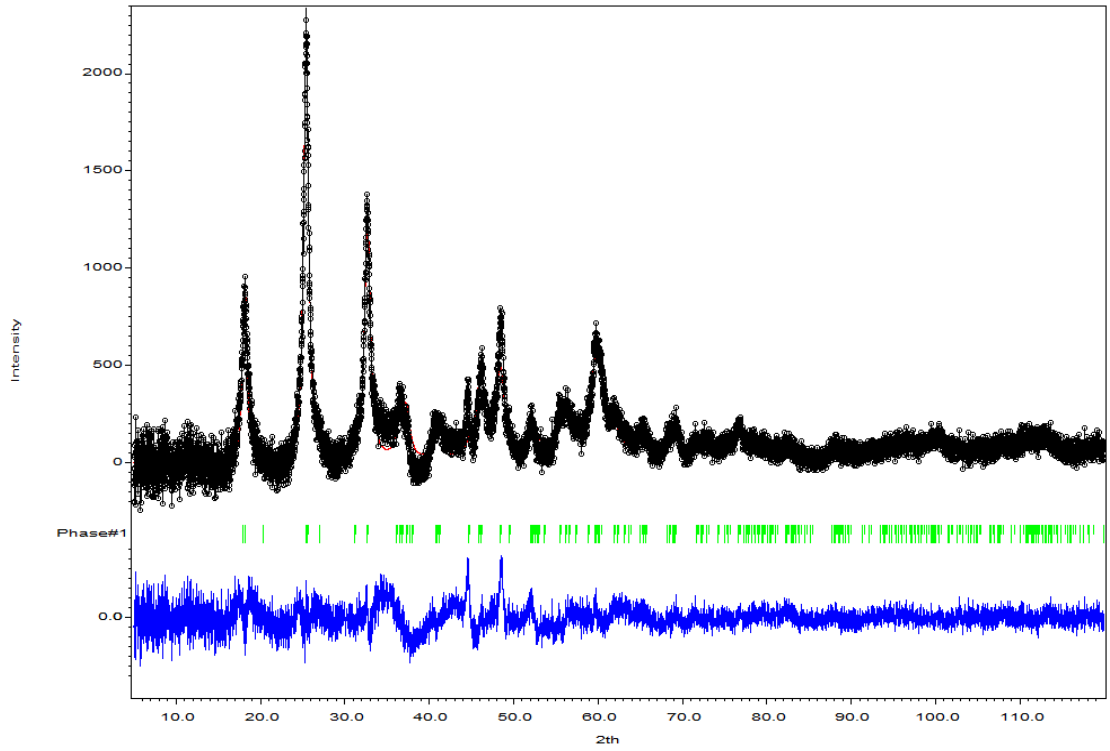

***Figure 74**. Plot of the Rietveld Refinement of $MgTi_2O_5$ against PXRD data. The observed data (black line), calculated pattern (red points) and the difference (blue line). The green lines correspond to peaks at the Bragg position.*

Space Group: Bbmm, *a* = *9.7663(31)* Å, *b* = 9.9409(24) Å, *c* = 3.76155(9) Å					
number of reflections=188; number of refined parameters=10; R_{obs}=5.18; R_{wp}=3.49					
Atom	**x**	**y**	**z**	**Occ**	**U(Å^2)**
Ti_1	0.8163(8)	0.25	0	0.485	0
Mg_1	0.8163(8)	0.25	0	0.515	0
Ti_2	0.1307(5)	0.4251(6)	0	0.757	0
Mg_2	0.1307(5)	0.4251(6)	0	0.243	0
O	0.260(2)	0.25	0	1.000	0
O	0.0538(15)	0.8884(11)	0	1.000	0
O	0.2938(11)	0.928(2)	0	1.000	0

***Table 47.** Structural parameters of MgTi2O5 from Rietveld refinement of PXRD data*

While better PXRD data may have been obtained with a different experimental setup, the determination of the Ti/Mg ratio from PXRD is not as straightforward when dealing with NPs, making it difficult to obtain reliable results.

5.2.3. 3D ED on $MgTi_2O_5$

As demonstrated throughout this thesis, 3D ED is a highly effective technique for obtaining precise structural information in NPs. Therefore, a PEDT experiment was performed on this compound to try to accurately determine the elemental ratio.

A TEM grid was prepared with the aim of maximizing the dispersion of the NPs. Since this compound did not exhibit any stability issues in a non-inert atmosphere, no special procedures were necessary. Then, the TEM grid was prepared using the standard procedure, which involved diluting the powder in ethanol and using a 30' ultrasonic bath. Additionally, an ion cleaner was applied for 1' to prevent degradation of the carbon film.

As shown in **Figure 75**. a, the NPs appeared highly agglomerated, however, it was possible to find isolated NPs **Figure 75**. b to perform 3D ED experiments using precession-assisted ED data collection protocol. Despite their small size, around 30 nm, the NPs did not exhibit beam sensitivity and could be studied at room temperature using the standard tomography holder. Only the dataset with the best refinement statistics will be described in detail.

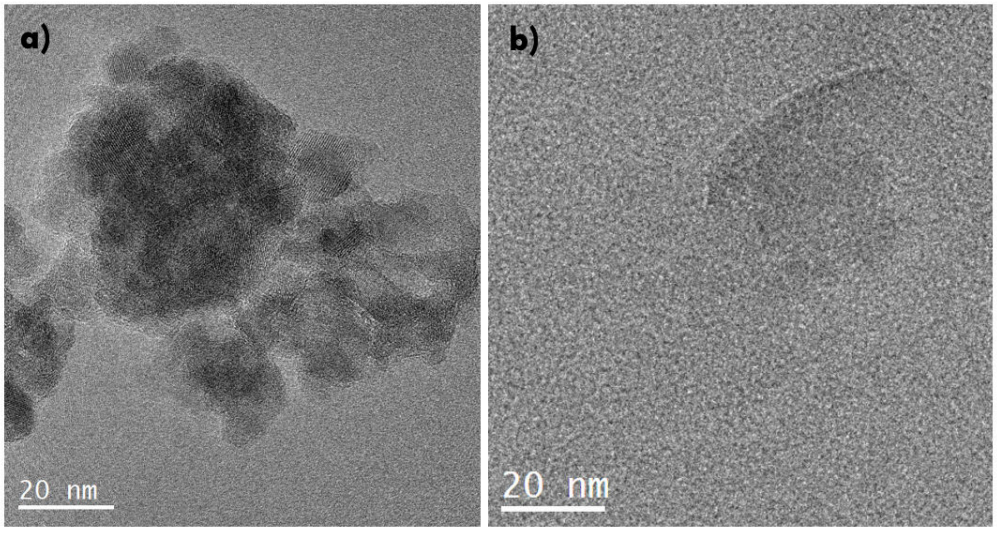

***Figure 75**. a) Overview of $MgTi_2O_5$ nanoparticles in a TEM grid. b) The isolated NP that led to the best statistical results.*

The data processing involved using PETS2. Initially, the reflections were indexed with orthorhombic symmetry, using cell parameters a = 9.7974(72) Å, b = 9.9944(71) Å, and c = 3.7640(16) Å. A B-centering lattice was confirmed after examining the reciprocal space sections. Although the standard settings correspond to space group Cmcm, they

were changed to Bbmm to allow for comparison with the reference structure. The structural solution in Jana2020 was achieved. The challenge with this material was to obtain sufficient high-quality data to allow free refinement of the occupancy of the atoms in the M1 and M2 sites and to obtain positively defined ADPs values for each atom, thus ensuring the reliability of the results.

First, the kinematical refinement of the structural model was carried out with the obtention of a very good Robs value of 10.7%, which is not so common for kinematical refinement (as I could judge from my PhD work). The atomic positions and ADPs were initially refined, with the occupancy of Ti_1, Mg_1, Ti_2, and Mg_2 fixed at the reference structure values of 0.485, 0.515, 0.757, and 0.243, respectively. As the ADPs showed some reasonable values, the model was further refined to include occupancy. The results obtained were promising and are actually an example of how kinematical refinement alone can sometimes produce surprisingly good results (see **Table 48**). However, as discussed throughout this thesis, accounting for the multiple scattering events and performing dynamical refinement improves refinement statistics, leading to a more precise final structure. Therefore, despite the favorable results from the kinematical refinement, dynamical refinement was conducted with a reduction of Robs value to 6.9%. The specifications for the final structural model are shown in **Table 49**.

Space Group: Bbmm(63), a = 9.7974(72) Å, b = 9.9943(71) Å, c = 3.7640(16) Å					
R(obs)=10.74, R(all)=11.23 , wR(all)=27.14, GoF(obs)=2.88					
measured / observed [I>3σ(I)] reflections=213 / 199, 15 refined parameters					
g_{max} (Å^{-1}) =1.6, Sg_{max} (Å^{-1}) =0.01, RSg_{max}=0.66, steps = 126					
Atom	**x**	**y**	**z**	**Occ**	**U (Å^2)**
Ti_1	0.6909(4)	0.75	0.5	0.541(2)	0.0062(13)
Mg_1	0.6909(4)	0.75	0.5	0.459(2)	0.0062(13)
Ti_2	0.3628(3)	0.5636(2)	0.5	0.730(12)	0.0072(10)
Mg_2	0.3628(3)	0.5636(2)	0.5	0.270(12)	0.0072(10)
O_1	0.5478(7)	0.6161(7)	0.5	1.0	0.0153(14)
O_2	0.8101(6)	0.9284(5)	0.5	1.0	0.0087(13)
O_3	0.7628(9)	0.75	0	1.0	0.0102(16)

***Table 48**. Structure model details for $MgTi_2O_5$ after kinematical refinement. The atomic positions, occupancy and Atomic displaced parameters were refined freely.*

Space Group: Bbmm(63), a = 9.7974(72) Å, b = 9.9943(71) Å, c = 3.7640(16) Å					
R(obs)=6.89, R(all)=8.17 , wR(all)=14.99, GoF(obs)=3.24					
measured / observed [I>3σ(I)] reflections=1218 / 834, 51 refined parameters					
g_{max} (Å^{-1}) =1.6, Sg_{max} (Å^{-1}) =0.01, RSg_{max}=0.66 steps = 126					
Atom	**x**	**y**	**z**	**Occ**	**U (Å^2)**
Ti_1	0.8106(2)	0.25	0	0.520(9)	0.0062(5)
Mg_1	0.8106(2)	0.25	0	0.480(9)	0.0062(5)
Ti_2	0.13736(14)	0.43643(14)	0	0.740(4)	0.0083(4)
Mg_2	0. 13736 (14)	0. 43643 (14)	0	0.260(4)	0.0083(4)
O_1	0.2394(4)	0.25	0	1.0	0.0118(8)
O_2	0.0483(3)	0.8830(3)	0	1.0	0.0152(6)
O_3	0.3099(3)	0.9287(3)	0	1.0	0.0129(6)

***Table 49**. Final Structure model details for $MgTi_2O_5$. The atomic positions, occupancy and Atomic displaced parameters were refined freely.*

The final results show that for the M1 site, the Ti/Mg ratio is 0.52/0.48, while for the M2 site, this ratio is 0.74/0.26, both with well-defined positive atomic displacement parameters. Additionally, these values were close to the ones observed in bulk, for compounds synthesized at high temperature (1400°) as reported from SCXRD by Yang *et al.* 1998 [107]. Although the results are not directly comparable, taking into account the work presented in the previous chapter, and the low reliability factors, we are confident that we have indeed been able to determine the occupancy of these two different atoms located at the same atomic positions, even from NPs as small as 30 nm.

5.3. $CuSi_2P_3$

5.3.1. Context and motivations

This study was conducted in collaboration with David Portehault, a CNRS researcher at the Laboratoire de Chimie de la Matière Condensée de Paris (LCMCP). At LCMCP, ongoing research on the $CuSi_2P_3$ compound is being carried out as part of the ERC Consolidator Grant project GENESIS and the PhD work of Anissa Ghoridi (2021-2024) at Sorbonne University. The work done at CRISMAT within this PhD work was solely focused on structure analysis.

The motivation for investigating this compound is related with the need to transform CO_2 into high-value chemicals, which is crucial for addressing the energy crisis and environmental pollution in the current era of sustainable development. Currently, the electrochemical conversion of carbon dioxide into feedstocks enables the transformation of waste emissions into valuable products, thus closing the carbon loop. An innovative approach to achieving this is by using tandem cells, which first converts CO_2 into CO and then transforms it into valuable organic molecules, particularly those with C-C bonds, such as ethylene, ethanol, or acetic acid [109, 110].

Since copper is the only metal that can produce a significant fraction of C^{2+} products from CO reduction (COR), it is the most commonly used metal in catalysts. Combining copper with other elements in alloys [111, 112, 113] has proven to be an effective strategy for tuning the selectivity of CO_2 reduction (CO2R) and COR electrocatalysis. This is achieved by controlling both the partial charge of copper ($Cu^{\delta+}$) and the absorption energy of reaction intermediates. Although doping copper with non-metals in small amounts can adjust the selectivity for CO2R, this approach has not been extended to COR. In most cases, the catalytic species are metallic copper with slightly modified local environments and charge states [114].

Designing copper compounds with non-metals could enhance doping techniques by allowing the selection of alternative crystal structures, thereby altering the local geometric and electronic environment of copper catalytic sites. An example of this is the exploration of copper-based nitrides, which have shown unprecedented selectivity in COR for propanol[82] although these nitrides were reduced to metallic copper under COR conditions, making copper the actual catalyst. Therefore, copper nitrides are strongly ionic solids that are prone to reduction.

Increasing covalence could inhibit this reactivity and provide new chemical environments to host copper atoms, thereby creating catalytic sites for the electroreduction of carbon monoxide. This technique could be achieved, for instance, by combining copper with silicon and phosphorous. Nonetheless, ternary compounds of copper, *a fortiori* $CuSi_2P_3$[115,116], have never been assessed in the context of COR electrocatalysis.

One of the key requirements for a suitable electrocatalytic materials is that it exposes a high density of catalytic sites, which necessitates a high surface-to-volume ratio, making nanomaterials the most appropriate. Previous studies have shown that $CuSi_2P_3$ was

exclusively used in high-temperature [116] solid-state reactions, which are not suitable for isolating nano-objects. However, the LCMCP has developed a new synthesis approach to design particles ranging from 50 to 200 nm in size by using inorganic molten salts as the liquid reaction media. In this method, the diffusion of reactants and thus the reaction and nucleation rates are accelerated compared to traditional solid-state processes. The reaction proceeds at 750 °C according to equation 5.1.

$$CuCl_2\,(s) + 3\,Pred(s) + \tfrac{1}{2}\,Na_4Si_4\,(s) \rightarrow CuSi_2P_3(s) + 2\,NaCl\,(s) \qquad (5.1)$$

The Laboratory of Chemistry of Biological Processes at the Collège de France, in collaboration with the LCMCP, was able to measure COR Faradaic efficiency of approximately 70% for C_2 oxygenated molecules (Ethanol and Acetate) at a current density of -150 mA cm^{-2}, achieving a 43% Faradaic efficiency specifically for acetate. These results are highly favorable in the context of COR as they are directly linked to the material's ability to maintain Cu^+ species, even under strongly reductive conditions, compared to more ionic compounds.

Understanding the structure and surface states is crucial for comprehending electrocatalytic properties. To ensure that the catalytic properties can be related to the bulk material, verifications were conducted to confirm that there are no differences in the surface layer in terms of structure and composition. The LCMCP group and collaborators performed HRTEM, STEM-HAADF, STEM-EDS maps, and XPS analyses to ensure this[1]. Specifically, for $CuSi_2P_3$ particles synthesized using molten salts, no deviations in composition or structure were observed at the surface compared to the core of the NPs. Catalytic selectivity is strongly linked to the spatial distribution of copper sites, which are believed to be the active catalytic sites. Therefore, an in-depth knowledge of the crystal structure is crucial for a comprehensive understanding of its properties.

$CuSi_2P_3$ was initially reported in 1961 by Folberth and Pfister [117] and found to adopt zinc blende structure (a=5.25 Å SG: F-43m) with the Cu and Si atoms having a mixed occupancy on one atomic site. Alloying $CuSi_2P_3$ with Si has been reported to produce zinc blende phases with a general formula of $CuSi_{2+x}P_3$ (where x = 1, 2 and 3), but the atomic distribution was not clearly established[118]. For instance, in $CuSi_4P_3$, Cu and P atoms must either statistically share a common position or be distributed across two

[1] These results are not presented in this work but will be detailed in a forthcoming article.

different sites in mixtures of Cu/Si and Si/P. Although these compounds were initially believed to exhibit a random distribution of chemical species across the zinc blende atomic sites, the potential for partial or complete ordering remained a subject of debate. In 2000, Mozharivskyj et al. [119] synthesized crystals of copper silicon phosphide using an iodine gas transport method and investigated them by SC-XRD. They evidence the existence of a commensurately modulated structure that was analyzed as a large superstructure (ICSD#92484 $Cu_{47}Si_{91}P_{144}$ i.e. Cu:Si:P = 1:1.94:3.06) with lattice parameters a = b = 44.510 Å and c = 20.772 Å (SG I-4m2) that exhibits some distinct sites (**Figure 76**.a). This superstructure was derived from a tetragonal substructure (ICSD#92483 $Cu_{0.71}Si_{1.29}P_2$ i.e. Cu:Si:P = 1.06:1.94:3) with parameters a = 3.7092 Å and c = 5.1930 Å (SG: I-4m2) that exhibits only Cu/Si random distribution (**Figure 76**.b). This last tetragonal subcell was retained in 2010 by Wang et al.[120] in a structural analysis that combines both SC-XRD and neutron powder diffraction (NPD).

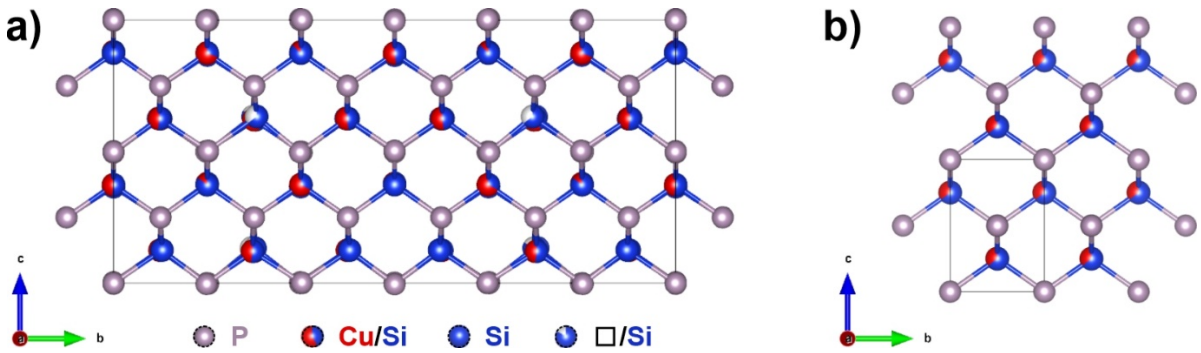

***Figure 76**. a) The supercell exhibits some distinct atomic sites with pure Si, mixed Cu/Si and even vacancy/Si. b) The subcell is derived from the cubic zinc blende structure due to a small difference in a, b, and c parameters. Only a random Cu/Si distribution is obtained.*

Although seemingly contradictory, these studies actually highlight the crucial role of synthesis conditions in determining the presence or absence of Cu/Si ordering. While "$CuSi_2P_3$" crystals prepared via iodine transport at 800°C [118] exhibit a large superstructure that is easily identified by SC-XRD, "$CuSi_2P_3$" crystals synthesized at 1000°C do not show such a superstructure [119].

5.3.2. Molten Salts Synthesis

All reagents were stored in an argon-filled glove box. Copper (II) chloride ($CuCl_2$, 97% Sigma-Aldrich) and red phosphorus (Pred, < 97% Sigma-Aldrich) were used as Cu and P sources, respectively. Na_4Si_4 was synthetized in the laboratory following a reported procedure [121] and was used as both silicon source and reducing agent. All reagents were

used as received. A mixture of LiCl (99.9% Alfa Aesar) and KCl (99.9% Sigma-Aldrich) (LiCl:KCl = 45/55 wt. %) was used as an inorganic solvent. The heat treatment was performed in vertical tubular ovens connected to temperature controllers from the Eraly company. These ovens were calibrated every 100 °C between 100 and 1100 °C. The temperatures we indicate are the effective temperatures in the synthesis crucible.

In a typical batch, $CuCl_2$ (1 mmol, 135 mg), Pred (3 mmol, 93 mg) and Na_4Si_4 (0.575 mmol, 117.3 mg) were mixed with 1.25 g of the eutectic LiCl:KCl mixture (45:55 wt. %). All precursors and the eutectic salt were finely ground at 20Hz for 2min by ball milling (Retsch MM400 ball miller, stainless steel airtight vials of 50 mL, one steel ball of 62.3 g and a diameter of 23 mm). The mixed powder was recovered in an argon-filled glove box and put into a glassy carbon crucible, which was placed into an airtight quartz tube. The quartz tube was connected to a Schlenk line under Ar flow and placed inside a vertical oven. A heating ramp of 10 °C·min−1 was used up to 750 °C followed by a dwell time of 4h, and then the sample was let to cool down until room temperature. To recover the particles, the solid mixture was washed one time with a mixture of H_2O/MeOH (1 :1) and then six times with MeOH by sequences of redispersion, sonication (2 min), and centrifugation (26 000 rpm, 5 min) until the conductivity of the supernatant dropped below 5 $\mu S \cdot cm^{-1}$. The powder was dried several hours under vacuum at room temperature until the pressure dropped below 10^{-3} mbar and then placed under argon atmosphere for further characterization.

5.3.3. PRXD investigation of $CuSi_2P_3$

The first crystallographic analysis after the synthesis is carried out by examining the PXRD patterns, and in the case of a cubic zinc blende structure, the expected patterns is simple. Upon preliminary inspection, the high-intensity peaks observed seem to correspond well with those anticipated for a $CuSi_2P_3$ phase (**Figure 77**). However, it was observed that the peaks in the PXRD patterns often appeared shifted or slightly doubled and did not exactly match a cubic F-centered cell. In addition, some peaks with very small intensities can be detected without being able to clearly associate them with the $CuSi_2P_3$ phase nor an impurity. Importantly for this study, it is worth mentioning that SEM-EDS and STEM-EDS analyses yield Cu/Si ratios of 1:2.1 and 1:1.9, respectively.

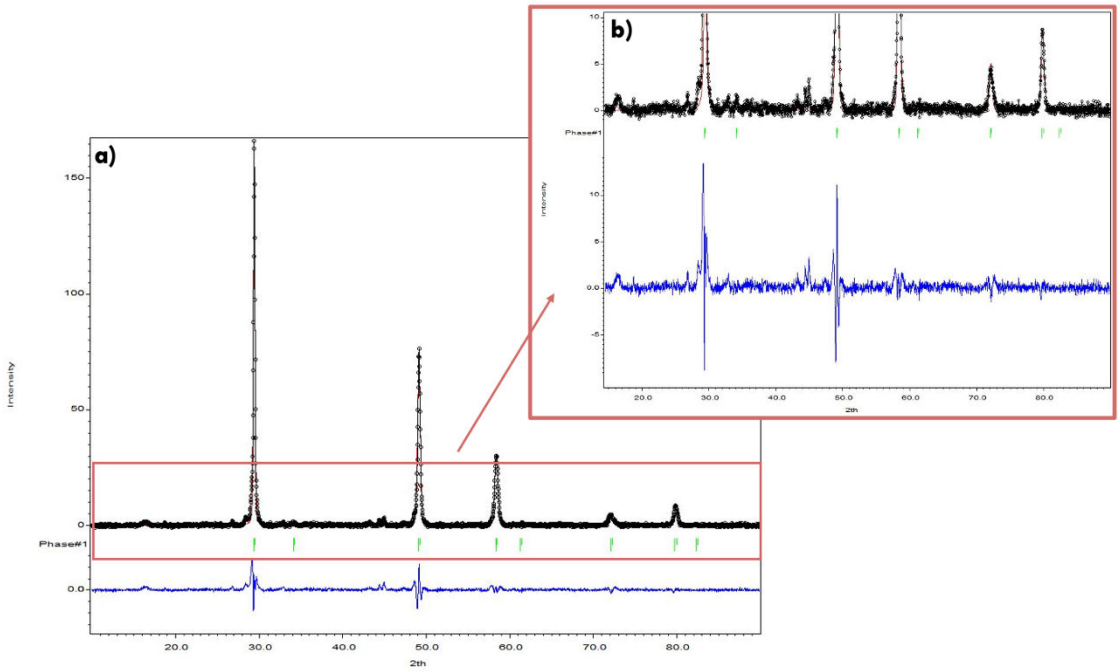

***Figure** 77. a) PXRD pattern of $CuSi_2P_3$ (radiation: Cu Kα). A Lebail profile fitting is performed considering the space group $F\bar{4}3m$ with a=5.226(1) Å. b) Zoomed-in view of the pink region where small unindexed peaks can be observed.*

Based on the bibliographic considerations outlined above, which emphasize a link between the synthesis conditions and the structure of $CuSi_2P_3$, the possibility of stabilizing a sample that exhibits Cu/Si ordering and consequently a superstructure relative to the zinc blende prototype should be explored. To further analyze the formed phase and investigate potential impurities, 3D ED was used to obtain structural information from individual nanocrystals.

5.3.4. 3D ED experiment for $CuSi_2P_3$

We were cautious with this sample as it may oxidize and degrade when exposed to air, necessitating its transport and storage in an inert atmosphere. The first attempt to prepare grids for TEM was therefore carried out inside the glove box where the use of an ultrasonic bath is prohibited. However, avoiding particle agglomeration under these conditions proved difficult, which made it impossible to obtain data from a single crystal. Given this difficulty, we decided to take the risk of preparing the grid outside the glove box in a much faster way, using the ultrasonic bath just for only 5 minutes. The dispersion improved, and although it was still challenging to find isolated crystals, several datasets could be collected.

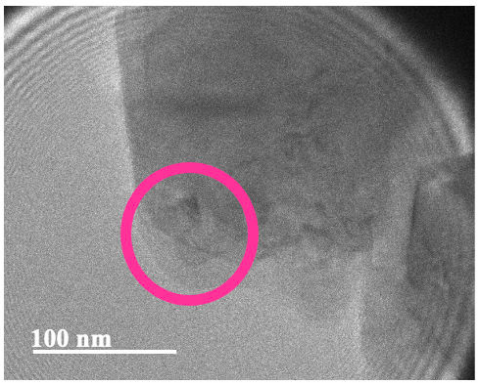

***Figure 78**. Image of a crystal bigger that the beam size (pink circle). Depending on the orientation of the crystal placed on the grid and its tilt axis, the crystal seen on the right side of the image, could interfere into the data acquisition.*

Once the sample was introduced into the microscope, it was observed to be quite stable under the electron beam, reducing the need for cryo-holder. It was also noted that the crystals varied in size and morphology, indicating at first look that the sample was not homogeneous. Additionally, the size of most of the crystals exceeded 100 nm, although few of them were only about 70 nm. When working with crystals larger than the electron beam, we selected a small section of the crystal for analysis (see **Figure 78**). Nonetheless, this approach had a drawback: during tilting, the probe area/volume changes, which can lead to contributions from different domains within the particle, as will be shown later. A total of about 30 datasets were collected on different days, of which about half were sufficiently high quality to proceed with the analysis. This was mainly due to the crystal being covered by another crystal or by the edge of the grid. In both cases, the inability to collect a sufficient number of frames hindered the reconstruction of the reciprocal space, thereby impacting the quality and completeness of the dataset. Despite being inhomogeneous in size and shape, the structures obtained from 3D ED were all consistent with the formation of a $CuSi_2P_3$ phase, though with some variations that will be detailed below.

5.3.5. The prototype zinc blende structure

For only one of the datasets obtained on a crystal with lateral dimensions about 80 nm by 30 nm (**Figure 79**), we found the prototype zinc blende structure. As it can be seen in **Figure 80**, the reflections were indexed using a cubic lattice with a=5.3012(13) Å and a F-centering. Examination of the reciprocal space sections (see **Figure 81**) confirms F centering, with no unindexed reflections present. After integrating the reflections and

importing them into Jana2020 software, the structure solution proceeded successfully with the F$\bar{4}$3m space group, as expected for a zinc blende structure. The statistical analysis for a resolution of 1.89 Å^{-1} in reciprocal space indicated a completeness of 91%, with an Rint of 13.05 for the Laue class m$\bar{3}$m.

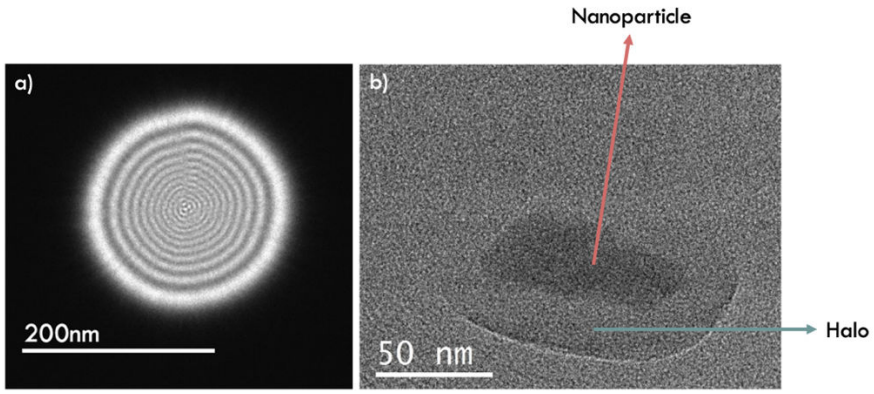

***Figure 79**. a) Beam size of approximately 150 nm used for data collection. b) Isolated NP where a halo around the crystal due to contamination after 3D ED data acquisition can be seen.*

In the case of this zinc blende structure, determining the structure poses no challenge, and the refinement process is minimal since only two atomic sites exist with fixed *x*, *y*, *z* parameters determined by symmetry. Consequently, for the kinematical refinement, only one scale factor and two atomic displacement parameters (ADPs) need to be refined. The interest lies in the fact that one of the atomic sites possesses a mixed Cu/Si occupancy, providing an opportunity to test the efficiency of 3D ED in estimating the ratio of different chemical species sharing a single atomic site. If the sample were composed solely of Si and P, it would be impossible to distinguish between them. However, since Cu has an atomic number twice that of Si, we should be able to determine their ratio through structure refinement.

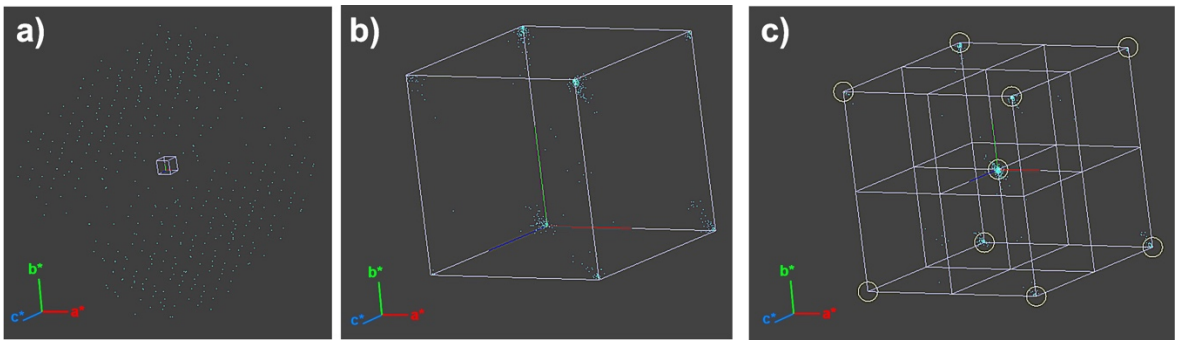

Figure 80. *In the PETS 2.0 program's menu, under the unit cell and orientation matrix options, you can index the reflections and gain insights into lattice centering. a) A 3D representation of the reciprocal space shows reflections in green and the unit cell in purple. b) Reflections can be folded into the unit cell, with indexed reflections appearing at the corners of the unit cell. If unindexed reflections are present in sufficient quantity, they may cluster within the unit cell, indicating a potential issue with the choice of unit cell. c) Folding can be applied in multiples of the unit cell (e.g., 2x2x2) to check for possible lattice centering. In this example, reflection clusters consistent with an F-lattice centering are encircled.*

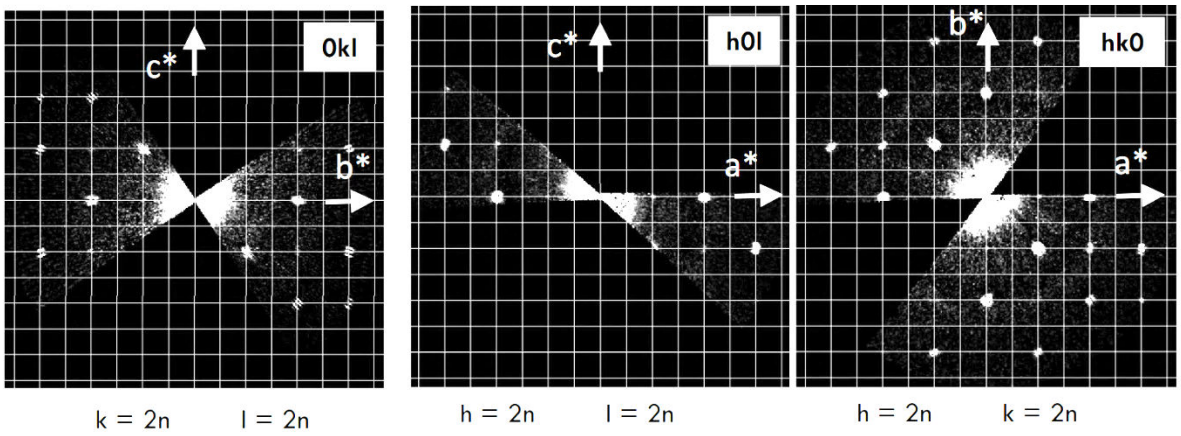

Figure 81*. The 0kl, h0l, and hk0 sections show all reflections as even and consistent with an F lattice centering. In contrast, for the 1kl, h1l, and hk1 sections (not shown here), it is verified that all reflections are odd.*

Regarding kinematical refinement and for testing purposes, we considered three scenarios for the mixed site occupancy: 100% Si, 100% Cu, and the expected Cu/Si = 1/2 ratio. For each refinement, the Cu/Si site occupancy was fixed, and a common ADP parameter was refined. As shown in **Figure 82**.a, the Robs value of approximately 20 obtained for the expected 1:2 ratio is a normal value, and with both ADPs positive, it can be regarded as a decent result. Nonetheless, in **Figure 82**.a, no minimum is observed in the Robs curve, and with a Robs value of 14.75, the solution with 100% Cu occupancy actually appears to be the best. The evolution of Uiso(Cu/Si) is somewhat illogical, as changing the Cu/Si ratio should typically result in an almost linear increase in Uiso, with lower values for 100% Si and higher values for 100% Cu. This simple test indicates that accurately

determining the atomic ratio in a mixed occupancy site remains challenging through kinematical refinement.

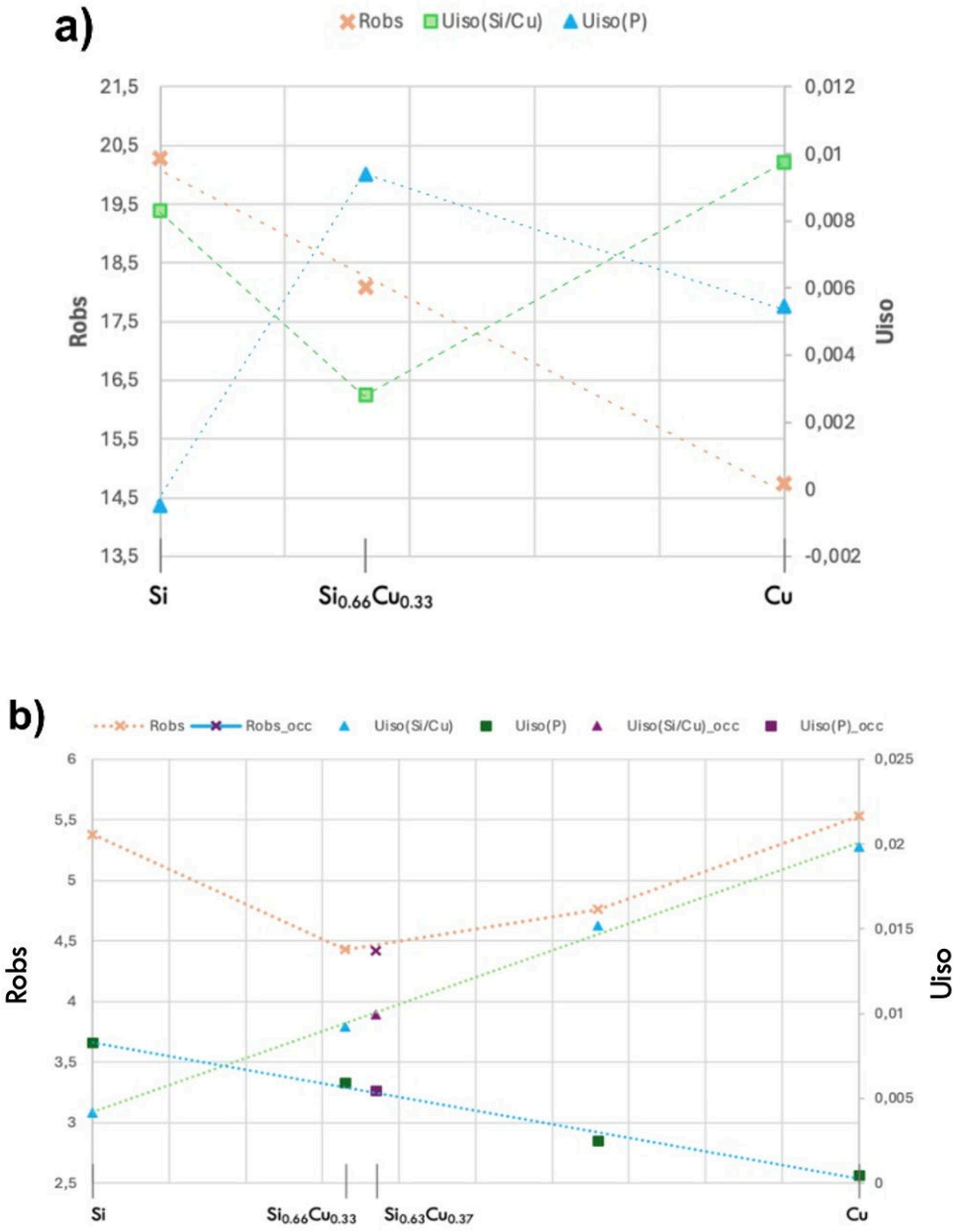

***Figure 82**. Obtained Robs values and Uiso parameters when imposing different ratios for the mixed Si/Cu site for a) kinematical and b) dynamical refinements. In b), Robs values show a minimum near the best match, allowing for refinement of the occupancy ratio. In a), Robs values form a straight line with no minimum. Uiso values, which correlate strongly with occupancy, show a trend in b) but not in a). In b), the purple marks indicate the results when the Cu/Si ratio is freely refined.*

Looking at the results of the dynamical refinement (**Figure 82**.b), as expected, the Robs values are significantly lower than those obtained from the kinematical refinement. This considerable reduction in Robs values underscores the necessity of accounting for

multiple scattering effects in our structural analysis. Additionally, we have now gained the sensitivity needed to obtain pertinent information about the Cu/Si ratio. The Robs value show a minimum with a refined ratio of 0.37(3):0.63(3), which is very close to the nominal 1:2 ratio. The evolution of Uiso(Si/Cu) versus the imposed Si/Cu ratio is also now more logical.

While studying a crystal with the zinc blende structure allows us to test the applicability of 3D ED for investigating fine details in the $CuSi_2P_3$ sample, it is important to remember that this should be considered a marginal case, as only one crystal with this structure was found.

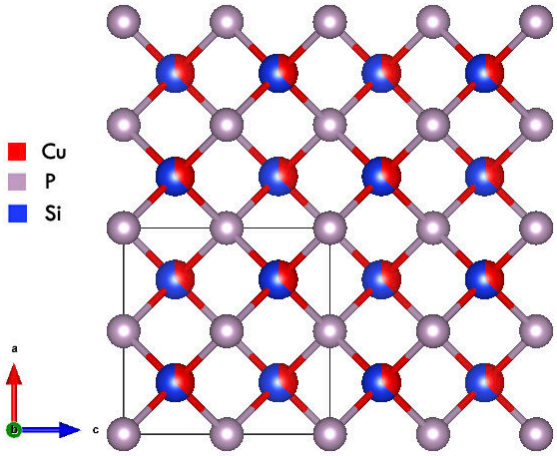

Figure 83. *$CuSi_2P_3$ structure with a fix Cu:Si ratio of 1:2.*

Space Group: F$\bar{4}$3m (216), a = 5.30116(4) Å					
R(obs)=4.42, R(all)=5.67 , wR(all)=11.22, GoF(obs)=2.65					
measured / observed [I>3σ(I)] reflections=902 / 725, 63 refined parameters					
g_{max} (Å^{-1}) =2.1, Sg_{max} (Å^{-1}) =0.01, RSg_{max}=0.66, steps = 126					
Atom	**x**	**y**	**z**	**Occ**	**U (Å^2)**
Cu_1	0.25	0.25	0.75	0.37(3)	0.0099(6)
Si_1	0.25	0.25	0.75	0.63(3)	0.0099(6)
P_1	0	0.5	0.5	1	0.0055(5)

Table 50. *Final structure model details for $Cu_{0.37}Si_{0.63}P$ after. The occupancy and atomic displaced parameters were refined freely.*

Structure type	$CuSi_2P_3$
Temperature (K)	293
Crystal system, space group	Cubic, F$\bar{4}$3m, *(SG: 216)*
***a*, *b*, *c* (Å)**	5.3012(13)
***V* (Å³)**	148.98
Crystal size (nm), thickness	Lateral: 80 x 30[(a)]; thickness 21.8[(b)]
Electron wavelength λ (Å)	0.0251
Electron beam size (nm)	150
Number of frames	61
Tilt range (°)	75
Precession angle (°)	1.4
Resolution sin(θ_{max})/λ (Å^{-1})	0.8
Cumulative coverage (%)	100
Measured,observed[$I>3\sigma(I)$] reflections	902, 725
No. of refined parameters, restraints	63, 1
g_{max} (Å^{-1}), $S_{g,max}$ (Å^{-1}), R_{Sg}, steps	2.1, 0.01, 0.66, 126
***R*(obs), *R*(all), *wR*(all), GoF(all)**	0.044, 0.057, 0.1122, 2.65

***Table 51**. Result of the statistics obtained in Dynamical refinement for the material $CuSi_2P_3$ with a space group F$\bar{4}$3m. Dimensions obtained from (a) TEM image and (b) dynamical refinement.*

5.3.6. Cu/Si ordering in $CuSi_2P_3$?

Except for the outlier described above, all other crystals investigated by 3D ED exhibit extra reflections with respect to the prototype zinc blende structure. This is illustrated in **Figure 84**. where the observed reflections are folded into the cubic zinc blende unit cell (option 'Fold to cell' in the part 'Find unit cell and orientation matrix' of the program PETS2) and viewed along the direction [111] of the unit cell. In **Figure 84**.a we can see that for the zinc blende prototype all observed reflections are folded at the corner of the unit cell which confirms this cell as a good match. In **Figure 84**.b and **Figure 84**.c, two other examples are shown where a part of the observed reflections folded out of the cubic unit cell corner with an indexation rate about 35-40%. Clearly, we need to find another unit cell to account for these extra reflections. At first, we can consider converting the F-centered cubic cell (a ≈ 5.2 Å) to a I-centered tetragonal cell (a=b ≈ 3.7 Å and c ≈ 5.2 Å). As pointed out by Wang et al. [120], for $CuSi_2P_3$ samples synthesized at lower temperatures, the I-centered tetragonal cell provides a better match than the 'cubic' cell, as a true cubic metric is not satisfied (**Figure 85**.a). Nonetheless, this operation does not increase the number of indexed reflections. Looking at the reflections folded into this new unit cell (**Figure 85**.b), some of the extra reflections seems to be accounted for multiplying the b-

axis by 3. The obtained orthorhombic I-centered cell (**Figure 85**.c) with parameters a=3.67 Å, b=11.05 Å and c=5.21 Å is actually equivalent to the one observed in the compound $NiSi_2P_3$[122] that was reported to have Ni/Si ordering. With such a unit cell, the indexation rate increases only marginally. Also, for the projection along [010] direction of the new cell, some unindexed reflections are still present.

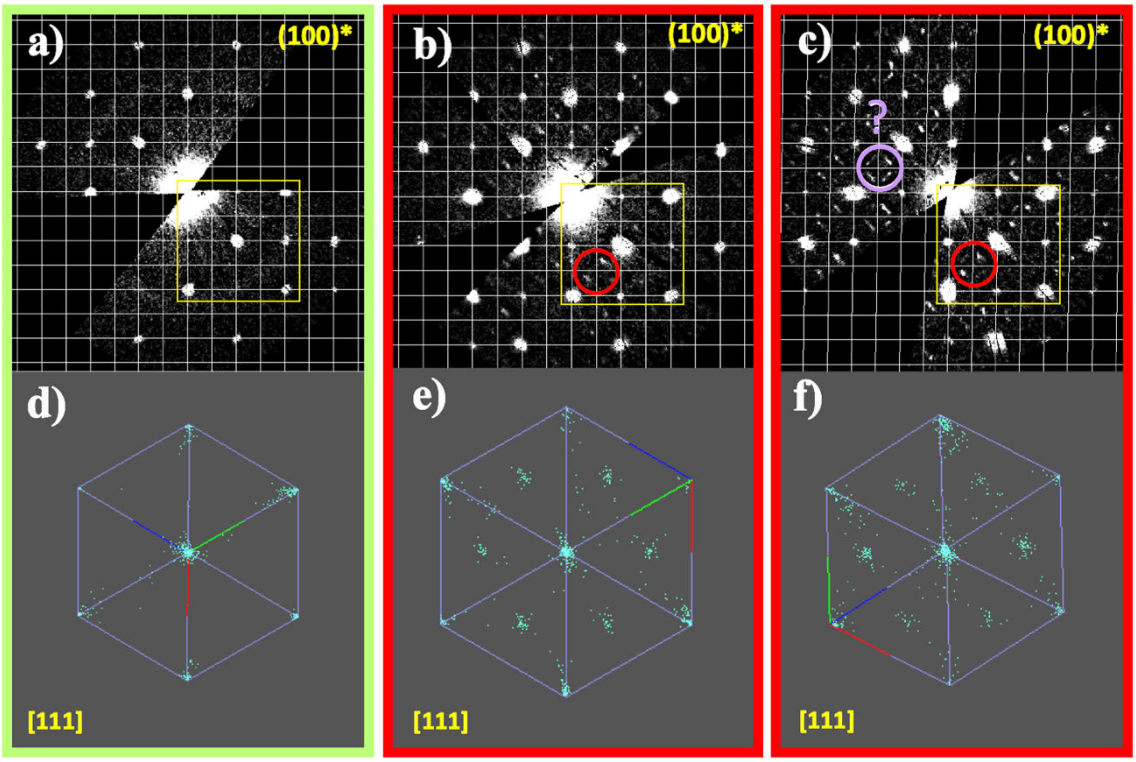

Figure 84. *Upper part: Reciprocal space sections obtained after indexing part of the reflections considering a cubic cell (a~5.2 Å). (a) corresponds to the zinc blende prototype described in the previous section, while (b) and (c) represent the majority of analyzed crystals. For both (b) and (c), extra reflections can be observed compared to (a) (encircled in red). Lower part: In (d), (e), and (f), the reflections are folded into the cubic unit cell and viewed along the [111] direction. Again, extra reflections are emphasized as clusters always located in the same position but with varying intensity from one crystal to another, as illustrated in (e) and (f).*

To have a better idea of what these reflections are and estimate how well (overall) is the new cell a good match for describing the observed reflections, we have reconstructed sections of the reciprocal space (**Figure 86**). By examining the 0kl and h0l sections, it is seen that some weak extra reflections encircled in red are now taken into consideration by the new cell with a b lattice parameter multiply by 3. Now, looking at the h0l section, similar weak reflections encircled in purple are present and not indexed in the new cell. If we imagine we have the presence of twinning with an interchange between a and b direction, then we may be able to explain these extra reflections. Nonetheless, the section

h2l exhibits lines made of both spots and streaks with suggest the presence of some kind of disorder that cannot be accounted for simply considering the new I centered lattice.

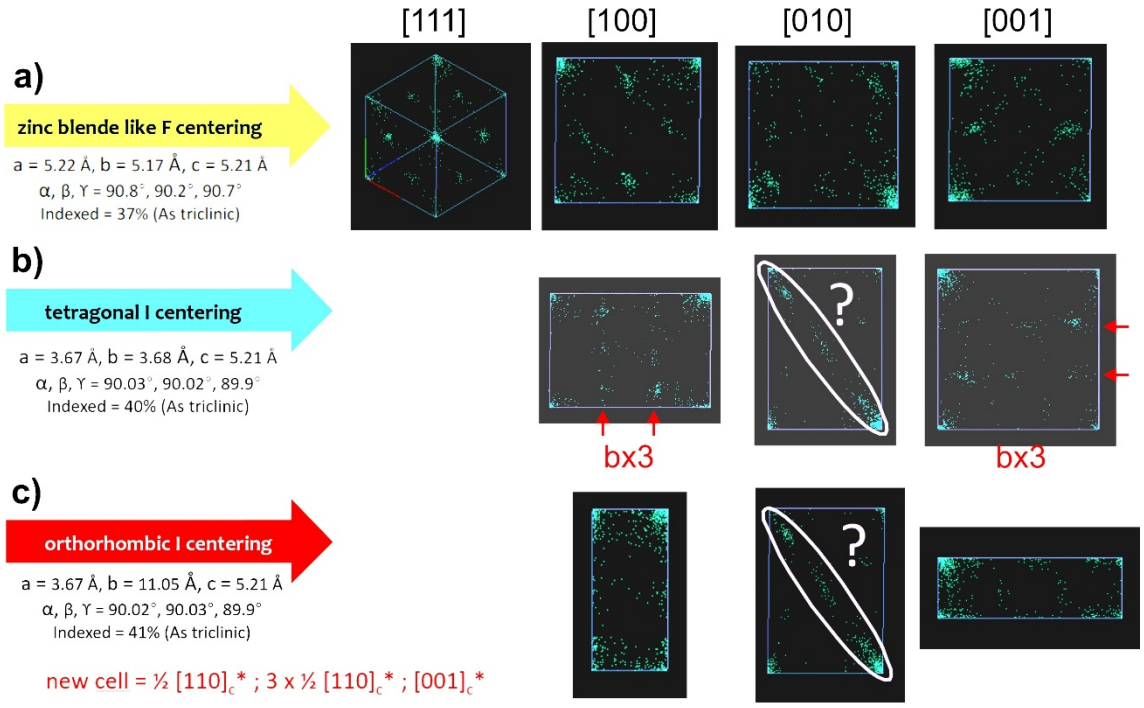

***Figure 85**. Observed reflections after being indexing with a specific geometry in a), b) and c).*

Nonetheless, we pursue to the structure resolution step considering this cell. While it was possible to obtain a structure comparable to the one published for $NiSi_2P_3$ (SG: Imm2), the structure refinements lead to high figure of merits (Robs kinematical = 38% and Robs dynamical = 23%) with negative non defined ADPs. With such results it is impossible to gain proper information about the Cu/Si ratio and a possible Cu/Si ordering. The examination of the reciprocal sections and the low indexation rate already raise some warnings about the possibility of $CuSi_2P_3$ having a structure similar to that reported for $NiSi_2P_3$. Additionally, the structure refinement failed to provide any supporting evidence either. Possible reasons for this failure can lie in the existence of crystal inhomogeneity i.e. only partial ordering is present and/or stacking faults or twinning at a fine scale as the streaks observed in reciprocal space sections seen to corroborate. Another possibility is also to simply consider that the proposed I centered supercell is not appropriate to describe the observed reflections. Still the extra reflections are almost systematically present and equivalent whatever dataset.

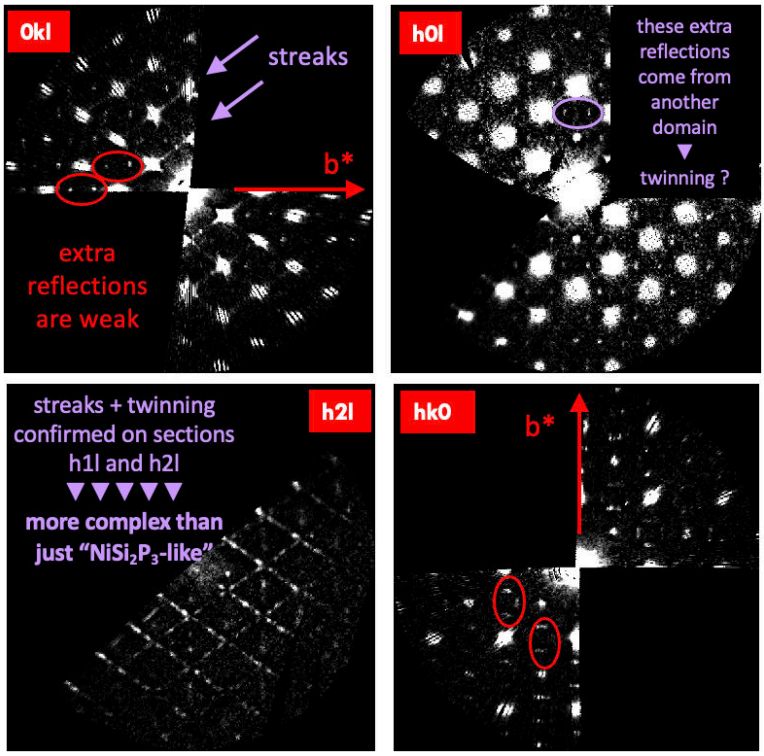

***Figure 86**. Fig. sections-index1. Reciprocal space sections corresponding to a supercell similar to $NiSi_2P_3$ as reported by Wallinda et al. (1995)[122]. In sections (0kl) and (hk0), the weak reflections (encircled in red) that triple the b-axis are visible. Nonetheless, diffuse scattering as well as twinning (highlighted in purple) complicate the analysis of the reciprocal space.*

Another option is to consider the work done previously by Mozharivskyj et al. [119] on the compound $Cu_{47}Si_{91}P_{144}$ with a composition very close to Cu:Si:P ratios 1:2:3. The structure was analyzed using single crystal XRD and considered as a commensurate modulated structure with an average cell a = 3.7092 Å and c = 5.1930 Å (SG: $I\bar{4}m2$). Considering this average cell (**Figure 85**.b) it is actually possible to refine the structure with decent R-values (

Figure 87). As mentioned earlier, this cell just allows to index exactly the same reflections as the cubic F-centered cell (indexation rate about 40%). In the model proposed by Mozharivskyj et al. [119] , the extra reflections are accounted for by considering a commensurate modulation vector $q = \frac{1}{2}a^* + \frac{1}{2}b^* + \frac{1}{2}c^*$ and the structure was analyzed as a supercell with all 3 lattice parameters of the average cell multiplied by 2.

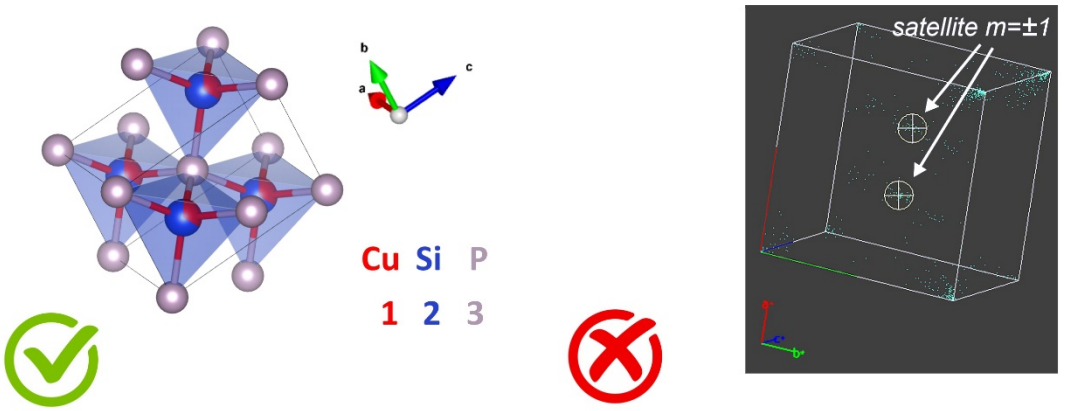

Figure 87. *The possibility of Cu/Si ordering in the form of a commensurate modulated structure, as described by Mozharivskyj et al.* [119]*, is not confirmed. (left panel) The first step of the analysis, considering an average tetragonal unit, cell seems plausible. (right panel) Considering the main clusters present in the folded cell, an incommensurate modulation vector appears to be more likely.*

Again, using the option fold to cell, it is possible to gain information about what could be the modulation vector in our case (

Figure 87). While several reflection clusters can be found, the main cluster leads to an incommensurate modulation vector q= 0.337(3) a* + 0.489(4) b* + 0.510(4) c*. Being close to a commensurate vector q = $\frac{1}{3}$ a* + $\frac{1}{2}$ b* + $\frac{1}{2}$ c*, we attempted to perform an analysis using a large 3x2x2 unit cell, but the results of the refinement were inconclusive. Still the hypothesis that part of the extra reflections can be indexed considering an incommensurate q vector is plausible since we significantly increase the indexation rate (from 40 to 50%). In such a case the modulated structure would be incommensurate and thus different from the one reported for $Cu_{47}Si_{91}P_{144}$. Having this in mind it also appeared to us that all our datasets are most probably originating from twinned crystals which complicate the clear identification of the modulation vector.

5.3.7. $CuSi_2P_3$: an incommensurate modulated structure.

Before developing our analysis of the incommensurately modulated structure of $CuSi_2P_3$, I will briefly recall some essential elements for understanding these structures and their

analysis in a 3+1 dimensional space (3+1D) involving so-called superspace groups (SSG). A detailed exposition of the theory of superspace groups and its application to the analysis of incommensurately modulated phases will not be provided here. More comprehensive information can be found in the following references[123][124]. The analysis of an incommensurately modulated structure begins by determining a basic or average unit cell that represents the average structure. For this basic unit cell, the indexing of reflections can be done using the three vectors a*, b*, and c*. The "modulation" can be considered a periodic perturbation of the average structure, characterized by the appearance of so-called "satellite" reflections. In the case of an incommensurately modulated structure, these satellite reflections can be indexed by considering a modulation vector $q = \sigma_1 a^* + \sigma_2 b^* + \sigma_3 c^*$, with at least one of the terms σ_i being irrational. The entire set of reflections can be indexed using four integer indices h, k, l, and m, associated with the vectors a*, b*, c*, and q respectively. The so-called fundamental reflections are associated with the average unit cell and will all have an index m = 0. The satellite reflections, on the other hand, will all have an index m different from 0. In the case of $CuSi_2P_3$, the presence of satellite reflections indicates the existence of ordering that is most likely associated with a Cu/Si ordering. To confirm this, it will be necessary first to identify the average unit cell and the associated modulation vector. The ab-initio resolution of modulated structures, referred as 3+1D structures, can then be carried out in the same way as for conventional 3D structures by using the charge-flipping method implemented in the Superflip program. The interpretation of the results, however, may not be as straightforward as in the case of 3D structures, which is why knowledge of the average structure is often a prerequisite.

Based on the dozen datasets collected from this sample, we can obtain qualitative information, such as the formation of an incommensurately modulated structure, the presence of twins, and defects. To go further, we need data obtained from a single domain, non-twinned, crystals. We therefore returned to the microscope to collect new data and, eventually, succeeded in finding a single-domain crystal. This crystal had a truncated ovoid shape with lateral dimensions of 30 by 45 nm (**Figure 88**.a). The PEDT data were obtained using an electron beam with a diameter of 60 nm (**Table 52**)

As done before, the examination of the reciprocal lattice folded onto the cubic zinc blende-type unit cell is used to estimate the quality of the dataset and to obtain the modulation vector. In b, the result obtained from twinned crystals is shown, to be compared with **Figure 88**.c, which presents the result from the single-domain crystal. In

Figure 88.d, the modulation vector can be unambiguously established, confirming the previously obtained results. Interestingly, in this multiple folded unit cell (2x2x2), it is possible to observe that nearly all reflections are now indexed, with an indexing rate increasing from 64 to 80%. This is achieved by considering a modulation vector q = 0.824(3) a* + 0.125(4) b* - 0.515(2) c* with only satellite reflections of order m=±1 being visible. We observed in the previous section that, from a metric perspective, the cubic unit cell of the F-centered zinc blende type does not seem to be the best choice for the average unit cell, favoring instead an I-centered tetragonal cell. If we considered this cell as the average cell, we obtained a modulation vector q = 0.350(2) a* + 0.480(3) b* + 0.513(2) c* close to the one obtained for the twinned crystals (

Figure 87).

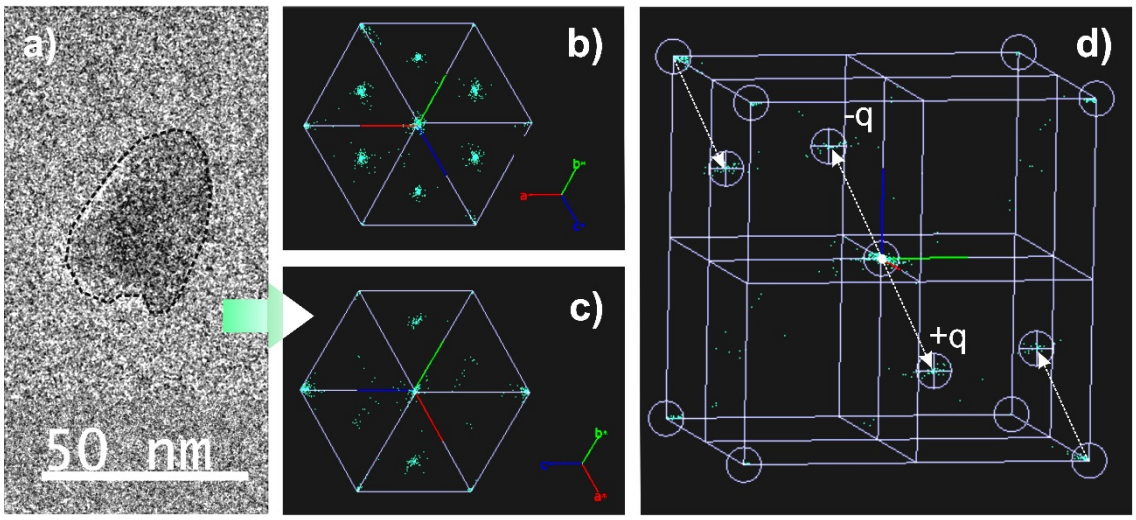

Figure 88. *In a) image of the crystal that allowed us to obtain PEDT data from a single domain. In b) collected reflections folded into the prototype zinc blende unit cell, showing twinning. In c) same for a single domain crystal. In d) using a 2x2x2 folded unit cell, the modulation vector is visualized, with only m=±1 satellites order observed.*

The modulation vector obtained in both cases has a component along each of the three directions of the reciprocal lattice (a*, b*, and c*), which is incompatible with either the cubic or tetragonal symmetry of the average unit cell. Taking the modulation vector into account implies that a triclinic symmetry must be considered. Under this condition, the deviation of the average zinc blende-type unit cell from cubic symmetry is no longer an issue. Therefore, we decided to use the zinc blende prototype structure as the basis for constructing the "modulated" model. This choice reflects the fact that the electron diffraction patterns obtained on the modulated $CuSi_2P_3$ crystals (all records except one)

shows intense reflections whose periodicity matches the lattice of the zinc blende prototype. Only the weak reflections require the introduction of a wave or modulation vector for indexing.

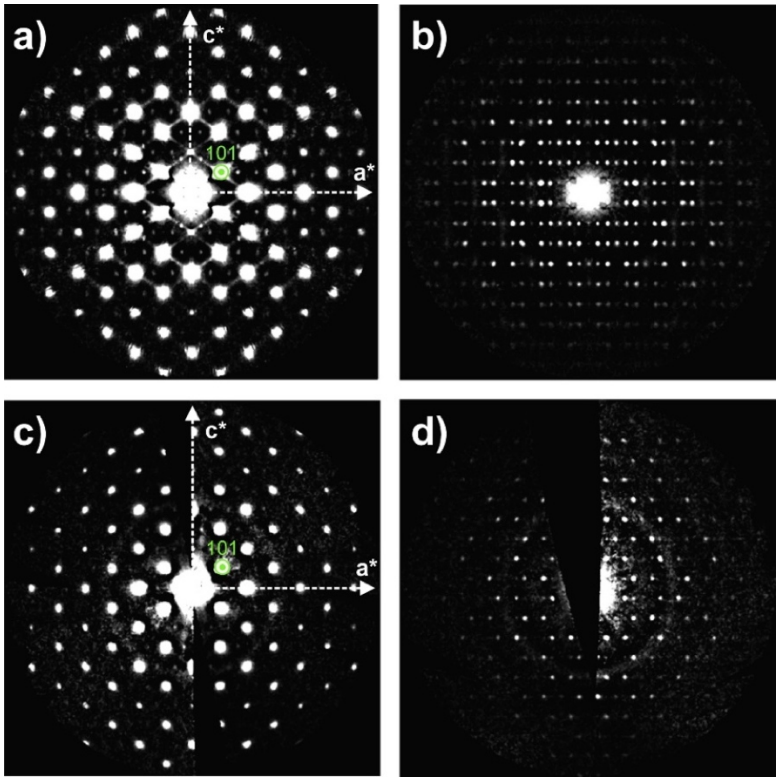

Figure 89. *Reciprocal space sections reconstructed from PEDT data collected on a twinned crystal (a and b) and a non-twinned crystal (c and d). Using the tetragonal unit cell (a ≈ 3.68 Å, c ≈ 5.21 Å) as the average unit cell, panels a and c show (h0l) sections with only fundamental reflections expected. Panels b and d show (h0.5l) sections with only satellite reflections*.

Nevertheless, it seems valuable to use the tetragonal unit cell one last time to demonstrate how the data collected from this new crystal surpasses that of all the other crystals analysed so far. The reason for using the tetragonal unit cell here is purely practical, as it allows for easier generation of reciprocal space sections where the satellite reflections are clearly separated from the fundamental reflections. By doing so, in **Figure 89**, the presence of twins, manifested as extra reflections (i.e. satellites reflections originating from twins), and disorder, visible as diffuse streaks, is striking in panels a and b compared to panels c and d.

After selecting the average unit cell as being related to the prototype zinc blende structure (a = 5.25 Å, SG: F-43m) and recognizing that the true symmetry is triclinic due to the modulation, only a few options were available for the superspace group. One of the main challenges in this study is the reduction in symmetry from cubic to triclinic. This change

significantly impacts the completeness of our dataset, reducing it from 92% to 43%. The resulting loss in data quality limits the number of parameters we can refine, thereby constraining our model. The possible SSG associated with the modulated structure can be either F1(σ1, σ2, σ3) or P1(σ1, σ2, σ3), with the base structure being non-centrosymmetric. Although F-centering is not compatible with a triclinic lattice, it was initially retained to stay as close as possible to the zinc blende prototype structure. This choice also accounts for the fact that the reflections from the average structure follow extinction rules characteristic of an F-centered lattice. In this case only two independent sites: M (4d) (where M = Cu or Si) and P (4a) are used for the average structure. After several trials, we realized that retaining the F-centering severely constrains the model for the functions describing the modulation. Therefore, in a second step, we decided to remove the centering and choose SSG P1(σ1, σ2, σ3). Four independent M sites and four independent P sites are then necessary to describe the structure. However, to limit correlations between the different parameters, we introduced constraints corresponding to the F-lattice mode for the average positions of the M and P atoms but now, the different modulation functions are not restricted.

To guide us in constructing the model, we plotted the De Wolff sections obtained from the Superflip results (**Figure 90**). To the expert eye, these De Wolff sections reveal the presence of a modulated structure primarily characterized by occupancy modulation. Specifically, the contour lines for the P and M atomic domains exhibit minimal undulation for P and no undulation for M along the x_4 direction. Strong undulations would indicate significant displacements of M and P atomic positions relative to the prototype zinc blende structure. However, this is not observed in the current case. The most notable feature is actually the presence of reinforcements (or nodes) in the contour lines for the M atomic domain (**Figure 90**.b). We correlated these nodes with the presence of high atomic number atoms (Cu) and the antinodes with the presence of lower atomic number atoms (Si).

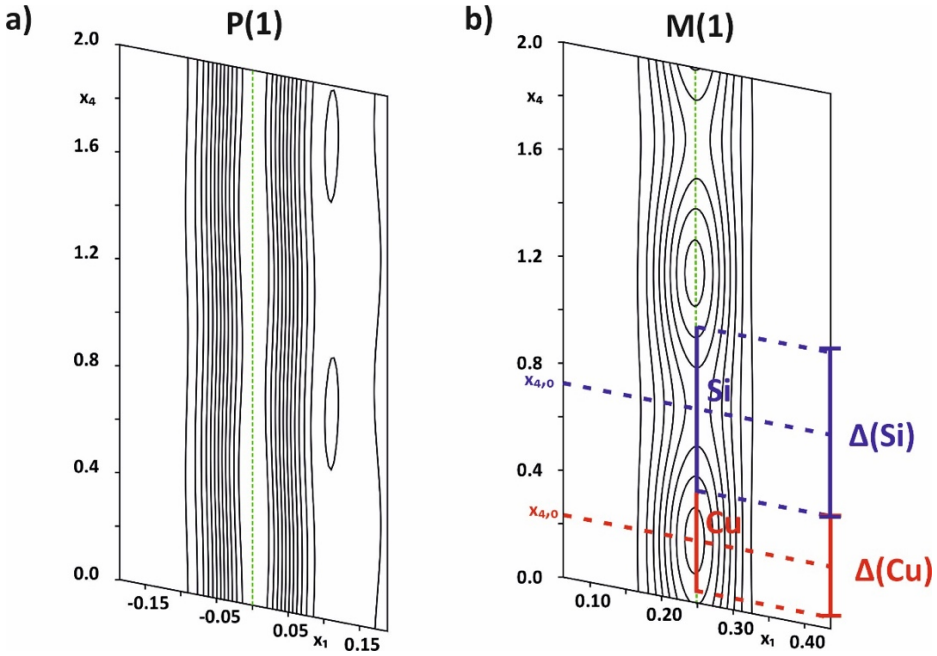

Figure 90. *De Wolff sections for the P(1) and M(1) atomic domains are shown in panels a) and b), respectively, with black contour lines. The green dashed line serves as a guide to the eye, indicating zero atomic displacement relative to the average structure. In a), along the x_4 direction, only very little displacement of the P(1) atomic domain is seen with no reinforcement. In b), no atomic displacements are observed for the Cu/Si position, but reinforcements can be seen. The centers $x_{4,0}$ and the width Δ of the crenel functions are reported for the Si and Cu species.*

We then decided to define a model of perfect order between the Si and Cu species by introducing crenel functions for Cu and Si (**Figure 91**). As their name suggests, these functions are "all or nothing," meaning they lead to sites that are either 100% Cu or 100% Si. The choice to describe the Cu/Si substitution using crenel functions is somewhat arbitrary; it stems from a desire to reflect a perfect long-range order. Of course, we cannot rule out a more imperfect ordering. In cases where mixed Si/Cu sites are present, the occupancy modulation can be described using a combination of sine and cosine functions (see **Figure 91**). This approach requires more parameters for refinement compared to crenel functions. The crenel functions are defined by the parameters x4,0 and Δ, which represent the center and the width of the crenel, respectively (**Figure 90**.b). The values of Δ were fixed in order to keep a ratio Cu:Si of 1:2. For each M# site (# ranging from 1 to 4), it was also imposed that x4,0(Si) = x4,0(Cu) + ½. No constraints were introduced between the different M# sites from the point of view of modulation functions.

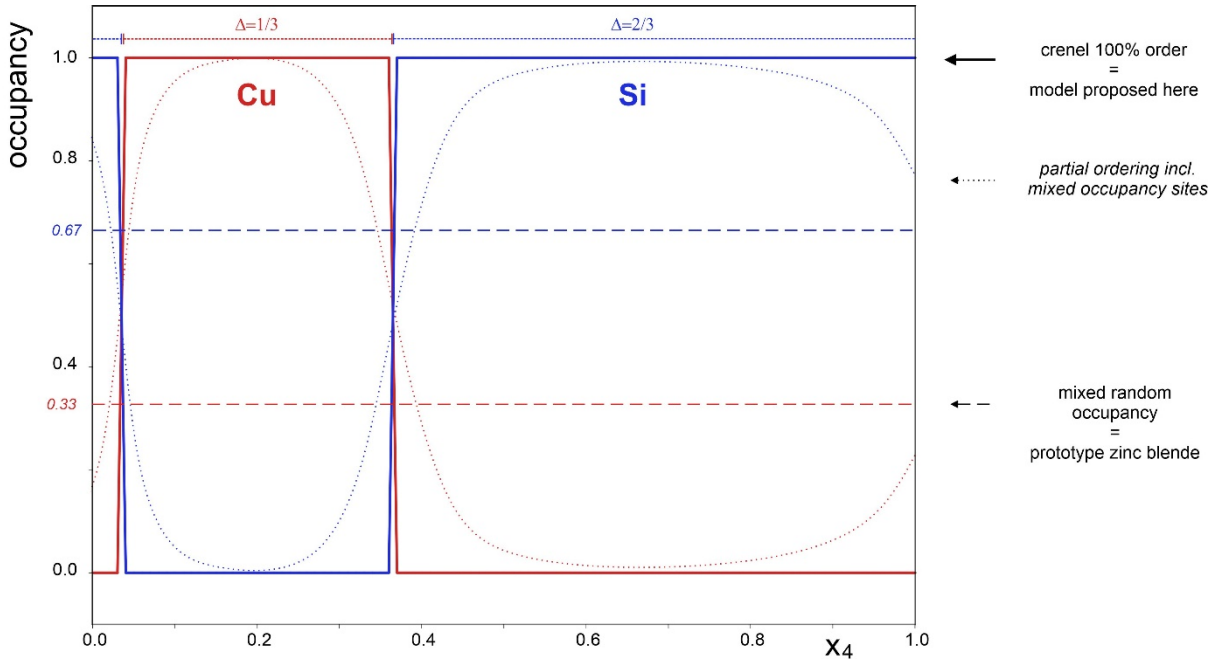

Figure 91. *Schematic showing some of the possibilities to model the distribution of Cu and Si onto the M sites. In the prototype structure, a mixed random occupancy is observed with a ratio Cu:Si being 1:2. Such a situation would be represented by the horizontal dashed lines. On the contrary, a situation where Cu and Si atoms would have distinct sites can be modelled considering crenel functions in bold continuous lines. The ratio Cu:Si of 1:2 is still preserved here and related to the ratio between the widths of the Si and Cu crenels. If only a Cu/Si partial ordering exist, sine functions in dotted lines could be used.*

Using crenel functions allows to get an ordered model without the need to refine any structural parameters, only the x4,0 position of each crenel needs to be given. To better visualize the effect of these crenels and the type of Si/Cu ordering produced, an approximate 3D structure can be generated from the 3+1D structure, represented within a supercell of the average cell. Using a 6x8x2 supercell (see **Figure 92**), it is seen that the proposed model leads to the alternation of CuP and SiP rich zones in the structure.

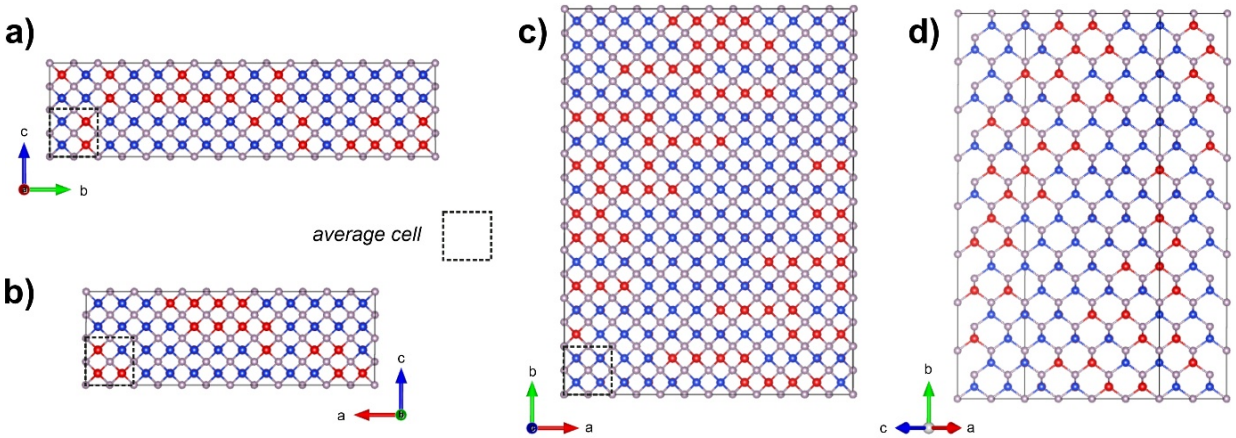

***Figure 92**. Initial model constructed using crenel functions to describe occupancy modulation and Cu/Si ordering. A 6x8x2 approximant structure is projected along the [100], [010], [001], and [101] directions of the average unit cell in panels a), b), c), and d), respectively. Cu, Si and P, are represented in red, blue, and pink, respectively.*

Building a model is one thing; validating it through structure refinement is another. With a P1(σ1, σ2, σ3) superspace group (SSG), all atomic positions and terms of the modulation functions are parameters that can be refined. This results in a considerable number of parameters for the eight atomic domains (4 P + 4 M). Given that the modulation results in a subtle modification of the highly symmetrical average cell (as evidenced by PXRD in **Figure 77**), we decided to fix as many parameters as possible, focusing on refining only the minimal and most significant ones. We specifically chose to fix the atomic coordinates *x, y, z* to those found in the prototype structure. Additionally, we opted to refine only two U_{iso} parameters: one common to all P atomic positions and one for the M atomic positions. A common modulation function was also applied to describe the small atomic displacements (as evidenced in **Figure 90**.a) associated with all P atomic domains. This approach resulted in a kinematic refinement with R_{obs} values of approximately 29% for the main reflections and 18% for the satellite reflections. Although this result was not entirely satisfactory, we proceeded with dynamical refinements to reach good R_{obs} values of approximately 8% for the main reflections and 13% for the satellite reflections (**Table 52**).

Structure type	**modulated zinc blende**
Temperature (K)	293
Crystal system, space group	Triclinic, *P1(σ1,σ2,σ3)*
σ1,σ2,σ3	0.824(3), 0.125(4), –0.515(2).
***a, b, c* (Å)**	5.368(2), 5.384(4), 5.215(1)
***α, β, γ* (°)**	89.76(3), 90.60(2), 89.68(4) °
Crystal size (nm)	lateral: 30 x 45 [(a)]; thickness: 36 [(b)]
Electron wavelength λ (Å)	0.0251
Electron beam size (nm)	60
Number of frames	51
Tilt range (°)	72
Precession angle (°)	1.25
Resolution $\sin(\theta_{max}) / \lambda$ ($Å^{-1}$)	0.9
Cumulative coverage (%)	43
Measured, observed [$I > 3\sigma(I)$] refl.	1746, 946
No. of refined parameters	59
g_{max} ($Å^{-1}$), $S_{g,max}$ ($Å^{-1}$), R_{Sg}, steps	2.0, 0.01, 0.6, 96
R(obs), R(all), wR(all), GoF(all)	0.088, 0.105, 0.200, 4.07
main: R(obs), R(all), wR(all)	*0.080, 0.081, 0.193*
satellites: R(obs), R(all), wR(all)	*0.130, 0.188, 0.336*

(a) measured from an electron microscopy image; (b) calculated from the structure refinement

***Table 52**. Crystallographic details of 3D ED data collection, data reduction and dynamical structure refinement obtained for $CuSi_2P_3$.*

Regarding the occupancy modulation of the four M sites (Si, Cu), only the center of the crenel functions was refined. For the sine modulation functions associated with atomic displacements, their amplitudes remain generally low or even negligible for the M(3) and M(4) sites. These low modulation amplitudes result in Cu-P and Si-P distances ranging from 2.22 to 2.4 Å (**Figure 94**), which is typical for similar compounds. Only the M(2) site exhibits higher modulation amplitudes, leading to distances that deviate from this range. It may be necessary to revisit some aspects of the refinement to determine if this anomaly persists or if an alternative solution can be found to limit these displacement amplitudes. With the limitations imposed during refinement, the resulting structure is only a minor modification of the initial model (**Figure 93**). However, the obtained reliability factors are sufficiently good to suggest that this model is a good descriptor of the order present in this compound.

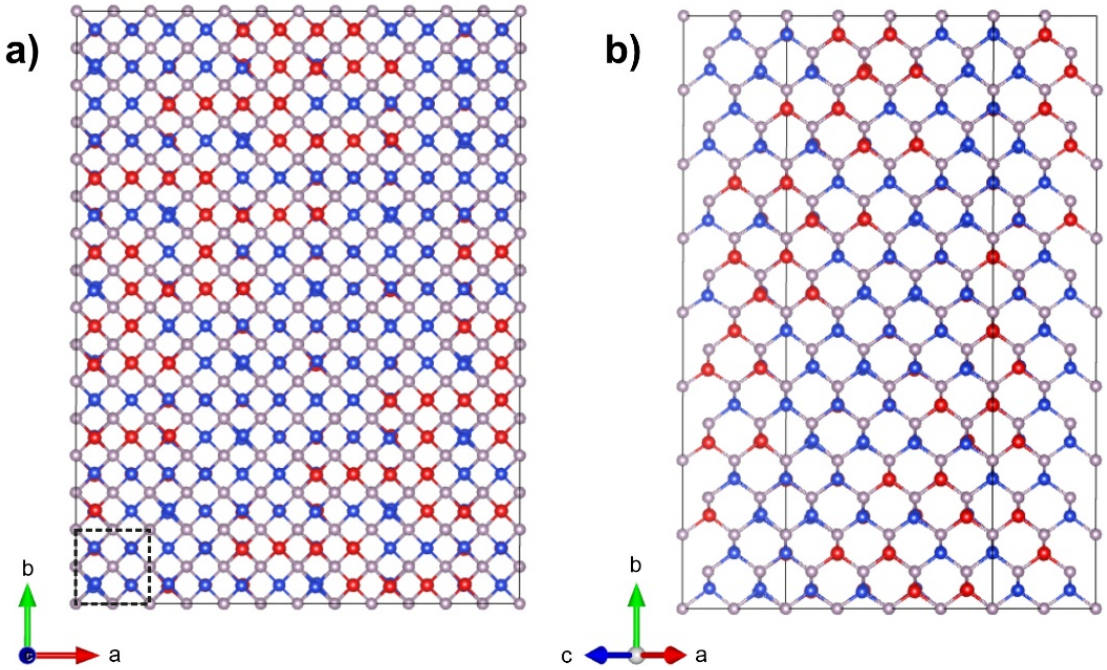

Figure 93. *Structure obtained after dynamical refinement of the PEDT data. A 6x8x2 approximant structure is projected along the [001] and [101] directions of the average unit cell in panels a) and b), c). Cu, Si and P, are represented in red, blue and pink, respectively.*

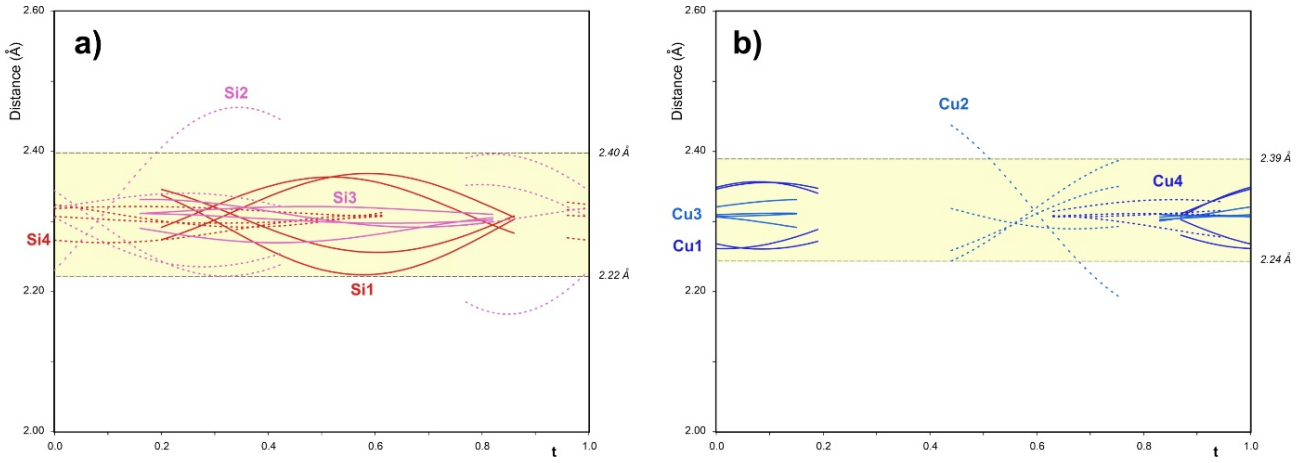

Figure 94. *Variation of Si-P and Cu-P distances as a function of the internal variable t in a) and b), respectively.*

Occupancy: Crenel functions			
Atomic sites / domains		Δ*	$x_{4,0}$
M(1)	Cu1	0.3333	-0.80(11)
	Si1	0.6667	-0.30(11)
M(2)	Cu2	0.3333	0.57(5)
	Si2	0.6667	1.07(5)
M(3)	Cu3	0.3333	0.32(16)
	Si3	0.6667	0.82(16)
M(4)	Cu4	0.3333	0.43(11)
	Si4	0.6667	0.93(11)

** fix parameters*

Positional parameters					
Atom	**Wave**	**x**	**y**	**z**	***U*(Å^2)**
M(1)		0.25*	0.75*	0.25*	0.0081(5)
	s,1	0*	-0.015(3)	0*	
	c,1	0*	0*	0*	
M(2)		0.25*	0.25*	0.75*	
	s,1	0.010(3)	0.026(4)	-0.0093(19)	
	c,1	-0.010(3)	-0.006(4)	0.0058(19)	
M(3)		0.75*	0.75*	0.75*	
M(4)		0.75*	0.25*	0.25*	
M(3-4)	s,1	0*	0*	0*	
	c,1	0*	0*	0*	
P(1)		0.5*	0.5*	0*	0.0052(3)
P(2)		0.5*	0*	0.5*	
P(3)		0*	0.5*	0.5*	
P(4)		0*	0*	0*	
P(1-4)	s,1	-0.0034(6)	0.0025(6)	0*	
	c,1	0*	0*	-0.0022(3)	

** fix parameters*

***Table 53**. $CuSi_2P_3$ structural parameters obtained from single crystal 3D ED data. See Table 3D ED details for lattice parameters and SSG.*

CONCLUSIONS

For many years, PXRD has been the most commonly used diffraction technique to obtain information about the crystal structure of NPs. However, due to the small size of the particles, which leads to diffraction peak broadening, it can be difficult to access fine details such as mixed site occupancy rates or reliable ADPs, even in the case of a known structure. If the crystal structure is "a priori" unknown, then PXRD patterns obtained from NPs will be of limited utility.

Although 3D ED was introduced in 2007 with the potential to characterize crystals smaller than 100nm and address the shortcomings of PXRD, there were no comprehensive guidelines on how to obtain data of sufficient quality to accurately analyze the structure of NPs. Consequently, this research has focused on investigating a range of materials with different NP sizes, which served as reference systems for addressing the challenges in achieving high-quality data. Moreover, standardized protocols were established, making it straightforward for any user to adopt and implement such analysis. Additionally, 3D ED has proven to be an exceptionally effective technique for studying NPs, enabling the resolution of structural challenges in compounds that would have been difficult or impossible to characterize with other available methods.

TESTING 3D ED TECHNIQUE

To gain a general understanding of this technique, a first experiment, known as *Round Robin*, was carried out within the NanED project. Each PhD student received two unknown samples, Epidote and Natrolite, without prior knowledge of their structures. However, these structures had already been thoroughly characterized by SC-XRD, and the results from that method served as a reference. In particular, the experiments at CRISMAT were conducted using a JEOL F200 microscope equipped with RIO16 and ASI Cheetah M3 detectors, applying parallel nanobeam diffraction with a 10 μm condenser aperture to collect data on both compounds. Both minerals had crystal sizes of around 200 nm, and simple grinding of the powder, mixing with ethanol, and applying a small drop onto a TEM grid was sufficient for sample preparation. The small beam size

used allowed for accurate data collection without needing perfect crystal dispersion (the beam had smaller dimensions than the crystal itself).

For Epidote, the main challenges were its small sensitivity to the electron beam, the mixed occupancy of Al and Fe, and the detection of hydrogen atoms. Fortunately, the beam sensitivity was manageable at room temperature, and sufficient frames were collected to reconstruct the reciprocal space in 3D. Dynamical refinement was crucial to distinguish between Al and Fe occupancy, yielding a refined Al/Fe ratio with well-defined ADP values. Hydrogen detection was also successful only after dynamical refinement due to the heavier multiple scattering events in thicker crystals.

In the case of Natrolite, the primary difficulty was differentiating between Al and Si positions, given that these atoms differ by only one electron, leading to similar intensities in the Fourier map. Additionally, since the material contains water molecules, detecting hydrogen is essential for obtaining an accurate structural model. The coordination geometry played a key role in distinguishing between Al (octahedral coordination) and Si (tetrahedral coordination), and five hydrogen atoms were successfully detected after refinement, with an absolute configuration determination yielding a Robs difference of 17% to 20%.

For Natrolite, the main challenge was distinguishing between the positions of Al and Si, as their difference of only one electron results in nearly identical intensities on the Fourier map. Furthermore, the presence of water molecules makes hydrogen detection critical for achieving an accurate structural model, but this is particularly difficult in every characterization technique. Determining the absolute configuration required a detailed evaluation of Robs values after dynamical refinement. The coordination geometry played a key role in distinguishing between Al (octahedral coordination) and Si (tetrahedral coordination), and five hydrogen atoms were successfully detected after refinement, with an absolute configuration determination yielding a Robs difference of 17% to 20%.

Results from other PhD students participating in the *Round Robin* confirmed that all of these structural challenges could be overcome, despite the use of different microscopes, experimental setups, data collection strategies, and data processing software. These results demonstrate the robustness and versatility of the technique, proving its ability to produce high quality data capable of addressing complex structural problems in “large

crystals". The next question we asked was whether this accurate information could be obtained for NPs

STRUCTURAL STUDY OF "LARGE NPs"

In this work, we adopt a relatively strict definition of NP, referring to nano-sized crystals with all dimensions less than 100 nm. To assess the accuracy of 3D electron diffraction (3D ED) for different NP sizes, two categories were distinguished: "large NPs", with the largest dimension up to 70 nm, and "small NPs", with sizes ranging between 20 and 10 nm.

TiO_2 brookite was used as a test sample for large NPs. This material was synthesized through a hydrothermal method at the CRISMAT laboratory, resulting in nanorods approximately 70 nm by 30 nm. Thanks to the secondments provided by the NanED project, this material was tested using different microscopes, setups, and approaches for data acquisition but all of them were carried out at room temperature using a tomography holder.

At IIT, a Zeiss Libra 120 microscope was used. This microscope, designed for analyzing larger crystals and beam-sensitive materials, presented a challenge in locating a single brookite nanorod within the 600 nm-wide electron beam, but it was achievable. To collect cRED data, a tracking system was necessary due to the goniometer's instability, ensuring that the isolated NP remained under the beam throughout the entire data collection process. An accurate structural solution was obtained with a final Robs value of 6.48%, significantly lower compared to the kinematic refinement value of 14.75%.

At UA, a FEI Tecnai G2 X-Twin F20 microscope was used. In this case, the smallest beam suitable for cRED experiments was 300 nm. Additionally, due to the stability of the goniometer, no tracking system was needed to keep the NP of interest within the beam size throughout the entire analysis. After data processing, the structure was successfully solved, and both kinematic and dynamical refinements were performed, yielding very good Robs values for cRED data acquisition: 14.9% for kinematic refinement and 5.56% for dynamical refinement.

For experiments conducted using the continuous rotation approach, data acquisition took only a few minutes, as the goniometer tilt and data collection are automated. When using a tracking system, the process took an additional few minutes because the system first

records the trajectory of the crystal and then reproduces it during data collection in diffraction mode.

At CNRS, a JEOL F200 microscope was utilized with the precession-assisted ED approach. To determine the optimal conditions for achieving the highest quality data, a beam of around 70 nm was used and four different setups were tested. For CNRS-01, the exposure time was set to 0.5 seconds per frame with a tilt step of 1 degree. In CNRS-02, the tilt step was increased to 2 degrees while keeping the exposure time the same. CNRS-03 retained the tilt step from CNRS-02 but extended the exposure time to 1.5 seconds per frame. Lastly, CNRS-04 adjusted both parameters, setting the exposure time to 1 second per frame and the tilt step to 1.5 degrees. For all setups, accurate structure solution was achieved, with Robs values below 8% (6.63%, 7.68%, 6.70%, and 6.48%, respectively) after dynamical refinements. All these setups then were then validated as effective protocols for obtaining high quality data, resulting in good reliability factors and high accuracy in structural analysis.

In contrast to the experiments conducted in continuous rotation mode, the performance time for precession-assisted ED increased significantly. This is because the goniometer rotation and data acquisition were performed manually (step-wise), requiring at least 15 minutes per dataset.

Finally, the material was tested using the ED_1 diffractometer developed by ELDICO Scientific AG company. The data acquisition process was quite similar to that of a conventional X-ray diffractometer used in SC-XRD experiments. In this case, a beam size of 750 nm was employed, and data were collected in STEM mode using continuous rotation. The main challenge with this setup was visualizing and identifying a single nanoparticle, as the large beam size limited image resolution. Despite this, data collection and structural resolution were successfully achieved. However, when refining the structure, the statistical results were not entirely reliable due to the low number of observed reflections.

Additionally, a PXRD experiment was performed in diffraction geometry using a 0.3 mm capillary at Elettra Synchrotron. The Rietveld refinement resulted in an excellent fit between the experimental data and the theoretical model, with RBragg and Rwp values of 3.87 and 13.6, respectively. Furthermore, the average volume of the nanoparticles was obtained, confirming a rod-like shape.

To conclude the study of brookite TiO_2, the final structures obtained from both PXRD, and all 3D ED experiments were compared with the bulk reference structure from the ICSI database. The comparison was performed using the Bilbao Crystallographic Server and its COMPSTRU utility, which provided values for the average and maximal deviations in atomic positions. The results revealed that the average and maximal deviations relative to the reference structure were 0.03 Å and 0.04 Å, respectively, for the PXRD experiment. In contrast, for all 3D ED experiments, the average and maximal deviations after dynamical refinement were both below 0.01 Å.

In summary, for 3D ED experiments, both cRED and precession-assisted ED approaches yield accurate structural solutions for the study of 'large NPs,' with excellent fits in dynamical refinement (**Figure 95**). Personally, if I had to choose between them, I would prefer the one that requires less time. Additionally, it is promising that the ED_1 diffractometer was able to collect data in a way similar to SC-XRD and achieve successful structural resolution. For future perspectives, increasing the exposure time and adjusting the goniometer rotation speed could enhance the number of observed reflections, thereby improving the structural refinement.

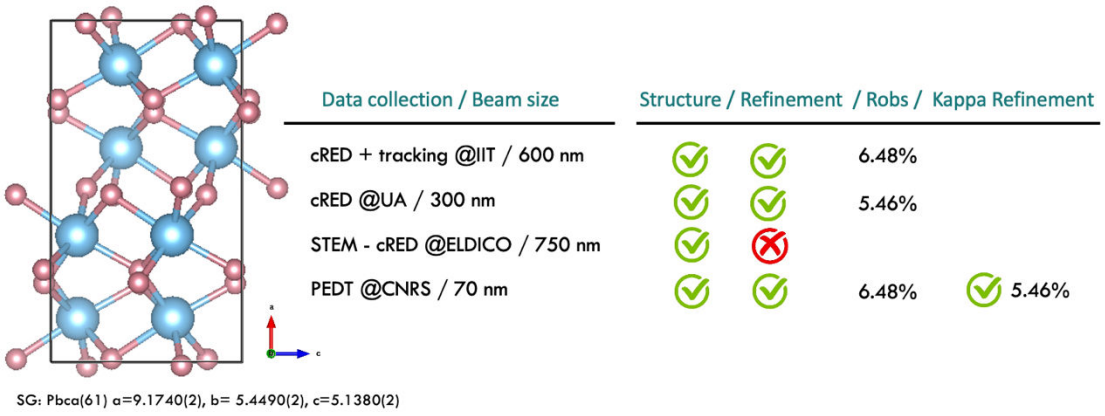

***Figure 95**. Representation of the reference structure for TiO_2 brookite, along with the data acquisition protocols, beam size, and facilities where the experiments were carried out, suitable for structure solution and refinement of these 'large NPs'. Additionally, the Robs value obtained after dynamical refinement for the best statistical results is provided. For PEDT, the Robs value from kappa refinement is also presented.*

A step further in terms of refinement was carried out, referred to as ***Kappa refinement***. This method requires a higher resolution, typically better than 2 Å, and a data completeness of around 99% (this is the reason why this type of refinement cannot be performed as a standard procedure for all compounds). However, the datasets collected

at CRISMAT on TiO_2 met these stringent requirements and were excellent candidate for this advanced refinement process. The kappa refinement on brookite extracted reasonable charge density information improving the structure model obtained after conventional IAM refinement just by the introduction of two extra parameters per atom. In addition to the added chemical value of this type of refinement, it undeniably demonstrates the quality of the 3D ED data that can be obtained even from very small crystals.

STRUCTURAL STUDY OF "SMALL NPs"

As observed, data acquisition for what we refer to as "large NPs" is quite similar to that for large crystals, with the primary difference being that a greater dispersion of the sample is required to ensure analysis of a single isolated NP. However, when reducing NP sizes to around 20–10 nm, new challenges arose when applying the same protocols used for "large NPs". For this study, a JEOL F200 microscope was used to test two different materials: TiO_2 anatase, with a non-uniform size of approximately 20–15 nm, and ITO, with spherical shape of 10 nm.

The first issue encountered was NPs agglomeration. Neither further diluting the sample nor increasing the time in the ultrasonic bath was sufficient to achieve the desired dispersion for isolating a single particle within a 70 nm beam size for the precession-assisted ED approach. Continuous rotation 3D ED was also not a viable option either as the larger beam size used exceeded the dimensions of the NPs, making the unwanted contribution from the other NPs more likely to be captured and also resulting in the membrane signal dominating over the diffracted signal from the NPs. The only potential solution would have been to reduce the beam size and use a tracking system, but this has not yet been developed, as reducing the beam to less than 50 nm falls below the confusion sphere of most, if not all, TEM goniometers. Consequently, the only viable solution was to use precession-assisted ED, reducing the beam size to approximately 30 nm, slightly larger than the NP itself. However, the combination of the small NP size and the focused 30 nm beam significantly reduced stability, making the NPs more beam-sensitive. To mitigate this issue, the cryo-tomography holder was employed instead of the standard tomography holder, allowing for work under cryogenic conditions, which provided greater stability to the NPs.

In the initial attempt to use the same exposure time as in the case of TiO_2 brookite, the signal-to-noise ratio proved too weak, resulting in an insufficient number of observed

reflections to yield reliable results. Consequently, the exposure time had to be increased to 4 seconds per frame to improve data quality. Even with the cryo-holder, using a small beam (30 nm) combined with a long exposure time (4 s/frame) reduced the stability of the NPs, necessitating the use of a larger tilt step (2° per tilt) to reduce the total acquisition time. Although this last option might be controversial in the sense that it reduces the number of reflections collected and their overlap between each mechanical tilt step, it allowed us to obtain convincing results.

In the case of these "small NPs", data acquisition and structural resolution were not as straightforward as with "large NPs". Various parameters had to be adjusted (**Figure 96**), and working under cryogenic conditions was crucial for the stability of these small particles. For both TiO_2 anatase and ITO, accurate structure solutions were achieved, with Robs values from dynamical refinement of 3.59% and 4.71%, respectively, in the best cases. Additionally, PXRD experiments were conducted using a 0.3 mm capillary at Elettra Synchrotron for both compounds. The Rietveld refinement resulted in an excellent fit between the experimental data and the theoretical model. For TiO_2 anatase, the RBragg and Rwp values were 4.34 and 13.3, respectively. For ITO, these values were 3.23 and 10.1.

To conclude the study of "small NPs", the final structures obtained from both PXRD and all 3D ED experiments were compared with the bulk reference structures from the ICSI database. This comparison was carried out using the Bilbao Crystallographic Server and its COMPSTRU utility, which provided values for the maximum deviations in atomic positions. The results showed that the largest deviations compared to the reference structure were observed in the PXRD experiments, with values of 0.02 Å for anatase and 0.05 Å for ITO. In contrast, the 3D ED experiments yielded average and maximum deviations of 0.01 Å for anatase and 0.009 Å for ITO after dynamical refinement. Confirming that a more accurate structural model is obtained using 3D ED compared to PXRD.

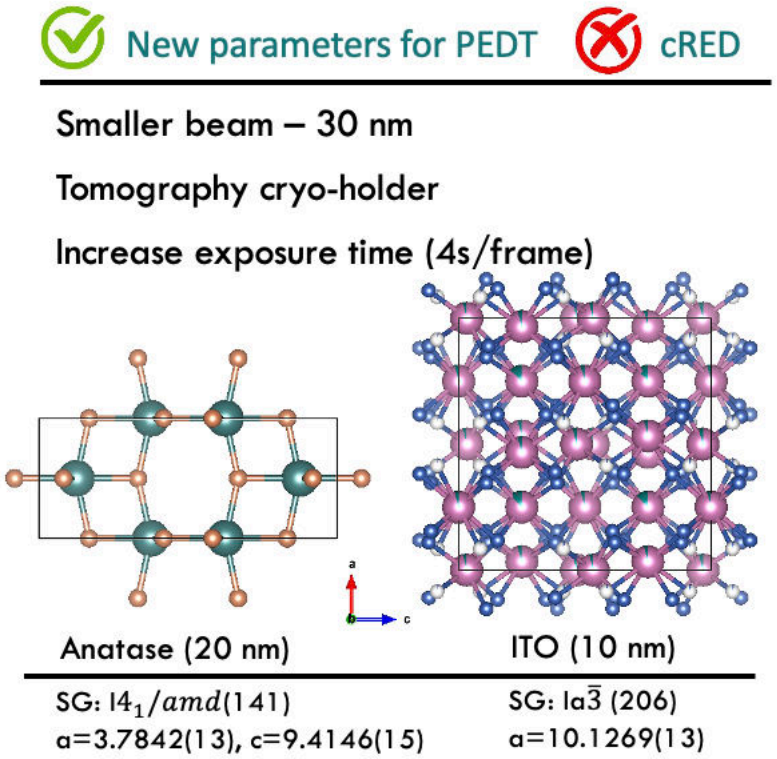

Figure 96. *Two different compounds were tested as a 'small NPs': Anatase (20 nm) and ITO (10 nm). New setting had to be adjusted to achieve the final structure model for NPs as small as 10 nm. Only PEDT was possible for data acquisition.*

MULTIPLE SCATTERING EVENTS AND SMALL NPs

Intuitively, electrons passing through thicker crystals are expected to undergo more multiple scattering events, resulting in diffracted intensities that are more affected by dynamical effects. Consequently, it seems logical to assume that as NP size decreases, the impact of these effects reduces, and the kinematical approximation might be sufficient for accurate structure determination. This assumption was consistent with the Robs values obtained from both kinematic and dynamical refinements, which differed from 7.91% to 4.71% in the case of ITO. Although for the TiO2 anatase we still observe a significant reduction in Robs values after dynamical refinement, one might think that the dynamic effects become negligible when a slightly smaller size is reached, as in the case of the 10 nm ITO NPs. However, this work demonstrated that this assumption is incorrect. Kinematical and dynamical values for standard refinements are not directly comparable because, in kinematic refinements, the average symmetry-equivalent reflections are used, assuming that symmetry-equivalent reflections have identical intensities regardless of

their collection during 3D ED data acquisition. In dynamical refinements, this is not the case, as systematically equivalent reflections recorded in different frames of the 3D ED data are not expected to be identical due to multiple scattering events.

To address this, we performed a kinematical-frame-based refinement. This approach involved using the file from the dynamical refinement and artificially reducing the interaction probability by modeling an electrostatic potential multiplied by a very small factor (occupancy reduced by a factor of 0.01). This simulates an unreal crystal with a density multiplied by the same small factor, simulating in this way the 'kinematical diffraction'. Under these conditions, another refinement was performed, and the values decreased from 7.3% to 4.7% in the best case. Although reduced, this confirmed the presence of multiple scattering events in NPs as small as 10 nm. Therefore, dynamical refinement remains essential to obtain accurate structure refinements.

NEW APPROACH FOR DATA ACQUISITION OF NPs: 'NPs in motion'

When we began collecting data on these very small NPs (10 nm) under cryogenic conditions, we noticed that in diffraction mode, it took at least a couple of minutes for the diffraction patterns to stop moving and stabilize. We realized this period of instability was due to the movement of the NP itself. Therefore, based on the same principle used in SerialED, we decided to collect data statically during those first two minutes, assuming that these frames acquired had different orientations. We were then able to process the data and solve the structure of the material under study.

Although the main disadvantage of this approach is that it requires template matching meaning the unit cell parameters and an estimated Laue class must be known, which precludes solving structures *ab-initio* this technique adds value to existing 3D ED data acquisition methods, offering significant advantages for beam-sensitive materials.

CHALLENGING THE ACCURACY OF 3D ED TECHNIQUE

Once standard protocols for obtaining high-quality data and accurate structure solutions for NPs of various sizes are established, we applied them to address other challenges that require very detailed structural information. In particular, three cases were presented, each with different issues.

Light atom detection in "large NPs"

Although standard protocols indicated that acquiring high-quality data for "large NPs" could be achieved at room temperature, in this case, working under cryogenic conditions was necessary due to the instability of the compound Li_xTiO_2. While the structure analysis of TiO_2 brookite was relatively straightforward and did not pose any significant challenges, the situation was quite different for Li_xTiO_2. Initially, we performed a kinematical refinement, but this approach did not reveal any evidence of Li in the difference Fourier map.

It was only after performing a dynamical refinement that we were able to detect the presence of Lithium in the difference Fourier map (**Figure 97**). Once we placed the lithium atoms in the positions and fixed the occupancy of these atoms, the Robs value decreased from 7.20% to 7.04%. This reduction in Robs confirmed the accuracy of the structural model and the detection of Li. This result is particularly significant given that the material is sensitive to air, which complicated the detection process. Finding a technique with high enough accuracy to detect lithium is crucial for the field of battery materials. 3D ED has proven to be a strong candidate for such experiments, even with low occupancy of light atoms (as in this case, where the value was 0.5 Li per formula unit).

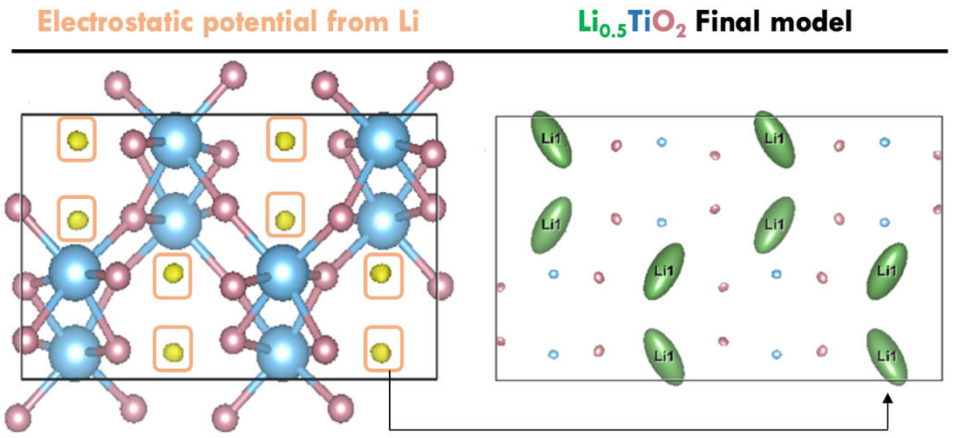

***Figure 97**. (left)Difference Fourier map showing the electrostatic potential contributions from Li, encircled in orange. (right) Placement of Li at the locations of these positive density charges results in the final structure model for $Li_{0.5}TiO_2$*

Mix occupancy ratio determination in $MgTi_2O_5$ compound.

The material $MgTi_2O_5$ was synthesized at the nanometer scale with NP sizes of approximately 30 nm. The unique feature of this compound was that all cations (Mg and Ti) occupied two non-equivalent, highly distorted sites, designated as M2 and M1, with M1 being larger and more distorted than M2. Additionally, the cell parameters are sensitive to the degree of disorder, so an accurate determination of both cations in M1 and M2 is crucial for establishing the structural model of this compound.

A PXRD experiment was conducted using a standard laboratory diffractometer with a Cu X-ray tube. Good statistics for the Rietveld refinement were achieved by fixing the mixed occupancy of these two cations using reference values from the ICSD database. However, determining the elemental ratio was not possible because the ADP parameters yielded negative values, undermining the reliability of the results (due to a strong dependence between occupancy and ADPs).

Therefore, to achieve an accurate determination of this ratio, 3D ED experiments using the precession-assisted ED approach were carried out. In this case, the compound was not beam-sensitive, so the experiments were performed at room temperature. The structure solution was feasible, and the refinement of both cations was possible even with kinematic refinement, resulting in well-defined positive ADPs. However, as demonstrated throughout this thesis, dynamical refinement always leads to a more accurate structure solution. Consequently, the final results (**Figure 98**) yielded an Mg/Li ratio of 0.520(9)/0.480(4) for the M1 site and 0.740(4)/0.260(4) for the M2 site, which are very similar to those of the bulk reference structure.

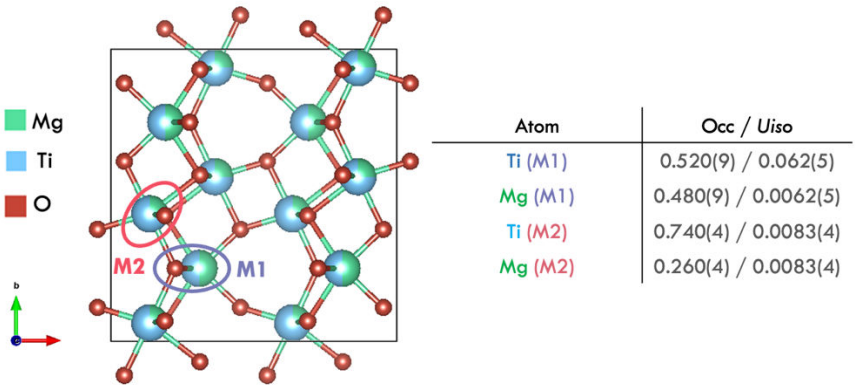

***Figure 98**. Final structure model for $MgTi_2O_5$ including the occupancy values for each cation at the M1 and M2 sites. ADPs values are positively defined.*

Thus, thanks to 3D ED, the precise determination of the mixed occupancy of these elements in the $MgTi_2O_5$ compound, considered to be in 'small NPs', was successful.

$CuSi_2P_3$: A new model for incommensurate structure.

The main goal of this study was to investigate whether there is an ordering between Cu and Si atoms in the $CuSi_2P_3$ compound, as understanding its structure and surface states will lead to a deeper understanding of its catalytic properties. A literature review was first conducted, which revealed two different structural reports. The first one described $CuSi_2P_3$ as having a cubic structure, with cell parameters of a = 5.25Å and a space group of F-43m, and it was identified as a zinc Blende type by Folberth and Pfister [117] . However, whether a partial or complete ordering of Cu and Si atoms exists remained unresolved.

The second structure, reported by Mozharivskyj *et al*. [119], presented a commensurately modulated structure, $Cu_{47}Si_{91}P_{144}$, which was analyzed as a large superstructure with cell parameters of a = b = 44.510 Å and c = 20.772 Å, showing distinct sites. This superstructure was derived from a tetragonal substructure reported by Wang *et al*.[120] with cell parameters of a = 3.7091 Å and c = 5.1930 Å and a space group of I-4m2, where a random distribution of atoms was observed.

In an initial analysis using PXRD, the structure seemed to match the one reported by Folberth and Pfister [117]. However, the peaks appeared shifted or slightly doubled, raising doubts about a complete match with the Zinc Blende-type structure. Additionally, low-intensity peaks were observed, which could not be associated with this phase or any impurities. Since this results were not conclusive for studying Cu/Si ordering, 3D ED experiments were carried out.

Different datasets from different crystals were acquired. For only one of them a simple Zinc Blende structure was found, and we were able to determine the Cu/Si ratio as 1:2. For the other datasets, while it was possible to index the reflections to a cubic or pseudo-cubic cell, the indexing success rate was very low, indicating significant discrepancies. After several attempts to index the various 3D ED datasets, it became clear that no satisfactory solution could be found based on the data available in the literature. The only plausible clue was the formation of an incommensurately modulated phase, the analysis of which was limited by the presence of twinning.

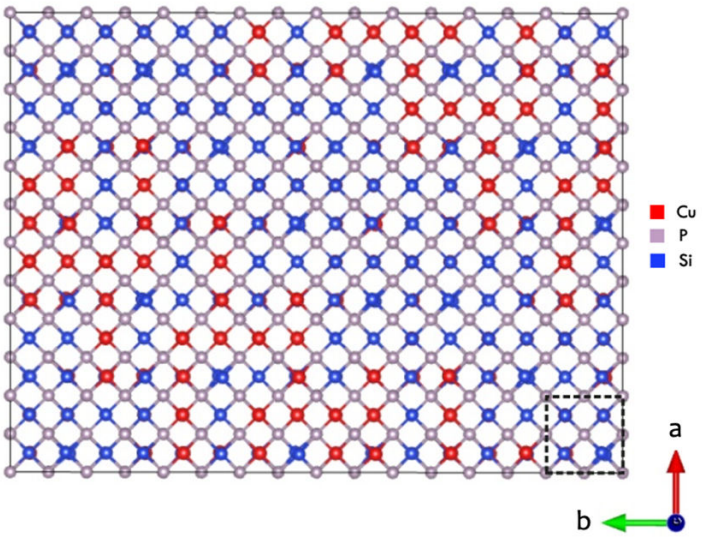

Figure 99. *Final ordered model for $CuSi_2P_3$.*

Although it was difficult to find, a successful analysis was carried out using a dataset obtained from an approximately 45 nm single-domain, non-twinned crystal. To account for the modulation vector, the symmetry was reduced to triclinic, which significantly reduced the completeness of the data set. Nevertheless, a structural model describing the incommensurately modulated structure could be proposed and refined against 3D ED data, thus addressing the question of Cu/Si ordering in this compound (**Figure 99**).

A BRIGHT FUTURE FOR 3D ED IN NP ANALYSIS.

In conclusion, throughout my PhD, I have developed and refined various protocols for acquiring high-quality data, which have enabled the accurate structural solution of NPs ranging from 100 nm down to just a few nanometers (10 nm). I have demonstrated that even at very small nanoparticle sizes, dynamical scattering remains significant and have introduced a novel approach for data acquisition in these tiny nanoparticles, similar to the SerialED method but significantly faster called “NPs in motion”. Additionally, the advanced capabilities of 3D ED over other characterization techniques have facilitated the creation of final structural models for materials where understanding their structure is crucial for elucidating their chemical-physical properties and potential applications.

The protocols developed throughout this research will greatly benefit users by streamlining routine procedures, thereby significantly reducing the time required for both data acquisition and data processing. These protocols are designed to facilitate more efficient and accurate structural analysis of NPs. In the context of synthesis, while the

expected product is often estimated based on theoretical predictions, the actual compound may differ from expectations or may be a novel material that has not been previously characterized. The high-quality data obtained through 3D ED analysis ensures that these protocols can be applied to solve *ab-initio* complex structures, even in cases where the material is unexpected or poorly characterized. By providing precise structural insights, these protocols will advance the understanding of novel compounds and enhance the ability to determine their detailed structures, contributing to more accurate and meaningful interpretations of their chemical and physical properties.

While recent informal reports indicate the potential to collect 3D ED data on 20 nm particles using commercial "electron diffractometers", the most effective instruments for studying NPs via 3D ED remain, to date, transmission electron microscopes. These instruments are particularly effective due to their ability to collect data with a highly focused parallel beam, typically of a few dozen of nanometers or less. In terms of data acquisition, we can also expect to see major developments, particularly in the ability to follow the movement of very small crystals when acquiring 3D ED data, whether stepwise or even using continuous rotation. This will enable automated data collection systems that will greatly facilitate the detailed study of the structure of NPs. My work shows that if it is possible to obtain quality data on NPs with new or adapted systems then the accuracy of the results should be equivalent to that obtained by 3D ED for larger crystals, and superior to that obtained by PXRD on NPs.

Finally, I would like to emphasize that the results presented here are only a part of my work during this PhD, and the analysis of NPs using 3D ED did not always yield the expected results. For example, in the case of core-shell NPs, it was not possible to clearly distinguish the contribution of the shell from that of the core. Also, to return to the question posed at the very beginning of this work, if 10 nm NP can be considered a record, the lower limit has not yet been reached. So, there is still room for improvement.

BIBLIOGRAPHY

1. Robert F. Molecular CT scan could speed drug discovery. *Science (1979)* **362**, 389–389 (2018). https://vis.sciencemag.org/breakthrough2018/ and https://www.science.org/doi/full/10.1126/science.362.6413.389.

2. Gemmi, M. *et al.* 3D electron diffraction: The nanocrystallography revolution. *ACS Central Science* **5** 1315–1329 (2019).

3. Bayda, S., Adeel, M., Tuccinardi, T., Cordani, M. & Rizzolio, F. The history of nanoscience and nanotechnology: From chemical-physical applications to nanomedicine. *Molecules* **25** 312 (2020).

4. Joudeh, N. & Linke, D. Nanoparticle classification, physicochemical properties, characterization, and applications: a comprehensive review for biologists. *Journal of Nanobiotechnology* **20** 262 (2022).

5. Lah, N. A. C., Zubir, M. N. M. & Samykano, M. A. Engineered nanomaterial in electronics and electrical industries. in *Handbook of Nanomaterials for Industrial Applications* 324–364 (Elsevier, 2018).

6. Cao W *et al.* The future transistors. *Nature* **620**, 501–515 (2023).

7. Yu, X., Marks, T. J. & Facchetti, A. Metal oxides for optoelectronic applications. *Nat Mater* **15**, 383–396 (2016).

8. Ndolomingo, M. J., Bingwa, N. & Meijboom, R. Review of supported metal nanoparticles: synthesis methodologies, advantages, and application as catalysts. *Journal of Materials Science* **55** 6195–6241 (2020).

9. Qiao, X. Q. *et al.* Enhanced Catalytic Reduction of p-Nitrophenol on Ultrathin MoS2 Nanosheets Decorated with Noble Metal Nanoparticles. *Cryst Growth Des* **17**, 3538–3547 (2017).

10. Gawande, M. B. *et al.* Cu and Cu-Based Nanoparticles: Synthesis and Applications in Catalysis. *Chemical Reviews* **116** 3722–3811 (2016).

11. Sankar, M. *et al.* Role of the Support in Gold-Containing Nanoparticles as Heterogeneous Catalysts. *Chemical Reviews* **120** 3890–3938 (2020).

12. Biehler, E., Quach, Q. & Abdel-Fattah, T. M. Application of Platinum Nanoparticles Decorating Mesoporous Carbon Derived from Sustainable Source for Hydrogen Evolution Reaction. *Catalysts* **14**, 423 (2024).

13. Buta, J. G., Dame, B. & Ayala, T. Nitrogen-doped ordered mesoporous carbon supported ruthenium metallic nanoparticles: Opportunity for efficient hydrogenolysis of biomass-derived 5-hydroxymethylfurfural to 2,5-dimethylfuran by catalytic transfer hydrogenation. *Heliyon* **10**, (2024).

14. Begum, R. *et al.* Reduction of nitroarenes catalyzed by microgel-stabilized silver nanoparticles. *J Hazard Mater* **377**, 399–408 (2019).

15. Seo, S., Perez, G. A., Tewari, K., Comas, X. & Kim, M. Catalytic activity of nickel nanoparticles stabilized by adsorbing polymers for enhanced carbon sequestration. *Sci Rep* **8**, (2018).

16. Jiao, D., Zheng, S., Wang, Y., Guan, R. & Cao, B. The tribology properties of alumina/silica composite nanoparticles as lubricant additives. *Appl Surf Sci* **257**, 5720–5725 (2011).

17. Erdemir, A. & Holmberg, K. Energy consumption due to friction in motored vehicles and low-friction coatings to reduce it. in *Coating Technology for Vehicle Applications* 1–24 (Springer International Publishing, 2015).

18. Shahnazar, S., Bagheri, S. & Abd Hamid, S. B. Enhancing lubricant properties by nanoparticle additives. *International Journal of Hydrogen Energy* **41** 3153–3170 (2016).

19. Singh, A. *et al.* Properties, functions and applications of commonly used lubricant additives: A review. in *Materials Today: Proceedings* vol. 44 5018–5022 (Elsevier Ltd, 2020).

20. Luo, T., Wei, X., Zhao, H., Cai, G. & Zheng, X. Tribology properties of Al2O3/TiO2 nanocomposites as lubricant additives. *Ceram Int* **40**, 10103–10109 (2014).

21. Wong, K. & Dia, S. Nanotechnology in Batteries. *Journal of Energy Resources Technology, Transactions of the ASME* **139**, (2017).

22. AbdelHamid, A. A., Mendoza-Garcia, A. & Ying, J. Y. Advances in and prospects of nanomaterials' morphological control for lithium rechargeable batteries. *Nano Energy* **93** (2022).

23. Nan, C. *et al.* Size and shape control of LiFePO4 nanocrystals for better lithium ion battery cathode materials. *Nano Res* **6**, 469–477 (2013).

24. Wu, C. Y. Nanoparticles and the environment. *J Air Waste Manage Assoc* **55**, 708–746 (2005).

25. Acharya, A. & Pal, P. K. Agriculture nanotechnology: Translating research outcome to field applications by influencing environmental sustainability. *NanoImpact* **19** (2020).

26. Zahin, N. *et al.* Nanoparticles and its biomedical applications in health and diseases: special focus on drug delivery. *Environmental Science and Pollution Research* **27**, 19151–19168 (2020).

27. Kučuk, N., Primožič, M., Knez, Ž. & Leitgeb, M. Sustainable Biodegradable Biopolymer-Based Nanoparticles for Healthcare Applications. *International Journal of Molecular Sciences* **24** (2023).

28. Weinstein, J. S. *et al.* Superparamagnetic iron oxide nanoparticles: Diagnostic magnetic resonance imaging and potential therapeutic applications in neurooncology and central nervous system inflammatory pathologies, a review. *Journal of Cerebral Blood Flow and Metabolism* **30** 15–35 (2010).

29. Modification and Improvement of Fe3O4-Embedded Poly(thiophene) Core/Shell Nanoparticles for Cadmium Removal by Cloud Point Extraction. *Advances in Applied NanoBio-Technologies* **1**, 20–27 (2020).

30. Unruh, D. K. & Forbes, T. Z. X-ray Diffraction Techniques. in *Analytical Geomicrobiology* 215–237 (Cambridge University Press, 2019).

31. Petříček, V., Palatinus, L., Plášil, J. & Dušek, M. J ana 2020 - a new version of the crystallographic computing system J ana. *Z Kristallogr Cryst Mater* **238**, 271–282 (2023).

32. J. Rodriguez-Carvajal. FullProf. *Physica B* **55**, 192 (1993).

33. Patterson, A. L. *The Scherrer Formula for I-Ray Particle Size Determination*. *REVIEW* vol. 56 (1939).

34. Bragg, M. W. L. *et al. The Structure o f Some Crystals as Indicated by Their Diffraction o f X-Rays*. *Camb. Phil. Soc. Proc* https://royalsocietypublishing.org/ (1912).

35. Knoll, V. M. & Ruska in Berlin, E. *Das Elektronenmikroskop*.

36. David B. Williams. *Transmission Electron Microscopy*. (Springer, 2009).

37. Li, F. H. *High-Resolution Electron Microscopy and Its Applications*. *JOURNAL OF ELECTRON MICROSCOPY TECHNIQUE* (1987).

38. House, S. D. *et al.* Statistical analysis of support thickness and particle size effects in HRTEM imaging of metal nanoparticles. *Ultramicroscopy* **169**, 22–29 (2016).

39. Li, X. J., He, L. L., Li, Y. S., Yang, Q. & Hirose, A. Characterization of boron doped diamond-like carbon film by HRTEM. *Appl Surf Sci* **357**, 2141–2146 (2015).

40. Sánchez-Legorreta, G., Rosendo-Francisco, P., Sumaya-Martínez, J., Olea-Mejia, O. & Rodríguez López, J. L. CdSe nanoparticles characterized by XRD and HRTEM in function of pH. *MRS Adv* **4**, 2921–2929 (2019).

41. Vanrompay, H. *et al.* Fast versus conventional HAADF-STEM tomography of nanoparticles: advantages and challenges. *Ultramicroscopy* **221**, (2021).

42. Mugnaioli, E. *et al.* Ab Initio Structure Determination of Cu2- xTe Plasmonic Nanocrystals by Precession-Assisted Electron Diffraction Tomography and HAADF-STEM Imaging. *Inorg Chem* **57**, 10241–10248 (2018).

43. Kolb, U., Gorelik, T., Kübel, C., Otten, M. T. & Hubert, D. Towards automated diffraction tomography: Part I-Data acquisition. *Ultramicroscopy* **107**, 507–513 (2007).

44. Kolb, U., Gorelik, T. & Otten, M. T. Towards automated diffraction tomography. Part II-Cell parameter determination. *Ultramicroscopy* **108**, 763–772 (2008).

45. Mugnaioli, E., Gorelik, T. & Kolb, U. 'Ab initio' structure solution from electron diffraction data obtained by a combination of automated diffraction tomography and precession technique. *Ultramicroscopy* **109**, 758–765 (2009).

46. Vincent, R. & Midgley, P. A. *Double Conical Beam-Rocking System for Measurement of Integrated Electron Diffraction Intensities*. *Ultramicroscopy* vol. 53 (1994).

47. Gemmi, M. *et al.* 3D electron diffraction: The nanocrystallography revolution. *ACS Central Science* **5** 1315–1329 (2019).

48. Chatterjee, D. *et al.* Nucleation of Metal Nanoparticles on Amorphous Substrate: Insights into Orientation Preference and Heterogeneous Catalysis. *Microscopy and Microanalysis* **23**, 2038–2039 (2017).

49. Das, P. P. *et al.* Structure Determination Feasibility of Three-Dimensional Electron Diffraction in Case of Limited Data. *Symmetry (Basel)* **14**, (2022).

50. Nederlof, I., Van Genderen, E., Li, Y. W. & Abrahams, J. P. A Medipix quantum area detector allows rotation electron diffraction data collection from submicrometre three-dimensional protein crystals. *Acta Crystallogr D Biol Crystallogr* **69**, 1223–1230 (2013).

51. Nannenga, B. L., Shi, D., Leslie, A. G. W. & Gonen, T. High-resolution structure determination by continuous-rotation data collection in MicroEDED. *Nat Methods* **11**, 927–930 (2014).

52. Smeets, S., Zou, X. & Wan, W. Serial electron crystallography for structure determination and phase analysis of nanocrystalline materials. *J Appl Crystallogr* **51**, 1262–1273 (2018).

53. Nam, K. H. Serial X-ray Crystallography. *Crystals* **12** (2022).

54. Bücker, R., Hogan-Lamarre, P. & Miller, R. J. D. Serial Electron Diffraction Data Processing With diffractem and CrystFEL. *Front Mol Biosci* **8**, (2021).

55. Bücker, R. *et al.* Serial protein crystallography in an electron microscope. *Nat Commun* **11**, (2020).

56. Palatinus, L. *et al.* Specifics of the data processing of precession electron diffraction tomography data and their implementation in the program PETS2.0. *Acta Crystallogr B Struct Sci Cryst Eng Mater* **75**, 512–522 (2019).

57. Palatinus, L. & Chapuis, G. SUPERFLIP - A computer program for the solution of crystal structures by charge flipping in arbitrary dimensions. *J Appl Crystallogr* **40**, 786–790 (2007).

58. Palatinus, L., Klementová, M., Dřínek, V., Jarošová, M. & Petříček, V. An incommensurately modulated structure of η0-phase of Cu 3+xsi determined by quantitative electron diffraction tomography. *Inorg Chem* **50**, 3743–3751 (2011).

59. Boullay, P., Palatinus, L. & Barrier, N. Precession electron diffraction tomography for solving complex modulated structures: The case of Bi5Nb3O15. *Inorg Chem* **52**, 6127–6135 (2013).

60. Jansen, J., Tang, D., Zandbergen, H. W. & Schenk, H. MSLS, a Least-Squares Procedure for Accurate Crystal Structure Refinement from Dynamical Electron Diffraction Patterns. *Acta Crystallogr A* **54**, 91–101 (1998).

61. Dudka, A. P., Avilov, A. S. & Lepeshov, G. G. Crystal structure refinement from electron diffraction data. *Crystallography Reports* **53**, 530–536 (2008).

62. Oleynikov, P. EMap and eSlice: A software package for crystallographic computing. in *Crystal Research and Technology* vol. 46 569–579 (2011).

63. Palatinus, L. *et al.* Structure refinement from precession electron diffraction data. *Acta Crystallogr A* **69**, 171–188 (2013).

64. Vincent, R. & Midgley, P. A. *Double Conical Beam-Rocking System for Measurement of Integrated Electron Diffraction Intensities*. *Ultramicroscopy* vol. 53 (1994).

65. Palatinus, L., Petříček, V. & Correâ, C. A. Structure refinement using precession electron diffraction tomography and dynamical diffraction: Theory and implementation. *Acta Crystallogr A Found Adv* **71**, 235–244 (2015).

66. Palatinus, L. *et al.* Structure refinement using precession electron diffraction tomography and dynamical diffraction: Tests on experimental data. *Acta Crystallogr B Struct Sci Cryst Eng Mater* **71**, 740–751 (2015).

67. Klar, P. B. *et al.* Accurate structure models and absolute configuration determination using dynamical effects in continuous-rotation 3D electron diffraction data. *Nat Chem* **15**, 848–855 (2023).

68. Cowley, J. M. & Moodie, A. F. The scattering of electrons by atoms and crystals. I. A new theoretical approach. *Acta Crystallogr* **10**, 609–619 (1957).

69. Goodman, P. & Moodie, A. F. Numerical evaluations of N-beam wave functions in electron scattering by the multi-slice method. *Acta Crystallographica Section A* **30**, 280–290 (1974).

70. Bethe, H. Theorie der Beugung von Elektronen an Kristallen. *Ann Phys* **392**, 55–129 (1928).

71. Bloeh, F. *Uber Die Quantenmechanik Der Elek~ronen in Kristallgittern*.

72. O'Keefe, M. A. n-Beam lattice images. IV. Computed two-dimensional images. *Acta Crystallographica Section A* **29**, 389–401 (1973).

73. Palatinus, L., Petříček, V. & Correâ, C. A. Structure refinement using precession electron diffraction tomography and dynamical diffraction: Theory and implementation. *Acta Crystallogr A Found Adv* **71**, 235–244 (2015).

74. Nelder, J. A. & Meadf, R. *A Simplex Method for Function Minimization*. http://comjnl.oxfordjournals.org/.

75. Stewart. A. When is a particle a crystal: electron diffraction will tell. *Eldico Scientific Webinars* vol. Part 14. https://landing.eldico-scientific.com/14th-webinar-recording.

76. Gemmi.M et al. Round Robin on structure refinement quality with 3D electron diffraction data. *in preparation*.

77. De La Flor, G., Orobengoa, D., Tasci, E., Perez-Mato, J. M. & Aroyo, M. I. Comparison of structures applying the tools available at the Bilbao Crystallographic Server. *J Appl Crystallogr* **49**, 653–664 (2016).

78. Passuti, S., Varignon, J., David, A. & Boullay, P. Scanning Precession Electron Tomography (SPET) for Structural Analysis of Thin Films along Their Thickness. *Symmetry (Basel)* **15**, (2023).

79. Passuti, S. Electron crystallography of nanodomains in functional materials. (Cnrs, CRISMAT, Caen, 2024).

80. Klar, P. B. *et al.* Accurate structure models and absolute configuration determination using dynamical effects in continuous-rotation 3D electron diffraction data. *Nat Chem* **15**, 848–855 (2023).

81. Meagher, E. P. & Lager, G. A. Polyhedral thermal expansion in the TiO 2 polymorphs; refinement of the crystal structures of rutile and brookite at high temperature. *The Canadian Mineralogist* **17**, 77–85 (1979).

82. Zhang, H. & Banfield, J. F. *Materials Thermodynamic Analysis of Phase Stability of Nanocrystalline Titania*. *J. Mater. Chem* vol. 8 (1998).

83. Kandiel, T. A., Feldhoff, A., Robben, L., Dillert, R. & Bahnemann, D. W. Tailored titanium dioxide nanomaterials: anatase nanoparticles and brookite nanorods as highly active photocatalysts. *Chemistry of Materials* **22**, 2050–2060 (2010).

84. Suresh, A. *et al.* Ionisation of atoms determined by kappa refinement against 3D electron diffraction data. (2024) doi:10.21203/rs.3.rs-4984819/v1.

85. Coppens, P. *et al.* Net atomic charges and molecular dipole moments from spherical-atom X-ray refinements, and the relation between atomic charge and shape. *Acta Crystallographica Section A* **35**, 63–72 (1979).

86. Zhao, D. *et al.* Recent Progress of Ion-Modified TiO2 for Enhanced Photocatalytic Hydrogen Production. *Molecules* **29** (2024).

87. Nagaraj, G. *et al.* Facile synthesis of improved anatase TiO2 nanoparticles for enhanced solar-light driven photocatalyst. *SN Appl Sci* **2**, (2020).

88. Yu, Z. *et al.* Indium tin oxide as a semiconductor material in efficient p-type dye-sensitized solar cells. *NPG Asia Mater* **8**, e305 (2016).

89. Maniyara, R. A. *et al.* Highly transparent and conductive ITO substrates for near infrared applications. *APL Mater* **9**, (2021).

90. Gross, M., Winnacker, A. & Wellmann, P. J. Electrical, optical and morphological properties of nanoparticle indium-tin-oxide layers. *Thin Solid Films* **515**, 8567–8572 (2007).

91. Sohn, H. Y. & Murali, A. Plasma synthesis of advanced metal oxide nanoparticles and their applications as transparent conducting oxide thin films. *Molecules* **26**, (2021).

92. Calatayud, D. G. *et al.* Highly photoactive anatase nanoparticles obtained using trifluoroacetic acid as an electron scavenger and morphological control agent. *J Mater Chem A Mater* **1**, 14358–14367 (2013).

93. horn, B. M. *et al. Refinement of the Structure of Anatase at Several Temperatures*. Bd* vol. 136 (1972).

94. Guizzardi, M. *et al.* Near-Infrared Plasmon-Induced Hot Electron Extraction Evidence in an Indium Tin Oxide Nanoparticle/Monolayer Molybdenum Disulfide Heterostructure. *Journal of Physical Chemistry Letters* **13**, 9903–9909 (2022).

95. González, G. B. *et al.* Neutron diffraction study on the defect structure of indium-tin-oxide. *J Appl Phys* **89**, 2550–2555 (2001).

96. Cichocka, M. O., Ångström, J., Wang, B., Zou, X. & Smeets, S. High-throughput continuous rotation electron diffraction data acquisition via software automation. *J Appl Crystallogr* **51**, 1652–1661 (2018).

97. Plana-Ruiz, S. *et al.* Fast-ADT: A fast and automated electron diffraction tomography setup for structure determination and refinement. *Ultramicroscopy* **211**, (2020).

98. Cichocka, M. O., Ångström, J., Wang, B., Zou, X. & Smeets, S. High-throughput continuous rotation electron diffraction data acquisition via software automation. *J Appl Crystallogr* **51**, 1652–1661 (2018).

99. Baker, E. N. Poetry in motion: catching molecules in action. *IUCrJ* **11** 129–130 (2024).

100. Klar, P. B. *et al.* Accurate structure models and absolute configuration determination using dynamical effects in continuous-rotation 3D electron diffraction data. *Nat Chem* **15**, 848–855 (2023).

101. Paul, S. *et al.* TiO2 as an Anode of High-Performance Lithium-Ion Batteries: A Comprehensive Review towards Practical Application. *Nanomaterials* vol. 12 Preprint at https://doi.org/10.3390/nano12122034 (2022).

102. Shi, H. *et al.* Titanium dioxide-based anode materials for lithium-ion batteries: structure and synthesis. *RSC Advances* **12** 33641–33652 (2022).

103. Momma, K. & Izumi, F. VESTA 3 for three-dimensional visualization of crystal, volumetric and morphology data. *J Appl Crystallogr* **44**, 1272–1276 (2011).

104. Dambournet, D. *et al.* Combining the pair distribution function and computational methods to understand lithium insertion in brookite (TiO2). *Inorg Chem* **50**, 5855–5857 (2011).

105. Anji Reddy, M. *et al.* Synthesis and lithium insertion into nanophase MgTi2O 5 with pseudo-brookite structure. *Chemistry of Materials* **20**, 2192–2197 (2008).

106. Wechsler, B. A. & Von Dreele, R. B. Structure refinements of Mg2TiO4, MgTiO3 and MgTi2O5 by time-of-flight neutron powder diffraction. *Acta Crystallographica Section B* **45**, 542–549 (1989).

107. Yang, H. & Hazen, R. M. *Crystal Chemistry of Cation Order-Disorder in Pseudobrookite-Type MgTi 2 O 5*. *Journal of Solid state chemistry* **138** (1998).

108. Selvamani, T., Anandan, S., Asiri, A. M., Maruthamuthu, P. & Ashokkumar, M. Preparation of MgTi2O5 nanoparticles for sonophotocatalytic degradation of triphenylmethane dyes. *Ultrason Sonochem* **75**, (2021).

109. De Luna, P. *et al.* What would it take for renewably powered electrosynthesis to displace petrochemical processes? *Science* **364** (2019).

110. Fan, L. *et al. Strategies in Catalysts and Electrolyzer Design for Electrochemical CO 2 Reduction toward C 2+ Products*. *Sci. Adv* vol. 6 http://advances.sciencemag.org/ (2020).

111. Roham Dorakhan, Ivan Grigioni & Byoung-Hoon Lee. A silver–copper oxide catalyst for acetate electrosynthesis from carbon monoxide. *Nature Synthesis* **2**, 448–457 (2023).

112. Phong Duong, H. *et al.* Silver and Copper Nitride Cooperate for CO Electroreduction to Propanol. *Angewandte Chemie - International Edition* **62**, (2023).

113. Xue Wang, Pengfei Ou & Adnan Ozden. Efficient electrosynthesis of n-propanol from carbon monoxide using a Ag–Ru–Cu catalyst. *Nat Energy* **7**, 170–176 (2022).

114. Creissen, C. E. & Fontecave, M. Keeping sight of copper in single-atom catalysts for electrochemical carbon dioxide reduction. *Nature Communications* **13** (2022).

115. Christensen, M., Johnsen, S. & Iversen, B. B. Thermoelectric clathrates of type i. *Dalton Transactions* **39**, 978–992 (2010).

116. Yox, P., Lee, S. J., Wang, L. L., Jing, D. & Kovnir, K. Crystal Structure and Properties of Layered Pnictides BaCuSi2Pn3(Pn = P, As). *Inorg Chem* **60**, 5627–5634 (2021).

117. Folberth, O. G. & Pfister, H. Neue ternäre halbleitende Phosphide MgGeP 2 , CuSi 2 P 3 und CuGe 2 P 3 . *Acta Crystallogr* **14**, 325–326 (1961).

118. Crystal Research and Technology - 1994 - Bhikshamaiah - X-ray determination of thermal lattice expansion of CuSi2 xP3 x .

119. Mozharivskyj, Y., Lang, O. & Franzen, H. F. Modulated crystal structure and electronic properties of semiconductor CU47Si91P144. *Z Anorg Allg Chem* **626**, 2153–2160 (2000).

120. Christensen, M., Johnsen, S. & Iversen, B. B. Thermoelectric clathrates of type i. *Dalton Transactions* **39**, 978–992 (2010).

121. Song, Y. *et al.* A straightforward approach to high purity sodium silicide Na4Si4. *Dalton Transactions.* **45** 50 (2021)

122. Wallinda, J. & Jeitshko, W. Ni1.282(4)Si1.284(5)P3 or NiSi2P3: Two Solutions with Different Atom Distributions for One Single-Crystal X-ray Data Set, Both Refined to Residuals of Less than 2.5%. *Solid State Chemistry* **114**, 476–480 (1995).

123. T. Janssen, A. Janner, A. Looijenga-Vos & P. M. de Wolff. Incommensurate and commensurate modulated structures. in *International Tables for Crystallography* vol. C 907–955 (2006).

124. Van Smaalen, S. *An Elementary Introduction to Superspace Crystallography*.

APPENDIX A

List of Author's contribution

Articles

2 articles (1 as first author) are in preparation and should be submitted soon.

Oral Presentations

'3D Electron Diffraction for accurate structure analysis of nanoparticles', 34th European Crystallographic Meeting. 26-30 August 2024 (ECM34). Padova, Italy.

'Precession Electron Diffraction Tomography for structural analysis of Nanoparticles: A study of minimal size and associated dynamical effects', 26th Congress and General Assembly of the International Union of Crystallography (IUCr 2023). 22-29 August 2023, Melbourne, Australia.

'Precession Electron Diffraction Tomography for structural analysis of Nanoparticles: A study of minimal size and associated dynamical effects', 18th Meeting of French Microscopy Society (*Sfmu*). 03-07 July 2023, Rouen, France.

'Challenges for 3D ED applied to small nanoparticles', Workshop on Electron Crystallography. 30-31 June 2023, Antwerp, Belgium.

Posters Presentations

'3D ED on isolated nanoparticles: exploring the size limit of crystals', 33rd European Crystallography Meeting (ECM33). 23-27 August 2022, Versailles, France.

'3D ED on isolated nanoparticles: exploring the size limit of crystals', Electron Crystallography School (ECS2022). 29-1 September 2022, Caen, France.

Scientific workshops

NanED workshop IV – NanED Meets Industry. 06-07 December 2023, Caen, France.

NanED workshop III on TEM Imaging and Spectroscopy. 01-02 June 2023, Antwerp, Belgium.

Workshop on Electron Crystallography. 30-31 June 2023, Antwerp, Belgium.

Destiny workshop in operando studies using synchrotron radiation. 15-19 May 2023, Trieste, Italy

NanED workshop II on Imperfect crystals, complementarity with XRPD, Intellectual properties and patent in Science. 06-08 December 2022, Mainz, Germany.

Electron Crystallography School (ECS2022). 29-01 September 2022, Caen, France.

Summer School on Neutron, Electrons and X-ray techniques. 19-21 July 2022, Almería, Spain

NanED workshop I on Structure Solution and Refinement. 25-27 May 2022, Prague, Czech Republic.

APPENDIX B

List of NanED Secondments

IIT, Pontedera, Italy. 01- 29 February 2024.

The goal of this collaboration was to learn how to use a microscope at a lower voltage, specifically the Zeiss Libra 120, for organic samples. Unlike the inorganic nanoparticles discussed in this thesis, the inorganic crystals were larger and also beam-sensitive, which required the adoption of different techniques for TEM grid preparation and data collection.

CODEX International, Lisieux, France. 30 October – 30 November 2023.

The main objective of collaborating with a company was to gain an understanding of the process involved in finding suppliers, researching prices, and reaching out to potential clients. This collaboration provided me with a broader perspective on what a company can accomplish in terms of sales, offering me the chance to explore areas outside of the purely scientific field.

Elettra Synchrotron, Trieste, Italy. 03 April – 12 May 2023.

The objective was to learn how to work on different beamlines at the synchrotron, write proposals, and spend time with different users to understand the challenges they faced with their samples. Additionally, I observed the different experiments that could be performed, specifically on the MCX beamline. I also had the opportunity of preparing capillaries and conducted measurements on the compounds previously mentioned in this thesis: TiO_2 brookite, TiO_2 anatase, and ITO.

Antwerp University (EMAT), Antwerp, Belgium. 1 February – 1 April 2023.

The primary objective was to gain expertise in performing in-situ experiments under both gas and liquid environments, as well as to broaden my experience with a variety of microscopes. During this period, I had the opportunity to work extensively with advanced instruments, including the FEI Tecnai, Osiris Tecnai, and Titan microscopes.

Electron crystallography of nanoparticles

Keywords: Transmission electron microscopy, 3D Electron diffraction, dynamical refinement, energy materials.

Abstract: Nanoparticles (NPs) are of great interest due to their unique properties, making them useful in different scientific fields. Understanding the crystallographic structure of NPs is crucial for uncovering their distinct characteristics and designing new materials. Single Crystal X-ray Diffraction is employed for accurate crystal structure determination; however, it is limited by the small size of NPs. Powder X-ray Diffraction (PXRD serves as an alternative for phase identification and average particle size, but it has limitations in structure refinement due to peak broadening and overlapping. In particular, 3D Electron Diffraction (3D ED) techniques have revolutionized the field, enabling detailed structural analysis of very small crystals. This work aims to test the limits of 3D ED for analyzing the structure of inorganic nanoparticles as small as 10 nm using various protocols, such as precession-assisted 3D ED, continuous rotation 3D ED, and serial ED. It also explores the potential of 3D ED compared to PXRD and its application to various structural characterization challenges in NPs, including the detection of light atoms, refinement of mixed occupancies, and solving complex unknown structures.

Mots clés: Microscopie électronique en transmission, Diffraction électronique 3D, Raffinement dynamique, Matériaux pour l'énergie.

Résumé : Les nanoparticules (NPs) suscitent un grand intérêt en raison de leurs propriétés uniques, ce qui les rend utiles dans différents domaines scientifiques. Comprendre la structure cristallographique des NPs est crucial pour découvrir leurs caractéristiques distinctes et concevoir de nouveaux matériaux. La diffraction des rayons X sur monocristal est utilisée pour la détermination précise de la structure cristalline ; cependant, elle est limitée par la petite taille des NPs. La diffraction des rayons X sur poudre (PXRD) constitue une alternative pour l'identification de phases et la taille moyenne des particules, mais elle présente des limitations en matière de raffinement de structure en raison de l'élargissement et du chevauchement des pics. La diffraction des électrons (ED) apparaît comme une méthode précieuse pour étudier des nanoparticules individuelles, car les électrons interagissent plus fortement avec la matière que les rayons X. En particulier, les techniques de diffraction des électrons en 3D (3D ED) ont révolutionné ce domaine, permettant une analyse structurelle détaillée de très petits cristaux. Ce travail vise à tester les limites de la 3D ED pour analyser la structure de nanoparticules inorganiques aussi petites que 10 nm en utilisant différents protocoles, tels que la 3D ED assistée par précession, la 3D ED en rotation continue ou la 3D ED en série. Il explore également le potentiel de la 3D ED par rapport à la PXRD et son application à divers défis de caractérisation structurelle des nanoparticules. Ceux-ci incluent, par exemple, la détection d'atomes légers, le raffinement des occupations mixtes ou la résolution de structures complexes inconnues.